


University of Cagliari

PhD Course in

Electronic and Computer Engineering

Class XXVI

PhD Dissertation title

Inkjet printing: technique and applications for organic electronic devices

Scientific field

ING-INF/01 – ELECTRONICS

Author: Alberto Loi

PhD Course Coordinator: Prof. Fabio Roli

Advisor: Prof. Annalisa Bonfiglio

Academic year of PhD defence 2012 – 2013


Università degli Studi di Cagliari

DOTTORATO DI RICERCA

Ingegneria Elettronica e Informatica

Ciclo XXVI

TITOLO TESI

Inkjet printing: technique and applications for organic electronic devices

Settore scientifico disciplinare di afferenza

ING-INF/01 - ELETTRONICA

Presentata da: Alberto Loi

Coordinatore Dottorato Prof. Fabio Roli

Tutor/Relatore Prof.ssa Annalisa Bonfiglio

Esame finale anno accademico 2012 – 2013

Devoutly dedicated to my past,
present and future family

Abstract

Since the discovery of the polyacetylene conductivity in 1977 by Shirakawa, MacDiarmid and Heeger, Organic Electronics has been growing and establishing for a new generation of electronic devices. On one hand, the unique properties of polymeric semiconductors and conductors, such as flexibility and transparency, allow the fabrication of low-cost devices over large area: the most common are the Organic Light Emitting Diodes (OLEDs) and the organic photovoltaic cells. On the other hand, much effort has been made to investigate new technologies and processes for the realization of high-performance organic transistors and sensors. Among them, Inkjet Printing is a promising technique which exploits all the advantages of organic materials, such as low-cost and solution processability, and allows the large-scale automated fabrication of large area devices.

This thesis describes the work carried out with a piezoelectric drop-on-demand inkjet printer, the Dimatix Materials Printer 2831. The first chapter gives an overview on Organic and Printed Electronics state-of-art, also describing the physical principles of conductivity in organic molecules. The second chapter is totally focused on the inkjet printing technique: after a brief description of the printer employed, a detailed description of the printing process, from the ink formulation to the drop deposition and drying phenomena, is presented. Moreover the materials employed are described together with the printing parameters set for achieving the best deposition condition. Chapter 3 is devoted to tactile sensing, which is the main application of the Organic Field-Effect Transistors (OFETs) in this work within the ROBOSKIN project. After an overview of inorganic tactile sensors and of the fundamentals of strain sensing in OFETs, the fabrication steps are described followed by the detailed electromechanical characterization of the various strain sensors realized. Finally, the fourth chapter describes other applications of inkjet printing developed in this work: organic diodes and photodiodes within the HYMEC project, patterned electrodes for the detection of cells electrical activity, both *in vivo* and *in vitro*, and a RFID tag antenna.

The author, Alberto Loi, gratefully acknowledges Sardinia Regional Government for the financial support of his PhD scholarship (P.O.R. Sardegna F.S.E. Operational Programme of the Autonomous Region of Sardinia, European Social Fund 2007-2013 - Axis IV Human Resources, Objective l.3, Line of Activity l.3.1).

Sommario

A partire dalla scoperta della conducibilità del poliacetilene, avvenuta nel 1977 ad opera di Shirakawa, MacDiarmid e Heeger, l'Elettronica Organica è cresciuta e si è affermata come tecnologia per una nuova generazione di dispositivi elettronici. Da una parte, le proprietà peculiari dei conduttori e semiconduttori a base polimerica, come la flessibilità e la trasparenza, permettono la produzione a basso costo di dispositivi su larga area: tra questi, i più comuni sono i Diodi Organici ad Emissione di Luce (OLED) e le celle fotovoltaiche a base organica. D'altra parte, si sta facendo un grande sforzo per studiare nuove tecnologie e processi che consentano la realizzazione di transistor e sensori organici ad alte prestazioni. Tra queste tecnologie, la Stampa a Getto d'Inchiostro risulta una tecnica promettente che sfrutta tutti i vantggi dei materiali organici, come i bassi costi e la processabilità in fase liquida, per fabbricare su larga scala in modo automatizzato dispositivi su larga area.

Questa tesi descrive il lavoro svolto con una stampante piezoelettrica di tipo drop-on-demand, la Dimatix Materials Printer 2831. Il primo capitolo presenta una panoramica sullo stato dell'arte dell'Elettronica Organica e dell'Elettronica Stampanta e descrive anche i principi fisici della conducibilità nelle molecole organiche. Il secondo capitolo è interamente incentrato sulla tecnica di stampa a getto d'inchiostro: dopo una breve introduzione della stampante adoperata, è presentata una descrizione dettagliata del processo di stampa, dalla formulazione dell'inchiostro ai fenomeni di deposizione e asciugatura delle gocce. Inoltre sono descritti i materiali impiegati in questa tesi assieme ai parametri di stampa impostati per ottenere, caso per caso, le migliori condizioni operative di deposizione. Il capitolo 3 è incentrato sui sensori tattili, principale applicazione dei transistor organici a effetto di campo in questa tesi, in particolare nell'ambito del progetto ROBOSKIN. Dopo una panoramica sui sensori tattili inorganici e sui fondamenti che consentono di ottenere sensori di deformazione a partire da transistor organici, sono presentate le fasi di fabbricazione seguite da una dettagliata caratterizzazione elettromeccanica dei vari sensori realizzati. Infine, il quarto capitolo descrive altre applicazioni della stampa a getto d'inchiostro sviluppate in questa tesi: diodi e fotodio-

di organici nell'ambito del progetto HYMEC, elettrodi per il rilevamento dell'attività elettrica cellulare, sia *in vivo* sia *in vitro*, e antenne per identificazione a radiofrequenza (RFID).

La presente tesi è stata prodotta durante la frequenza del corso di dottorato in Ingegneria Elettronica e Informatica dell'Università degli Studi di Cagliari, a.a. 2012/2013 - XXVI ciclo, con il supporto di una borsa di studio finanziata con le risorse del P.O.R. SARDEGNA F.S.E. 2007-2013 - Obiettivo competitività regionale e occupazione, Asse IV Capitale umano, Linea di Attività l.3.1 "Finanziamento di corsi di dottorato finalizzati alla formazione di capitale umano altamente specializzato, in particolare per i settori dell'ICT, delle nanotecnologie e delle biotecnologie, dell'energia e dello sviluppo sostenibile, dell'agroalimentare e dei materiali tradizionali".

List of related publications

Journal articles

- **Piezoelectric Polymer Transducer Arrays for Flexible Tactile Sensors**.
  L. Seminara, L. Pinna, L. Valle, L. Basiricò, **A. Loi**, P. Cosseddu, A. Bonfiglio, A. Ascia, M. Biso, A. Ansaldo, D. Ricci, and G. Metta.
  IEEE Sensors Journal, vol. 13, no. 10, p. 4764-4772, 2013.

- **Organic Bendable and Stretchable Field Effect Devices for Sensing Applications**.
  A. Loi, L. Basiricò, P. Cosseddu, S. Lai, M. Barbaro, A. Bonfiglio, P. Maiolino, E. Baglini, S. Denei, F. Mastrogiovanni, and G. Cannata.
  IEEE Sensors Journal, vol. 13, no. 12, p. 4764-4772, 2013.

- **A Wideband PET Inkjet-Printed Antenna for UHF RFID**.
  G. A. Casula, G. Montisci, and G. Mazzarella.
  IEEE Antennas and Wireless Propagation Letters, vol. 12, p. 1400-1403, 2013.

- **Investigation on inkjet printing conditions of TIPS-pentacene as active layer for organic thin film transistors**.
  A. Loi, L. Basiricò, P. Cosseddu, B. Fraboni, A. Scidà, S. Milita, I. A. Grimaldi, F. Loffredo, F. Villani, and A. Bonfiglio.
  In preparation.

Book chapter

- **Chemical and Physical Sensors based on organic transistors**.
  P. Cosseddu, M. Demelas, S. Lai, **A. Loi**, M. Barbaro, and A. Bonfiglio.
  Invited contribution in *Handbook of flexible organic electronics. Materials, manufacturing and applications*, under revision.

Proceedings of international conferences

- **Matrices of inkjet printed OFETs for the realization of artificial robotic skin**.
  A. Loi, L. Basiricò, P. Cosseddu, S. Lai, P. Maiolino, E. Baglini, S. Denei, F. Mastrogiovanni, G. Cannata, C. Palomba, M. Barbaro, and A. Bonfiglio.
  Material Research Society (MRS) Symposium Proceedings, Vol. 1401 - MRS Fall Meeting 2011.

- **Inkjet printed OTFTs for the Realization of Artificial Robot Skin**.
  A. Loi, L. Basiricò, P. Cosseddu, S. Lai, M. Barbaro, A. Bonfiglio, E. Baglini, S. Denei, P. Maiolino, F. Mastrogiovanni, and G. Cannata.
  Human-Robot Interaction (HRI) 2012 Workshop on Advances in Tactile Sensing and Touch, extended abstract.

- **Design, fabrication and test of arrays of piezoelectric transducers for robotic tactile sensors**.
  L. Seminara, L. Pinna, L. Valle, L. Basiricò, **A. Loi**, P. Cosseddu, A. Bonfiglio, A. Ascia, M. Biso, A. Ansaldo, D. Ricci, and G. Metta.
  Human-Robot Interaction (HRI) 2012 Workshop on Advances in Tactile Sensing and Touch, extended abstract.

- **Inkjet printed Organic Thin Film Transistors based tactile transducers for artificial robotic skin**.
  P. Cosseddu, L. Basiricò, **A. Loi**, S. Lai, P. Maiolino, E. Baglini, S. Denei, F. Mastrogiovanni, G. Cannata, and A. Bonfiglio.
  The Fourth IEEE RAS/EMBS International Conference on Biomedical Robotics and Biomechatronics, p. 1907-1912, 2012.

- **Organic Bendable and Stretchable Field Effect Devices for Sensing Applications**.
  A. Loi, P. Cosseddu, L. Basiricò, S. Lai, and A. Bonfiglio.
  2012 IEEE Sensors.

- **Piezoelectric Polymer Transducer Arrays for Flexible Tactile Sensors**.
  L. Seminara, L. Pinna, L. Valle, L. Basiricò, **A. Loi**, P. Cosseddu, A. Bonfiglio, A. Ascia, M. Biso, A. Ansaldo, D. Ricci, and G. Metta.
  2012 IEEE Sensors.

Contents

List of Figures

List of Tables

1 Printed Organic Electronics

This first chapter is intended to be an introduction, from many points of view, of the work carried out for this thesis.
In the section 1.1 a comparison between silicon-based and polymer-based electronics is given, in order to understand the state of the art of organic electronics, the trends in the scientific research together with its market perspective.
Section 1.2 is devoted to an overview of the chemical and physical principles of the conduction in organic electronics. In particular, the morphology and the classes of organic molecules are described since they are fundamental part for the comprehension of the following chapters.
Finally, section 1.3 focuses on the technology employed in this work: starting with a general overview on printed electronics, then the key feature of this thesis, *i. e.* inkjet printing, is analyzed more in detail.

1.1 Compared history of inorganic and organic electronics

The potentiality, the development and the diffusion of modern Microelectronics and Nanoelectronics in everyday life, from telecommunications to biomedicine, can be fully understood only with a deep and careful insight into the materials employed, along with the theoretical basis and the technological knowledge. These points are mandatory for those who want to understand how simple chemical elements can be transformed into very complex and miniaturized systems and how the distance between the organic world and the inorganic world is continuously decreasing, especially at micro- and nanometer scale.

1.1.1 History of inorganic electronics

The Maxwell's equations, published in the second half of the XIX century [26], constituted a complete theoretical basis for the analysis of the electromagnetic fields. This theory divided materials into two general groups: conductive materials (metals) and insulating materials (dielectrics) [27]. During the XIX century, non-ohmic characteristics for some materials were recorded: in 1839 Michael Faraday described the electrical conductivity increased with temperature of silver sulfide crystals, which is the opposite as expected for metals [28]; also, in 1874 Ferdinand Braun discovered the rectifier effect under the contact between a metal point and a galena crystal.

The first patents regarding electronic devices, as we mean them today, were deposited in the early years of the XX century: in 1904 the semiconductor rectifier by Jagadish Chandra Bose and in 1926 the field-effect semiconductor device by Julius Lilienfeld. Anyway, only after the formulation of the quantum mechanics and the development of the solid state physics, theoretical demonstrations to the previously discovered effects could be given.

In 1931 Alan Wilson explained the properties of semiconductors, which represent the core of modern electronics [29, 30]. The solution of the time-independent Schrödinger equation:

$$E\psi(\vec{r}) = \left[-\frac{\hbar^2}{2m}\nabla^2 + V(\vec{r})\right]\psi(\vec{r}) \tag{1.1}$$

gives the eigenvectors, *i. e.* the wave-function $\psi(\vec{r})$, and the eigenvalues, *i. e.* the associated energy states E_n of the quantum system constituted of nuclei and electrons. In particular in crystalline solids, included semiconductors, charged and ideally clamped atoms are arranged in a periodic structure among the three dimensions: electrons, which can be strongly or weakly bound to their nuclei on the basis of the specific material considered, are subjected to a periodic potential $V(\vec{r})$. This ensemble of energy states E_n for all the electrons in a crystalline solid results in physically continuous energy bands, whose energy ranges are permitted for the charge carriers, separated by energy band gaps, whose energy ranges are forbidden for the charge carriers. Basically, the transition from single atoms to a 'many body' crystalline structure is described, in solid state physics, by the transition from single energy levels to separated energy bands.

The physical explanation of the different behavior for metals, dielectrics and semiconductors is easily achieved from the band diagram theory and is depicted in figure 1.1. The Fermi level E_F is the highest occupied energy level at absolute zero temperature or, equivalently,

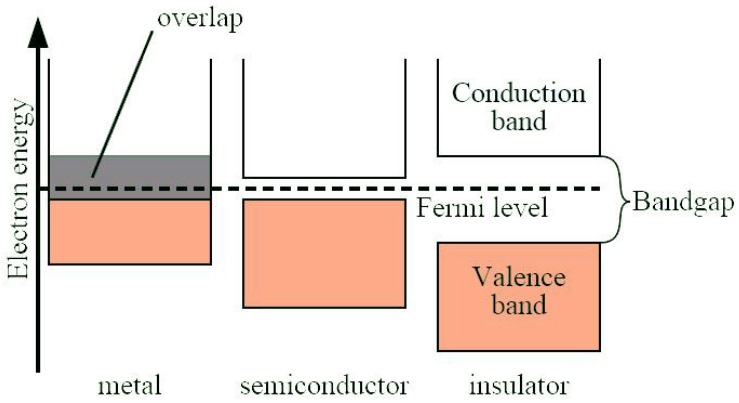

Figure 1.1: Energy bands for metals, semiconductors and insulators.

the energy level whose occupation probability is 1/2 at higher temperatures. E_F is located inside an allowed energy band in conductors, while it is inside the forbidden energy gap in insulators and semiconductors. As a consequence, in metals the thermal energy is sufficient for electrons to break the bounds with their nuclei and move across the solid under a very weak electric field applied, therefore allowing a current flow. On the contrary, in dielectrics the electrons fill an entire energy band and their band gaps is too large (generally above 5 eV) with respect to the thermal energy, which at room temperature is 26 meV: they are strictly bound to their nuclei and, as a consequence, even a strong electric field induces an almost-zero current flow. Semiconductors are formally insulators whose band gaps are quite smaller, generally between 1 and 2 eV: in this case, electrons excited with thermal energy have a non-zero probability to jump from the highest fully occupied band, called valence band, to the lowest unoccupied band, called conduction band, thus generating a very moderate current flow.

The crystal structure of extremely pure semiconductors, referred as intrinsic semiconductors, can be modified by adding atoms of other elements, called dopant, thus giving origin to extrinsic semiconductors: this doping process causes an increase of electrons (n-type doping) or an increase of holes, *i. e.* a deficiency of electrons (p-type doping), depending on the specific materials employed. In the band diagram theory, this results in the addition of extra energy levels and in the repositioning of the Fermi level E_F: a fine tuning of the doping process allows a good control of the electrical properties of the semiconductor.

The band diagram theory and the role of doping opened the way to the development of semiconductor-based electronic devices: in 1940 Russel Ohl discovered the p-n junction; in

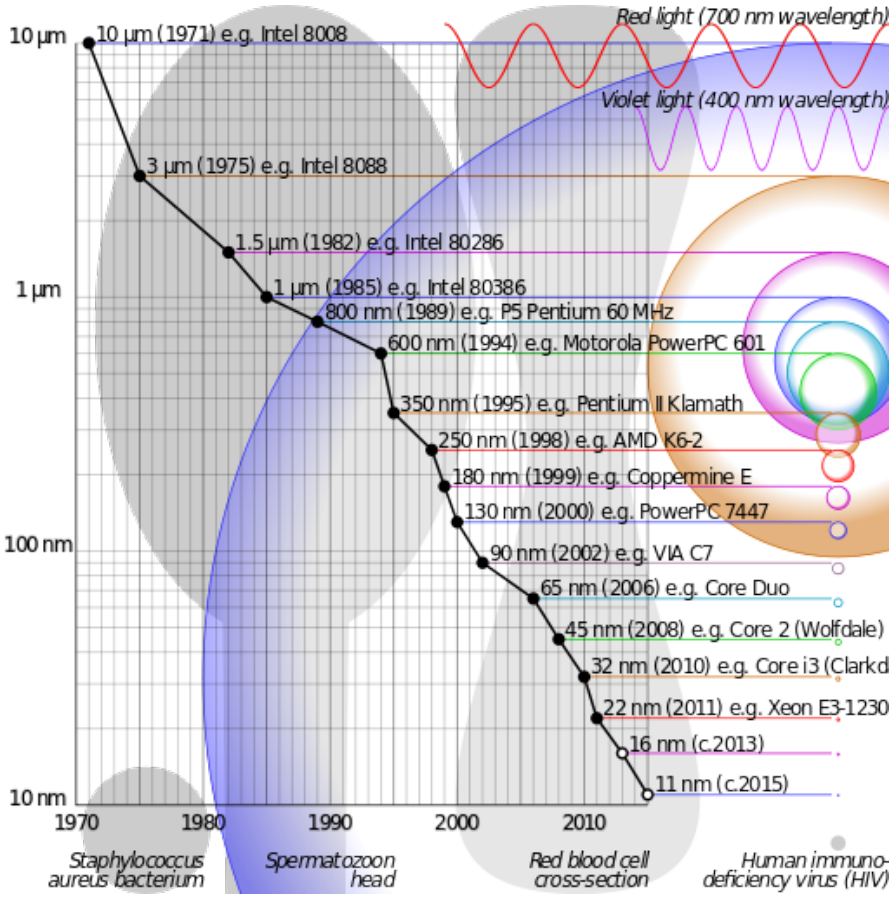

Figure 1.2: Evolution of computer processors during the last decades: the scaling down of the transistors size correctly follows Moore's prediction.

1948 William Shockley conceived the junction transistor, while the first n-p-n bipolar junction transistor (BJT) was fabricated in 1951 by Gordon Teal and Morgan Sparks at Bell Laboratories. Until 1954 Germanium was the most employed semiconductor for the fabrication of transistors: in this year, Morris Tanenbaum realized the first n-p-n transistor with Silicon, which offered better performances and soon became the main element that contributed to the development and the diffusion of electronic devices. After the improvement of the fabrication processes, the first Metal-Oxide-Semiconductor Field-Effect Transistor (MOSFET) was demonstrated and realized in 1960 by John Atalla and Dawon Kahng: from this point on, MOSFETs became the key devices of electronic circuits and still today they are the most employed devices in Microelectronics.

The road to modern electronics was ready: in particular the fabrication of the silicon-based Read-Only-Memory (ROM, in 1965) and the Programmable ROM (in 1971 by Dov Frohman) opened the way to the realization of personal computers. It is important to remark that ev-

ery single step could be possible only with the refinement of the fabrication processes of the devices, obtaining better performances in smaller size. This point was observed by Gordon Moore in 1965, who predicted that the density of transistors would double every two years [31]: this trend still stands nowadays. Beyond its electrical properties, Silicon and other inorganic semiconductors are subjected to interesting effects: they are sensitive to many external agents, such as light, pressure, temperature and magnetic fields. Thus this sensitivity, if properly tuned and controlled, can be used for the fabrication of different types of sensors and actuators, such as MEMS, photodetectors, lasers, diode thermometers, which can be integrated within the electronic circuits. Nowadays Silicon technology has reached extremely advanced levels: the scaling down of the transistors size, which correctly follows Moore's prediction, allows to achieve device dimensions comparable to those of cells and viruses (figure 1.2).

1.1.2 History of organic electronics

Parallel to this interesting progress, another adventure was taking place during the XX century [32–34]. The term *polymer*, used for the first time in 1832 by Jacob Berzelius [35], refers to a large Carbon-based molecule composed of many repeated units, the *monomers*. Polymers were historically known to have an insulating behavior: their conductivity decreases at low temperatures, same as semiconductors, while for metallic materials it increases, leading to superconductivity. This is summarized in figure 1.3. Experiments on polymer conductivity have been carried out since the XIX century. In 1862 Henry Letheby obtained a partly-conductive 'blue substance', probably polyaniline, by oxidation of aniline in sulphuric acid [36]. Moreover, in 1906 Pochettino reported the photovoltaic effect in anthracene [37], an organic molecule widely used in the following decades for the interpretation of many physical properties by means of quantum physics. However the first synthesized crystals were too thick and they needed a very high voltage to observe electroluminescence, and this limited further developments.

Only in the second half of the XX century a deep comprehension of this phenomenon was achieved. Inspired by the discovery of the transistor and the advances in condensed matter theory, in 1954 Akamatu *et al.* reported fairly good electrical conductivity (10^{-3} S/cm) achieved with a polycyclic aromatic hydrocarbon, *perylene* [38], which actually is a small molecule and not a polymer. Preliminary studies of electrical and optical properties of poly-

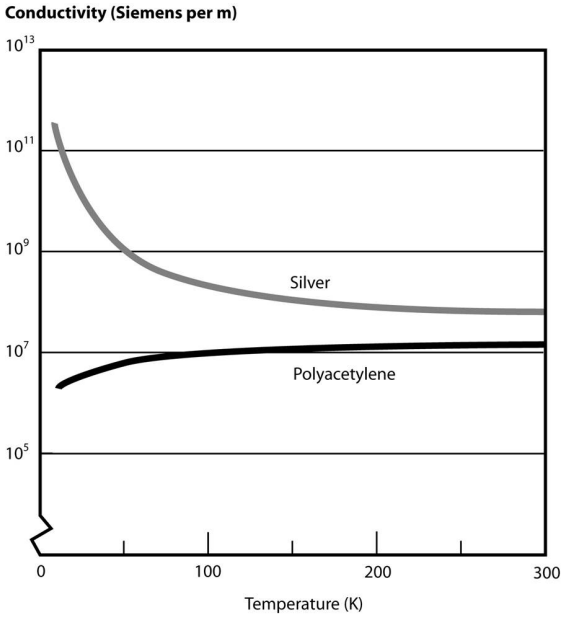

Figure 1.3: Conductivity dependance on temperature: while in metals it increases at low temperature, in polymers, like polyacetylene, as well as in semiconductors, it decreases.

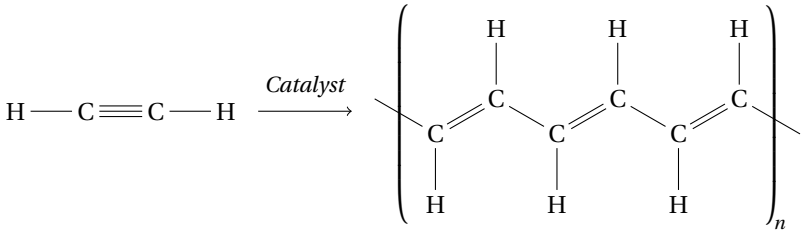

Figure 1.4: Polymerization of polyacetylene from the acetylene molecule.

mer chains were made around 1960 [39]. The interest in polymers increased and chemists investigated new methods to obtain longer organic molecules. In 1957 Giulio Natta and coworkers studied a method to polymerize polyacetylene starting from acetylene, known as Ziegler-Natta polymerization: the result was a black powder, which was air-sensitive, insoluble and infusible [40]. This method represented a great step forward to obtain long polymeric chains and Giulio Natta and Karl Ziegler were awarded with the Nobel Prize in 1963 [41].
In the following decade, major attention was devoted to superconductivity of some organic polymers, which showed a metal-like behavior, opposite as expected. Even though some attempts to achieve it at room temperature were carried out by means of excitonic theory [42], major interest was devoted to superconductivity at ultra low temperature, as low as than 10 K: particolar attention was given to poly(sulfur nitride) [43].

But in the same years, another route was being followed to the investigation of polymer

electrical conductivity: π-conjugated materials, that will be discussed in detail in Section 1.2. In the early 1970s Hideki Shirakawa worked on the polymerization of polyacetylene trying different catalysts with respect to Ziegler-Natta nethod. He obtained a silvery powder, but despite its metallic appearance it conductivity was very low: $10^{-8} - 10^{-7}$ S/m for *cis*-polyacetylene and $10^{-3} - 10^{-2}$ S/m for *trans*-polyacetylene [44]. Some years later, in 1975, he met Alan Heeger and Alan MacDiarmid, who were studying the metallic properties of poly(sulfur nitride).

Applying their experience with polymers, they decided to treat silvery polyacetylene, prepared by Shirakawa, with iodine vapour: they obtained a conductivity of 3000 S/m for *trans*-polyacetylene, with an increase of six orders of magnitudes over the untreated material. The same results were obtained by treating silvery polyacetylene with other halogen vapours, like chlorine or bromine: this treatment was called 'doping' by analogy with the doping of Silicon-based semiconductors [45, 46]. Several experiments followed, which showed even a major conductivity *cis*-polyacetylene, eleven orders of magnitude more than the undoped molecule, when treated with AsF_5. Since it was found out that doping plays a fundamental role for the achievement of conductivity, several studies were focused on it in the next years [47–49].

Together with electrical conductivity, also optical properties of organic materials were investigated in the following decade, giving rise to the organic optoelectronics. Actually, the first working polymer-based devices were Organic Light Emitting Diodes (OLEDs), realized both by means of small molecules [50] and long-chain polymers [51]. The direct and most natural consequence of organic optoelectronics was the birth of organic photovoltaics, which is the field where organic electronics has reached its maximum commercial applications. Although the photovoltaic effect had been already discovered for organic molecules towards the end of the 1960s [52], a deep and systematic study was carried on since the last decade of the XX century. The comprehension on matter-radiation interactions and the progress on the fabrication process allowed the realization of devices with even higher efficiency since the early 1990s: the first devices were based on the Schottky-type diode [53], but donor-acceptor based systems were soon revealed to bea more promising route to generating separate photo-induced charges [54]. Finally, composites of a donor and an acceptor forming a bulk heterojunction system prevailed [55] and still nowadays these are the most employed and advanced solution.

Also transistor-type devices were developed since the last years of the 1980s: in particular the

works by Richard Friend in 1988 [56] and Francis Garnier in 1990 [57] gave the highest contribute to the growth and the diffusion of the Organic Field-Effect Transistors (OFETs). While the original structure was created following the inorganic counterpart, along the time several new structures have been created which could achieve specific requirements, for example dedicated area to external stimuli for sensing applications [58]. The most important figure-of-merit for OFETs is the field-effect mobility (μ): progress, carried on especially in chemical synthesis of organic semiconductors and in interface engineering between different layers, increased the mobility from values lower than 10^{-3} $cm^2V^{-1}s^{-1}$ of the first years to values in the range 1-10 $cm^2V^{-1}s^{-1}$ of the present days. The actual development of OFETs has come since the 2000 and the achievements have been reported in detail on several reviews over the last years [59–61].

The importance and the potentiality of Organic Electronics have been revealed to all the world, more than to the scientific community, when in 2000 Shirakawa, McDiarmid and Heeger were awarded with the Nobel Prize for Chemistry, since their work on electrical conductivity in polymers is considered as the fundamental step to the development of branch of knowledge [32]. Also, the *Millennium Technology Prize* was awarded in 2010 by the Finnish Accademy to Michael Grätzel for the development of the dye-sensitized solar cells and to Richard Friend for his great work on electroluminescent polymer-based diodes, on OFETs and in general on organic photovoltaics [62].

1.1.3 Overview on contemporary trend of organic electronics

Today, the global market of semiconductors is still dominated by silicon-based devices. In figure 1.5 the top 20 sales leaders of inorganic semiconductors are shown [63]. Integrated circuits, as well as optoelectronics, discrete components and sensors are included. The top-leader still remains Intel, with a sales volume almost reaching 50B $, followed by Samsung and two fast-growing East-Asian companies (TSMC from Taiwan and SK Hynix from South Korea). In this scenario, the first european sales leader is the franco-italian ST Microelectronics, which in 2013 still suffers from the recent economical crisis.

Fabrication steps of silicon-based circuits involve extremely expensive technological processes. Ultra-pure silicon wafers are created in clean room, at ultra-high vacuum levels and temperatures as high as 1500 K. Also, doping, oxidation and photolithography require even higher-level processing conditions as the scaling down of the device dimensions (above all

2013 Top 20 Semiconductor Sales Leaders Forecast
($M, Including Foundries)

2013F Rank	2012 Rank	Company	Headquarters	2012 Tot Semi	1Q13 Tot Semi	2Q13 Tot Semi	3Q13 Tot Semi	4Q13F Tot Semi	2013F Tot Semi	2013F/2012 % Change
1	1	Intel	U.S.	49,114	11,555	11,785	12,366	12,615	48,321	-2%
2	2	Samsung	South Korea	32,251	7,946	7,769	8,805	9,070	33,590	4%
3	3	TSMC*	Taiwan	16,951	4,460	5,152	5,377	4,815	19,804	17%
4	4	Qualcomm**	U.S.	13,177	3,916	4,222	4,457	4,550	17,145	30%
5	8	SK Hynix	South Korea	9,057	2,577	3,521	3,692	3,250	13,040	44%
6	6	Toshiba	Japan	11,217	2,938	2,868	3,356	3,035	12,197	9%
7	5	TI	U.S.	12,081	2,718	2,872	3,064	2,820	11,474	-5%
8	10	Micron	U.S.	8,002	2,158	2,493	2,900	3,000	10,551	32%
9	9	ST	Europe	8,364	1,994	2,033	2,077	2,080	8,184	-2%
10	11	Broadcom**	U.S.	7,793	1,954	2,035	2,146	1,975	8,110	4%
11	7	Renesas	Japan	9,314	1,886	1,920	2,101	1,920	7,827	-16%
12	14	Infineon	Europe	4,928	1,208	1,327	1,390	1,340	5,265	7%
13	13	AMD**	U.S.	5,422	1,088	1,161	1,461	1,534	5,244	-3%
14	12	Sony	Japan	5,709	1,247	1,144	1,203	1,295	4,889	-14%
15	15	NXP	Europe	4,325	1,085	1,188	1,249	1,265	4,787	11%
16	22	MediaTek**	Taiwan	3,366	817	1,115	1,308	1,275	4,515	34%
17	17	GlobalFoundries*	U.S.	4,013	946	1,020	1,125	1,170	4,261	6%
18	19	Freescale	U.S.	3,803	925	987	1,030	1,000	3,942	4%
19	20	UMC*	Taiwan	3,730	898	1,016	1,060	945	3,919	5%
20	18	Nvidia**	U.S.	3,965	939	903	1,005	905	3,752	-5%
Top 20 Total				216,582	53,255	56,531	61,172	59,859	230,817	7%

*Foundry **Fabless

Source: IC Insights' Strategic Reviews Database

Figure 1.5: World market of silicon-based top 20 sales leaders in 2013.

the channel length of a MOSFET) requires even more accuracy and resolution. Such expensive fabrication requirements can be amortized only with a large-scale production, thus only relatively few companies can afford them. The applications for inorganic technology widely range from personal computers, smartphones and tablet to biomedicine, electrical appliances, automotive and aerospace. The diffusion of microelectronics in every part of modern life constantly demands for the devices' miniaturization: personal computers, formerly heavy and bulky, have been replaced by light portable devices, touchable screens, electronic textiles with integrated functions. This trends leads to the disappearance of the "electrical object" as it is integrated within "common-use objects", and it is not hard to depict a future where everybody activates and employs complex electronic circuits almost without being aware of it.

The top-down approach mentioned above starts from electronic devices, which form "many-body" complex systems, and constantly reduces their physical dimensions. The limit is being reached as, almost controlling the deposition atom-by-atom, the many-body approximations are not fulfilled anymore and thus the scaling down bumps towards second-order collateral effects.

A totally different, bottom-up approach guides the development of organic electronics: in this case, starting from a molecular level, basic functions can be satisfied by single molecules

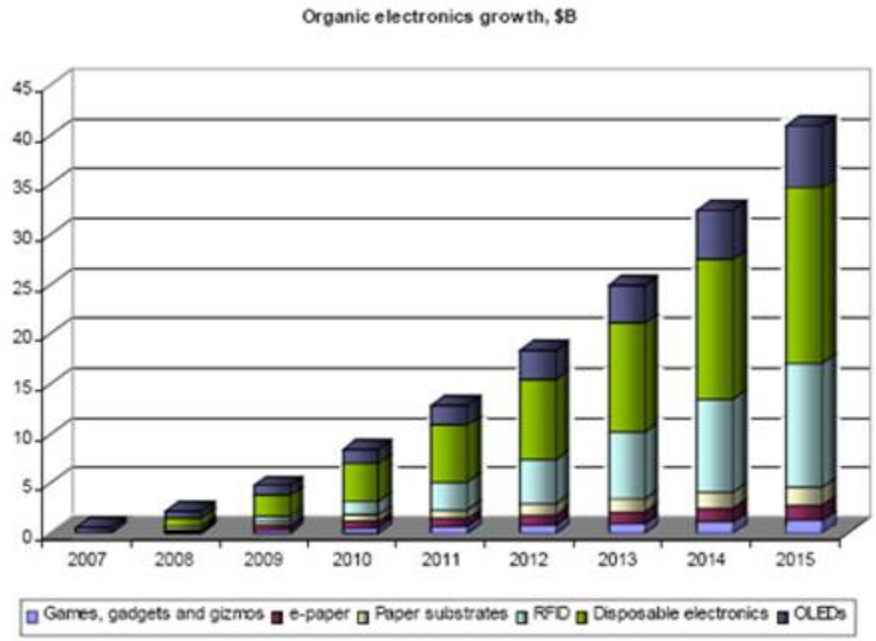

Figure 1.6: Organic electronics market actual and forecast growth rate by segment.

and complex functions can be carried out by systems of molecules or polymers.
The organic electronics market can be divided into six major segments, which have different economic impact and outlook [64]. Figure 1.6 summarized the actual and forecast growth rate or the organic electronics market for each one of these segments. The overall sales volume in 2013, forecast to be around 25B $, is half of the sales volume of Intel. But even if nowadays inorganic and organic electronics are not comparable in terms of market share, the latter is exponentially developing, as the forecast growth rate shows.

- *Radio Frequency IDentification Tags.*
  Organic Radio Frequency IDentification Tags (RFID) [65] find their primary application as barcode replacement, *i. e.* they generate a specific code sequence when stimulated with a RF field. Commercially available RFIDs work in the HF range and employ 64 bit of data. They are mainly used as a low cost solution for item-level identification, since they can carry and read out the standard Electronic Product Code (EPC). In figure 1.7 a 64-bit organic RFID is shown. This market is expected to generate 12.4B $ by 2015.

- *E-paper.* Electronic paper, also know as e-paper or e-ink, is a set of technologies which mimic the appearance of ordinary ink and paper [66]. It differs from traditional flat panel displays since it is not backlit, but it simply reflects the environmental light and

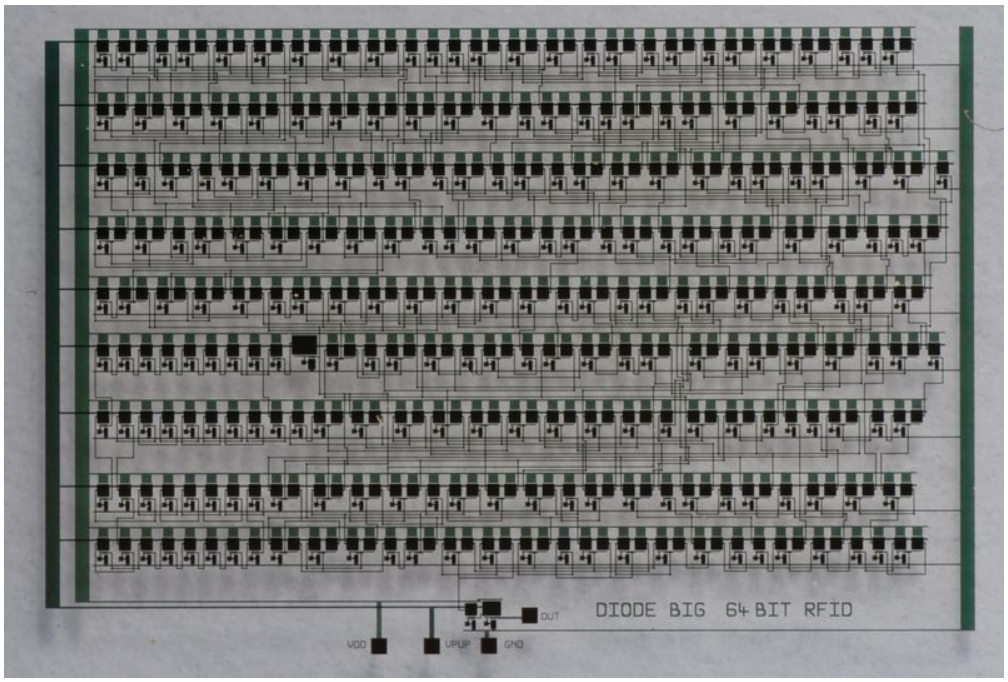

Figure 1.7: 64-bit Organic Radio Frequency IDentification Tag.

results in a more confortable reading. The leader Company for e-paper is *E-ink*. E-paper is expected to replace the paper pricing labels with Point-of-Purchase (POP) displays, and to significantly impact on smart-card and smart-packing. An example of e-paper is shown in figure 1.8. This market is forecast to reach a share of 1.6B $ by 2015.

- *Organic Field-Effect Transistors and Organic Memory.* Organic Field-Effect Transistors (OFETs) and Organic Memories have been investigated especially since the 2000s, therefore their industrial application is not comparable yet with other segments. Anyways, some Companies, such as Plastic Logic, have fully industrialized OFET technology and demonstrated that amorphous silicon performance and LCD industry typical yield and reliability levels can be achieved with OFETs in a full manufacturing environment [61]. Their application ranges from multifunction smart-cards and pharmaceutical packaging to the game, toy and greeting cards businesses. This last segment realized by means of printed organic electronics is expected to reach 1.2B $ by 2015.

- *Disposable Electronics.* This segment includes all the organic materials suppliers, such as organic conductive inks, for disposable applications. Since disposable devices are less demanding than other applications, like large displays or solar cells, they can easily be home-made and not limited to the major companies. Therefore this market share

Figure 1.8: Example of flexible e-paper.

is expected to have the gratest impact of the total sales volume and is forecast to reach 17.5B $ by 2015.

- *Paper substrates.* Paper electronics is a research field which focuses on creating conductive structures on cellulose foils [67]. This is a very low-cost and diffused material which can easily employed as a substrate for printed circuits for printed graphics applications. This is still a tricky issue since paper is very rough and porous. Anyways, this paper electronics is expected to grow and find concrete industrial applications, arriving at a market share of 1.8B $ in 2015. Figure 1.9 show a nice example of paper electronics: a matrix of OLEDs realized on a paper foil.

- *Organic Light Emitting Diodes.* Organic Light Emitting Diodes (OLEDs) were the first devices realized in organic technology [68] and today represent the most diffused application of organic electronics. In particular manufacturers of wireless devices, such as mobile phones, are attracted by OLEDs performance since they combine high-quality video with low power consumption. Moreover, OLED lifetime and efficiency have been increased in the last years: during 2008, lifetime rose from 24 kHrs to 100 kHrs and efficiency reached 150 lm/W in 2012, two years before expected. Its market volume is forecast to reach 7B $ in 2015. Figure 1.10 shows a OLED-based display by LG.

The great interest addressed to organic electronics lies to its exclusive unique features, such as flexibility, transparency, conformability, and low-cost process. But before them, the great-

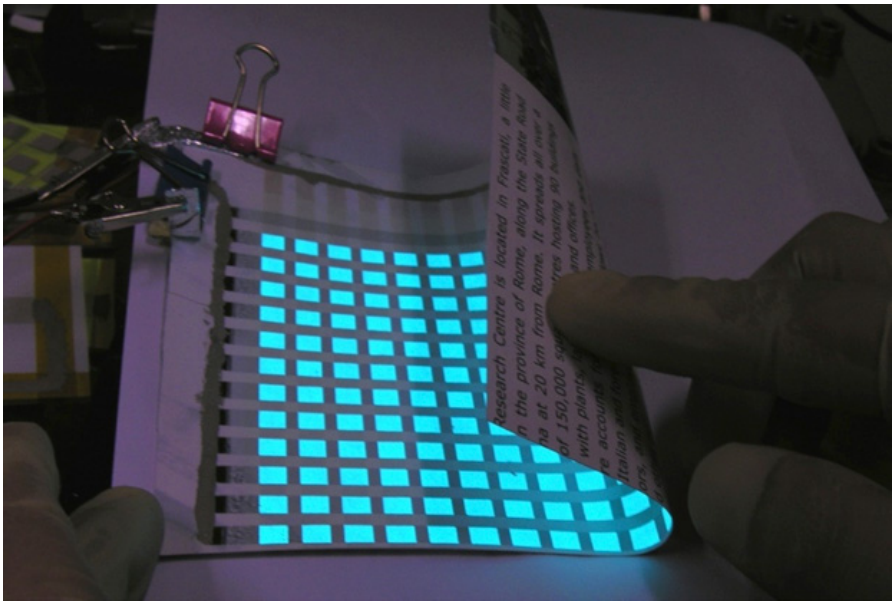

Figure 1.9: Prototype of OLEDs realized on a paper foil.

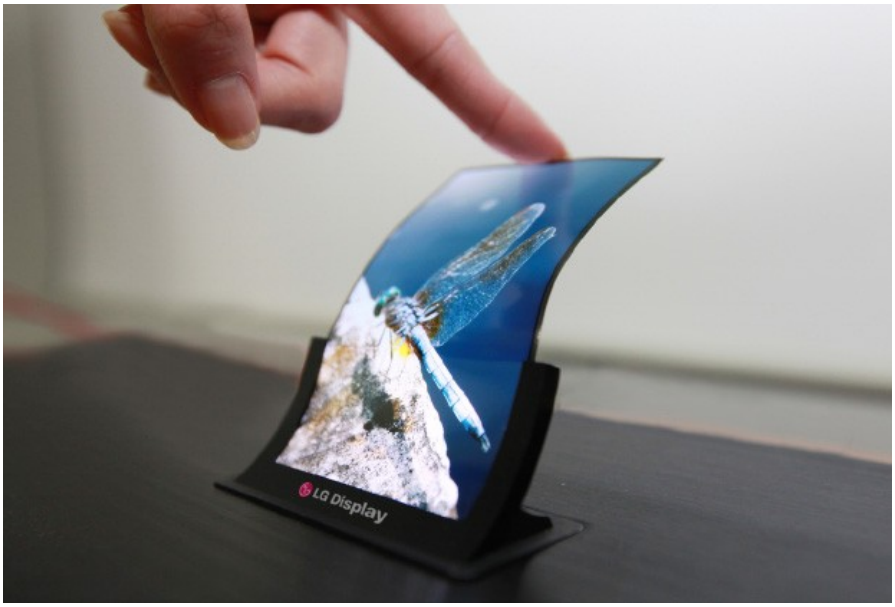

Figure 1.10: 5-inch display realized by means of OLEDs by LG.

est advantage of polymers is their versatility. On one hand, Silicon and the other inorganic semiconductors have intrinsic physical properties, such as piezoelectricity, piroelectricity and light sensitivity, and each one can be emphasized for a specific application by conveniently modeling the geometric shape of the devices and the fabrication process. On the other hand, nearly an infinite number of organic polymers can be synthesized which differ for their chemical and physical properties and can be adapted, for example, for specific sensing applications.

However, among the properties of each molecule, it is worth pointing out the most important one in this context: the solubility, *i. e.* the possibility for a compound, either solid or liquid, to be dissolved in a solid, liquid or gaseous, possibly organic solvent to form a homogeneous solution of the solute in the solvent. This is the most powerful advantage of organic electronics, since neither high temperature nor high vacuum levels are required: if a polymer is soluble, it can be transformed in an "ink" and deposited in liquid form. This is the reason why printed electronics, described in section 1.3, is gaining even more interest by the scientific community as well as by the commercial and industrial community. Printed electronics is the ideal candidate for large area, low-cost and easy fabrication of an ample range of circuits and devices. The aim of this work is the study of inkjet printing, one of the most diffuse printing techniques, for the fabrication of polymer-based electrodes, diodes and transistors and for several sensing applications.

1.2 Physical and chemical basics of organic electronics

1.2.1 Conduction in Carbon-based molecules

In order to gain a better comprehension of the phenomena involving conduction in Carbon-based polymers, it is mandatory to recall some basics of Organic Chemistry [69, 70].

The Carbon atom has six electrons, four of those are located in the valence shell: its most stable configuration is therefore $1s^2 2s^2 2p^2$ and the orbital of each electron can be calculated by solving the Schrödinger equation for the wave-function $\psi(\vec{r})$ of the isolated atom. A Carbon atom forms molecules by binding with other atoms, especially with Carbon, Hydrogen, Oxygen, Nitrogen and Phosphor. Since in this case an analytical solution of the Schrödinger equation is not possible, several quantum theories have been developed to obtain acceptable approximations of the molecular wave functions. In particular, two of them are noteworthy:

- *Valence Bond theory*, based on the atomic orbitals of the dissociated atoms that combine together giving origin to individual chemical bonds when the molecule is formed:

the molecular orbital is the superposition of these atomic orbitals.

- *Molecular Orbital theory (MO)*, based on the orbital of the whole molecule, *i. e.* the wave-function of all the electrons which move around all the nuclei. The best approximation which leads to the molecular orbital is the *Linear Combination of Atomic Orbitals (LCAO)* theory, which defines the molecular wave-function $\Psi(\vec{r})$ as a linear combination of the atomic wave functions $\psi(\vec{r})$.

Hydrogen (H_2), the simplest molecule, consists of two nuclei and two electrons which move around them. The two atomic s-orbitals have spherical symmetry and, according to the MO-LCAO theory, the can combine in two ways. On one hand, if they sum up, a molecular orbital is obtained with its maximum in the internuclear axis: this is called bonding orbital σ. Also, since the location probability of the negative-charged electrons is maximum between the positive-charged nuclei, the potential energy of the molecule is lower than that of the two dissociated atoms and the σ bond is stable. On the other hand, if the atomic orbitals are subtracted, *i. e.* they are combined with opposite signs, an antibonding orbital σ^* is obtained. In this case the molecular orbital has a node surface in the internuclear axis, leading to a higher potential energy and to a less stable system with rispect to the two isolated atoms. From two single atomic orbitals two molecular orbitals, σ and σ^*, are formed. Extending this reasoning, the number of molecular orbitals is equal to the number of atomic orbitals linearly combined to produce them.
Moreover, for the MO-LCAO only two half-filled orbitals can overlap and form covalent bonds: therefore in theory a Carbon atom in its base configuration $1s^2 2s^2 2p^2$ should be able to create only two bonds, but this does not justify the fact that Carbon can have up to four bonds, as in methane (CH_4). The explanation is given by assuming that when a Carbon atom is bound to other atoms an electron from the full-filled $2s$ orbital jump to the vacant $2p$ orbital. The four new orbitals "hybridize" and combine in three possible different orbital geometries:

- sp^3: the $2s$ orbital combines with all the $2p$ orbitals giving origin to four degenerate half-filled orbitals oriented in a tetrahedral geometry which form σ bonds along the internuclear axis (figure 1.11a).

- sp^2: the $2s$ orbital combines with two $2p$ orbitals and gives origin to three degenerate orbitals oriented in a trigonal planar geometry which form three σ bonds; the unhybridized $2p$ orbital arranges perpendicularly with respect to the other orbitals in a two-lobe structure with a nodal plane containing the two bound nuclei (figure 1.11b).

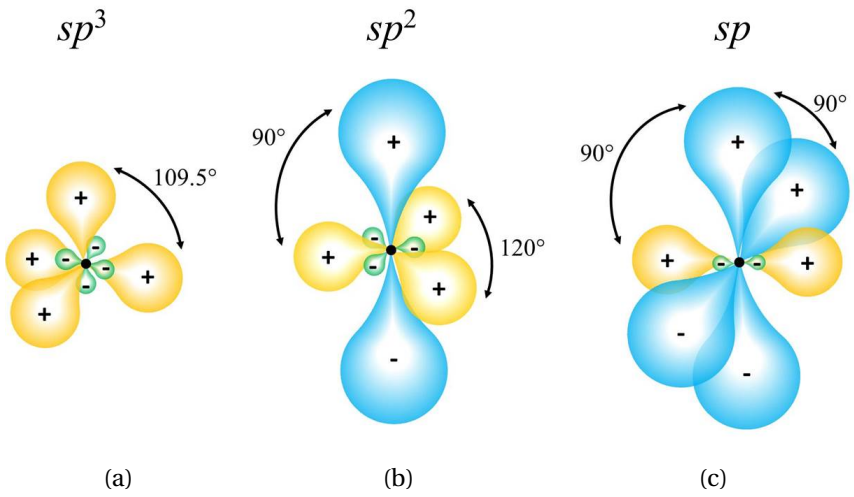

Figure 1.11: Hybridized orbitals for a Carbon atom: (a) sp^3, (b) sp^2 and (c) sp.

Similarly to the σ bonds, when two of these unhybridized $2p$ orbitals overlap, a π bond is formed.

- sp: the $2s$ orbital combines only with one $2p$ orbital giving origin to two degenerate orbitals linearly oriented, which form two σ bonds, while the two unhybridized orbitals form two π bonds perpendicular to each other and to the direction of the hybridized sp orbitals (figure 1.11c).

π bonds are weaker than σ bonds since their symmetry does not allow molecular twisting. From a quantum mechanics point-of-view, this weakness is explained by a poor overlapping of the two parallel $2p$ orbitals: furthermore, since they are in contact through two areas of overlap, they form diffuse bonds. On the contrary, the grater overlapping of the bonding orbitals between the two nuclei results in much stronger and less diffuse σ bonds. From a chemical perspective, the Carbon-Carbon double bond, composed of a σ bond and a π bond, has a binding energy less than twice that of the Carbon-Carbon single bond, composed of a single σ bond. Also $2p$ orbitals, according to the MO-LCAO approximation, can sum up or subtract, thus a obtaining bonding orbital π or an anti-bonding orbital π^*, respectively. The latter has an additional nodal plane in the internuclear axis, resulting much more unstable (figure 1.12).

Organic molecules are composed of many atoms, and especially Carbon, connected by covalent chemical bonds. When a polymer is considered, the energetic structure is obtained from the bonding and antibonding orbitals of the single atoms. Although polymer chains can be

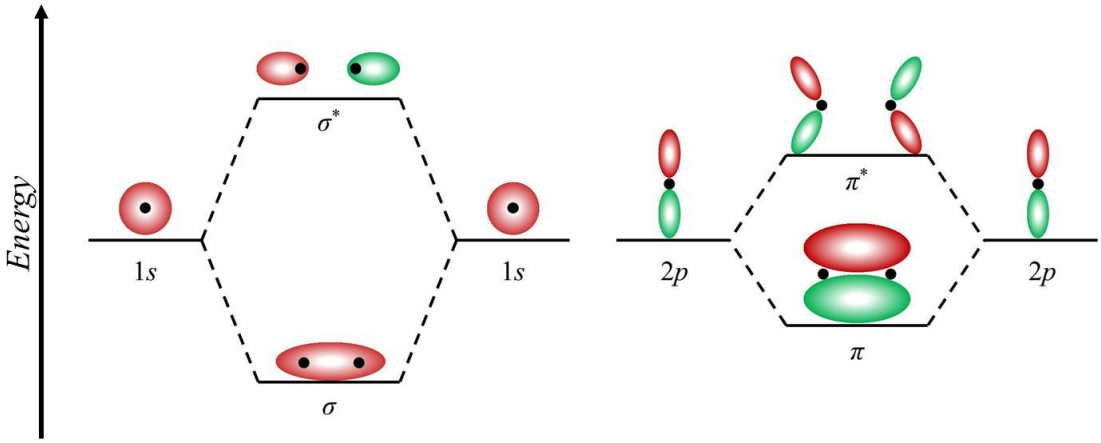

Figure 1.12: Bonding and antibonding molecular orbitals.

large and consist of many repeated units, their energy levels cannot be as numerous as those of the crystal Silicon: in this case, it is not possible to consider them as continuous bands, but only as discrete levels. Anyways, these are divided in bonding levels and anti-bonding levels. The highest bonding level, referred as the *Highest Occupied Molecular Orbital* (HOMO), and the lowest anti-bonding level, referred as the *Lowest Unoccupied Molecular Orbital* (LUMO), are separated by an energetic gap. A direct comparison with the upper limit of the valence band E_V, the lower limit of the conduction band E_C, and the band gap E_G can be done.
When two atoms are bound, the energy separation between bonding and anti-bonding levels is much higher for σ-σ^* orbitals than for π-π^* orbitals. When many atoms build up a polymer, the energy gap, *i. e.* the energy difference between LUMO and HOMO, is much higher when single σ bonds prevail: these polymers show an insulating behavior. On the other hand, when single bonds are alternated with double bonds (σ and π), the energy gap is reduced down to the range 1.5-3 eV and thus the molecule exhibits semiconducting properties.

The alternation of single and double bonds is called conjugation: in conjugated molecules, π bonds are not localized between specific atoms, but alternate between adjacent atoms creating a resonant structure. As a result, electrons of π_{p-p} molecular orbitals are not bound to specific nuclei but are delocalized across all the adjacent aligned $2p$ orbitals. One of the most illustrative examples is the benzene cyclic molecule, as shown in figure 1.13: the six Carbon atoms are alternatively single- and double-bound, but the resulting π_{p-p} orbitals are spread along the whole molecule. The same happens for conjugated polymers: delocalization of π-electrons along the entire polymeric chain is one of the basic requirements for the electrical

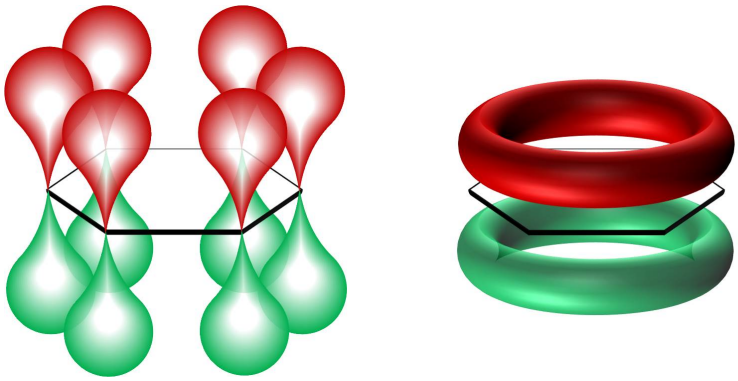

Figure 1.13: Delocalized π_{p-p} orbitals in the benzene molecule.

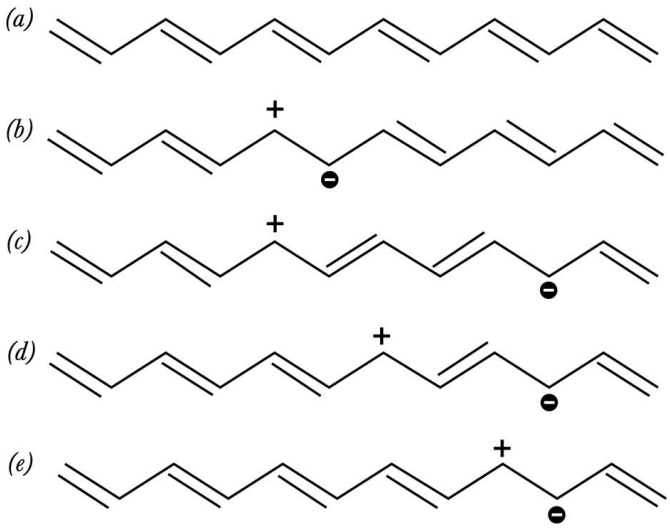

Figure 1.14: Charge transport in organic polymers by means of a *polaron*.

conduction in organic molecules.

The "doping" of organic semiconductors [71], which actually allows the charge transport along the molecule, consists of charge injection by means of dopants, or molecular impurities (halogen vapours in the first experiments carried out by Shirakawa *et al.*), that deform the polymeric chain (figure 1.14). The charged particle, together with the geometrical deformation induced, is called *polaron*. This is a quasi-particle with its own effective mass and total momentum energy: in particular, the effective mass is much higher than that of the free charge carriers and therefore its effective mobility is much lower; because of this intrinsic property the effective mobility in organic semiconductors can reach values as high as 10 $cm^2V^{-1}s^{-1}$, much lower than 10^4 $cm^2V^{-1}s^{-1}$ of inorganic semiconductors. The polaron induces some atom displacement and its charge is self-trapped by the deformation it has

induced: in terms of energy diagram, this effect can be included with an additive localized energy level in the gap between the HOMO and the LUMO of the molecule.
Transport between adjacent polymers takes place via $\pi - \pi$ stacking: delocalized π orbitals of a molecule overlap the delocalized π orbitals of the adjacent molecule and the polarons can move, with a certain probability, along stacked polymers. The charge transport is strongly influenced by the morphological and structural characteristics of the organic film. While pure inorganic semiconductors are characterized by an ordered crystal structure, organic semiconductors usually have a more disordered, multi-crystalline structure: domains of stacked polymers, called grains, are separated by grain boundaries.
Fundamentally, charge transport occurs at three different levels:

- *intrachain*, along an individual polymeric chain: this is the easiest level for polaron transport, thanks to the delocalized π orbitals all over the molecule.
- *interchain*, between adjacent polymeric chains: this transport is ruled by the $\pi - \pi$ stacking and by the molecular order of the semiconductor film. In rod-like molecules (small molecules and oligomers), the highest mobility is achieved when molecules are stacked perpendicularly with respect to the current flow, and therefore vertical or horizontal stacking is desired for horizontal and vertical conduction, respectively.
- *intergrain*, between adjacent grains: this is the most critical level, since charge carriers have to pass from a domain to another physically-separated domain.

Since in this case an exact quantum-mechanics dissertation is not possible as for inorganic crystal structures, several models have been proposed which explain the transport phenomena in organic films.
For highly-disordered structures, the prevailing model is *variable range hopping* (VHR) [72]: conduction occurs since thermally-activated charge carriers tunnel between localized states. The phonon-assisted hopping between two sites depends on their distance and on the activation energy: carriers can hop with higher probability between two distant states with low activation energy than between two near states with high activation energy.
For highly-ordered structures, the *multiple trapping and release* (MTR) model assumes that a high concentration of localized levels forms a narrow delocalized band and that lattice defects or impurities give rise to levels near the band, allowing tunneling [73]. Also, since traps are mostly localized in the grain boundaries, the overall mobility is limited especially by the mobility in these regions. In both cases the tunnel probability is inversely proportional to

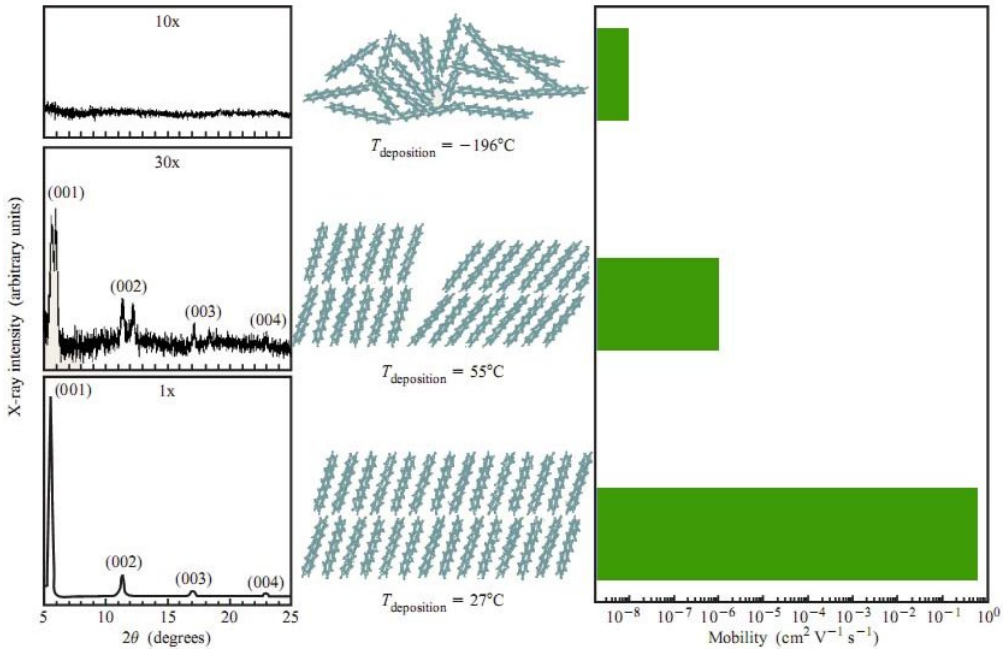

Figure 1.15: Dependence of the effective mobility on the morphology of the organic semiconductor film [1].

the grain-to-grain distance: increasing that distance induces a decrease of tunnel probability. This principle will be later discussed, in chapter 3, as the intergrain distance increase can be caused by bending the semiconductor film, and the consequent current decrease allows to employ organic devices, especially transistors, as strain sensors.

Figure 1.15 shows an interesting example of how the morphology plays an important role on the final mobility [1]. By processing the organic layer at different temperatures, different final morphologies can be obtained, investigated via X-ray diffraction: the higher molecular order is achieved, the higher effective mobility is obtained.
The morphology of a semiconductor layer can be tuned by appropriate deposition parameters and conditions which allow to improve the final electrical performances of the organic semiconductor. In particular, morphology can be correlated to five main factors:

- *substrate roughness.* Experiments carried on different substrates showed that surface roughness, expressed as *Root Mean Square Roughness* (RMSR), strongly influences the grains' dimension. High values of RMSR indicate the presence of deep valleys and high peaks on the surfaces which reduce the possibility for the polymeric chains to be stacked and form extended domains. Moreover, roughness increases the intergrain spacing, thus reducing the tunnel probability for charge carriers between adjacent grains.

Generally, a small RMSR is desired to overcome these problems, and this is the reason why glass substrates, which have a very small roughness, are still employed in lieu of flexible plastic substrates, which suffer from a higher value of RMSR.

- *Surface energy*. Organic layer growth is influenced by the surface energy of the substrate. Also, this is a very important issue when polymers are deposited in liquid form, such as in inkjet printing; surface energy will be discussed in detail in section 2.2. Here it is worth considering that several techniques can be adopted to modify the surface energy. Among them, plasma treatment and deposition of *Self-Assembled Monolayers* (SAMs), which can increase or decrease the surface energy and the interfacial energy between substrate and deposited layer.

- *Temperature*. Processing and post-processing temperature is another very important parameter to account for in order to obtain regular and large crystal domains. Moreover, this influences the drop annealing when solution processable semiconductors are deposited. Even if an absolute rule cannot be defined, in general a higher processing temperature gives origin to more extended grains and thus to higher mobility. Therefore, compatibly with the operative conditions, high-temperature processing and post-processing are desired.

- *Deposition rate*. Experimental results [24] show that the deposition rate, measured in Å/s, directly influence the grain dimensions. A higher rate leads to smaller domains, since the polymeric chains have less time to stack up and build ordered structures. On the contrary, in general, lower deposition rate allow the formation of extended grains. Provided that the grain boundaries are not improved, a low deposition rate is desirable.

- *Layer thickness*. Depending on the particular application considered, and depending whether electrical conduction is vertical or horizontal, the layer thickness influences the final performances of the active layer. In fact, the first deposited layers arrange themselves over a smooth surface that eases the formation of long domains. When upper layers are deposited, they have to arrange themselves over an irregular "grain" substrate: therefore the grain size decreases layer-by-layer. Even if for organic transistors the current flow in the very first layers of the semiconductor, an overall ordered structure limit the off-current and damage caused by environmental agents, such as Oxygen and Water, which reduce the electrical performance.

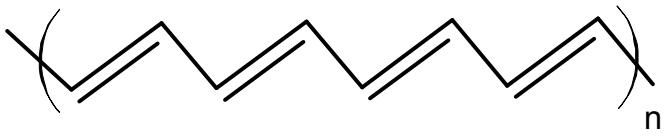

Figure 1.16: Polyacetylene.

1.2.2 Classification of conducting and semi-conducting polymers

The progress in Organic Chemistry has been giving rise to an infinite number of molecules, therefore a thorough and univocal description of all the organic polymers goes beyond the aim of this work. The physical principle common to all the conducting molecules is the conjugation and the π-electron delocalization, as discussed in the previous section. Several articles, such as [74], provide list and description of organic molecules employed for specific applications of organic electronics. Anyways, from a chemical point of view, it is worth to depict a general classification of organic polymers on the basis of their structure.
Feast *et al.* [75] suggested to classify them into three major groups: Hydrocarbons, Heterocyclic Polymers and Oligomers.

1. *Hydrocarbons*. These molecules constitute the most general group of organic polymers and can form long, high-weight 1-dimensional and 2-dimensional structures. Basically, they differ each other in the functional groups their equivalent monomers are made of, such as aliphatic compounds and aromatic compounds. This results also in different chemical stability and physical properties.

    - *Polyacetylenes*. Polyacetylene is the simplest polyconjugated organic polymer and the first ever obtained, as described before. It is composed of a linear chain of Carbon atoms with alternating single bonds and double bonds between them, as shown in figure 1.16; each Carbon atom is linked with one Hydrogen atom. Its properties, such as stability and conductivity, strongly depend on the specific polymerizing catalyst. Several polymerization methods have been developed: Shirakawa's method is one of the most widely employed, whereas Luttinger's and Edwards' methods have been gaining importance. Moreover, solubility of polyacetylene has been obtained, together with high conductivity, by sostitution of an Hydrogen atom with a proper functional group.

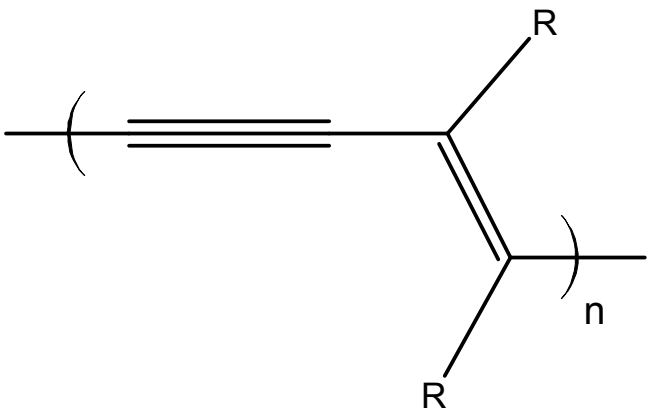

Figure 1.17: Polydiacetylene.

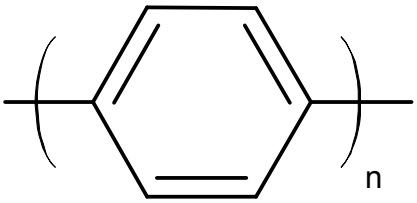

Figure 1.18: Poly(*p*-phenylene).

- *Polydiacetylenes.* Polydiacetylenes are a class of conducting polymers whose monomers are formed by Carbon atoms, with alternating single and triple bonds between them, and two different functional groups (figure 1.17). The main synthesizing method is the solid state polymerization, *i. e.* the polymerization of unsimmetrically distributed crystalline diacetylene molecules. Also the polymerizations in the liquid-crystalline state and as Langmuir-Blodgett multilayers have been achieved. Due to the variety of the possible functional groups, they are mainly employed for the development of several organic films and for the immobilization of other molecules.

- *Polyphenylenes.* Polyphenylenes are another class of conducting polymers, based on the benzenic ring. In particular the most diffused member of this group, the poly(*p*-phenylene), is obtained by the polymerization of the *p*-phenylene monomers, which are composed of simple benzene molecules with single bonds between them(figure 1.18). The polymerization methods include oxidative coupling (the most commonly employed one), organometallic coupling, dehydrogenation

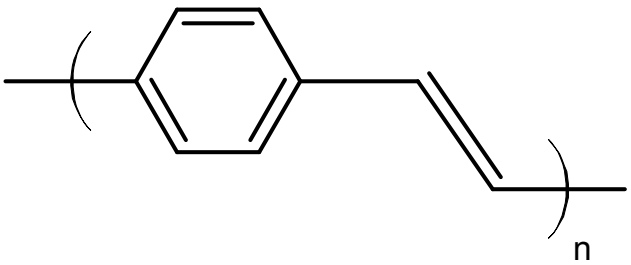

Figure 1.19: Poly(phenylene-vinylene).

of polycyclohexylenes and cycloaddition reactions. It is mostly used as precursor of other organic composites, especially poly(*p*-phenylene sulfide), which has good thermoplastic properties together with good electrical properties under oxidation or use of dopants.

- *Poly(phenylene vinylene)s.* Poly(phenylene vinylene) (PPV), as its name suggests, possess a chemical structure that is halfway between that of polyacetylene and polyphenylene: its monomer is composed of a phenylene benzenic ring in series with an acetylene molecule (figure 1.19). The main polymerization method, highly reproducible, is the Wessling-Zimmermann water-precursor route. Oriented PPV is highly crystalline, mechanically strong and environmentally stable. The versatility of this molecule allows the inclusion of many functional side groups, especially in the benzenic ring, which strongly influence its physical and chemical properties. In particular, its small optical band gap can be precisely tuned by addition of proper functional molecules. Therefore PPV, thanks to its electroluminescent properties, is today the one of the major candidates for polymer-based optoelectronic applications, such as Organic Light Emitting Diodes (OLED) for mobile telephone displays and photovoltaic devices.

- *Polyarylenes and Polyacenes.* Two-dimensional molecular structures are composed of polycyclic aromatic hydrocarbons, which can be considered as two-dimensional subunits of graphite. They have better conducting properties as well as higher rigidity with respect to their one-dimensional analogues. Polyarylenes and especially polyacenes are the most representative molecules of this group. Polyarylene are composed of pairs of fused benzene rings, that is they have two Carbon atoms in common, and each pair is linked to the adjacent pair by means of two single bonds figure (1.20-left). They are prepared from oligonaphthalene precursors

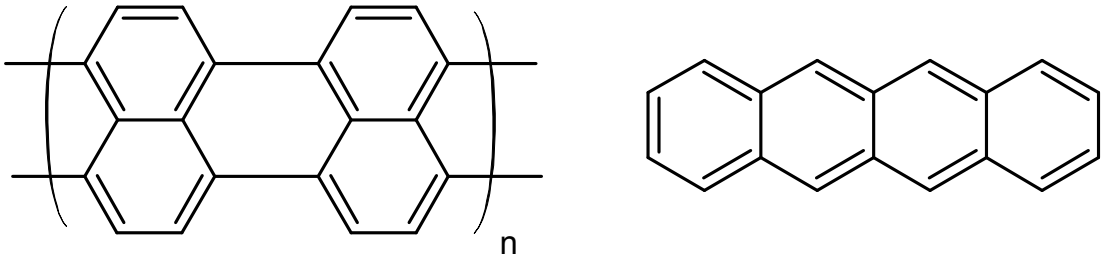

Figure 1.20: Polyarylene (left) and tetracene (right) from the polyacenes group.

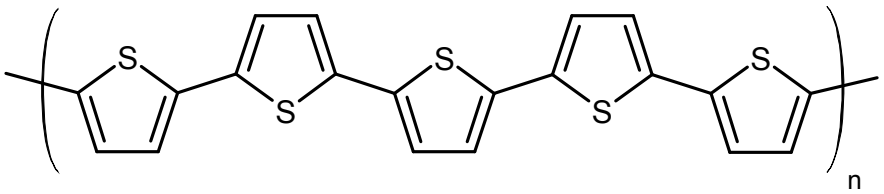

Figure 1.21: Polythiophene.

via oxidation or reduction process and show good thermal stability. Polyacenes are made up of linear fused single benzene rings, which are the monomers. The molecule composed of two rings is naphthalene, with three rings is anthracene, and so on with tetracene (figure 1.20-right), pentacene, hexacene, heptacene. Polyacenes are not stable if more than a few repeating units long, being hexacene and heptacene very reactive and only isolated in a matrix. Pentacene, on the contrary, is very stable: thanks to its high conductivity and to the possibility of obtain a solution-processable molecule by adding functional side groups, nowadays it is one of the most employed semiconductor in organic electronics.

2. *Heterocyclic Polymers.* Heterocyclic polymers are organic polymers whose monomers are composed of a cyclic compound with at least two different elements as members of the ring. The base element is Carbon, while depending on the substituting element several classes of heterocyclic polymers are formed. This substrution strongly influence the final chemical and physical properties of the molecule, therefore this is the group with the most extended range of applications in organic electronics.

   - *Polythiophenes.* Polythiophene is made up of five-membered rings where one of the Carbon atoms has been replaced with Sulfur (figure 1.21). Its polymerization processes can be divided into three main cathegories: electrochemical coupling,

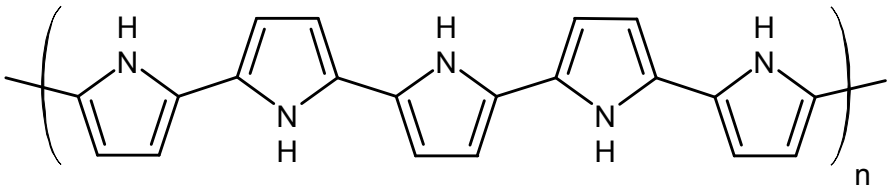

Figure 1.22: Polypyrrole.

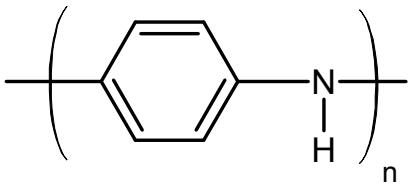

Figure 1.23: Polyaniline.

oxidative coupling and organometallic coupling of 2,5-disubstituted monomers. It was first synthesized at the end of the XIX century, but only after 1980 its importance has grown. Polythiophene is insoluble in organic solvents, due to its rigid backbone. Anyways, addition of flexible side-chains in 3- or 4-position allowed solubility has overcome this problem. The electrical conductivity is the most interesting property of this class of molecules, especially achieved in polymers with perfectly 2,5-linked repeating units. Moreover, its good optical properties as well as reactivity to environmental condition make polythiophenes the best candidates for the realization of Organic Field-Effect Transistors (OFET) and organic sensor devices that can provide a range of optical and electronic responses.

- *Polypyrroles.* Polypyrrole is composed of five-membered rings where one of the Carbon atoms has been replaced with Nitrum (figure 1.22). The polymerization is quite similar to that of Polythiophenes, the electrochemical oxidation method being the most employed. Polypyrroles have high stability over time and temperature, and their application range is not very different from that of Polythiophenes; they are mainly used in OFETs and in chemical sensors.
- *Polyanilines.* Polyaniline is another polymer of the heterocyclic polymers group. Its monomer, the aniline, is composed of a series of a benzene ring and a Nitrum atom, which is linked to a Hydrogen atom (figure 1.23). It is synthesized especially

via electrochemical and chemical oxidation, the most diffused method for these classes of polymers. Although it was obtained for the first time in the XIX century, the interest on polyaniline grew only in the last three decades. The main advantages for using this molecule are the low-cost and easy production processes and the stability of its conducting forms. Polyaniline can occur in a number of well-defined different oxidation states, namely from the fully reduced leucoemeraldine via protoemeraldine, emeraldine and nigraniline to the fully oxidized pernigraniline, which differ in color and in acid/base doping response: therefore this molecule is suitable for realizing acid/base chemical vapour sensors and biosensors. Other applications include manufacturing as electrically conducting systems, electromagnetic shielding of electronic circuits and as a corrosion inhibitor.

- *Copolymers*. Copolymers can be considered a hybrid class, since they are made of the repetition of two or more monomeric species. The result should enable, in principle, the combination of the properties of different homopolymers into one material, increasing the scope of synthesis and applications. Three main polymerization method have been studied for this group of molecules: the direct polymerization of the different aromatics by either oxidative or chemical coupling methods, the ring closure of precursor polymers, and polymerization of oligomers which already contain the desired array of units. According on how the monomeric species are arranged along the polymeric chain, four classes of copolymers can be obtained: (i) alternating copolymers, where the monomeric units are regularly alternated; (ii) periodic copolymers, where the monomeric units are arranged in a 'macro-monomeric' repeated sequence; (iii) statistical copolymers, where the presence of the monomeric units follow a statistical rule, without any periodical repetition; (iiii) block copolymers, where two or more homopolymer subunits are linked by covalent bonds.

3. *Oligomers*. Whereas polymers are made of ideally unlimited repetitions of monomers, oligomers are composed of a small number of these units, tipically less than ten. The interest in oligomers has grown up during the last 15 years since they can be used as model low-weight compounds for the different polymers with respect to the synthesis, spectroscopic analysis and physical properties as well as their potential applications. High electron mobility was achieved with π-conjugated oligomers, almost comparable to amorphous Silicon, which makes them very good candidates for the realization of

all-organic FETs, both as conductors and as active layers. Pentacene, previously classified within two-dimensional hydrocarbons as a member of the polyacenes group, could be seen as an oligomer, since its monomeric unit, the benzene ring, is replicated only five times. Oligothiophenes are by far the oligomer that have achieved most attentions by scientists; beyond them, also oligopyrroles and oligoanilines show interesting properties.

- *Oligothiophenes.* Oligothiophenes are oligomers made up of few thiophene monomers. Their synthesizing methods are based on the cross-coupling reaction of a dihalo-compound with organometallics, on the copper(II) chloride oxidation of a lithiated thiophene and on the ring closure reaction of a 1,4-diketone with Lawesson's reagent. One of the most known member of this group is α-sexithiophene, widely used for the realization of organic transistors. Oligomers containing more than six thiophene rings is restricted to substituted compounds due to the insolubility of the unsubstituted oligomers. Beyond their good electrical conductivity, oligothiophenes show other interesting properties, such as thermochromism and hyperpolarizability.
- *Oligopyrroles and Oligoanilines.* Oligopyrroles, composed of few units of pyrroles, have not been studied as much as oligothiophenes, mainly due to their complexity. Synthesis of oligopyrroles include oxidative coupling, Stille coupling, and Ullmann polymerization. They are employed especially as receptors and chemosensors, as their polymeric counterparts. Oligoanilines, as well as oligopyrroles, have not been widely investigated due to the complexity of their structure. They are prepared by an oxidative coupling/reduction sequence. These oligomers have attracted considerable interest due to the electroluminescent properties of the parent polymer.

1.3 Printed Electronics

Printed Electronics (PE) is a set of materials deposition techniques which literally "print" electronics materials (insulating, conducting, and semiconducting) to create a wide range of devices, such as transistors, diodes, detectors, sensors or simple conducting structures and circuits. Generally these devices are obtained by patterning, layer by layer, thin or thick structures on rigid or flexible substrates. A large number of printing technologies, described in the

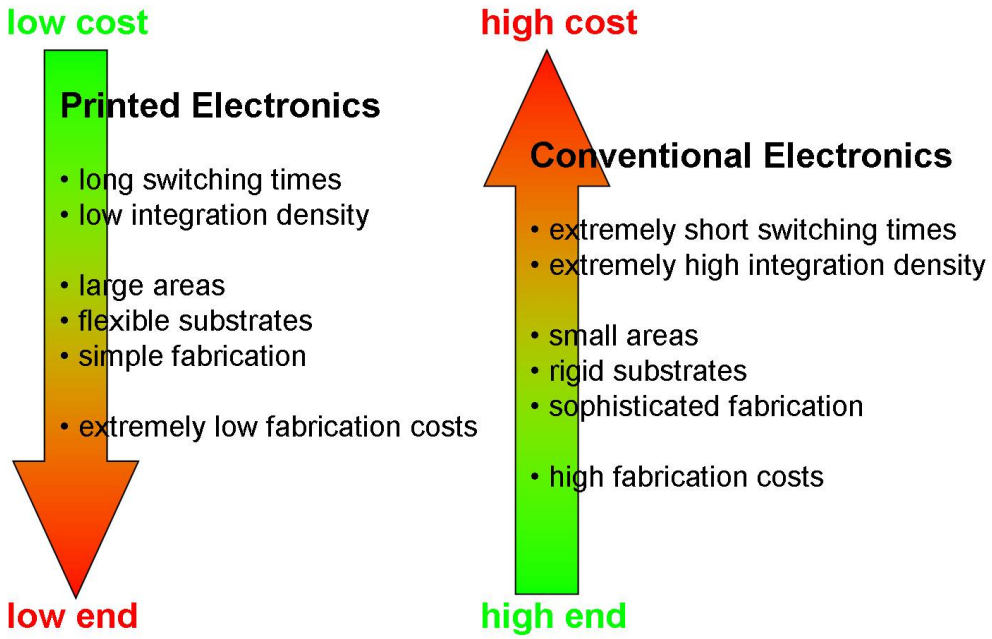

Figure 1.24: Comparison between printed and conventional electronics.

followings, are included, which differ in several parameters, such as costs, printable materials, resolution, and their choice is strictly related to the final application they are employed for. The common basic requirement is that printed materials are processable in liquid form, *i. e.* they can be processed as inks, and that such inks fulfill specific chemical and physical requirements depending on the specific technique employed.

PE is related to Organic Electronics, even though they are not equivalent: printable inks can contain both inorganic and organic materials. On one hand inorganic-based inks usually contain metal nanoparticles, such as gold, silver, copper, aluminum, dispersed in a liquid vehicle, which form continuous conductive layers once they are deposited. On the other hand, organic-based inks are composed of solution-processable organic molecules which, according to the specific deposition parameters, are arranged in continuous molti-domain layers which allow (or block) the charge transport and the electrical conductivity. From this point of view, PE is the most interesting and promising deposition technology for Organic Electronics, since it takes advantage and employs all the characteristics of the organic molecules to create a competitive counterpart of inorganic electronics: figure 1.24 shows a thorough comparison between PE and Conventional Electronics properties and performances.

All the advantages of PE are well known and widely employed at industrial level. The current main limitations of organic electronics are continuously under investigation: scientific

research, from chemical synthesis of organic molecules to the fabrication of complex device architectures, is totally devoted to overcome these problems. The main advantages and disadvantages of PE with respect of conventional electronics are listed below:

- *Low fabrication costs.* This is probably the most interesting feature of PE. Since materials are deposited in liquid form, they can be processed at room temperature and then annealed at medium temperature, usually not exceeding 150-200 °C. On the contrary other techniques, among all thermal evaporation, require high temperatures and high-vacuum conditions, which dramatically increase the fabrication costs especially at industrial level. Moreover, although working in a clean room is always desirable when depositing electrical materials in order to reduce impurities, this specification is less pressing when dealing with PE, provided that inks are stable at room conditions. Another very important characteristic is that PE is an additive process: only the material quantity of interest is deposited on specific patterns, thus in principle all the ink at disposal is used to create desired devices and circuits. On the other hand, thermal deposition is a subtractive process: a full, non-patterned layer is evaporated and the final pattern is obtained by removing exceeding material, *e. g.* by means of photolithography. Therefore only part of the material at disposal form the final patter, the remaining part being wasted.

- *Flexible and transparent substrates.* These advantages are strictly related to Plastic Electronics. Silicon-based electronics use pure, monocrystalline Silicon wafers as bulk substrates for the fabrication of electronic devices: therefore they are rigid and opaque and cannot be conformed to every surface's shape. PE uses a totally different approach: plastic substrates are employed as bulk structures over whom organic layers are deposited. This allows the low weight, the flexibility and the transparency of the final structures, directly related to their portability and their conformability almost to every surface.

- *Large areas.* Thermal evaporation, due to its high costs, can be performed only over limited areas where high-vacuum conditions are hold. Instead PE can employ flexible plastic rolls as substrates and therefore easily extend a single deposition process to large areas.

- *Mass production.* This point is a direct consequence of the processability over large areas and of the simple fabrication method. Since PE does not require photolithography

and other post-processing chemical treatments, but carries out all the fabrication in a single step, it is suitable for mass production since it is easily adapted to the industrial-level fabrication. Rolls of virgin plastic substrates, continuously sliding inside industrial printers, result in device-covered printed rolls.

- *Low resolution.* This is the main drawback of PE. The photolithography resolution is defined by the wavelength of the radiation to which the photoresist is exposed, and this results in very precise nano-scale patterns. In PE the pattern resolution is defined on how mechanically the ink drops can be nearby without degenerate in a single bigger drop. Nowadays it is hard to obtain resolutions under 1 μm. Hence low miniaturization and integration density can be obtained.

- *Long switching times.* This is caused by the low mobility of charge carriers in organic semiconductors with respect to the mobility obtained in inorganic conductors. Low mobilities result in longer switching transient regimes and thus in lower maximum working frequencies.

The characteristics above described are generally valid for all the printing techniques. Beyond this general description each technique has its own peculiarity and its own advantages/disadvantages, therefore their employment depends on the specific target to be obtained.
PE technologies are basically divided in two major classes: *contact printing*, which deposits inks by direct contact between the printing plate and the bulk substrate, and *non-contact printing*, by which ink is deposited on the substrate without any contacts with the printing plate. A general description of all the printing techniques goes beyond the aim of this thesis: some most relevant examples are described in the following sections. In particular, the latter class also includes inkjet printing, the technique employed in this work: thus it is described more in detail with respect to the other technologies. A wide literature has been published [76–78] which compares in detail the different printing techniques: for more specific information, a careful reading of these articles is warmly advisable.

1.3.1 Contact printing techniques

A schematic classification of contact printing techniques is shown in figure 1.25. Contact printing techniques can be divided into two major groups: in the first one the ink is located on the printing plate, in raised, recessed or planar position, and is directly transferred from

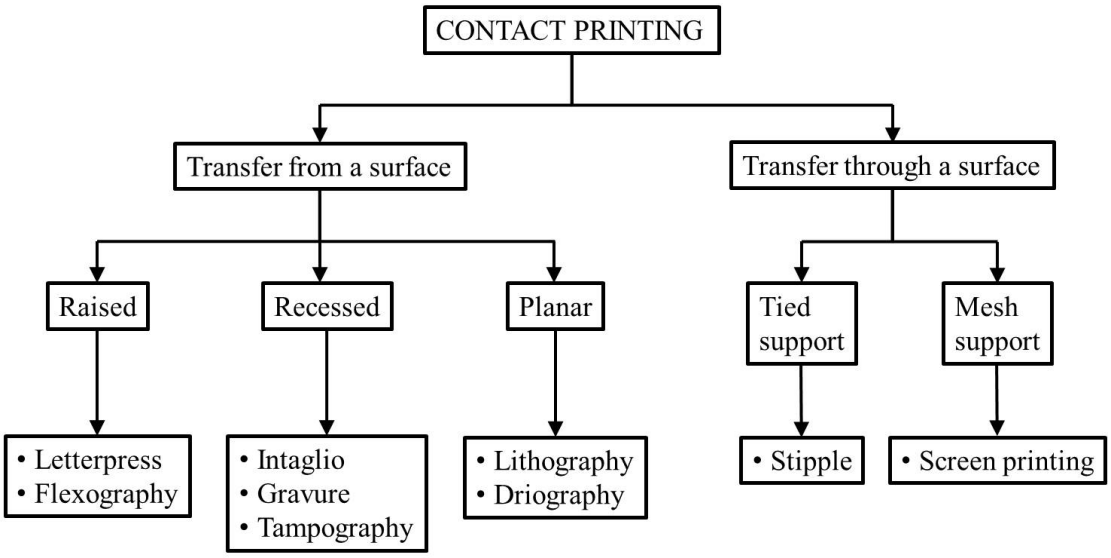

Figure 1.25: Schematic classification of the main contact printing techniques.

the plate to the substrate by direct contact; in the second group the ink passes through a perforated surface in contact with the substrate. Four important examples are analyzed in the following: flexography, gravure printing, lithography and screen printing.

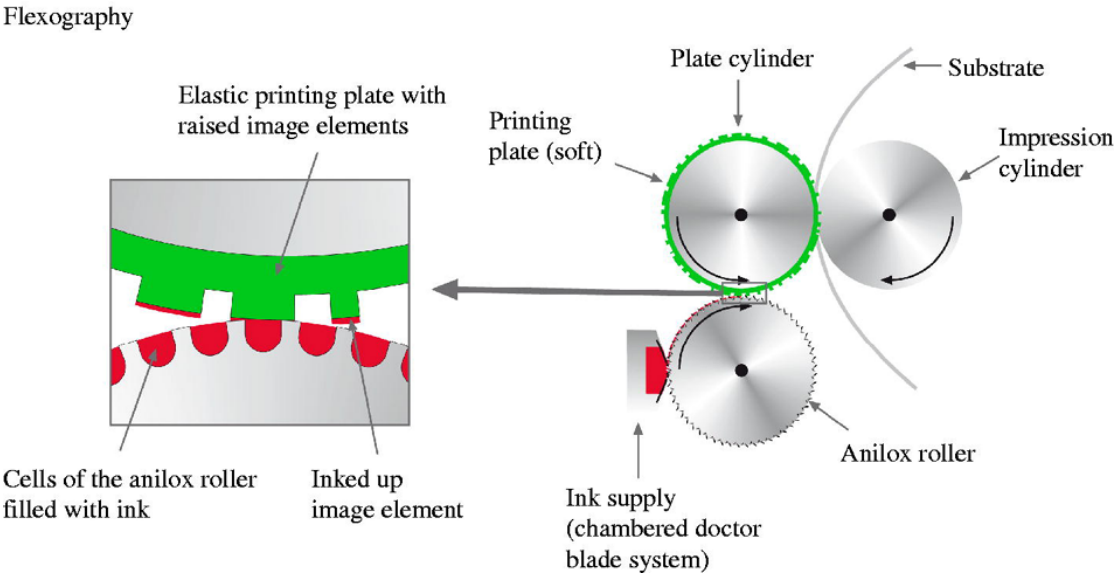

Figure 1.26: Schematic of the flexography technique.

Flexography, schematized in figure 1.26, is a roll-to-roll contact printing technique which employs a set of cylinders. The first cylinder, called *anilox*, is characterized by engravings,

i. e. small cavities separated by small walls, where the ink is deposited by an ink supplier. From the anilox, the ink is transferred to a second cylinder, the printing cylinder, surrounded by a soft mold, the printing plate, that reproduces the positive image of the final pattern. The ink is transferred in a precise controlled way to the molded printing plane, in a raised position. The printing substrate is pressured between the rolling plate cylinder and a third hard cylinder, called impression cylinder: the ink is impressed from the raised position of the soft mold to the sliding substrate and the final pattern is the exact positive reproduction of the patterned soft mold. A wide range of inks can be printed with such technology, and no strict physical requirements are necessary for the ink formulation. On the contrary, the major drawback is the *halo* effect, *i. e.* the spreading of the ink outside the image areas due to the compression applied, which limits the resolution of this process.

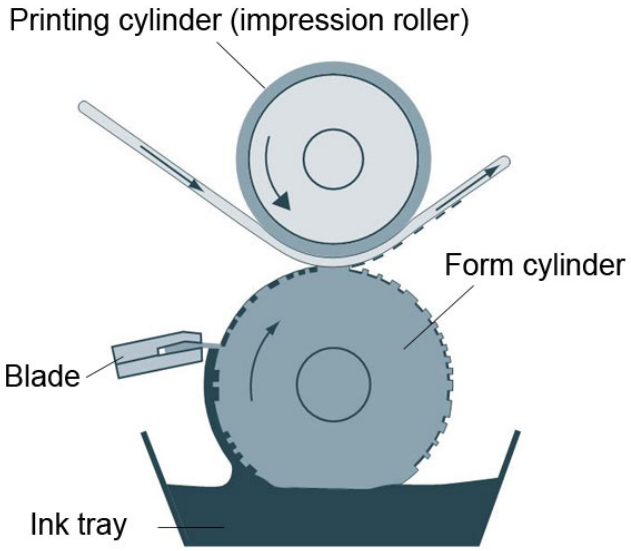

Figure 1.27: Schematic of the gravure printing technique.

Gravure printing is another roll-to-roll printing technique based on the opposite principle with respect to flexography. It is schematized in figure 1.27. An ink tray covers a molded form cylinder with inks, while a blade removes the surplus. Therefore the ink is kept only in the cavities of the mold in a recessed position and, when the printing cylinder and the printing cylinder press the sliding plastic substrate, the printed pattern is the negative pattern of the molded form. This technique is generally characterized by the same advantages (versatility, speed) and disadvantages (non-high resolution) as flexography. Standard molds

are made of small separated points which allow the fabrication of electronic device components. Where continuous conductive elements are required, such as RFID tags, the mold is engraved with linear structures: in this case the technique is called *intaglio*.

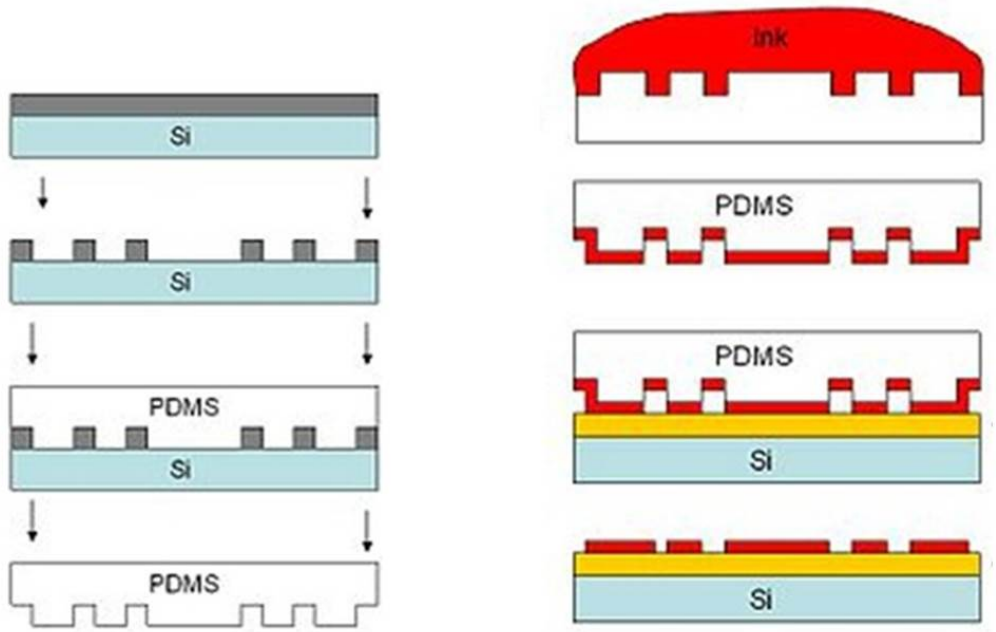

Figure 1.28: Schematic of the soft lithography technique.

Soft lithography is a planar contact printing technique which employs a soft conformable mold usually made of *poly(dimethylsiloxane)* (PDMS). It is described in figure 1.28. First, the negative patter is reproduced on a master rigid structure via photolithography, which is the reusable primary template for several PDMS molds without degradation. A soft mold is created by pouring and polymerizing PDMS on the rigid structure and then pealing it off. This soft mold reproduces the positive pattern to be printed on the substrate. The ink is deposited all over the structure, both in raised and recessed position. When this PDMS mold is put in contact with the substrate, due to the conformability of PDMS, a continuous pattern is deposited on it. The main advantage is the high resolution achievable by this technique, as low as 20 nm. On the contrary, the main disadvantage is that it is not suitable for low-cost mass production as roll-to-roll printing, since it is a slower process that requires several steps to obtain the final structure.

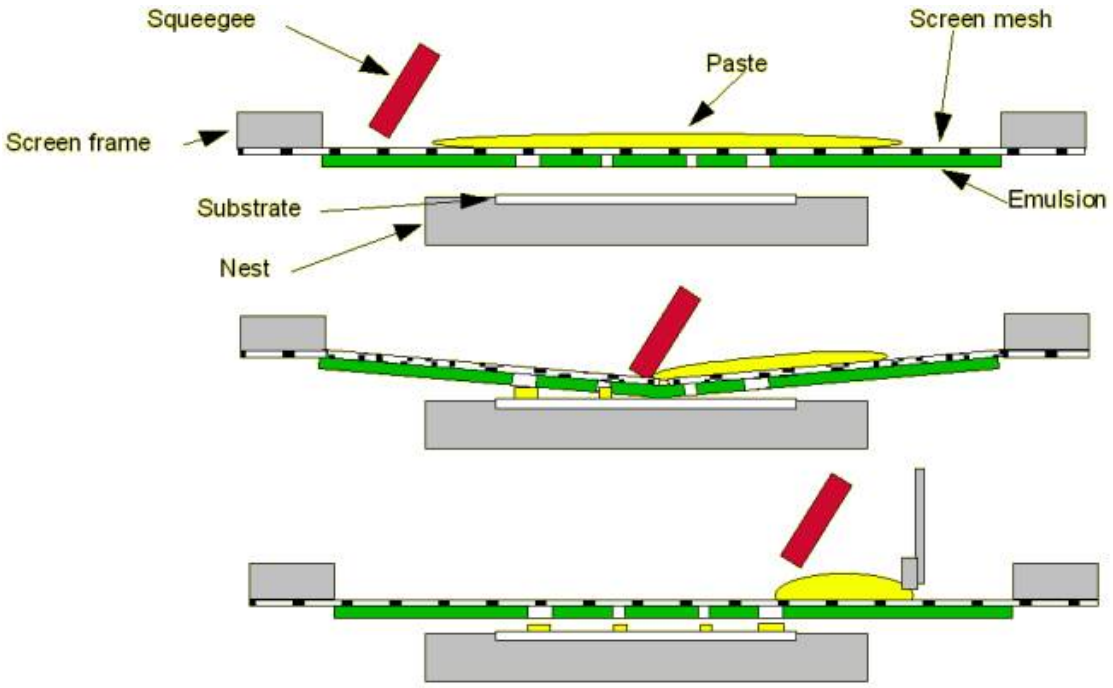

Figure 1.29: Schematic of the screen printing technique.

Screen printing is a contact printing technology where ink is transferred through, and not from, a patterned surface. This deposition technique is well schematized in figure 1.29. It is composed of a screen mesh stretched over a screen frame. In a pre-printing process, an emulsion, whose properties depend on the chemical and physical properties of the ink to be printed, is poured onto the back side of the mesh. An *exposure unit* removes the unnecessary emulsion, leaving a pattern which represents the negative image of the desired final pattern. Then the screen is placed atop the plastic substrate and the ink is poured on the front side of then mesh; a flood bar is used to push the ink through the mesh holes. The actual printing process starts when a rubber blade, called *squeegee*, is slid along the screen, moving the mesh down in contact with the substrate. The ink which fills the mesh holes is therefore pumped through the openings, *i. e.* the emulsion vacancies, directly to the substrate: by an opportune tuning of the printing parameters, such as the ink's properties, the thickness of the mesh and the pressure applied to the squeegee, only the desired amount of ink in the desired position creates the final pattern. This technique is most employed for the fabrication of organic photovoltaic cells [79].

1.3.2 Non-contact printing techniques

Figure 1.30 shows a schematic classification of the main non-contact printing techniques. This class includes a wide range of printing technologies, therefore it is not possible to de-

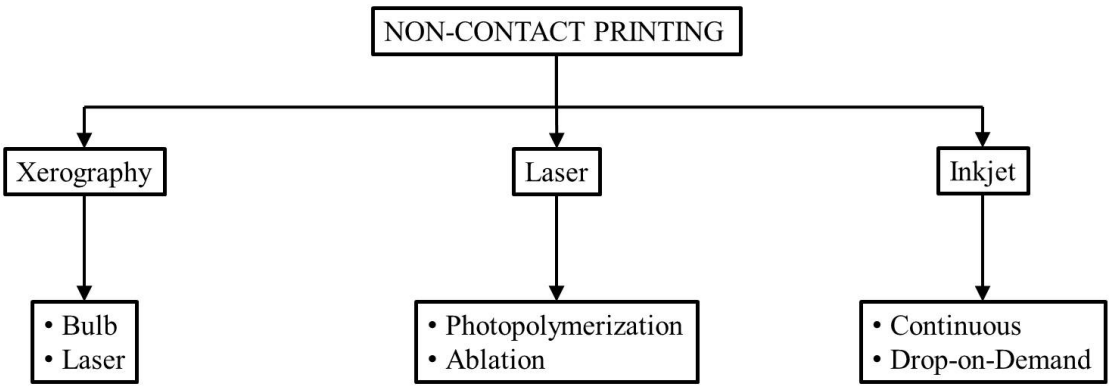

Figure 1.30: Schematic classification of the main non-contact printing techniques.

scribe them all. Roughly, they can be divided into three main sub-classes, depending on the physical principle they work by: Xerography, Laser-based techniques and Inkjet printing. In the following, an example is given of the laser group, namely the Laser Direct Writing, and then all the attention is focused on the inkjet printing technology, which has been developed during this thesis and which actually is one of the most promising processes for the deposition of organic electronics materials.

Laser Direct Writing is a set of non-contact printing techniques used both for the deposition of inorganic and organic materials. A detailed overview of the process is given by Hon *et al.* [80], while an example of specific application in the organic field is reported by Ribierre *et al.* [81]. A wide range of materials can be printed by means of this technologies, from metals to polymers to ceramics, and they also can be deposited from a vapour, liquid or solid precursors. Three examples, one for each phase, are given.
Laser Chemical Vapour Deposition (LCVD) uses an argon ion laser that can focus on spots as small as 2 μm by means of optical microscope lenses. In this case the precursor is in gaseous phase and contains the material to be deposited. When the laser beam scans over the substrates, the increased temperature causes the material to dissociate from the gas and to be deposited on the substrate, forming a uniform layer. The repetition of this process over the same spot leads to the deposition of multiple layers. Figure 1.31 shows a simplified schematic of the LCVD working principle. The main limits of this technique are the relatively high pro-

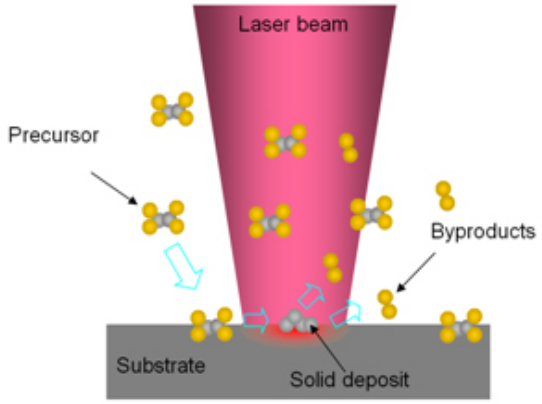

Figure 1.31: Laser Chemical Vapour Deposition working principle.

cessing costs, due to the sophisticated equipment employed, such as the vacuum pump, and the employment only of volatile materials. A detailed review was presented by Duty *et al.* [82].
Laser-Enhanced Electrodes Plating (LEEP) employs a liquid precursor forming a solution in which the substrate is immersed. As for LCVD, the laser beam, focused on a spot, causes a rapid heating that leads to the liquid decomposition and to the printing of a metallic plate on the substrate. This technique, described in many reviews [83], does not allow a precise control of the layer thickness.
Laser-induced forward transfer (LIFT), finally, is based on a solid transparent support containing the material to be deposited. The target substrate is placed in parallel at a distance of about 100 μm below or above. In this case, the laser beam vaporizes the solid precursor which rapidly condenses on the substrate. The versatility of this technique allows the deposition of a wide range of materials, since it does not have strict physical requirements, while the main limitation is that target surfaces must be very flat due to the proximity with the solid support containing the material precursor. Figure 1.32 shows a schematic of the LIFT working principle, while more details can be found in [84].

1.3.3 Inkjet printing technique

Inkjet Printing is the main material deposition technique employed in this thesis. It mainly consists of the ejection of fixed quantities of ink from a chamber through a hole, called *nozzle*. The ink droplets, under the gravity force, fall on the target substrate and form a patterned layer. An annealing process is then necessary to make the ink solvents evaporate leaving a solid layer on the substrate. The drop ejection can be caused by various transducers and in different ways: the most common, described in the followings, include countinu-

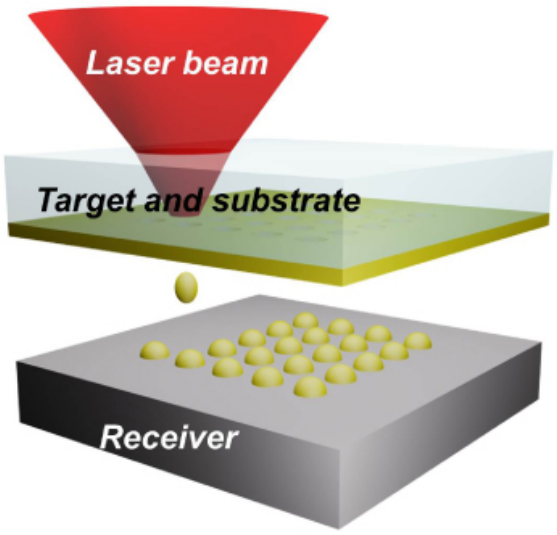

Figure 1.32: Laser-induced Forward Transfer working principle.

ous Inkjet Printing and Drop-on-Demand Inkjet printing. Moreover, the latter can be actuated most commonly by means of a thermoelectric or a piezoelectric transducer. Figure 1.33 gives a summary of all the possible Inkjet printing technologies [85]. Several interesting articles [3,86,87] describe them and offer an overview on their versatility and on the different possible applications.

Figure 1.34 shows a schematic of *Continuous Inkjet Printing* mode. The ink is continuously pumped from a "drop generator" module through a nozzle, by means of a transducer, usually piezoelectric. The ejected ink flow breaks down into drops, due to the Rayleigh instability. These drops pass through a system of charging plates and, under the effect of an electrostatic field, they get electrically charged. Then they pass through a system of high-voltage deflection plates which generate a variable electromagnetic field: the charged drops are deflected to the desired direction onto the substrate and, together, form the patterned layer. The more the droplets are charged, the more they are deflected: thus the charging plates actually receive the digital input and control the printing process. When a drop is not required to be printed, the charging plates turn off, the drop does not get neither charged nor deflected, but it is collected in a recirculation system. Thus, they are conveyed into the main ink reservoir and then pumped again to the drop generator. With the continuous approach high printing frequencies (up to 80 kHz) and jet velocity (20 m/s) can be reached [80], but a resolution not better then 100 μn can be achieved. Moreover, due to the recirculation

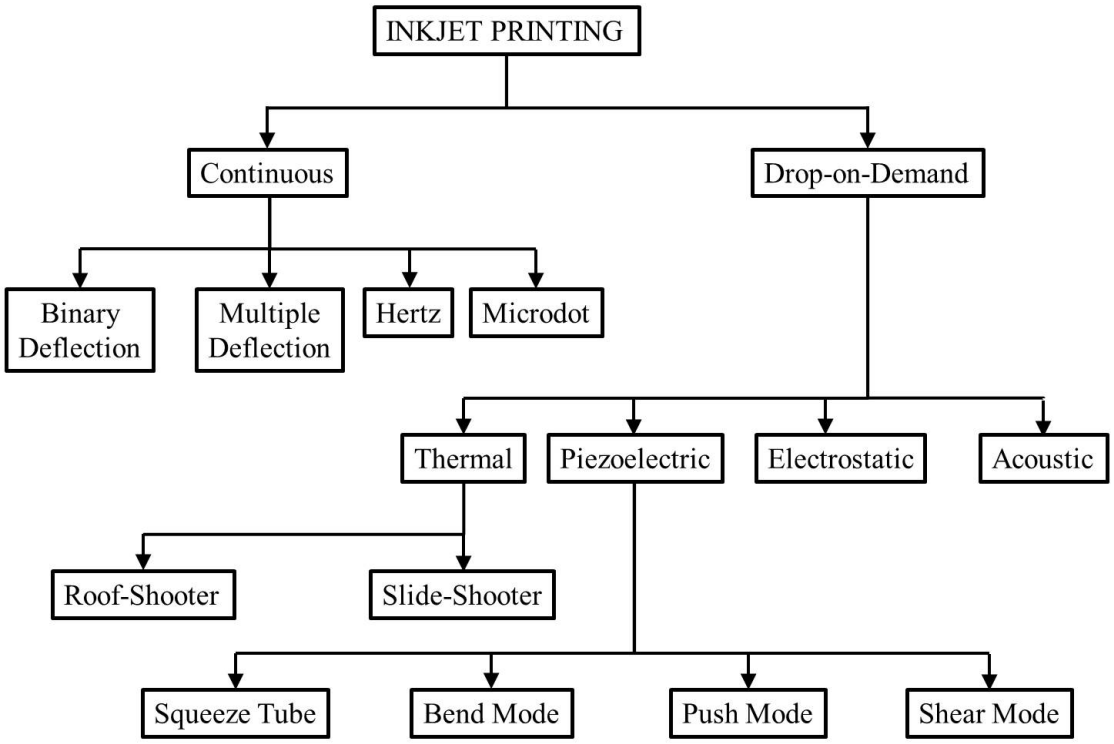

Figure 1.33: Schematic classification of the different inkjet-based printing technologies.

process, a high contamination probability can degrade the ink. This technique finds its best application in high-speed textile printing [3].

A different approach is used with *Drop-on-Demand Inkjet Printing* (DoD), schematized in figure 1.35. Here the drop ejection is not continuous, but occurs only when the transducer, that can be based on the thermoelectric or piezoelectric effect, is biased with a voltage pulse. Therefore all the droplets ejected are directly deposited to the target substrate and form the patterned layer, without passing across charging plates or deflection plates. Moreover, no re-circulation system is needed, leading to a reduced contamination risk.
The working principle of a *Thermal* DoD inkjet printer is based on the Joule effect. The transducer of the drop chamber is a simple heating resistor. When it is subjected to a considerable current flow, its temperature increases rapidly (Joule effect) as well as that of the surrounding ink. If the ink solvent is volatile, it starts to vaporize and a vapor bubble is generated, causing an abrupt pressure increase. Thus, the ink is forced through the nozzle. As the current is suddenly cut off, the resistor temperature decreases and the vapor bubble vanishes: the ink previously forced outside is then detached from the nozzle and a droplet is formed.

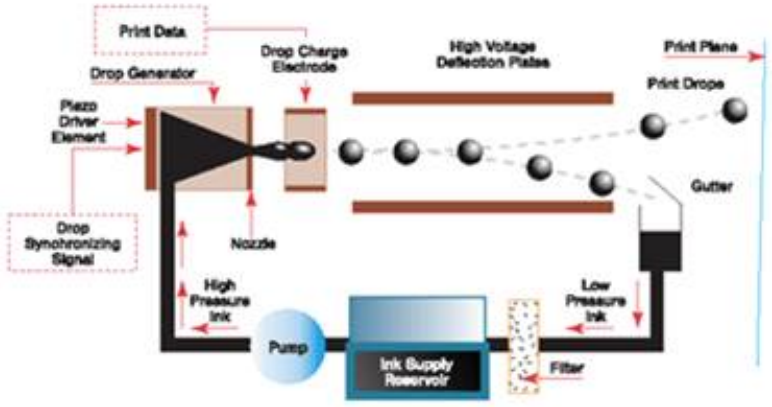

Figure 1.34: Schematic of the countinuous inkjet working principle.

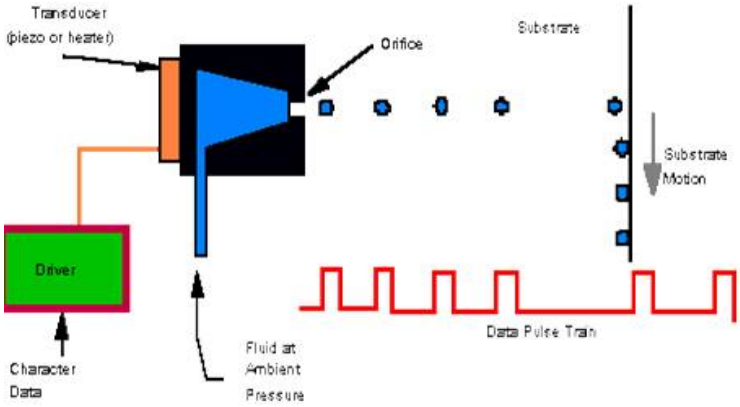

Figure 1.35: Schematic of the Drop-on-Demand inkjet working principle.

The other most commonly used inkjet printer is based on the *piezoelectric* DoD mode. It is based on the piezoelectric effect: a piezoelectric crystal is deformed when a high voltage is applied on it. In this case the transducer is a piezoelectric crystal biased with a desired voltage waveform. In its stand-by position, the crystal is slightly depressed in order to prevent the ink to flow out of the nozzle. Then, in rapid sequence, the crystal is set to its neutral position and then to its maximum deflection: due to the initial depression the ink is first drawn from the ink reservoir and then, after a rapid pressure increase, suddenly ejected from the nozzle. This multi-phase working principle is explained more in detail in paragraph 2.1.1 and in figure 2.5, where the piezoelectric DoD inkjet printer used in this work is shown. In conclusion, it is worth remarking that piezoelectric DoD does not have any specific limitation about the ink volatility, as for thermal DoD, thus the former is theoretically more versatile.
Specific ink requirements regard their chemical and physical properties, in order to obtain

a good and controlled jet, and depend on the printer characteristics. This paragraph was intended as a general description of the working principles of the inkjet technologies. The ink and printing specifications required for this work are given in the experimental section, chapter 2.

2 Inkjet Printing technique

This chapter contains an experimental insight on the inkjet printing activity. The first part (section 2.1) describes the printer employed, namely the *Dimatix Materials Printer 2831*, with all the relevant features for the optimization of the printed layers. Since the setting of the best parameters involves a deep knowledge on the drop deposition process, section 2.2 provides a step-by-step description of all the phenomena which occur from the ink formulation to the formation of a solid patterned layer. A detailed overview on the materials employed is given in section 2.3, where the chemical and physical printing-related properties are listed for each material. Finally, the specific printing parameters and results for each ink employed are described in the last three section: 2.4 for conductive inks, 2.5 for semiconducting inks, and 2.6 for insulating inks. These are intended to be empirical guidelines for achieving the best required performances for each ink. The overall structures of the complete devices are described in the last two chapters together with their specific application.

2.1 Working principle and parameters

This thesis is mainly based on the inkjet printing technology for the fabrication of organic devices. The inkjet printer employed is the *Dimatix Materials Printer 2831* (DMP2831), a piezoelectric Drop-on-Demand printer purchased from FUJIFILM Dimatix [88], shown in figure 2.1. All the description below is a summary of the DMP2831 main functionalities. For further information read in detail the related user manual [89]. The printer is composed of four main parts, as schematically shown in figure 2.2:

- *Print Carriage*. It is the carriage where the cartridge, *i. e.* the ink container, is placed. Its controlled movement over the substrate is an essential parameter to obtain a good printing. It includes a videocamera, called *fiducial camera*, that allows the pattern

Figure 2.1: Picture of the Fujifilm Dimatix Materials Printer 2831.

alignment and the screening, at micro-scale, of the printed patterns.

- *Platen.* It is movable metallic plane where the substrate is placed during the printing process. Its temperature can be set floating or raised up to 60 °C. It also includes a vacuum system with many holes that should keep the substrate fixed during the printing. However, in most cases the substrates are too thick and an additional adhesive tape is required.

- *Drop Watcher.* It consists of a videocamera and a small pad. Here the ejected drops can be directly viewed before the actual printing, in order to optimize the printing parameters and obtain a good final pattern. This is a fundamental preliminary step, since every type of ink require a fine calibration of all the possible printing parameters.

- *Cleaning Station.* It consists of a single cleaning pad and a small pressure tube: they provide for the cartridge maintenance and are generally used before and during the printing process.

The DMP2831 is controlled via software, provided by Dimatix, which manages all the printing steps and allows the setting of some important parameters (such as the platen temperature or the cartridge height). It is also employed to the management of the printing patterns, both by means of a pattern editor and by importing external images and converting them to "printable" files. In the followings a general and practical description of these features is presented, with a particular emphasis on those considered most important for the

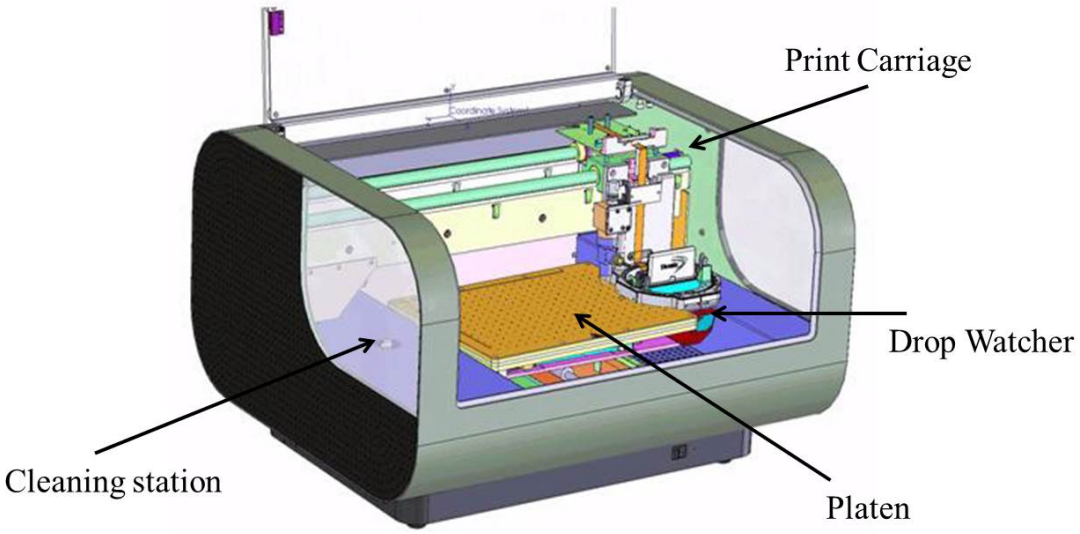

Figure 2.2: Schematic of the Fujifilm Dimatix Materials Printer 2831.

development of the work carried out in this thesis.

2.1.1 Print Carriage

The *Print Carriage* is the core of the DMP2831. It is schematized in figure 2.3. During the printing process the carriage moves horizontally (X direction) above the substrate, while the vertical shift (Y direction) is achieved by the platen motion. The carriage speed is directly related to the pattern resolution and to the maximum jetting frequency set: high-resolution patterns in the low-frequency range (up to 1 kHz) result in a slow carriage motion, while low-resolution patterns at high-frequency range give raise to a faster motion. The total printing procedure is composed of consecutive horizontal scans followed by vertical shifts of the platen, just like a raster scan. Since the ink deposited during a horizontal run is affected by the ink deposited in the previous run, especially due to capillarity phenomena, a proper calibration of the drop spacing and of the carriage speed is mandatory. Also, the distance between substrate and printing nozzle plate (Z direction) influences the final pattern, since a higher distance results in a longer drop fall and in a different impact with the substrate.
Figure 2.4 shows a schematic of the *Cartridge*. Is is composed of two main parts: a fluid module, containing a fluid bag which acts as ink reservoir, and a jetting module, where 16 nozzles, *i. e.* holes where the ink is ejected from and whose diameter is 21.5 μm, are aligned in a single row at a distance of 254 μm. Two types of cartridges can be used, depending on the volume of the ejected drops: 10 pL and 1 pL.

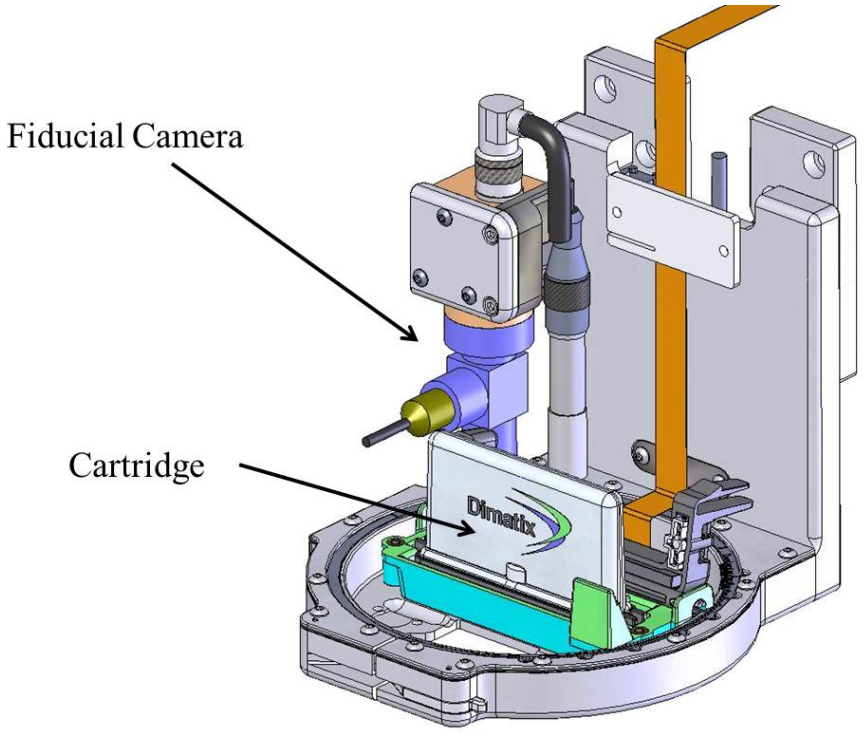

Figure 2.3: Schematic of the DMP2831 Print Carriage.

The *Fluid Module* with the ink reservoir can contain up to 3 mL of ink, even though the producer indicates a limit of 1.5 mL. This cartridge is compatible with most solvents:

- aliphatic alcohols (high boiling points better than low in all cases)
- aromatic hydrocarbons such as anisole and trimethylbenzene
- aliphatandic hydrocarbons such as hexane and dodecane
- cellosolves
- glycols
- lactate esters
- aliphatic and aromatic ketones
- polyethylene glycols and polypropylene glycols

The *Jetting Module*, where the nozzles are located, is the most fragile and important element of the cartridge. Often nozzle clogging causes a fatal degradation of the printing performance, thus an accurate cleaning and an opportune parameter setting is highly desirable.

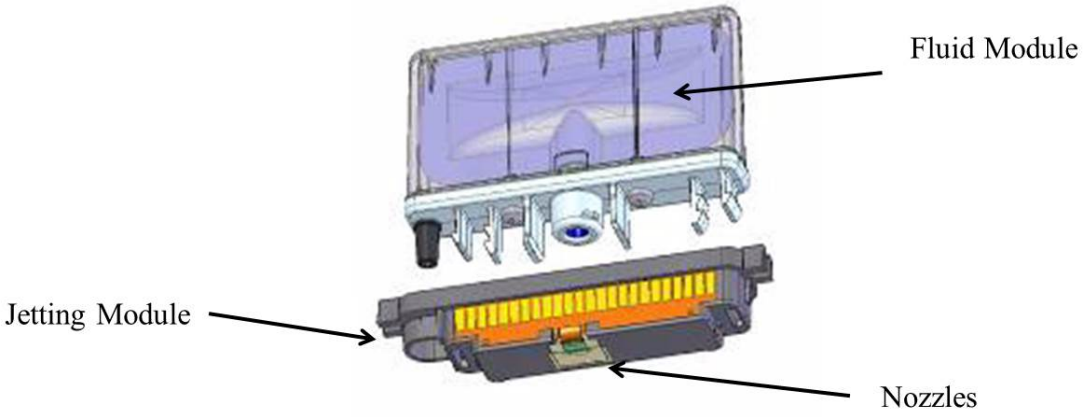

Figure 2.4: Schematic of the DMP2831 Cartridge.

The producer gives the chemical and physical characteristics of ideal ink to obtain the best printing performances:

- viscosity: 10-12 cP at jetting temperature
- surface tension: 28-33 dyne/cm at jetting temperature
- low volatility: boiling points higher than 100 °C
- degassing: is can be done with a vacuum system, by ultrasonic baths or by spinning
- filtering: it is recommended to filter the fluids with a 0.2 μm nylon filter
- acidity: pH between 4 and 9 is suggested

The parameters mentioned above are essential to achieve good printing results and are the starting point when a new ink is formulated. Degassing and filtering is always done before filling any new cartridges. Low solvent volatility is desirable to reduce solvent evaporation and fatal nozzle clogging. Above all, viscosity and surface tension are the most important parameters which strongly influence the final printing performance. The ranges of values indicated are the best to obtain very good printed layers, but less strict ranges are also satisfactory for fine printing. For example, even at a viscosity of 5 cP a regular layer with low resolution can be obtained. Section 2.2 analyzes in detail the influence of these two parameters on the ink formulation.

The piezoelectric crystal of each nozzle chamber is activate by a four-phase voltage wave described in figure 2.5:

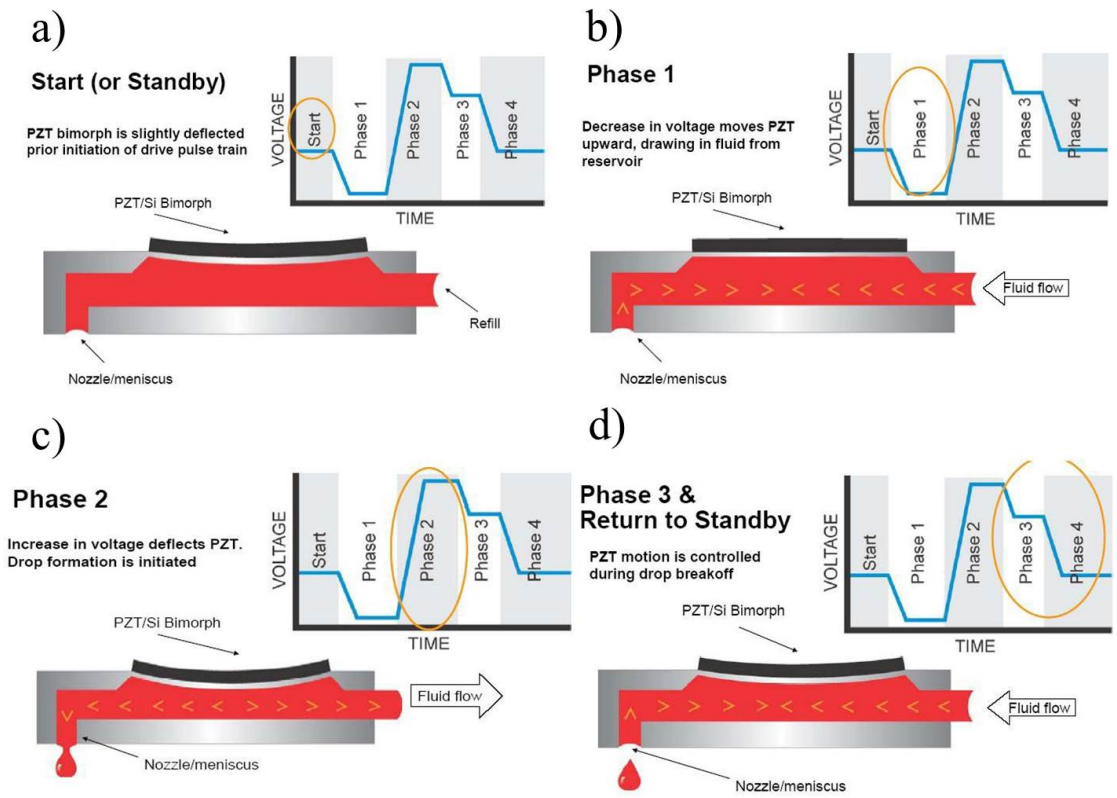

Figure 2.5: Four-phases voltage wave of the piezoelectric crystal: (a) standby, (b) voltage decrease, (c) rapid voltage increase and (d) gradual return to standby.

1. *Standby*: a small voltage keeps the piezoelectric crystal slightly deflected and thus a small pressure is applied inside the micro-chamber.

2. *Phase 1*: the voltage is set to zero and the crystal returns to its neutral position. The depression arisen inside the micro-chamber beckons the fluid from the ink reservoir.

3. *Phase 2*: the voltage is rapidly set to its maximum value and the piezoelectric crystal is subjected to a very high deflection. The volume inside the micro-chamber decreases and an ink drop is ejected from the nozzle.

4. *Phase 3 and Return to Standby*: the voltage is decreased and the crystal gradually reduces its deflection, returning to its standby position described above.

This four-phase wave can be adjusted in terms of duration, slew rate between consecutive phases, and maximum jetting frequency, resulting in a proper calibration for each specific ink. Anyways, the standard waveform provided by Dimatix generally is fit for most inks. It

is worth reminding that also a non-jetting waveform can be modified, which is applied to non-jetting piezoelectric crystals to maintain the fluid dynamics and reduce the probability of nozzle clogging. In this case, since the deformation of the piezoelectric crystals must not cause a drop ejection, low voltages (about 10% of the voltage applied to the jetting waveform) are used.

2.1.2 Cartridge maintenance

The cartridge maintenance is a fundamental step to obtain good final printed patterns. Since most of the printing quality depends on the quality of the ejected drops, a good cleaning of the nozzle plate is mandatory. The DMP2831 includes a cleaning station where three different cleaning operations can be performed in order to avoid, or at least to reduce, the probability of nozzle clogging:

- *Spit*: all the 16 nozzles eject drops at the frequency and firing voltage previously set. This operation cleans the nozzles and the ink path from the reservoir to the nozzle plate.

- *Purge*: this is a sharper operation than Spit and consists of applying air pressure from the cartridge pressure tube. The fluid bad, or ink reservoir, is compressed and the ink is forced outside the nozzles. Purge is the best way to unclog eventual path where solid agglomerates avoid the natural ink flow. This operation is successful until the ink is not too dried, *i. e.* until the ink solvent is not totally evaporated. Moreover, it causes a remarkable ink waste especially for low-viscosity inks: an opportune tuning and employment of Purge must be done before and often during the printing operations.

- *Blot*: it consists of the cartridge coming down to keep the nozzle plate in contact with the cleaning pad. This causes the pad to absorb exceeding ink in the nozzle plate, which could clog the nozzles or deviate the jets from the vertical direction.

Each one of these operation can be performed for a desired time: usually Spit and Blot operation are set to no more than 1 second long, while Purge requires variable duration, from 0.5 to 5 seconds, depending on the ink. The combination of these operations, with an inter-operation delay, is called *Cleaning Cycle*. The standard cleaning cycle consists of 0.5 s Spit, 1 s Purge and again 0.5 s Spit, which is suitable for most inks. The major modifications are applied to the Purge operation and to the number of consecutive cleaning steps. Since the cleaning pad, where the ink is conveyed, gets easily drenched when several cleaning cy-

cles are performed, a frequent replacement is desirable to improve the cleaning operations. Moreover, a new cleaning pad must be used when replacing the cartridge containing a new ink, to avoid ink contamination.

2.1.3 Cartridge settings

In figure 2.6 an image from the Drop Watcher station is presented: it shows the drops ejected by the cartridge nozzles. They are an example of ideal ink: vertical direction, reduced drop tails, no nozzle clogged, perfect alignment. To approach this ideal condition, several printing

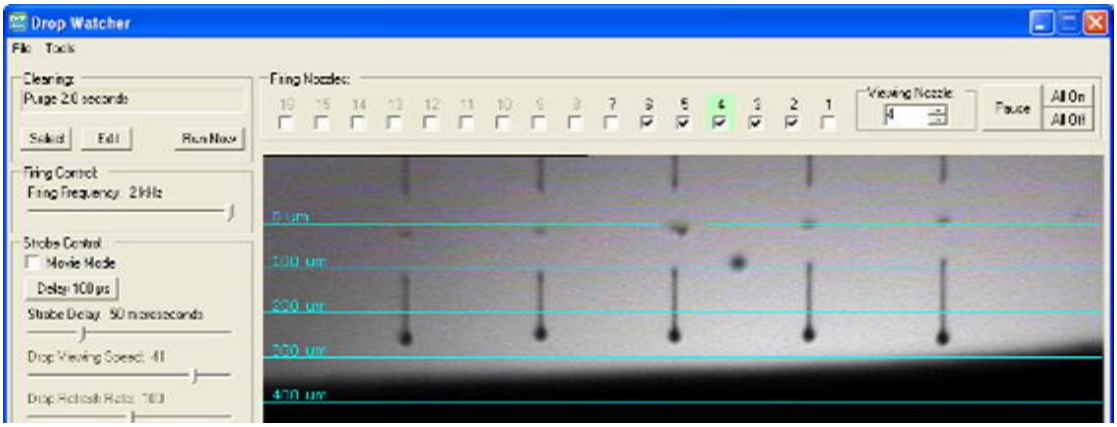

Figure 2.6: Video capture of the ejected drops in the Drop Watcher station.

parameters can be modified from the Cartridge settings:

- *Voltage Waveform*: it has been described in subsection 2.1.1 and consists on the voltage waveform applied to the piezoelectric crystals for the drop ejection. The default waveform provided fits the requirements for almost all the inks employed in this thesis.

- *Firing Voltage*: it is the maximum voltage reached by the jetting waveform, *i. e.* the voltage level of the Phase 2, where the drop is ejected. Higher firing voltages result in bigger and faster drops with longer tails, while on the contrary lower firing voltages produce smaller and slower ejected drops with reduced tails. The voltage values range from 1 V up to a maximum of 40 V and each nozzle can be independently biased with its own voltage. This is maybe the most important parameter to set: high-viscosity inks require higher voltages to be ejected, otherwise they could clog nozzles; on the other hand for low-viscosity inks medium or low voltages are sufficient. For high-precision patterns, such as the interdigitated source and drain electrodes of a transistor, a moderate voltage should be applied, in order to reduce the tails and the probability to form satellite

drops when the main drop impact on the surface, which could lead to short-circuits.

- *Jetting Frequency*: this is the maximum frequency at which the nozzles eject drops and it is directly correlated with the carriage speed in the X direction. The upper value of the jetting frequency is 80 kHz, while the default value is 20 kHz. In general, high-precision patterns should be printed at low frequencies, no more than 1-2 kHz, while the other patterns can be printed at higher frequencies.

- *Number of Jetting Nozzles*: it is the number of adjacent nozzles employed to print a pattern and range from 1 to all the 16 nozzles. For high-precision patterns, as the interdigitated structure mentioned above, only 1 nozzle should be used, while for rough patterns more nozzles can be used. In some cases, to obtain a small but smooth patterned surface, many nozzles must be used: it is the example of P3HT-PCBM layers (section 2.4), where 13 adjacent nozzles are used to reduce the roughness and print the whole layer just in one carriage run.

- *Cleaning Cycles*: they have been described in detail in the previous paragraph. From the Cartridge Settings window the single cleaning operations can be combined in actual cleaning cycles. Here it is also possible to set whether cleaning cycles are performed before, after and during the printing, and, when during, how often (based on a set number of seconds or on a set number of carriage runs). Cleaning cycles before printing are almost always highly recommended to prevent nozzle clogging, while setting cleaning cycles during the printing process depends on the specific ink employed and on the pattern dimension. Frequent cleaning is mostly recommended for inks whose particles tend to agglomerate and also for standard inks when printing wide patterns.

2.1.4 Drop Spacing

The *Drop Spacing* is the distance between the centers of two contiguous drops. It is another fundamental parameter and is related to the required resolution of the printed pattern. The latter depends on the drop dimension and on the surface contact between drop and substrate. A further detailed description is given in section 2.2. The drops spacing in the X direction d_x is determined by the motor encoder which controls the carriage run speed. Given a

jetting frequency f_j and a drop spacing d_x, the encoded speed of the carriage v_c is:

$$v_c = f_j \cdot d_x \tag{2.1}$$

The drop spacing in the Y direction, on the other hand, is given by controlled movements of the platen. Both the X and Y drop spacing must have the same value.
When a single nozzle is used, each carriage run gives origin to a single printed line, and the overall pattern is formed by multiple contiguous lines. On the contrary, when multiple nozzles are used, a proper angle between the nozzle row and the X direction, namely the *sabre angle* α_s, must be set. Figure 2.7 schematizes the influence of the sabre angle on the drop spacing. If the nozzle row is orthogonal with respect to the X direction, *i. e.* the sabre angle

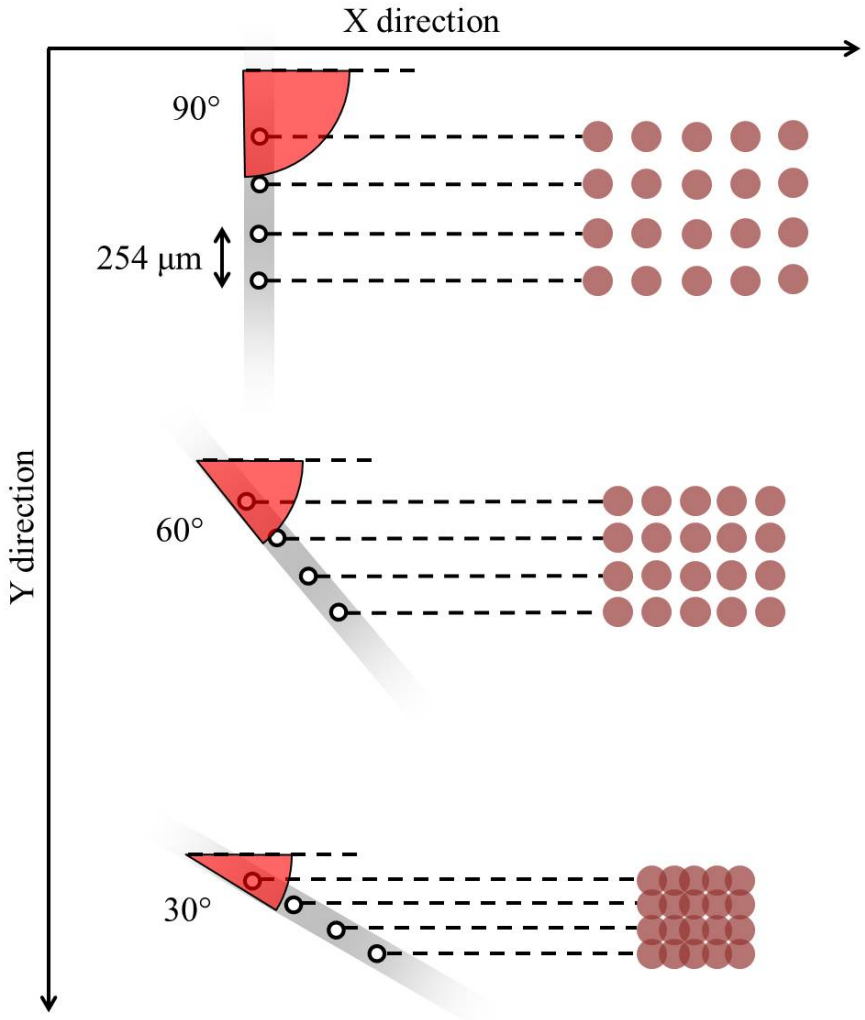

Figure 2.7: Schematic representation of the influence of the sabre angle on the drop spacing.

α_s = 90°, the spacing between adjacent drops in the Y direction is set by the fixed distance of adjacent nozzles, 254 μm. For smaller angles, the drop spacing d_y is set by the following formula:

$$d_y = 254 \cdot \sin(\alpha_s) \tag{2.2}$$

For example, by setting α_s to 30° the resulting drop spacing is 127 μm. For this reason, a zero value of the sabre angle results in a null vertical drop spacing, since the droplets ejected from all the nozzles would be overlapped. When using n nozzles, in a single carriage run n lines are printed and the encoder makes the platen moving by a distance of $n \cdot d_y$ before a new carriage run prints the subsequent n lines. Therefore, when possible, printing with n nozzles reduces the overall process duration by a factor n with respect to the single nozzle.
The desired drop spacing is correlated to the desired resolution of the final pattern, usually measured in *dot per inch* (dpi). Since one inch is equal to 2.54 cm, that is 25400 μm, the relation between printing drop spacing and image resolution is:

$$DropSpacing[\mu m] = \frac{25400}{Resolution[dpi]} \tag{2.3}$$

In conclusion, once the operator sets the desired drop spacing, the horizontal component d_x is set by the carriage motor encoder, while the vertical component d_y is set by manually adjusting the sabre angle, as shown in figure 2.8.

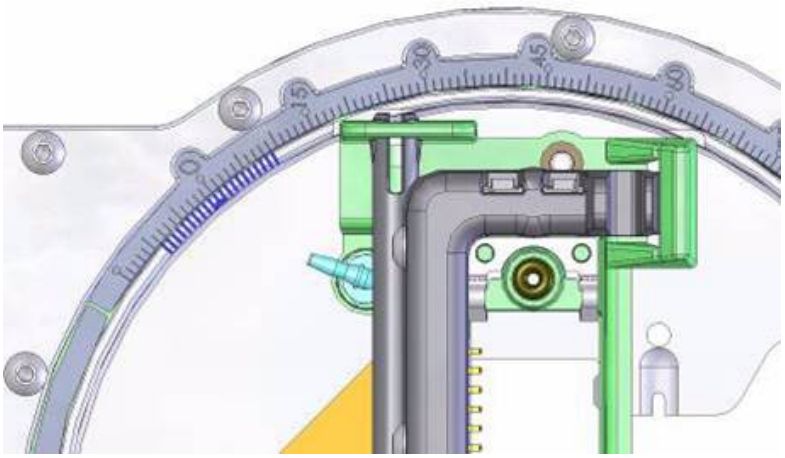

Figure 2.8: Schematic of the sabre angle manual adjustment.

2.1.5 Pattern Editor

The DMP2831 includes a software for pattern editing. It can only edit combinations of rectangles, which can have various shapes and dimensions. Figure 2.9 shows a typical layout of a pattern created by means of the DMP2831 *Patter Editor*. In the pattern editor several pa-

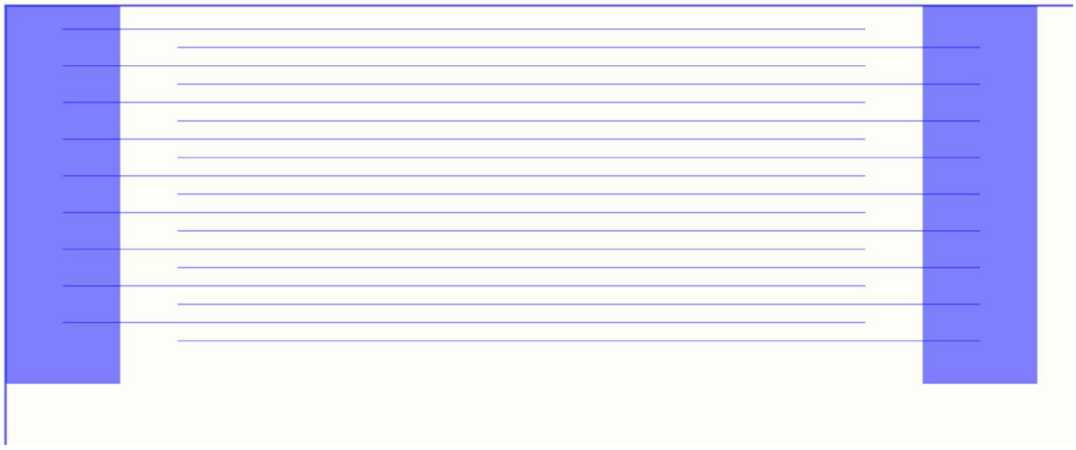

Figure 2.9: Layout of a pattern created by the DMP2831 Pattern Editor.

rameters can be set, such as the drop spacing, the number of layers and the inter-layer delay. It is possible to use a *leader bar*, *i. e.* a vertical line at the left of the actual pattern which can improve the printing performance. Also, basic layers can be replied both in the X and Y directions when periodic layouts must be printed. The drop spacing, *i. e.* the pattern resolution, decides the number of drops that will be printed in a carriage run to fill the pattern: if a pattern dimension, for example the X dimension, is lower than the resolution, one drop will be printed anyways. The software also provides the number of dots which compose the pattern, useful to calculate the carriage runs and the total amount of ink deposited to print a single layer. The origin of the pattern, placed in the top left angle of the layout, corresponds to the *printing origin* set in the platen.
As mentioned above, the DMP2831 Pattern Editor can draw only orthogonal rectangles: neither oblique nor curved patterns are possible. In order to overcome this limitation and print more complex layouts, a 1-bit image file, in *.bmp* format, must be realized with another software and then imported to the DMP2831 software which provides to convert it in the "printable" *.ptn* format.

2.1.6 Platen and Fiducial Camera

The *Platen* is the metallic plate where the substrates are firmly placed and the actual printing process takes place. The *Fiducial Camera* mounted on the carriage allows to display all the parts of the platen by means of a controlled and calibrated movement of the carriage. Figure 2.10 shows the command window of the fiducial camera. The camera field of view has a width

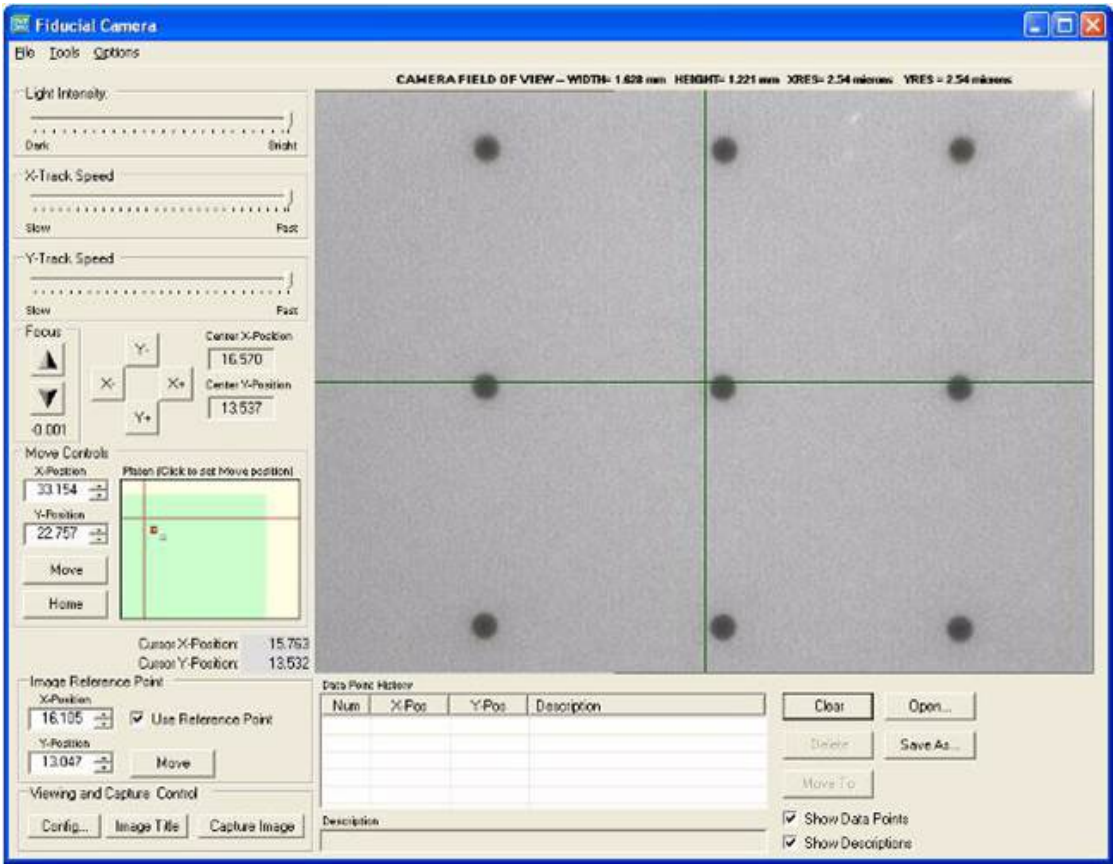

Figure 2.10: Fiducial camera window.

of 1.62 mm and a height of 1.22 mm with a resolution of 2.54 μm per pixel. Moreover, there are three possible lighting modes: dark field, bright field or both combined. The fiducial camera is used to set the printing origin, corresponding to the top left angle of the pattern, and to adjust the possible offset between the set printing origin and the actual printing origin. A measurement tool gives the possibility to measure the printed patterns with a pixel resolution (2.54 μm). The screenshots taken with the fiducial camera can be recorded in a grey-scale picture: they will be frequently shown in this thesis.

2.2 From ink to printed layers

This section provides the chemical and physical fundamentals for the comprehension of the phenomena involved to obtain a solid patterned layer from a liquid-phase solution. Starting from the ink formulation requirements (2.2.1), the viscosity is analyzed (2.2.2) which allow the drop formation in the specific printing system (2.2.3). Once the drop is deposited on the substrate, the surface energy balance (2.2.4) and the drop drying (2.2.5) phenomena are described which give origin to a solid printed continuous layer. For each one of these features, the theoretical description of the properties is followed by empirical considerations gained during the work and specific connections with the DMP2831 working mode.

2.2.1 Ink formulation

The formulation of a new ink is a challenging task since several chemical and physical requirements must be fulfilled. Below the major ones are described which have been important, and sometimes critical, for the work related to this thesis.

- *Solubility.* Solubility is the property for a solid, liquid or gaseous chemical substance, namely *solute*, to dissolve most commonly in a liquid substance, namely *solvent*, to form a homogeneous *solution*. For a specific solute and a specific solvent, solubility defines the maximum concentration, namely *saturation*, beyond which the solute does not dissolve anymore and starts to precipitate. In this context, the most common ways to describe a concentration are the mass fraction:

$$w_i = \frac{m_i}{m_{tot}} \tag{2.4}$$

  defined as the mass of the i-th solute divided by the mass of the whole solution, and the molar concentration:

$$c_i = \frac{n_i}{V} \tag{2.5}$$

  defined as the molar amount of the i-th solute divided by the volume of the whole solution. The first concentration is expressed as the weight percentage (*wt.%*), while the second is expressed as moles per milliliter (*mol/mL*). Usually a high solubility is desired, since at the end of the drying process, when all the solvent is evaporated, the amount of active material is directly proportional to its solubility.

- *Solvent orthogonality.* Often printed devices are not made of one single material but

are the result of multiple stacked layers, as for transistor structures or vertical diode structures. Each layer is printed using a different ink and the deposition of multiple layers gives origin to a structure where each layer has its own properties and, from an electrical point of view, it can be an insulator, a conductor or a semiconductor. In this case, all the solvents of the printed inks must be mutually orthogonal, *i. e.* the solute of the lower layers must not be solved also by the solvent of the upper layers. Otherwise the materials of interest, already printed and dried, could be easily redissolved and the solid layer could vanish. Even though some pre-processing or post-processing treatments are able to improve the chemical and mechanical stability of the printed materials, the formulation of a single ink has to take account also of the other inks which compose the same printed device. As a very general rule, two alcoholic solvents, such as ethyl alcohol and isopropyl alcohol, can never be used for two layers of the same structure, while alcoholic and aromatic solvents, such as ethyl alcohol and toluene, tend to be quite orthogonal.

- *Boiling point.* The boiling point of a substance is defined as the temperature at which the vapor pressure of the liquid equals the pressure surrounding the liquid and it changes into a vapor. The vapor pressure, that is the pressure at which at a given temperature the gaseous phase and the liquid phase are in equilibrium, is strictly related to tendency of a substance to vaporize, namely *volatility*. A high boiling point is related to low volatility, while on the contrary a low boiling point results in high volatility. During the ink formulation, high-volatility solvents are generally undesired since in this case the drying time would be reduced and uncontrollable, negative effects on the printed layers could occur. Moreover, if the ink solvent starts to evaporate before a high temperature is set, as during the printing process, *de facto* it increases the ink concentration and leads to agglomeration of solute particles and to nozzle clogging. On the other hand, the boiling point cannot be too high since the thermal drying of the ink must not occur at very high temperature, not to degrade the plastic structure.

- *Stability.* The stability of an ink is the property to maintain its chemical and physical properties, as well as the electrical properties of the active material, over the time. In particular, inks should be stable at environmental condition and show no degradation under contamination with oxygen and water, especially at short-run. This is not a mandatory requirement, since usually the printing process takes place immediately af-

ter the ink preparation. Nevertheless for some inks, such as those based on PEDOT:PSS, electrical degradation could occur that must be taken into account.

- *Particle agglomeration.* Particle agglomeration is an "empirical" feature to consider when preparing a new ink. Beyond the agglomeration caused by the solvent volatility, mentioned above, it could be take place also at natural conditions and is related to the surface tension balance between solute and solvent. This is obviously an undesired effect: ink is ejected through nozzles whose diameter is 21.5 μm and, if solute molecules agglomerate in micrometric particles, nozzle clogging could easily take place. On one hand, in order to overcome this problem, surfactants can be added in the ink formulation, which lower the interfacial energy between solute and solvent. On the other hand, pre-processing treatments must be performed to the ink, such as ultrasonic bath or filtering, in order to dissolve or block agglomerates.

- *Blending.* The requirements for an ink are not uncorrelated: adjusting the ink formulation to modify one parameter almost always affects also the other parameters, thus it is very challenging to fulfill all these ink specification by one simple combination of one solute and one solvent. The most common situation involves one active material, *i. e.* one solute, which is solved in a blend of solvents and possibly other solutes. Each solvent or accessory solute individually satisfies one single requirement, and the overall blend, if well formulated, should satisfy all the requirements.

In addition to these properties, additional viscosity and surface energy requirements, dependent on the specific printer employed, are analyzed in detail in the following paragraphs. All the specifications followed during this work are listed in paragraph 2.1.1.

2.2.2 Viscosity

The *viscosity* is maybe the most important parameter to adjust in the ink formulation in order to obtain a high printing quality. In this paragraph the physical basics of viscosity are explained: for wider details it is recommended a further reading, as for example the excellent book of Dabir Viswanath *et al.* [2]. Moreover, in the appendix B a description of the viscometer working principle is given.
Viscosity is a characteristic property of all liquids: it measures the liquid resistance to flow or shear as well as the frictional properties of the fluid. It depends on the temperature and pressure: in this work, both are implied to be at room condition. Basically, two form of viscosity

can be discerned:

- Absolute or dynamic viscosity
- Kinematic viscosity

Dynamic viscosity is the one measured in this context and required on the DMP2831 cartridge specifications. Figure 2.11 exemplifies the shear of a liquid film, which defines the dy-

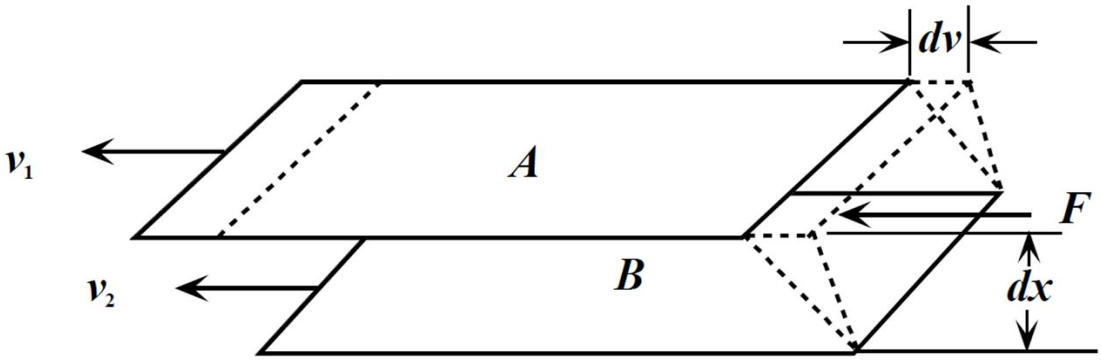

Figure 2.11: Exemplification of the shear of a liquid film [2].

namic viscosity. It is the tangential force F per unit area required to slide one layer A against another layer B at velocities v_1 and v_2 respectively when they are maintained at a given distance x. In a mathematical form, since the viscosity η defines the fluid resistivity to flow, it can be described as the proportional factor between shear stress σ and strain rate $\dot{e}$:

$$\sigma = \eta \cdot \dot{e} \tag{2.6}$$

The strain rate is usually defined as:

$$\dot{e} = \frac{1}{x} \cdot \frac{dx}{dt} = \frac{v}{x} \tag{2.7}$$

where v is the velocity in the direction perpendicular to the two layers. Therefore the dynamic viscosity is expressed by the following formula:

$$\eta = \sigma \cdot \frac{x}{v} \tag{2.8}$$

The kinematic viscosity, which also involves the fluid density ρ, is defined as:

$$u = \frac{\eta}{\rho} \tag{2.9}$$

The most common unit for viscosity, also used in this work, is *centipoise* (cP), defined as 0.001 Pa·s.
According to viscosity dependence on shear stress and on time, liquids can be divided into three categories:

1. *Newtonian*: the viscosity is a constant parameter independent of the applied shear stress, *i. e.* the shear rate is a linear function of the shear stress.

2. *Time-independent Non-Newtonian*: the viscosity is a time-independent function of the shear stress, *i. e.* the shear rate is a non-linear function of the shear stress.

3. *Time-dependent Non-Newtonian*: the viscosity itself is time-dependent, therefore no shear rate function of the shear stress can be univocally defined.

Ideal inks are newtonian fluids: actually, the ink dynamics depends on their composition. Polymer-based inks show a marked non-newtonian behavior, since long polymeric chains give origin to viscoelastic forces: this results in the typical tail of an ejected droplet.
The viscosity range required by the DMP2831 is 10-12 cP: this is intended as an ideal viscosity to obtain a perfect printing process, but actually "printable" inks have a wider range of viscosity. From 10 cP to 18 cP very good printing can be performed, with a very good control of the drop formation, vertical direction and reduced drop tails. Over 18-20 cP viscosity may be too high and the deformation of the piezoelectric crystal is not sufficient to eject a drop. On the other side, viscosities in the range 6-10 cP result in fair good printing with generally vertical drops but with a poor control on the drop volume: satellite drops can arise which do not allow the printing of very accurate patterns. The range 1-6 cP includes printable inks with poor or very poor control on the drop and the final result: these inks are generally used to create full non-patterned layers whose surface roughness is not a critical issue for the device performance. Under 1 cP the printing is almost impossible: the very low viscosity results in material waste during the cleaning cycles and in a very poor control of the droplets, which can be of various dimensions, rarely vertical and that are deposited in a totally chaotic way on the substrate.
The best solution to modify the ink viscosity during its formulation is to employ different solvents, when possible. The main problem is with low viscosity inks, since most solvents have low intrinsic viscosity. To overcome it, a small quantity of a high-viscosity substance can be added to the solution, which does not affect neither the surface tension nor the final electrical performance of the device.

2.2.3 Drop formation and drop impact

The actual *drop formation* occurs only if specific combinations of viscosity, described above, and surface tension, described later, are fulfilled. One of the most indicative parameter which encloses the two properties is the *Ohnesorge number* (Oh):

$$Oh = \frac{\eta}{\sqrt{\rho D \gamma}} \tag{2.10}$$

where η is the viscosity, ρ the density, γ the surface tension and D the nozzle diameter. Often, the inverse of the Ohnesorge number is used: $Z = Oh^{-1}$. Several studies have been performed in order to investigate which is the best working range for the Z parameter [3, 86, 90, 91]: a careful reading of these articles is recommended for a deeper comprehension of this phenomenon, which goes over the purpose of this thesis.

Figure 2.12 shows the comparison, in stroboscopic images, between the formation of new-

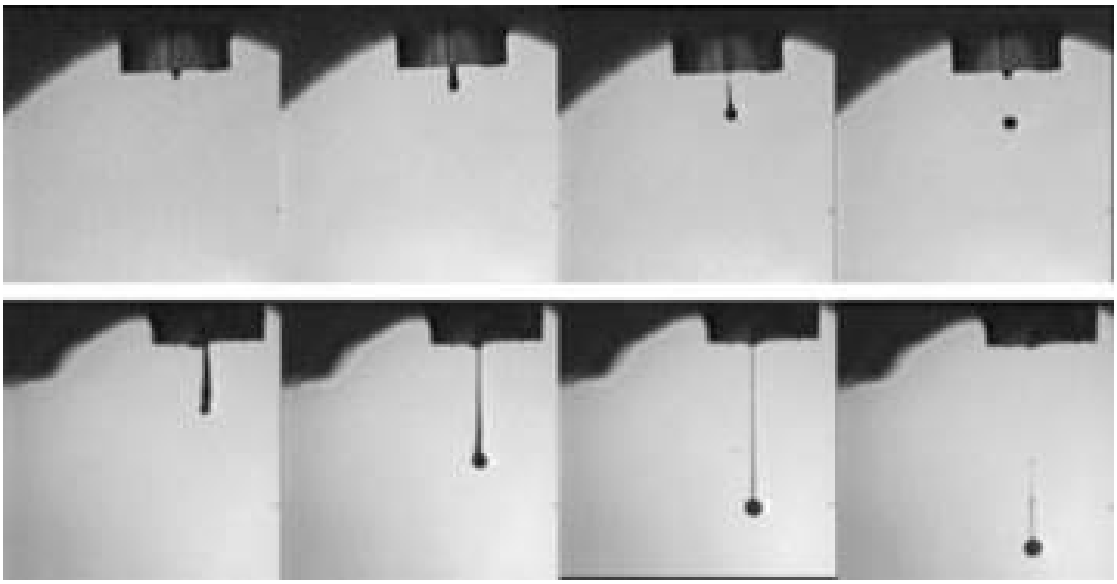

Figure 2.12: Stroboscopic images of the droplet formation: newtonian fluid (top) and the same fluid become non-newtonian just by the addition of a small amount of polymer (bottom) [3].

tonian and non-newtonian drops. In the top, a newtonian fluid is ejected through the nozzle with a vertical direction and without tail. By adding even a small amount of polymer, the liquid become non-newtonian, as shown in the bottom: a marked droplet tail is noticed and the ejection time is increased. Although the former is the ideal condition for inkjet printing, most of the employed inks show a behavior similar to the latter case. As a general rule, the more

the polymer chains are long, the more the viscosity increases and non ideal effects occur. Once the droplet is ejected, it falls down to the substrate and impact on it: *drop impact* phenomena are another very important feature to take into account, since an optimized impact results in an optimized and controlled ink deposition and therefore in a better pattern resolution. It is influenced by several factors, both depending on the droplet itself (such as its velocity, its volume and its direction) and on the substrate (wettability and roughness). Figure

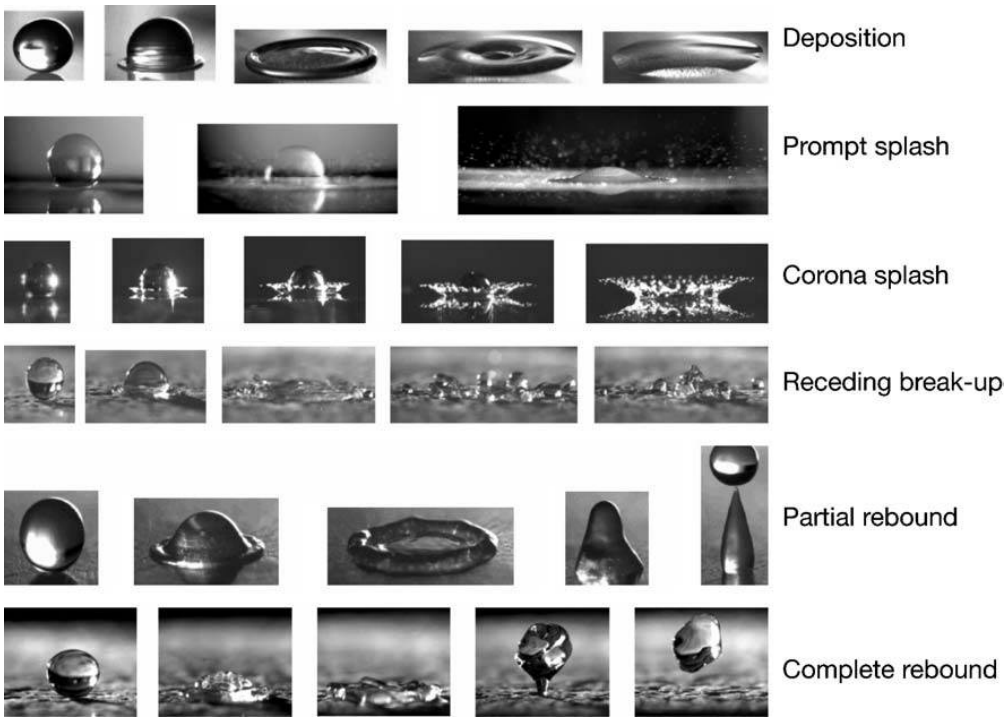

Figure 2.13: Morphology of a drop impact on a dry surface [4].

2.13 shows some possible examples of drop impact: from simple deposition to hard deposition, or splash, to partial or complete rebound of the droplet. Some interesting studies have investigated this phenomenon [4, 92]. In particular in [92] the *spreading factor*, related to the drop diameter, has been studied during the drop impact and four phases have been characterized:

1. *Kinematic phase*: the drop falls down towards the substrate until it impacts. The spreading factor is proportional to $t^{1/2}$ and depends only on the initial diameter and the drop velocity.

2. *Spreading phase*: the drop has impacted on the substrate and it starts to spread on it. The spreading factor increases linearly with t. This phase is generally influenced by the

drop viscosity, while the surface tension is not relevant.

3. *Relaxation phase*: the drop, after the initial spreading, starts to contract. The surface energy balance between drop and substrate dominates this phase: it is described more in detail in the next section.

4. *Wetting phase*: if the substrate is wettable, the drop continue to expand proportionally to $t^{1/10}$.

A further undesired effect, *splashing*, can occur especially if the drop volume or the drop velocity are too high. In inkjet printing this effect results in the formation of satellite drops which dramatically decrease the process resolution.

2.2.4 Surface energy

The *surface energy* plays a fundamental role both in drop formation and in drop deposition on the substrate, as mentioned before. In this paragraph an overview on surface tension is given, with a particular focus on the surface wettability. More detailed description can be found, for expample, in the book by Jacob Israelachvili [93].

In order to understand the principles of wetting phenomena, some definitions are mandatory. The *work of cohesion* W_{11} is the free energy change, or reversible work done, to separate unit areas of the same substance from contact to infinity in vacuum (figure 2.14a). This is a density of energy, measure therefore in J/m^2, and since all media attract each other in vacuum W_{11} is always positive. Similarly, the *work of adhesion* W_{12} is the free energy change, or reversible work done, to separate unit areas of two different media 1 and 2 from contact to infinity in vacuum (figure 2.14b). The *surface energy* γ_1 of the substance 1, generally solid, is defined as the free energy change when the area of that substance is increased by unit area. Since the process of creating a new unit area is equivalent to separating two half unit areas from contact (as in figure 2.14a), the surface energy can be defined as:

$$\gamma_1 = \frac{1}{2} W_{11} \tag{2.11}$$

γ_1, as for the other quantities, is measured in J/m^2 or, more commonly, in mJ/m^2. When dealing with liquids, an equivalent term, *surface tension*, is preferred. This is the force per unit length required to keep still a movable side of a frame over which the liquid is stretched. This is measure in mN/m or often in dyn/cm. Surface energy and tension are related to the latent heat and to the boiling point: this is high for metals ($\gamma_M < 1000$ mJ/m^2) and low for

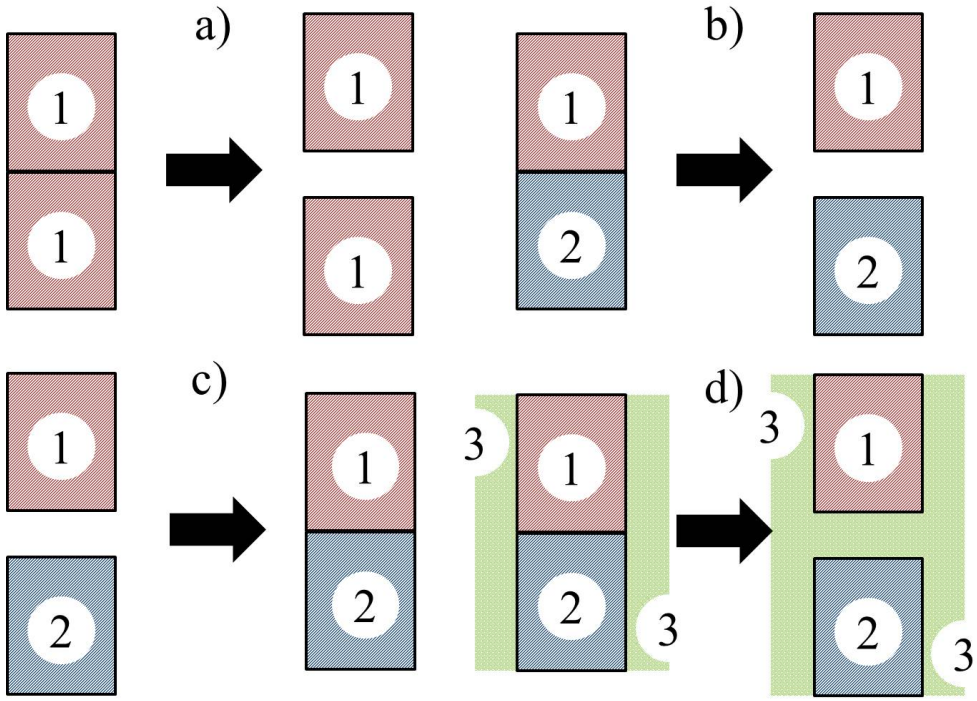

Figure 2.14: Phenomena involving surface energy: (a) separation of the same substance in vacuum, (b) separation of two different substances in vacuum, (c) contact of two different substances in vacuum, (d) separation of two different substances in a third medium.

gases ($\gamma_G \approx 2$ mJ/m^2).

The *interfacial energy* γ_{12} of two immiscible liquids 1 and 2 is the free energy change in expanding their interfacial area by unit area in vacuum (figure 2.14c). According to the previously defined quantities, the interfacial energy can be defined as follows:

$$\gamma_{12} = \frac{1}{2}W_{11} + \frac{1}{2}W_{12} - W_{12} = \gamma_1 + \gamma_2 - W_{12} \tag{2.12}$$

This could be explained by splitting the surface expansion process into two steps: first, two unit ares are created, thus leading to an increase of the surface energy for each substance; then, they are brought into contact, thus leading to a decrease of the adhesion energy. Equation 2.12 is known as *Dupré equation*.

The situations described above are all ideal, since in vacuum all substances attract each other. If they are inside a third medium 3, even at ultra high-vacuum laboratory conditions, the adsorption of chemical species on the surface *de facto* change the energy balance and reduces the adhesion and interfacial energies. In fact, if substances 1 and 2 are immersed in a medium

3 and are separated (figure 2.14d), the total balance energy W_{123} is:

$$\begin{aligned} W_{123} &= W_{12} + W_{33} - W_{13} - W_{23} \\ &= (\gamma_1 + \gamma_2 - \gamma_{12}) + 2\gamma_3 - (\gamma_1 + \gamma_3 - \gamma_{13}) - (\gamma_2 + \gamma_3 - \gamma_{23}) \\ &= \gamma_{13} + \gamma_{23} - \gamma_{12} \end{aligned} \tag{2.13}$$

Similarly as before, the overall balance can be split into three different hypothetical steps: first, the interface of substances 1 and 2 are separated; second, the surface area of the medium 3 is increased of two unit areas; finally, substances 1 e 2 are contacted with surface 3, each one of one unit area. If $W_{123} > 0$, substances 1 and 2 attract each over in medium 3; on the contrary, if $W_{123} < 0$, substances 1 and 2 are subjected to a repulsive force in medium 3.
The definitions stated above are valid for all the physical states of the substances: they can be all solid, all liquid or all gaseous, or any other combinations of these states. In particular, one of the most interesting case occurs when when a solid S and a liquid L are put in contact immersed in gaseous environment G, for example in air. Therefore equation 2.13 becomes:

$$W_{SGL} = \gamma_{SG} + \gamma_{LG} - \gamma_{SL} \tag{2.14}$$

In the followings an ideal condition is described: perfectly spherical droplets and perfectly smooth surface. This is a simplified situation which allows to understand how the energy balance between an inkjet printed droplet and the substrate influences the drop spreading and thus the printing resolution.
When a droplet of volume V_0 is deposited on a flat substrate, at first approximation it acquires a spherical cap shape, as shown in figures 2.15 and 2.16. It is mainly characterized by the *contact angle* θ formed with the substrate. Since the volume V_0 is constant, there is a dependence between the radius of the deposited drop, r, and the contact angle θ. The volume of a spherical cap is defined as:

$$V_0 = \frac{\pi h}{6} \cdot \left(3r^2 + h^2\right) \tag{2.15}$$

which can be expressed by means of the contact angle θ and the radius r:

$$V_0 = \frac{\pi r^3}{3\sin^3\theta} \cdot \left(2 - 2\cos\theta - \sin^2\theta\cos\theta\right) \tag{2.16}$$

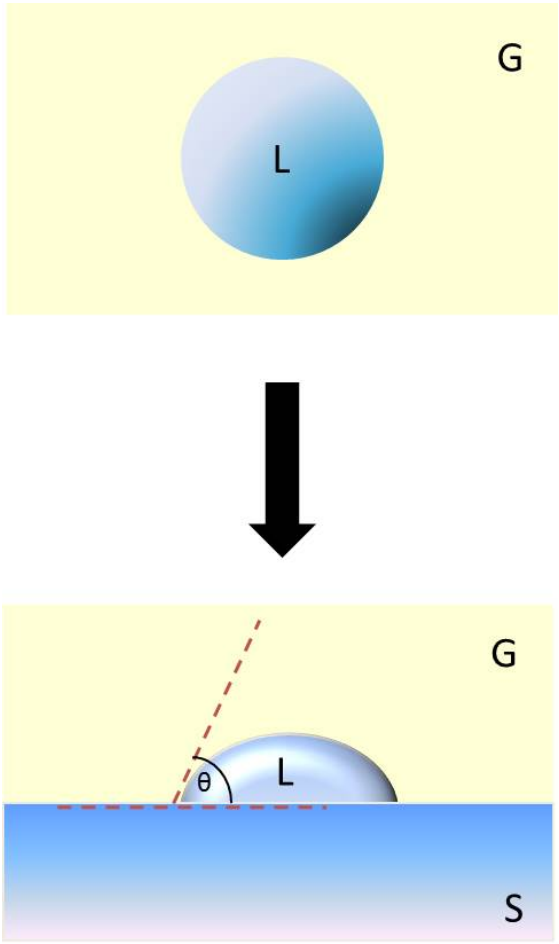

Figure 2.15: Drop deposition on the substrate: its shape, ideally a spherical cap, is characterized by the contact angle θ.

From equation 2.16, given a constant volume V_0 of the ejected drop, the relation between r and θ is defined as:

$$r = \sqrt[3]{\frac{3V_0 \sin^3\theta}{\pi\left(2-2\cos\theta-\sin^2\theta\cos\theta\right)}} \tag{2.17}$$

The Gibbs free energy G [5] of the drop is expressed as follows:

$$\begin{aligned} G &= S_{SL}\left(\gamma_{SL}-\gamma_{SG}\right)+S_{LG}\gamma_{LG} \\ &= \pi\left(R\sin\theta\right)^2\left(\gamma_{SL}-\gamma_{SG}\right)+2\pi R^2\left(1-\cos\theta\right)\gamma_{LG} \\ &= \sqrt[3]{\frac{9\pi V_0^2}{\left(1-\cos\theta\right)\left(2+\cos\theta\right)^2}}\left(2\gamma_{LG}-\left(\gamma_{SG}-\gamma_{SL}\right)\left(1+\cos\theta\right)\right) \end{aligned} \tag{2.18}$$

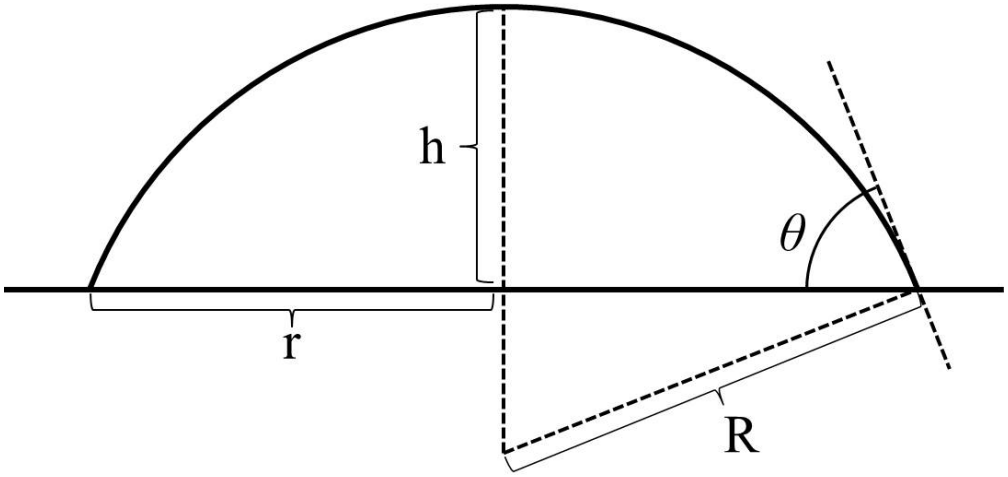

Figure 2.16: Schematization of the geometrical properties of a deposited drop.

Its minimum is found by equaling its derivative to zero. The following relation is obtained:

$$\gamma_{SG} - \gamma_{SL} - \gamma_{LG}\cos\theta_0 = 0 \tag{2.19}$$

where θ_0 is the contact angle at equilibrium. Equation 2.19 is know as *Young's equation*. It settles a relation between the overall energetic balance and the geometrical shape of the deposited drop, which is directly related to the pattern resolution, as stated before. More complex models, *i. e.* Wenzel regime and Cassie-Baxter regime, are shown in figure 2.17 [5] but they are not discussed in this thesis.

Directly related with surface tension, also the *capillarity* effect takes place once the drop is

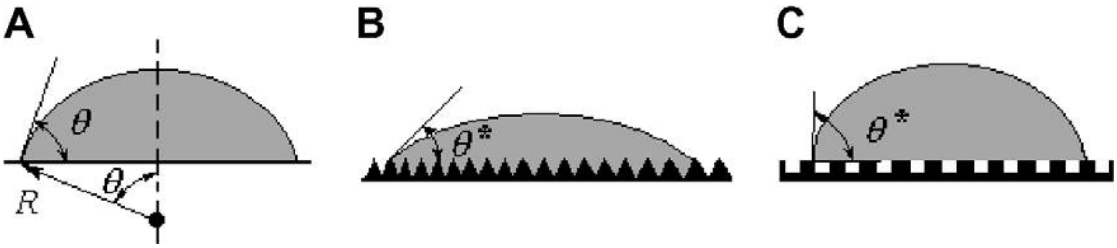

Figure 2.17: Scheme of three different wetting regimes: (a) flat substrate (Young regime), (b) rough substrate (Wenzel regime) and (c) rough substrate with air trapped under the drop (Cassie-Baxter regime) [5].

deposited on the substrate. It is defined as the property of a liquid to flow in narrow spaces without any influence of external forces, such as gravity. In this context, if an ejected drop falls in contact with, or overlapping, another drop previously deposited, the system of two

drop rearranges itself to form a single bigger drop. This overlapping, set by the drop spacing in the DMP2831, is a critical parameter especially for high-resolution patterns: too low overlapping can result in pattern discontinuity, especially in the Y direction, while too high drop overlapping can result in drop displacement towards the early deposited drops, thus causing undesired short-circuits. Given the diameter of the deposited drop, that is $2r$ from figure 2.16, a suitable drop-spacing value should range from r to $1.5r$, depending on the ink employed and on the required characteristics for the printed pattern.

2.2.5 Drop drying

The last step towards the formation of a solid layer by inkjet printing is the *drop drying*. This usually takes place under heating of the substrate: the overall process is called *annealing*. Several studies have been carried out explaining how the experimental parameters influence the evaporation process, the final morphology and the electrical performance of the printed layer [6, 94]. This is important for the deposition of conducting or insulating layers and is critical for improving the inkjet printing of organic semiconductors.
A typical effect occurring during the drop drying is the "coffee stain" [95]: when the contact line, *i. e.* the drop boundary, is pinned during drying, the drop has a fixed contact area so a capillarity flow of the solvent occurs from the center to the periphery, which transports an undesired amount of material. This is usually disadvantageous for the device performance. Several parameters play a crucial role in this process, such as the drop viscosity and surface tension, the substrate temperature and the solvents boiling point. In particular, the latter was studied in [6] as the key point to improve the self organization of TIPS-pentacene crystals.
Figure 2.18 shows a schematic of the different flows involved in the drop drying process. As stated before, since the solvent starts to evaporate at the drop boundary, an outward convective flow transports the active material, or solute, from the center to the periphery. This undesired effect could be balanced by employing a mixed solvent system: by adding a minor component in the solvent mixture with a high boiling point, another flow, called *Marangoni flow*, is generated [7]. This flow, directed from the periphery to the interior of the droplet, is induced by the surface tension gradient from regions with low surface tension to regions with high surface tension. When the minor component in the solvent mixture has a higher boiling point and a lower surface tension then the major solvent, a Marangoni flow with a direction counter to that of the convective flow can be induced. Figure 2.19 shows the flow field in a drying octane droplet: the convective flow and the Marangoni flow form a Marangoni vortex.

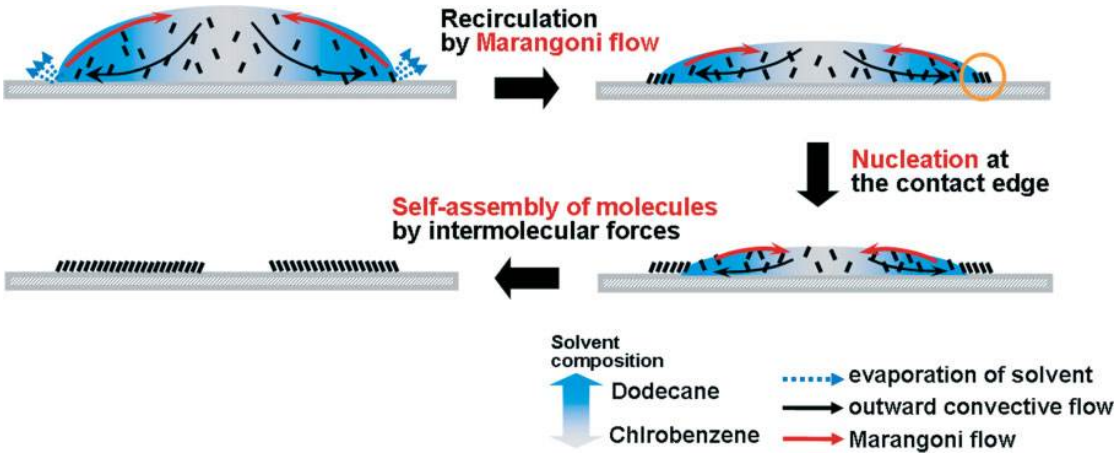

Figure 2.18: A schematic representation of the different flows involved in the drop drying process [6].

As a general rule, the annealing process should be carried out at as higher temperature as

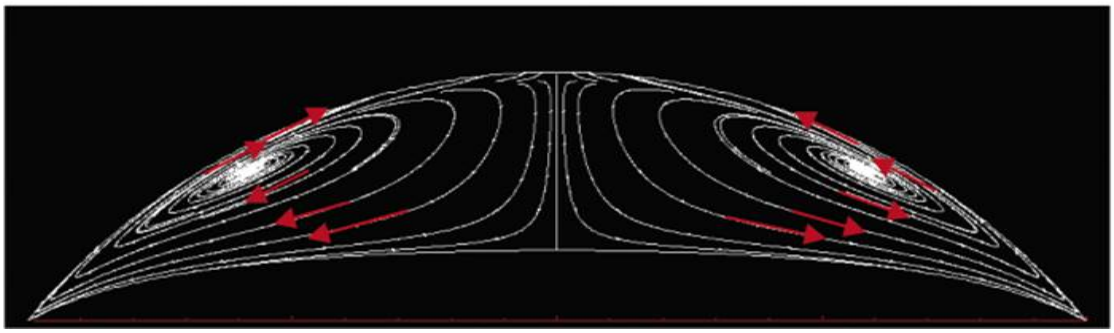

Figure 2.19: Flow field in a drying octane droplet [7].

possible, in order to reduce the outward convective flow when the Marangoni flow is not sufficient. The drawback is that plastic substrates, where typically organic devices are printed, can be treated only at moderate temperature, otherwise a substrate irreversible deformation occurs. Solvent mixture and blending are other possible solutions to enhance the drying process and, therefore, the final electric performance of the printed devices.

2.3 Materials

This section provides a chemical library with all the materials employed during the work related to this thesis. They are divided into six groups, according to their feature: substrates, conductors, semiconductors, dielectrics, solvents and surface modifiers. For each material, a short description is given with the relevant chemical and physical properties. In sections

2.4, 2.5 and 2.6 a more detailed description of the inkjet printing parameters for ink-type materials is given

2.3.1 Substrates

Six different types of substrate are discussed: three of them (PET, PEN and Kapton®) were the most employed as actual substrate; PVDF was employed as substrate for its piezoelectric behavior, but was also inkjet printed in liquid form; PDMS was used both as substrate and as encapsulation layer for its mechanical properties; finally, acrylic-based substrates were used as electroactivated membrane for a particular application described in chapter 4.

Poly(ethylene therephthalate)

Poly(ethylene therephthalate) (PET) is a thermoplastic polymer of the polyester family. Its monomer, the *ethylene therephthalate*, is shown in figure 2.20. It is used for a wide range of

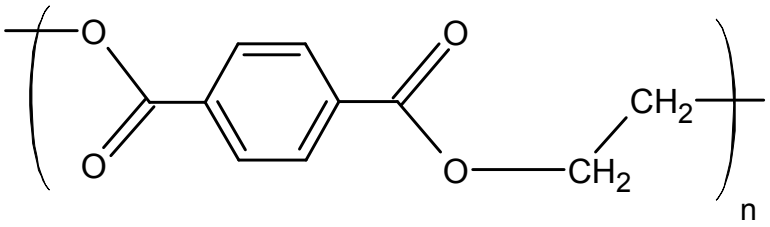

Figure 2.20: Poly(ethylene therephthalate).

applications, especially as food and liquid container. It has very interesting physical properties, such as a tensile strength between 190 and 260 MPa and good resistance to most solvents, excluded alkalis. It was purchased from Goodfellow© [96] as transparent and flexible biaxially-oriented films with three different thicknesses: 175 μm, 50 μm and 13 μm. Its nominal temperature working range is -40 to 115 °C. However empirical experience shows that it can be processed at a maximum of 60 °C, since for higher temperature it undergoes irreversible deformation, an undesired effect especially for the fabrication of OFET-based strain sensors.

Poly(ethylene naphthalate)

Poly(ethylene naphthalate) (PEN) is another thermoplastic polymer quite similar to PEN. It is shown in figure 2.21. It has better chemical properties, since it can resist also to alkalis, and physical properties, since it can be heated nominally up to 150 °C. However, empirical experience shows that is can be processed at a maximum of 90 °C, since for higher temperature

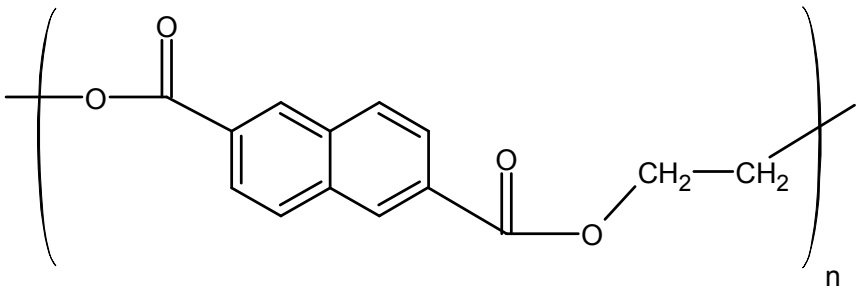

Figure 2.21: Poly(ethylene naphthalate).

it undergoes irreversible deformation. It was purchased from Goodfellow© [96] as transparent and flexible biaxially-oriented films with two different thicknesses: 125 μm and 50 μm. The main disadvantage is the high surface roughness, which is an undesired feature for the deposition of thin layers.

Poly(4,4'-oxydiphenilene pyromellitimide)

Poly(4,4'-oxydiphenilene pyromellitimide) is a polyimide film developed by DuPont® [97] under the name Kapton HN®. It is shown in figure 2.22. Thanks to its wide temperature working

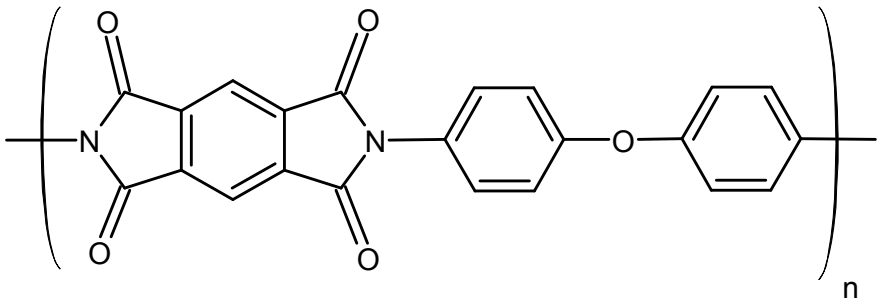

Figure 2.22: Kapton HN®.

range (-270 to 300 °C) and to its radiation resistance, it finds applications in many fields, such as coverage for aircraft, spacecraft and x-ray instrumentation. It was purchased from Goodfellow© [96] as transparent and flexible yellowish films with two different thicknesses: 125 μm and 13 μm. Experimental tests confirmed its thermal resistance for temperatures as high as 200 °C, thus it was chosen as best candidate substrate for post-processing annealing of organic printed layers.

Poly(1,1-difluoroethylene-1,1,2-trifluoroethylene)

Poly(1,1-difluoroethylene-1,1,2-trifluoroethylene), also known as *poly(vinylidene difluoride trifluoroethylene)* (PVDF-TrFE), is a special plastic material in the fluoropolymer family. PVDF-TrFE is a copolymer composed by the alternated repetition of two monomers, 1,1-difluoroethylene and 1,1,2-trifluoroethylene respectively. They are shown in figure 2.23. This substrate was

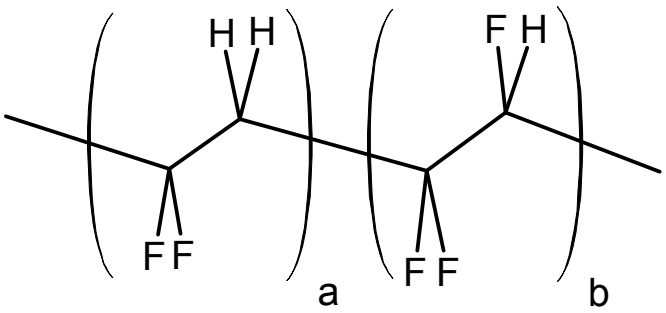

Figure 2.23: Poly(1,1-difluoroethylene-1,1,2-trifluoroethylene).

purchased by Piezotech [98] as transparent films with two different thickness: 110 μm and 50 μm. The most interesting properties of PVDF-TrFE are *piezoelectricity* and *pyroelectricity*. The first one is typical of piezoelectric materials: when they are subjected to mechanical stress, electrical charges, proportional to the stress, appear on their surface; and conversely, when an electric potential difference is applied to these materials, mechanical deformation occurs. Similarly, pyroelectric materials give origin to electrical charges on their surface proportional to the temperature applied on them. Piezoelectricity is induced in PVDF-TrFE by application of an intense electric field which cause a rearrangement of the molecular orientation. It is mainly employed in applications which require pressure sensing: acoustic components, medical instrumentation, optical devices, transport, and more. In this work it has been employed in the robotic field, as a possible tactile sensor technology for robots. Related to inkjet printing, its main disadvantage is the low thermal resistance: post processing cannot be performed at temperature higher than 50 °C without undergoing irreversible deformation. Also, solutions of PVDF-TrFE powder were prepared for being deposited by inkjet printing to form insulating layers.

Poly(dimethylsiloxane)

Poly(dimethylsiloxane) (PDMS) is the name of a group of polymeric organosilicon compounds commonly know as silicones. Figure 2.24 shows its chemical structure. PDMS in its solid form

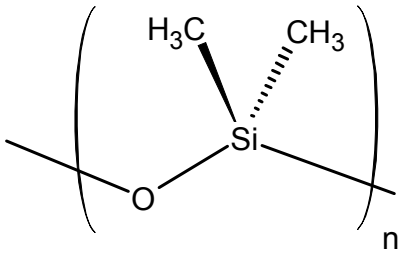

Figure 2.24: Poly(dimethylsiloxane).

is an elastomer, *i. e.* an amorphous polymer with viscoelastic properties, with low Young's modulus and high failure strain compared with other materials. In this wark it was used both as substrate and as encapsulating layer for the realization of artificial robotic skin. Two types of PDMS were employed. The first type, vey soft, was Ecoflex® Supersoft 0030, purchased from Smooth-on©(type OO, shore 30 in the durometer scale) [99]. The second, slightly harder PDMS was Sylgard® Silicone Elastomer, purchased from Dow Corning© (type OO, shore 50 in the durometer scale) [100]. Both types were provided as two-part liquid component kit, an elastomer and a curing agent. The polymerization procedure varied according to the specific employment and will be discussed in chapter 3. They generally are very hydrophobic, thus a surface treatment is required in order before printing on them.

Acrylic

As mentioned above, the acrylic-based substrates were employed together with rubber rings to form electroactuated mambranes. They were purchased from 3M™ with the commercial name VHB™ Acrylic Foam Bonding Tapes [101]. As their fundamental property, they undergo strong reversible deformation when they are subjected to high voltages. VHM™ substrates are usually more hydrophobic with respect to standard plastic substrates.

2.3.2 Conductors

In this paragraph all the conductive materials employed are briefly discussed, both those deposited via thermal evaporation (gold, silver and aluminum) and those deposited by inkjet printing (CCI-300, PEDOT:PSS and carbon black).

Gold

Gold (Au) is a dense, soft, malleable and ductile metal, one of the least reactive chemical elements. It widely employed in the electronic industry thanks to its very high conductiv-

ity ($4.1 \cdot 10^7$ S/m). From an electronic point of view it is a good hole injector since its work function is 5.1 eV, a value in the range of most HOMO levels of conjugated polymers.

Silver

Silver (Ag) is the chemical element with the highest electrical conductivity ($6.3 \cdot 10^7$ S/m) and the highest thermal conductivity of any metal. It is generally less ductile and malleable than gold, but it is employed as well in the electronic industry. Its work function is about 4.3 eV, thus it is a worse hole injector with respect to gold.

Aluminum

Aluminum (Al) is a silvery white, soft, ductile metal. As opposite of gold, it is a very reactive element, oxidizes very quickly and its native specimens are very rare. Its nominal work function is 4.2 eV, near to that of silver, even though surface impurities strongly affect this value. Al conductivity is ($3.5 \cdot 10^7$ S/m). Thanks to its high reactivity with Oxygen, Cosseddu *et al.* have patented a new method to obtain low operating voltage OFETs by substantially reducing the thickness of the gate dielectric and increasing its capacitance [102].

CCI-300 Silver ink

Cabot conductive Ink 300 (CCI-300) is a conductive ink composed of surface modified ultrafine (average size 20 nm) silver nanoparticles dispersed in a liquid vehicle composed of ethanol and ethylene glycol. It was purchased from Cabot© [103]. Its formulation is engineered for reliable piezoelectric inkjet printing to form high-resolution, low-resistivity conductive patterns on a variety of substrates. Moreover, since metal nanoparticles have reduced melting and sintering temperatures as compared to their micron-sized counterparts, CCI-300 can be processed at temperatures as low as 60 °C. Concerning this thesis, CCI-300 was the best printable ink, whose physical parameters matched perfectly the DMP2831 requirements. Its durability was high, as well as the pattern resolution achievable. For this reason, CCI-300 was always chosen as the gold standard for the formulation of any new inks. Its main physical properties provided by Cabot are listed below:

- *Viscosity*: 11-15 cP at 22 °C.
- *Surface tension*: 30-33 mN/m at 25 °C.
- *Silver solid loading*: 19-21 wt.%.
- *density*: 1.23-1.24 g/mL.

- *Curing temperature*: 100-350 °C in air.
- *Curing time*: 1-30 min.
- *Bulk resistivity*: 4-80 $\mu\Omega$·cm.

As described in section 2.4, several types of pattern were printed using CCI-300, both at high, medium and low resolution. The annealing process, under the melting temperature, involves a phenomenon, called *sintering*, by which the particles aggregate in a continuous conductive matrix without melting [104]. The annealing temperature and duration strongly depend on the particular pattern and substrate considered, thus they will be specified at every application described.

Poly(3,4-ethylenedioxithiophene):Poly(stirenesulphonate)

Poly(3,4-ethylenedioxithiophene):Poly(stirenesulphonate) (PEDOT:PSS) is a mixture composed of two polymers, shown on figure 2.25. Poly(3,4-ethylenedioxithiophene) (PEDOT) is a con-

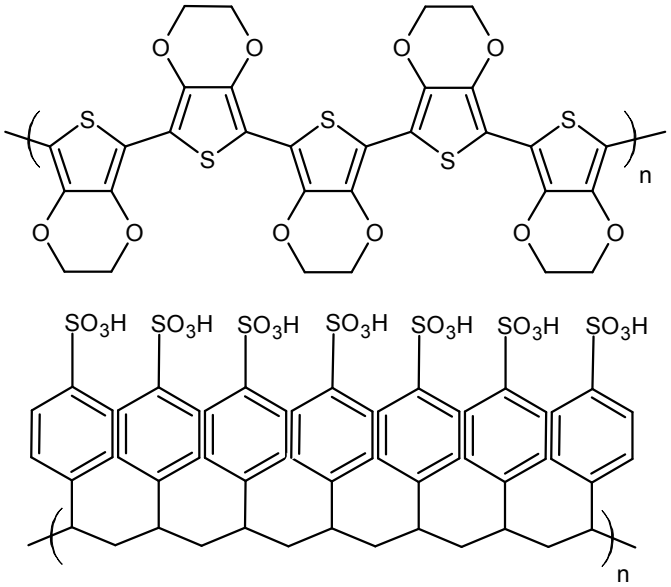

Figure 2.25: Poly(3,4-ethylenedioxithiophene):Poly(stirenesulphonate).

jugated polymer of the thiophenes family, developed in 1980 by the scientists at the Bayer AG research laboratories [105]. It is a transparent conductive polymer (conductivity up to 300 S/m), but it is insoluble in common solvents. To overcome this problem, chemical doping is provided by Poly(stirenesulphonate) (PSS), a deprotonate polymer which acts as an oxidant removing electrons from the thiophenic rings of PEDOT chain. The resulting polar blend

($PEDOT_+$:PSS^-) is soluble in polar solvent, such as water. Additional tratment with ethylene glycol improves its condactivity but also reduces its solubility in water.
Two types of PEDOT:PSS-based ink were employed, both purchased from Heraeus™ [106]: Clevios™ P Jet HC and Clevios™ CPP 105D. The first one was developed specifically for inkjet printing: is in aqueous solution, with solid content between 0.6% and 1.2%, viscosity between 5 and 20 cP andconductivity between 30 and 90 S/cm. The second one, not formulated specifically for inkjet printing, has a lower viscosity (under 10 cP) and is in a mixture of aqueous and alcoholic solution.

Vulcan® XC72

Vulcan® XC72, hereafter referred as *carbon black*, is a black conductive powder purchased from Cabot© [103]. It is part of a class of materials obtained by the incomplete combustion of heavy petroleum products. Carbon black is a polycrystalline carbon, whose particles are declared to be smaller than 50 nm, with a high surface-volume ratio. It is characterized by a good conductivity, good chemical and physical cleanliness, and good processability. Carbon black is mainly used for packaging power cables and electrostatic discharge protection components, as its good conductivity facilitates the heat and charge dissipation.

2.3.3 Semiconductors

In this section, a list of the organic semiconductors employed is given, with a brief description of the relevant properties. In particular, pentacene was deposited by thermal evaporation, TIPS-pentacene both by drop casting and inkjet printing, P3HT-PCBM by inkjet printing only and ActivInk™ N1400 by spin coating.

Pentacene

Pentacene is a small conjugated molecule of the polyacenes family. It is formed by the union of five benzene rings, as shown in figure 2.26. Pentacene was purchased from Sigma Aldrich® [107].

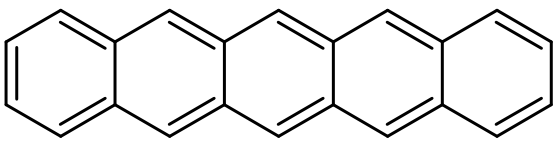

Figure 2.26: Pentacene.

It is one of the most employed p-type semiconductors in organic electronics [108–111], with the HOMO at 5 eV and LUMO at 3 eV nominally. It is almost insoluble in common solvents,

thus the main deposition technique is thermal evaporation. The major disadvantage of pentacene is it instability in air, since it is quite reactive with oxygen that, by forming molecular bounds at positions 6 and 13, reduces its conductivity. Both problems, insolubility and instability, are overcome with one of its most employed derivatives, TIPS-pentacene.

6,13-bis(triisopropylsilylethynyl)pentacene

6,13-bis(triisopropylsilylethynyl)pentacene (TIPS-pentacene) is derived from the pentacene molecule with the addiction of side chains in position 6 and 13. The molecular structure is shown in figure 2.27. This addiction has two beneficial effects with respect to the simple pen-

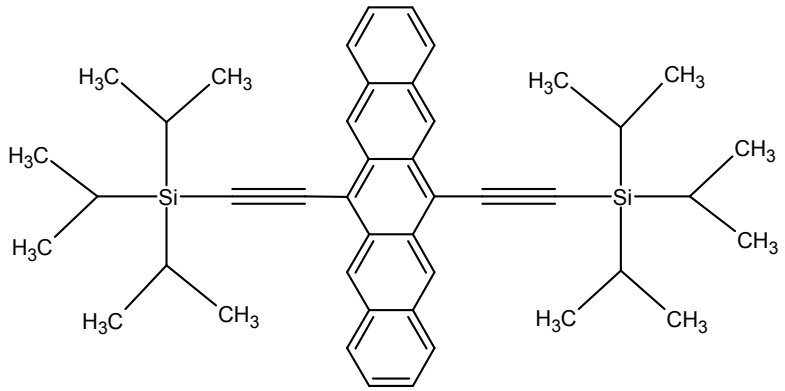

Figure 2.27: 6,13-bis(triisopropylsilylethynyl)pentacene.

tacene molecule: it allows its solubility, and thus its processability as an ink, and it strongly reduces its instability. In facts, TIPS-pentacene is one of the most employed p-type organic semiconductor thanks to its resistance to water and oxygen, giving rise to the possibility to use TIPS-pentacene based device also at room condition over the time without degradation. It was purchased from Sigma Aldrich® [107]. The values of HOMO and LUMO are quite similar to those of pentacene, being 5.1 eV and 3.4 eV respectively [112–114]. It is best soluble in toluene (6.57 wt.%), *n*-butylbenzene (3.43 wt.%), anisole (2.03 wt.%) and acetone (0.16 wt%). The standard deposition method is by drop basting: in this thesis, experiments on inkjet printing of TIPS-pentacene have been carried out.

Poly(3-hexylthiophene-2,5-diyl):[6,6]-phenyl-C_{61}-butyric acid methyl ester

Poly(3-hexylthiophene-2,5-diyl):[6,6]-phenyl-C_{61}-butyric acid methyl ester (P3HT:PCBM)is an organic heterojunction composed of the p-type organic semiconductor *Poly(3-hexylthiophene-2,5-diyl)* and the n-type organic semiconductor *[6,6]-phenyl-C_{61}-butyric acid methyl ester*.

The molecular structure is shown in figure 2.28. This blend, specifically formulated for print-

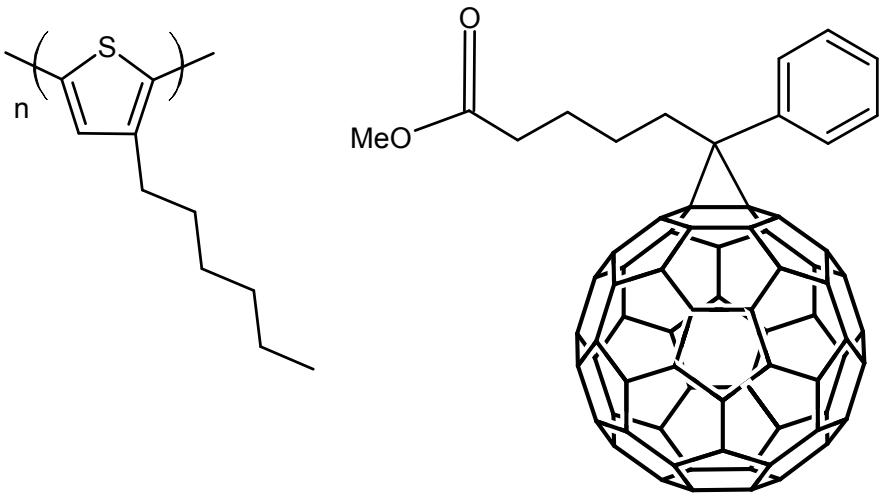

Figure 2.28: Poly(3-hexylthiophene-2,5-diyl):[6,6]-phenyl-C_{61}-butyric acid methyl ester.

ing purpose, consists of a matrix of P3HT with separated PCBM spots. It is mainly employed in the organic photovoltaics for the production of organic solar cells [115]. In this work, organic photodiodes have been realized employing P3HT:PCBM as active layer [116, 117]. The HOMO and LUMO of P3HT are 3 eV and 5.2 eV respectively, while the HOMO and LUMO of PCBM are 3.7 eV and 6.1 eV respectively. Due to the matrix structure of this blend, the P3HT energetic levels dominate the charge carrier transport phenomena. It has been purchased from Sigma Aldrich® [107] in reddish liquid form, with a reported viscosity of 4-8 cP. The major disadvantage of P3HT:PCBM ink is its instability in air, thus it requires processing and post-processing in controlled environment. A detailed description of the activity carried out with it is reported in section 4.1.

ActivInk™ N1400

ActivInk™ N1400 (N1400) is a n-type organic semiconductor developed and commercialized by Polyera© [118] and shown in figure 2.29. The declared LUMO and HOMO are 4.3 eV and 6.4 eV respectively. It is a red crystalline solid best solved in chloroform, dichlorobenzene and anisole. The preferred deposition technique is spin coating.

2.3.4 Dielectrics

This section provides a short description of two dielectric materials employed in this work: parylene-C, the most employed, and polystyrene blend, deposited by inkjet printing.

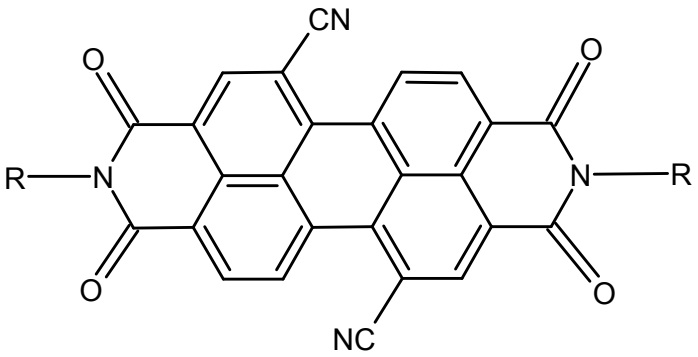

Figure 2.29: ActivInk™ N1400.

Poly(p-xylylene)

Poly(p-xylylene), in the *parylene-C* version, is the standard insulator employed during the work related to this thesis. It was purchased from Specialty Coating Systems™ [119] as white dimer solid. The molecular structure is presented in figure 2.30. The polymerization takes

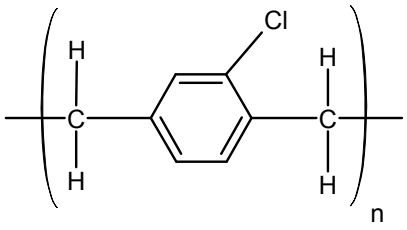

Figure 2.30: Parylene-C.

place within the parylene coating process: the result is a totally transparent thin dielectric layer, with dielectric constant $\varepsilon_r \approx 3$. It is largely employed in aerospace, as it is resistant to a wide range of electromagnetic waves, and in biomedicine, since it is biocompatible. Moreover, it makes a conformal contact,thus it is the ideal candidate as gate dielectric in OFETs.

Poly(1-phenylethylene)

Poly(1-phenylethylene), or polystyrene, is an aromatic polymer widely used in the plastic industry. It is shown in figure 2.31. Polystyrene was purchased from Sigma Aldrich® [107] in different molecular weights: M_w = 2000, M_w = 20000 and M_w = 200000. It is best solved in toluene and dichlorobenzene. Starting from polystyrene, a dielectric ink has been formulated as described in the following sections. Moreover, blends of TIPS-pentacene and polystyrene have been prepared in order to enhance the printing performance of this semiconductor.

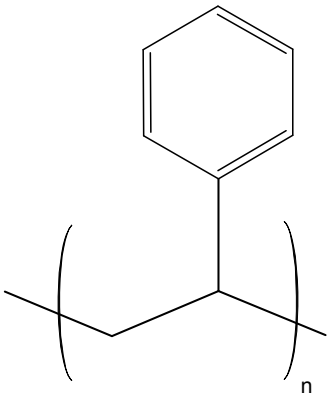

Figure 2.31: Polystyrene.

2.3.5 Solvents

Since this work is based on the formulation of inks, a wide range of solvents have been employed and mixed. For each one, a brief description and the main physical properties are given.

Ethyl alcohol

Ethyl alcohol, or ethanol, is one of the most common solvent employed. It was purchased from Sigma Aldrich® [107]. Its viscosity is 1.2 cP, its boiling point is 78.8 °C and its density is 0.789 g/mL.

Isopropyl alcohol

Isopropyl alcohol is another very common solvent. It was purchased from Sigma Aldrich® [107]. Its viscosity is 2.04 cP, its boiling point is 82 °C and its density is 0.785 g/mL.

Propanone

Propanone, or acetone, is a stronger solvent than the previous two. It is the simplest molecule of the ketones group. It was purchased from Sigma Aldrich® [107]. Its viscosity is 0.33 cP, its boiling point is 56 °C and its density is 0.791 g/mL.

Methylbenzene

Methylbenzene, or toluene, is an aromatic hydrocarbon widely used as an industrial feedstock and as a solvent. It is the best solvent of TIPS-pentacene. Toluene was purchased from Sigma Aldrich® [107]. Its viscosity is 0.55 cP, its boiling point is 111 °C and its density is 0.87 g/mL.

Methoxybenzene

Methoxybenzene, best known as anisole, is an aromatic hydrocarbon employed especially as a precursor to perfumes and pharmaceuticals. It was purchased from Sigma Aldrich® [107]. Its viscosity is 1.05 cP, its boiling point is 154 °C and its density is 0.995 g/mL.

1,2-dichlorobenzene

1,2-dichlorobenzene, or *orto*-dichlorobenzene, is a derivative of benzene with the addiction of two adjacent chlorine atoms. Due to safety risk connected to long exposure, this material must be managed carefully. It is mainly used in the agrochemical, as insecticide. It was purchased from Sigma Aldrich® [107]. Its viscosity is 1.32 cP, its boiling point is 180 °C and its density is 1.30 g/mL.

2-methoxyethanol

2-methoxyethanol is an organic solvent of the glycol ethers group. It can solve a wide range of chemical compounds and can mixed with water and other solvents. It was purchased from Sigma Aldrich® [107]. Its viscosity is 1.72 cP, its boiling point is 124 °C and its density is 0.965 g/mL.

Methyl benzoate

Methyl benzoate (MB) is a colorless ester mainly employed in perfumery or as a chemical pesticide. It was purchased from Sigma Aldrich® [107]. Its viscosity is 1.673 cP, its boiling point is 199 °C and its density is 1.084 g/mL.

Arch Chemicals RER™500

Arch Chemicals RER™500 is a photoresist used in this thesis as the solvent for PVDF. It is mainly composed of methyethylketone, or butanone. It was purchased from Arch Chemicals® [120]. Its viscosity is 0.43 cP, its boiling point is 79 °C and its density is 0.805 g/mL.

2.3.6 Surface modifiers

Finally, the last part of this chemical library includes all the molecules employed to modify the chemical and physical properties of other materials. On one hand, when the molecules are deposited upon an already deposited pattern, they arrange themselves to form a continuous layer, often referred as *Self-Assembled Monolayer* (SAM) [121], which influences the interaction with the forthcoming upper material. On the other hand, molecules added to a

solution within the ink formulation can change the solution properties, such as viscosity and surface tension, and enhance the deposition process and the final electrical performance of the layer.

Ethane-1,2-diol

Ethane-1,2-diol, commonly referred as ethylene glycol, is an odorless, colorless, syrupy organic compound mainly used in the plastic industry as well as component for antifreeze solutions. It was purchased from Sigma Aldrich® [107] and its molecule is shown in figure 2.32. It is soluble in water and miscible with most organic solvents. Its boiling point is 197 °C and its

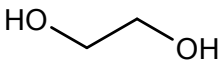

Figure 2.32: Ethane-1,2-diol.

density is 1.113 g/mL. Its relatively high viscosity, 20 cP, does not allow the direct deposition by inkjet printing. Anyways, if added in small quantity, it improve the physical performance of other low-viscosity solutions and allow their deposition as inks. Moreover, treatment of PEDOT:PSS with ethylene glycol has two effects: enhancement of the electrical conductivity of PEDOT:PSS up to 200 times and enhancement of the solid deposited PEDOT:PSS layer resistance to water [122, 123].

4-dodecylbenzenesulfonic acid

4-dodecylbenzenesulfonic acid (DBSA) is a colorless organic compound mostly employed as laundry detergent. It was purchased from Sigma Aldrich® [107] and its molecule is shown in figure 2.33. It is soluble in water and miscible with most organic solvents. Its boiling point

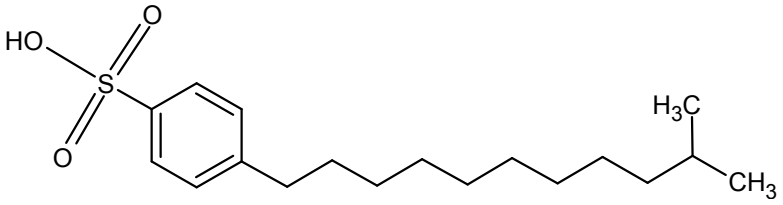

Figure 2.33: 4-dodecylbenzenesulfonic acid.

is 82 °C and its density is 1.06 g/mL. Its high viscosity does not allow direct deposition by inkjet printing. The DBSA is a good surfactant, *i. e.* it reduces the surface tension between two liquids or between a solid and a liquid. For this property, it can be successfully used to lower the surface tension of an ink and to reduce the probability of undesired particle

agglomeration.

4-fluorothiophenol and 2,3,4,5,6-pentafluorothiophenol

4-fluorothiophenol (FTP) and *2,3,4,5,6-pentafluorothiophenol* (5FTP) are two self-assembled monolayers, derivatives of the thiophenol molecule with the addiction of one and five fluorine atoms respectively. They were purchased from Sigma Aldrich® [107] and are shown in figures 2.34a and 2.34b respectively. When deposited on metals, they form SAMs which mod-

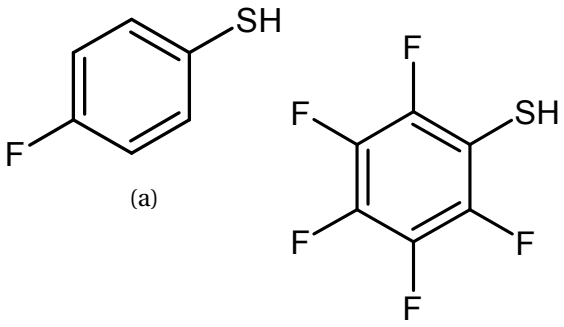

(a)

(b)

Figure 2.34: 4-fluorothiophenol (a) and 2,3,4,5,6-pentafluorothiophenol (b)

ify the work function of the electrode and thus improve or worsen the charge injection to the semiconductor [124].

Poly(ethylenimine ethoxylated)

Poly(ethylenimine ethoxylated) (PEIE) is a viscous colorless organic compound which acts as a SAM to lower the work function of metals. It was developed and investigated by Zhou *et al.* [125] and results show that is applicable both to metals, to metal oxides and to polymer-based conductors, such as PEDOT:PSS. This compound was purchased from Sigma Aldrich® [107] and its chemical structure is shown in figure 2.35. In this work PEIE was used to increase the energy barrier between metal and semiconductor in order to reduce the off current in organic photodiodes (see section 4.1 for a detailed experimental description).

3-methacryloxypropyltrimethoxysilane

3-methacryloxypropyltrimethoxysilane, commercially known as *Silane A-174* (A174), is a molecule employed in adhesive and sealant systems cured via a free radical mechanism, such as polyesters, polyurethanes, acrylics, and many thermoplastics such as PVC, polyolefins and polyurethanes. In this work it was used as an adhesion promoter for parylene-C to metal

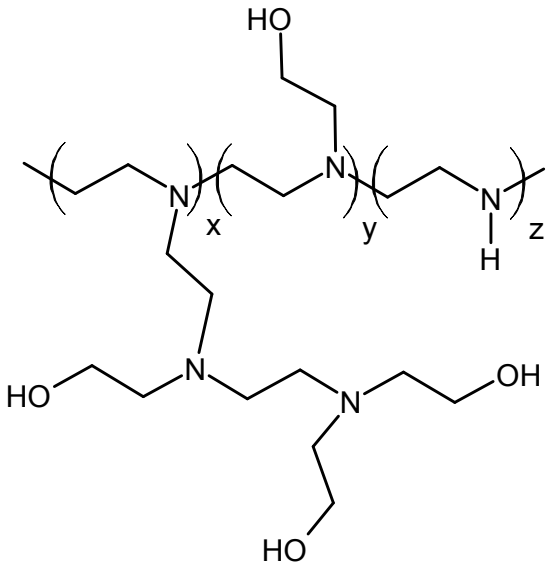

Figure 2.35: Poly(ethylenimine ethoxylated).

electrodes. Its molecular structure is shown in figure 2.36. It is deposited by chemical evapo-

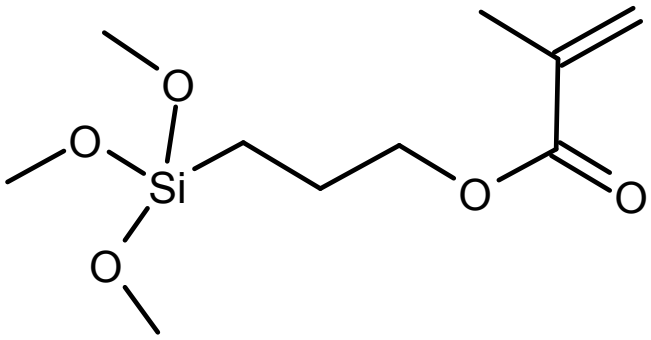

Figure 2.36: 3-methacryloxypropyltrimethoxysilane.

ration within the parylene coating process.

2.4 Inkjet printing of conductors

Within this thesis, inkjet printing of conductive layers was the main task performed. From simple linear electrodes to complex systems of devices, with conductive inks the major results have been achieved. Basically, two inks were employed: CCI-300 silver ink and PEDOT:PSS-based inks. Moreover, preliminary results on the inkjet printing of carbon-black are presented. In this section, for each ink the general printing parameters and a description of the printing process are given. The complete devices are presented in chapters 3 and 4 together with their applications.

2.4.1 CCI-300 silver ink

CCI-300 was by far the most reliable ink printed in this thesis. Its chemical and physical properties, described in the previous section, perfectly fit the requirements of DMP2831. Several types of pattern have been printed employing CCI-300, which can be divided into two major groups: low-resolution patterns, such as conductive tracks and large electrodes, and high-resolution patterns, such as interdigitated source and drain electrodes. They are both described in the followings. Before filling the cartridge, CCI-300 was subjected to 30 min ultrasonic bath and filtered with 0.2 μm poly(tetrafluoroethylene) (PTFE) filters, in order to reduce particle agglomeration that could clog the nozzles.

Drop calibration

Both 10 pL and 1 pL cartridges were employed, depending on the specific pattern to be printed. CCI-300 droplets have different spread on different substrate, according to the energy balance described in section 2.2. Therefore, preliminary experiments have been carried on in order to investigate the drop diameter, *i. e.* the pixel of the printed pattern, and thus to have a reference for setting the drop spacing. Table 2.1 shows the drop diameters of CCI-300

Substrate	**CCI-300 10 pL**	**CCI-300 1 pL**
PET	32 ± 3 μm	21 ± 2 μm
PEN	34 ± 2 μm	22 ± 3 μm
Kapton	32 ± 4 μm	21 ± 3 μm
PVDF	31 ± 4 μm	20 ± 2 μm
PDMS	21 ± 5 μm	12 ± 2 μm
Parylene	31 ± 3 μm	20 ± 2 μm
PVDF + plasma	48 ± 5 μm	————
PDMS + plasma	38 ± 5 μm	————
Parylene + plasma	43 ± 6 μm	30 ± 4 μm
Parylene + plasma after 1 day	————	25 ± 3 μm

Table 2.1: Drop diameters of inkjet printed CC-300 silver ink on different substrates.

on different substrates, performed both with 10 pL and 1 pL cartridges. For each value, a total of 20 measurements, 10 in the X direction and 10 in the Y direction of the platen, have been performed by means of the fiducial camera of the DMP2831, which has an intrinsic resolution of 2.54 μm; the mean value and the standard error of the mean have been then evaluated and reported.

As it can be seen from the table, the plastic substrates (PET, PEN, Kapton, and PVDF) have a quite similar surface energy and, at first approximation, drops deposited on them spread

in the same way and result in similar drop diameters. When parylene-C covers a substrate, it slightly changes its surface energy and therefore the deposited drops have slightly smaller diameters, especially those of 1 pL volume, going from a mean value of 21-22 μm to 20 μm. A totally different situation occurs when printing on PDMS layers, which are know to be very

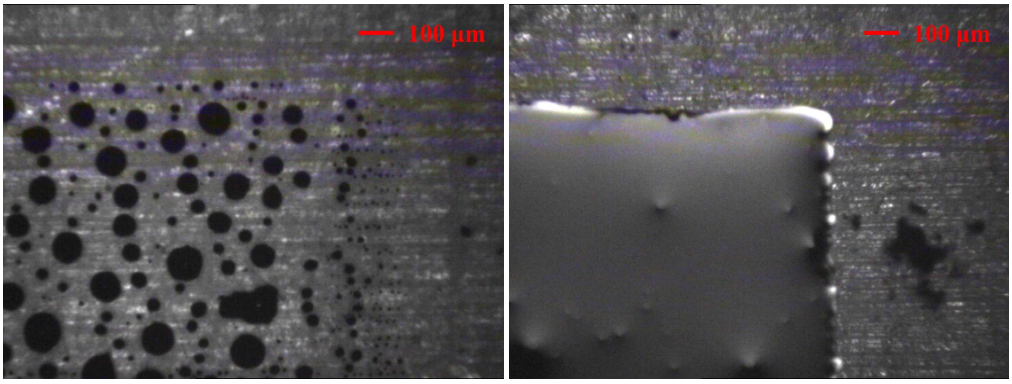

(a) (b)

Figure 2.37: CCI-300 layer deposited on PDMS without plasma treatment (a) and after plasma treatment (b).

hydrophobic and its interfacial energy with most organic solvent is very low. Moreover, in this case capillarity plays a crucial role, since the droplets tend to move towards the previously printed ink and form bigger drops: this results in an unavoidable pattern discontinuity also for reduced drop spacing, as shown in figure 2.37a. Surface treatment, and especially plasma treatment, can be performed in order to increase the wettability of the substrates. After 60 s of plasma treatment at 75 W, the droplets spread much more even on PDMS, arriving, in the case of 10 pL drops, at a mean value of 38 μm from the measured 21 μm of the untreated state (figure 2.37b). In the previous example the drop deposition occurred immediately after the plasma treatment, whose effects are stable for 30 min and then slowly start to decrease. Taking advantage of this phenomenon, a calibration of the drop spreading can be done according to the delay time between the plasma treatment and the actual drop deposition. For example, printing 1 pL CCI-300 drops on parylene result in the followings:

- *Untreated state*: the drop diameter is 20 μm.
- *Immediately after plasma treatment*: the drop diameter rise up to 30-31 μm.
- *1 day after plasma treatment*: the drop diameter is reduced to 25 μm.

In particular, the last case was successfully employed for the inkjet printing of high-resolution interdigitated electrodes, as described below.

Low-resolution patterns

Low-resolution patterns include all those patterns whose dimensions, both in X and Y direction, exceed the drop diameter and therefore they have to be printed with multiple lines. Moreover, the distance between adjacent pattern must be higher, at least 8-10 times, the drop diameter, in order to avoid short-circuit caused by possible drop deflections during the printing process. In this category are included: electrical traces which carry the electrical signals from the devices to the contact pads used for measurements, the gate electrodes, the capacitors plates and in general all the electrodes not being part of a more complex device. In such cases the resolution is not a major issue, since the there are not short-circuit problems. On the contrary, the trace continuity is the main requirement in order to allow the signal transmission along the structure. Low-resolution patterns are usually printed with 10 pL drops, but also 1 pL drops can be employed.

Parameter	**CCI-300 10 pL**	**CCI-300 1 pL**
Drop spacing	15-20 μm	10-15 μm
Firing voltage	30-40 V	25-40 V
Maximum jetting frequency	5-20 kHz	5-10 kHz
Printing nozzles	2-5	2-5
Platen temperature	50-60 °C	50-60 °C
Cartridge print height	1 mm	700 μm
Number of layers	*ad libitum*	*ad libitum*
Cleaning before	S-P-S	S-P-S
Cleaning during	S-P-S (50-100 bands)	S-P-S (50-100 bands)

Table 2.2: Printing parameters for low-resolution patterns with CCI-300 silver ink.

Table 2.2 lists the printing parameters for low-resolution patterns with CCI-300 silver ink. Predictably, the most important is the *drop spacing*: it should be low enough to guarantee the full continuity of the printed layer, but not extremely low not to deposit too much ink which could prolong the annealing process. A good choice is to set the drop spacing to half of the drop diameter. The *firing voltage* can be set either at an acceptable minimum (30 V for 10 pL and 25 V for 1 pL drops) to obtain plain vertical droplets or to the maximum (40 V). In the latter case the probable formation of satellite drops does not represent a problem, since they usually merge with the main pattern. In order to speed up the printing process, the *jetting*

frequency should be set to the maximum achievable: 20 kHz. Lower values are desirable only when an accurate aligning with other layers, already printed, is required. This feature also influence the choice on the number of *printing nozzles*: the typical value is 3 nozzles, but a higher number can be chosen, up to the total 16 nozzles. However, using more than 5-6 nozzle is not recommended, since nozzle clogging could occur which decrease the quality of the printed layer. The *plate temperature* is usually set to its maximum, 60 °C, in order to promote the sintering process. Lower temperatures are required for substrates, such as PVDF, which are less temperature-resistant. The *cleaning cycles* are another important issue to account for. Cleaning before printing is highly recommended, with a standard Spit-Purge-Spit cycle. But also cleaning during printing is desirable, generally every 50 or 100 bands with the same cycle, in order to avoid nozzle clogging especially for large area patterns.
During printing some event can occur, such as temporary nozzle clogging, which interrupt the continuity of the pattern, as shown in figure 2.38a. In such case an additional *ad-hoc* pat-

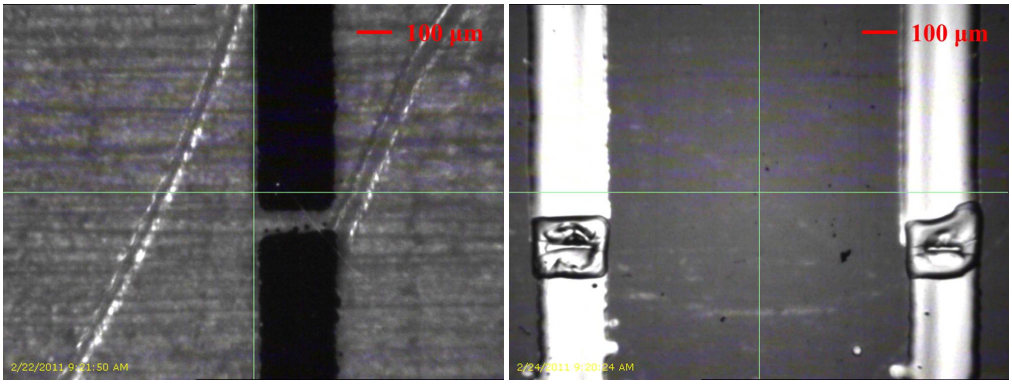

(a) (b)

Figure 2.38: (a) Discontinuity of a printed layer; (b) restoration of the continuity by means of an additional layer.

tern can be printed in order to restore the layer continuity. Provided that this goal is achieved and that no undesired short-circuit is created, no specific setting for printing this extra layer is required.
The thermal annealing should be performed, in over or up an hot plate, at as high temperature as possible, in order to promote the sintering process and enhance the conductivity of the layer. The limitations only depend on the specific substrate employed. Below, a short list of the empirical annealing conditions (duration and temperature) of CCI-300 according to the different substrates:

- *PET*: 60-65 °C for 1-2 days.

- *PEN*: 80-90 °C for 6-8 hours.
- *Kapton*: 100 °C for 1 hour.
- *PVDF*: 50-55 °C for 2-3 days.

The duration also depend on the effective size of the printed layer: large size result in a slower drying, especially in the middle zone of the layer. In some sporadic occasions even after 10 days of thermal annealing on PVDF at 55 °C, one or more spot of liquid ink was still visible in large patterns.
The final shape of the solid layer was investigated though profilometry measurements. Fig-

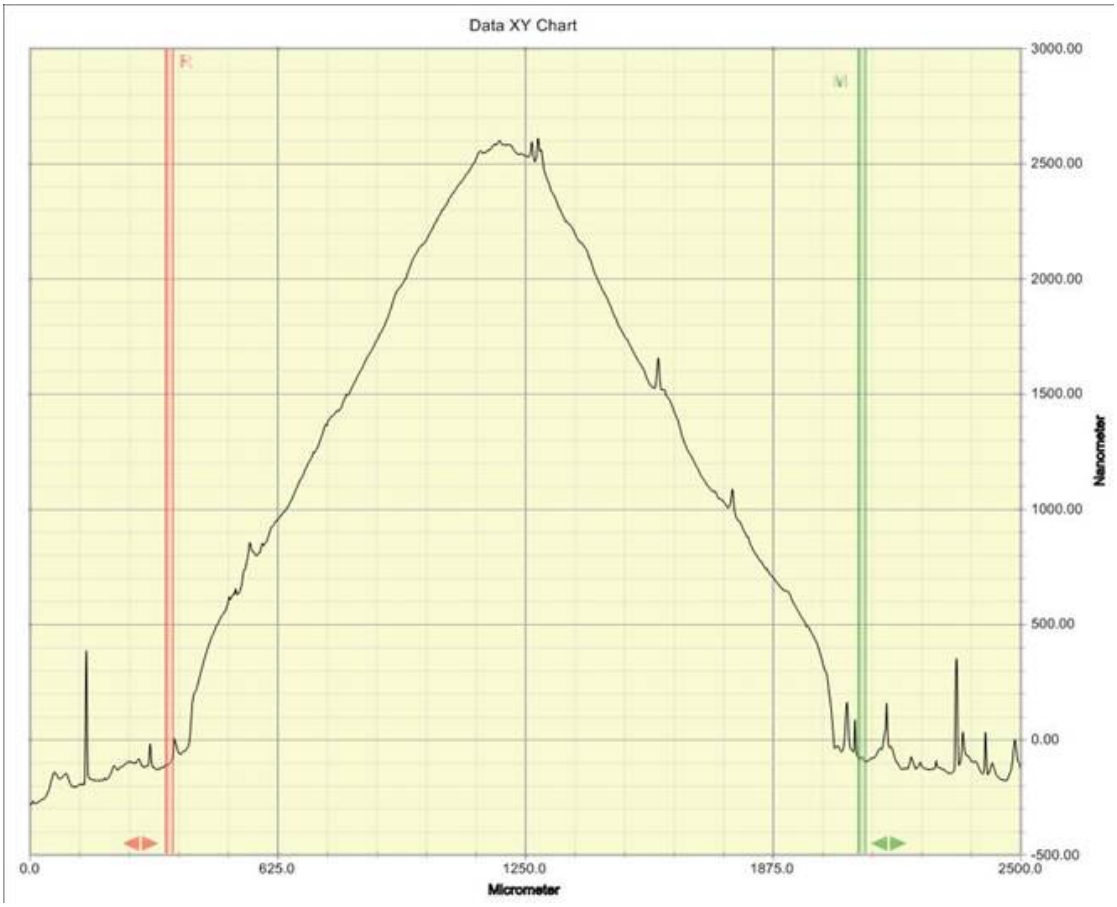

Figure 2.39: Cross-section of an inkjet printed CCI-300 electrode, obtained with a profilometry measurement.

ure 2.39 shows the cross-section of a printed large electrode made with CCI-300 and, for comparison, figure 2.40 shows the same cross-section for a thermally evaporated silver electrode. While the latter has a sharp profile, with height comprised between 80 and 100 nm,

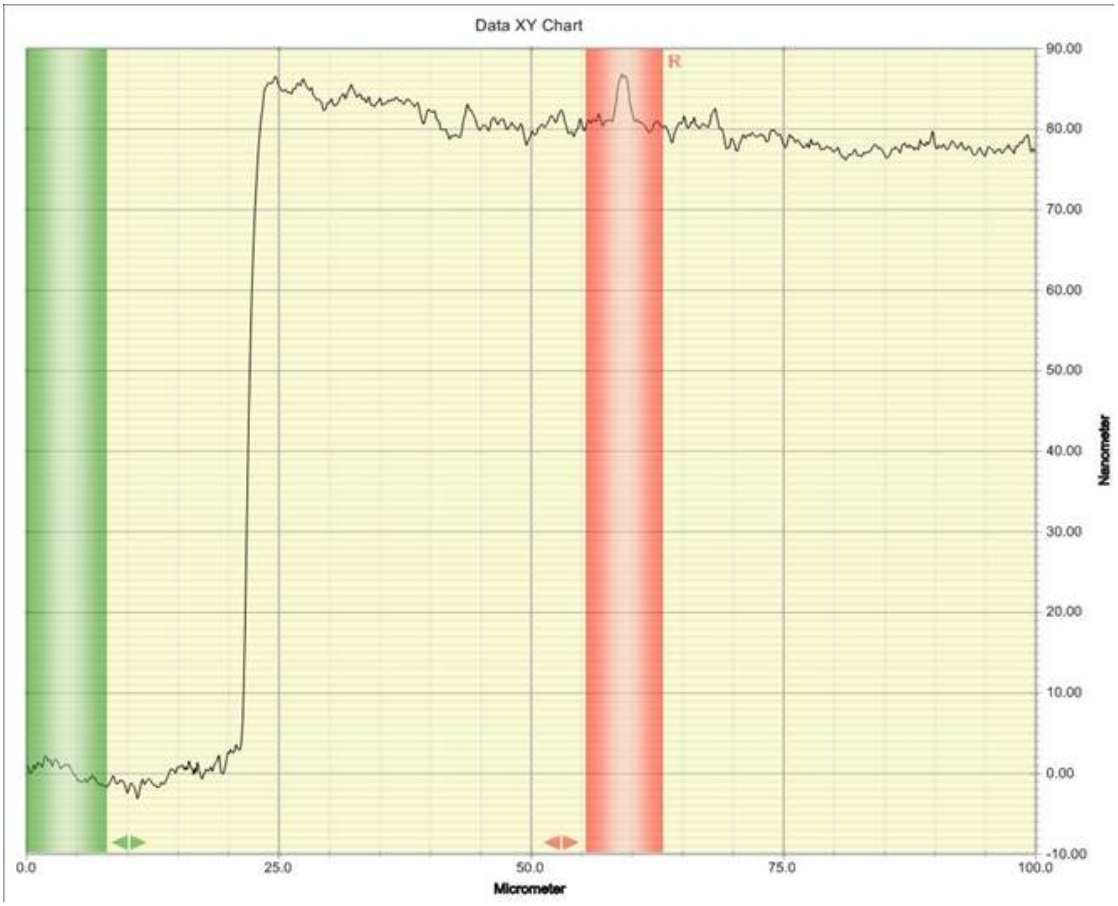

Figure 2.40: Cross-section of an evaporated silver electrode, obtained with a profilometry measurement.

the printed electrode has a smooth rounded profile with a middle peak in the range 2-2.5 μm. Plasma treatment on substrate result in a far lower thickness of the printed layer that could not be evaluated by profilometry.

High-resolution patterns

High-resolution patterns include all the patterns whose nominal dimensions are lower or comparable with the drop diameter. The most typical example of this group is the interdigitated source and drain electrodes of an OFET. Moreover, larger patterns where the distance between adjacent electrodes is small, at first approximation smaller than 8 times the drop diameter, are included in this group. As expected, this is the most challenging and fragile step of the whole printing process, therefore an accurate preliminary calibration of the printing parameters must be performed. Table 2.3 lists the printing parameter for high-resolution

Parameter	CCI-300 10 pL	CCI-300 1 pL
Drop spacing	20 μm	20 μm
Firing voltage	30 V	25 V
Maximum jetting frequency	5 kHz	1-2 kHz
Printing nozzles	1	1
Platen temperature	50-60 °C	50-60 °C
Cartridge print height	700 μm	700 μm
Number of layers	1	1
Cleaning before	S-P-S	S-P-S
Cleaning during	None	None

Table 2.3: Printing parameters for high-resolution patterns with CCI-300 silver ink.

patterns printed with CCI-300 silver ink. It is important to highlight that the printing parameters for 1 pL drops are intended for plasma treatment of the substrate 1 day before the printing process: for this reason the *drop spacing* required, 20 μm, has the same value as that of the 10 pL untreated case. In both cases, setting a higher drop spacing could cause the pattern discontinuity, while for lower values capillarity effects occur, as shown in figure 2.41a. The *firing voltage* must be moderate, since the formation of satellite drops, typical of high-

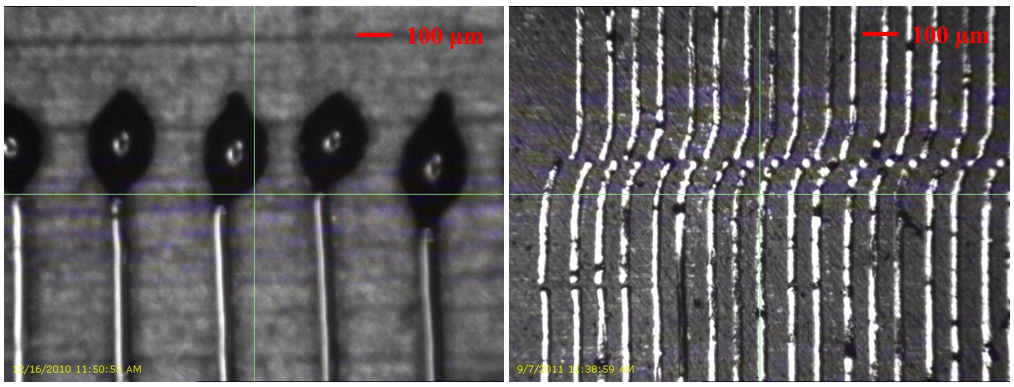

(a) (b)

Figure 2.41: (a) Capillarity effect on a printed pattern due to low drop spacing; (b) misalignment of the printed pattern caused by high frequency.

voltage printing, could affect the pattern resolution and create short-circuits. After the drop spacing, the most important parameter is the *jetting frequency*: lower values must be chosen, with respect to low-resolution pattern, in order to avoid misalignment that could cause discontinuties and short-circuits. Figure 2.41b shows the effect of high-frequency printing. Only one nozzle can be selected for high-precision patterns, only one layer can be deposited,

and no *cleaning cycles* during printing can be performed, otherwise a discontinuity is highly probable to occur.

Interdigitated electrodes can be printed in two different modes. In the first approach the

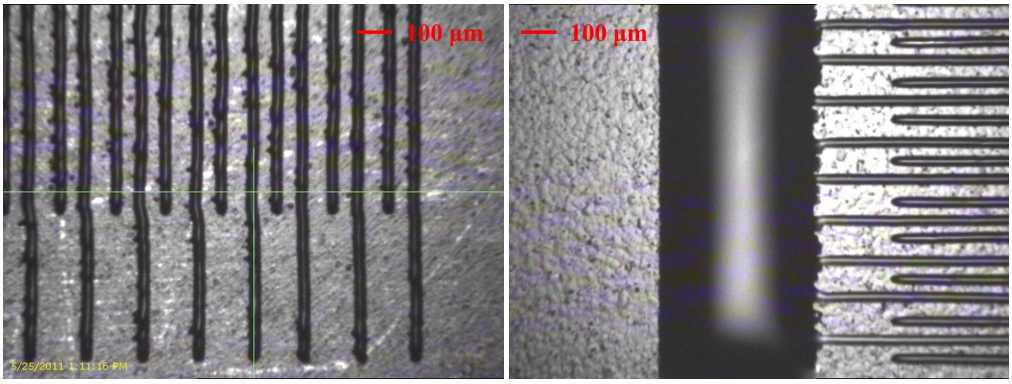

(a) (b)

Figure 2.42: Inkjet printed interdigitated contacts: (a) vertical direction and (b) horizontal direction.

electrodes are printed with 10 pL droplets and are oriented in the Y direction, *i. e.* they are perpendicular to the carriage run, as shown in figure 2.42a. In this case the minimum distance achievable between contiguous electrodes without short-circuits is 50 μm. The second approach, as mentioned before, takes advantage of the plasma treatment: the actual printing process takes place 1 day after the treatment and the 1 pL droplets employed in this case have the right spreading on the substrate. The interdigitated electrodes are oriented along the X direction, parallel to the carriage run, as shown in figure 2.42b: the inter-electrode distance can be reduced down to 25 μ and the possibility of short-circuits or discontinuities is reduced.

Since the high-resolution patterns are small compared to the low-resolution ones, the thermal annealing is much faster. In detail:

- *PET*: 60-65 °C for 8 hours.
- *PEN*: 80-90 °C for 1 hour.
- *Kapton*: 100 °C for 15 min.

Also in this case, the shape of the printed lines is smooth and rounded, as shown in figure 2.43. Since the amount of ink deposited is much lower, due to the higher drop spacing and to the low width of the line, the height of this pattern is in the range 250-300 μm.

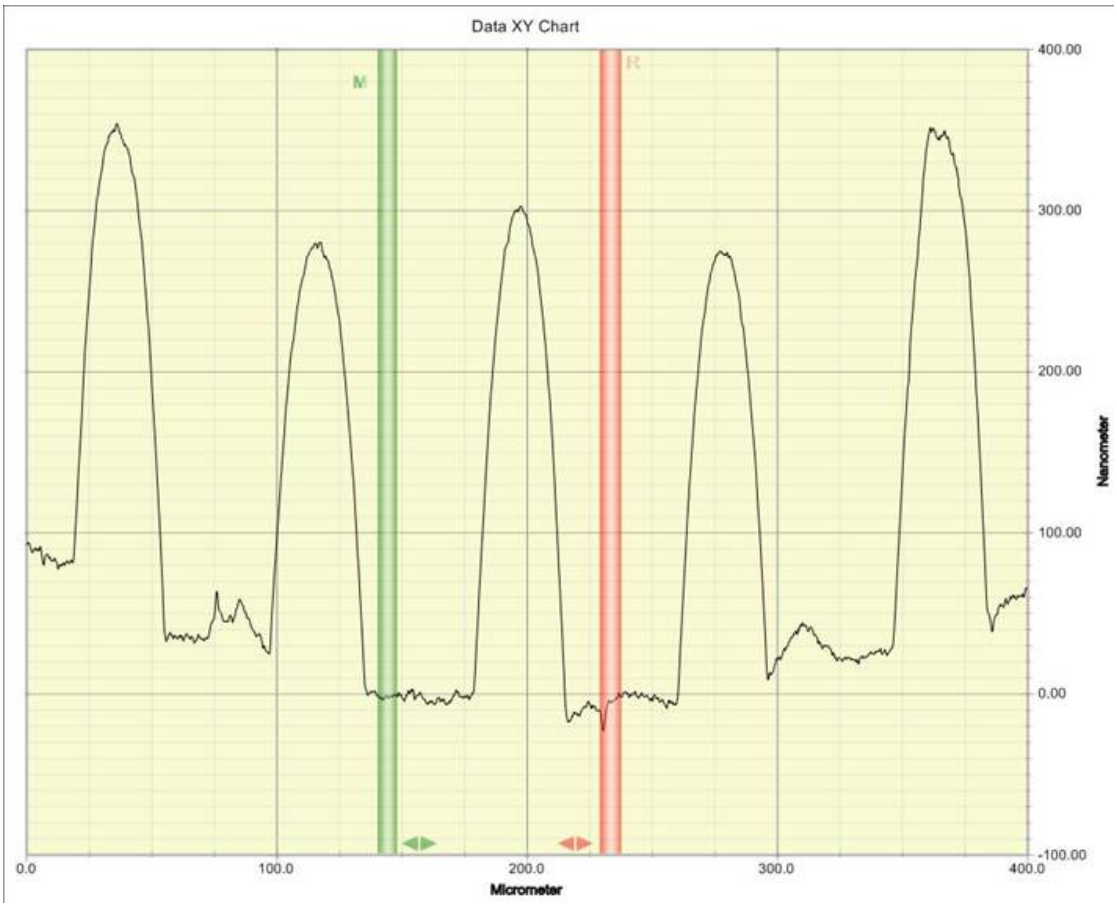

Figure 2.43: Cross-section of inkjet printed CCI-300 interdigitated electrodes, obtained with a profilometry measurement.

2.4.2 PEDOT:PSS

PEDOT:PSS is another conductive ink employed in this thesis. Even though its performance, both in terms of inkjet pringin and of electrical conductivity, is not as high as CCI-300 silver ink, it offers some interesting properties, such as transparency and biocompatibility. It has been mainly used to create electrodes for cell-signal detection and transparent top contact for organic photodiodes. Two main types of PEDOT:PSS were printed: Clevios™ P Jet HC (P-Jet) and Clevios™ CPP 105D (CPP). The former is developed *ad hoc* for inkjet printing purpose, while the latter is intended for general purpose. This difference result in different printing parameters. Low-resolution and hig-resolution patterns were printed, but in this case only 10 pL cartridges have been employed since the final printed layer satisfied the specific requirements. Before filling the cartridge, the PEDOT:PSS-based ink was subjected to ultrasonic bath for 30 min in order to avoid nozzle clogging. Moreover, 0.2 μm filtering was

made only for P-Jet, while CPP could not be filtered and therefore it was directly poured into the cartridge.
Since the printed droplets are transparent, no measurements on the drop diameter could be done, because with the resolution and the contrast of the fiducial camera the drop boundaries could not be detected. Anyways, some general considerations can be done:

- PEDOT:PSS-based droplets have a bigger spread on substrates with respect to CCI-300. Therefore the maximum resolution achievable is lower. A diameter of 50 μm was estimated in PET substrates from the drop spacing: even setting this parameter to 40μm, a continuous layer is deposited, while for higher values some discontinuities occur.

- Plasma treatment enhance the wettability of all the substrates. In particular for standard treated substrates, such as PET, the drops diameter rise up to an estimated value of 70-75 μm, while for the highly hydrophobic PDMS substrates the plasma treatment resulted in a variation of the drop diameter from 30 μm to 50 μm.

- Acylic substrates have lower interfacial energy with PEDOT:PSS, therefore the deposited drops spread less than on other standard substrates. In this case the drop diameter is estimated to be 40 μm.

- P3HT-PCBM is very hydrophobic, even more than PDMS. Since no plasma treatment could be done on this material, pattern continuity could sometimes be achieved printing more layers. More details are given in chapter 4.

Low-resolution patterns

As stated for the CCI-300 silver ink, low-resolution patterns include mainly conductive traces, pads, and electrodes. The main printing parameters are listed in table 2.4. The *drop spacing* can be varied from 25 μm to 40 μm for both inks, depending on the desired resolution; the standard value is 30 μm. The main difference for parameter setting between the two inks is the *firing voltage*. P-Jet, developed specifically for inkjet printing, shows a good drop ejection also for moderate voltage, such as 30 V. On the contrary, CCP 105D required the maximum voltage, 40 V, to obtain an acceptable drop ejection. Moreover, only up to 3 consecutive nozzles can be used, since their clogging is quite probable. For the same reason, no *cleaning cycle* should be performed during the printing process. For both the inks, the *platen temperature* should be set at 45 °C in order to reduce the solvent evaporation and therefore the nozzle clogging.

Parameter	P Jet HC 10 pL	CCP 105D 10 pL
Drop spacing	25-40 μm	25-40 μm
Firing voltage	30-35 V	40 V
Maximum jetting frequency	10-20 kHz	10-20 kHz
Printing nozzles	3-6	2-3
Platen temperature	40-50 °C	40-50 °C
Cartridge print height	1000 μm	1000 μm
Number of layers	3-6	3-6
Cleaning before	S-P-S	S-P-S
Cleaning during	S-P-S (30-50 bands)	None

Table 2.4: Printing parameters for low-resolution patterns with PEDOT:PSS-based ink.

Figure 2.44 shows the low-resolution pattern composed of 3 stacked layers of PEDOT:PSS.

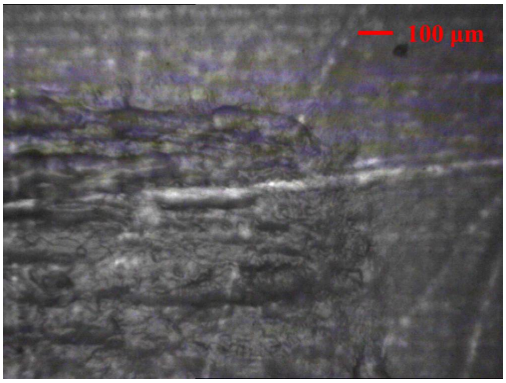

Figure 2.44: Inkjet printed PEDOT:PSS low-resolution pattern (3 layers).

The resolution is much lower than that of CCI-300, but for contact purpose this is not a critical issue.

High-resolution patterns

Medium and high resolutions can be obtained when PEDOT:PSS is printed on acrylic, since the droplet diameter is smaller, and by employing 1 pL cartridges. The relative printing parameters are listed in table 2.5. In this case, the main difference with the high-resolution patter is the *number of nozzles* employed, no more than 1, and the *maximum jetting frequency*, usually set to 2 kHz. Moreover, in order to decrease the electrical resistance of the thin layers, as shown in figure 2.45, more *layers* usually have to be printed. The standard value is 5 layers. In the picture, the channel is 4 mm long and 45 μm width; the estimated thickness is roughly

Parameter	P Jet HC 1 pL	CCP 105D 1 pL
Drop spacing	40 μm	40 μm
Firing voltage	30 V	40 V
Maximum jetting frequency	1-2 kHz	1-2 kHz
Printing nozzles	1	1
Platen temperature	40-50 °C	40-50 °C
Cartridge print height	700 μm	700 μm
Number of layers	5	5
Cleaning before	S-P-S	S-P-S
Cleaning during	None	None

Table 2.5: Printing parameters for high-resolution patterns with PEDOT:PSS-based ink.

1 μm.

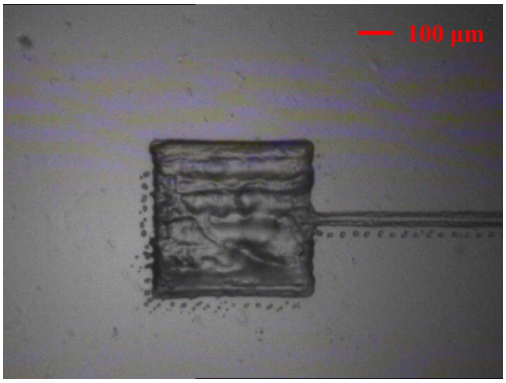

Figure 2.45: Inkjet printed PEDOT:PSS high-resolution pattern (5 layers).

2.4.3 Carbon Black

The inkjet printing of Carbon black is described in chapter 4, section 4.2.

2.5 Inkjet printing of semiconductors

The inkjet printing of semiconductors has been one of the most challenging issues done in this work. Two types of semiconductors have been printed: TIPS-pentacene and P3HT-PCBM. While the latter was purchased and was developed specifically for inkjet printing, the former was home-made and ink solution required carefully experiments about ink formulation. They are described in section 2.5.1 and 2.5.2, respectively.

2.5.1 TIPS-pentacene

TIPS-pentacene is one of the most employed semiconductor in organic electronics, due to its stability and especially to its processability in liquid form. The preferred deposition method is by drop casting, with the ink formulation below referred as *TIPS1*. Since the electrical performance of OFETs with TIPS-pentacene strongly depends on the active layer, a standard and reproducible deposition method, such as inkjet printing, is highly desirable.
In the followings, the different formulations employed, namely *TIPS1*, *TIPS2* and *TIPS3* are described together with the main printing parameters. These are preliminary results, since an electrical performance could not be achieved as good as drop casting. Here only the printing issues are described. The electrical preliminary results are reported in chapter 3.

TIPS1

Toluene	TIPS-pentacene
99.5 wt.%	0.5 wt.%

Table 2.6: Formulation of the ink *TIPS1*.

Table 2.6 report the standard solution for TIPS-pentacene. The solution must be stirred for 1 h in a hotplate at 90 °C. Figure 2.46 shows a picture, taken with the DMP2831 fiducial camera, of a drop-casted layer of TIPS1. The formation of crystals can be noticed. This solution was mainly drop-casted. Its measured viscosity was under 1 cP, therefore it was not suitable for inkket printing. Some inkjet printing trials have been performed: although some drop ejection occurred, the frequent nozzle clogging required very frequent cleaning cycles, which in turn resulted in a very fast depletion of the ink filled in the cartridge. For example,

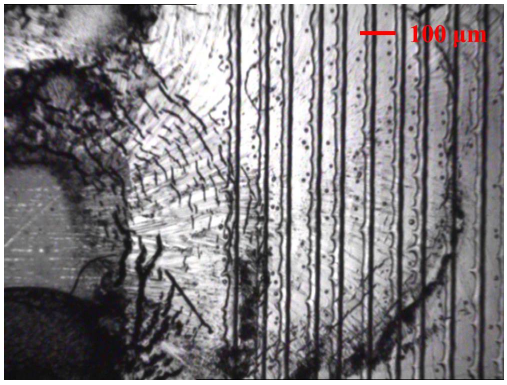

Figure 2.46: Picture taken with the fiducial camera of a drop-casted layer of TIPS1.

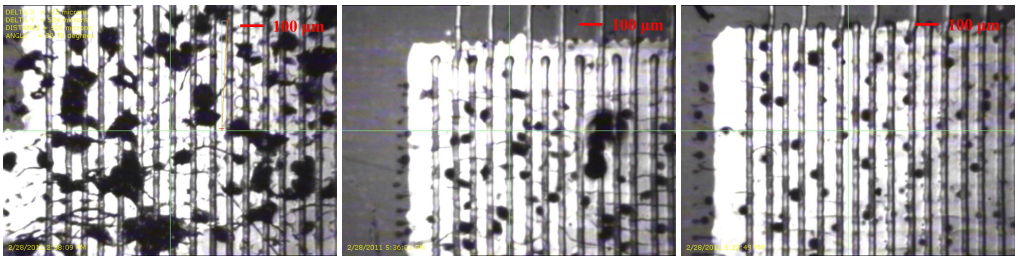

(a) (b) (c)

Figure 2.47: Inkjet printed TIPS1 layers with different drops spacing: (a) 10 μm, (b) 30 μm, and (c) 40 μm.

5 mL of TIPS1 ink were enough only to print 2-3 layers of of a 3x5 cm^2 pattern. The results are shown in figure 2.47, where different drop spacing have been set: a disordered deposition can be noticed, with some agglomerates more evident in the first case, with the smallest drop spacing. Table 2.7 lists the main printing parameters for the TIPS1 ink. Here, the manda-

Parameter	**TIPS1 10 pL**
Drop spacing	10-40 μm
Firing voltage	40 V
Maximum jetting frequency	5-10 kHz
Printing nozzles	3-5
Platen temperature	50-60 °C
Cartridge print height	700 μm
Number of layers	3-6
Cleaning before	S-P(0.5)-S
Cleaning during	S-P(0.5)-S (5 bands)

Table 2.7: Printing parameters for TIPS1 ink.

tory requirement is the continuous cleaning of the cartridge: usually a cleaning cycle every 5 bands must be performed in order to avoid the nozzle clogging. As state before, this results a fast ink depletion on the cleaning pad. This problem has been partially reduced by decreasing the purge time to 0.5 s, thus causing a reduced ink flow during the cleaning process.

TIPS2

Table 2.8 reports the second ink formulation involving TIPS-pentacene. The solution was stirred for 1 h in a hotplate at 90 °C. Basically, the TIPS-pentacene concentration was increased in order to achieve a higher viscosity suitable for inkjet printing. The measured viscosity, in this case, was 1.05 cP, slightly better than TIPS1 but anyways far from the DMP2831

Toluene	TIPS-pentacene
95 wt.%	5 wt.%

Table 2.8: Formulation of the ink *TIPS2*.

requirements. The printed layers are shown in figure 2.48 with different drop spacing: 15

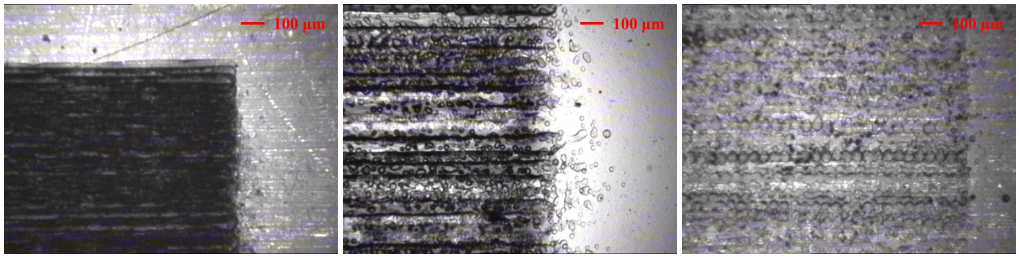

(a) (b) (c)

Figure 2.48: Inkjet printed TIPS2 layers with different drops spacing: (a) 15 μm, (b) 30 μm, and (c) 50 μm.

μm in 2.48a, 30 μm in 2.48b, and 50 μm in 2.48c. The higher viscosity of TIPS2 resulted in better drop ejection and lower cartridge depletion, but also in a more probable nozzle clogging during the printing process. The higher concentration can be noticed also in the darker layer deposited, especially for low drop spacing. The drop diameter for this ink was at first approximation the same as that of TIPS1 droplets, therefore setting a drop spacing of 50 μm the pattern approaches the limit of discontinuity. The printing parameters are listed in table

Parameter	TIPS2 10 pL
Drop spacing	10-40 μm
Firing voltage	35-40 V
Maximum jetting frequency	5-10 kHz
Printing nozzles	3-5
Platen temperature	50-60 °C
Cartridge print height	700 μm
Number of layers	1-3
Cleaning before	S-P-S
Cleaning during	S-P-S (5 bands)

Table 2.9: Printing parameters for TIPS2 ink.

2.9. Their values are similar as in the TIPS1 case, since changing the TIPS-pentacene concentration does not dramatically influences the printing performance. The major precaution is

restoring the Purge cleaning to the standard value of 1 s, since the ink depletion is partially reduced.

TIPS3

Since the viscosity of pure toluene is 0.59 cP at room temperature and the solute concentration does not affect this value over a 1 cP range, changing the solvent was the best solution to achieve a higher viscosity. Anisole is another good solvent for TIPS-pentacene and its viscosity is 1.05 cP, therefore it was chosen as a possible candidate for TIPS-pentacene based inks. Moreover, according to the current literature [126, 127], ink was formulated using a blend with polystyrene (M_w ≈240000). Many inks with different TIPS-pentacene and polystyrene concentrations were formulated, but the main results are based on the ink, hereafter named *TIPS3*, whose concentration is specified in table 2.10. The solution was stirred for 1 h in a

Anisole	TIPS-pentacene	Polystyrene
95 wt.%	2.5 wt.%	2.5 wt.%

Table 2.10: Formulation of the ink *TIPS3*.

hotplate at 90 °C. With this formulation, the printing performance was much better than the previous cases: the drop ejection was more controllable and constant, the nozzle clogging reduced and the achieved resolution higher. The printing parameters employed are listed in table 2.11. Two approaches were used to print TIPS3:

Parameter	TIPS3 10 pL
Drop spacing	10-40 μm
Firing voltage	30-40 V
Maximum jetting frequency	5-10 kHz
Printing nozzles	1-16
Platen temperature	50-60 °C
Cartridge print height	700 μm
Number of layers	1-3
Cleaning before	S-P-S
Cleaning during	None

Table 2.11: Printing parameters for TIPS2 ink.

- Printing a single line with few nozzles, in order to have all the inks deposited in a carriage run.

- Covering a large area employing many nozzles, up to 16, in order to pour a uniform extended layer of semiconductor over the substrate.

The number of *printing nozzles* and the *drop spacing* depend on the specific layer to be deposited. Moreover, since the main aim was the elimination of the boundary effects between two consecutive bands, no *cleaning cycle* was performed during printing. The printing re-

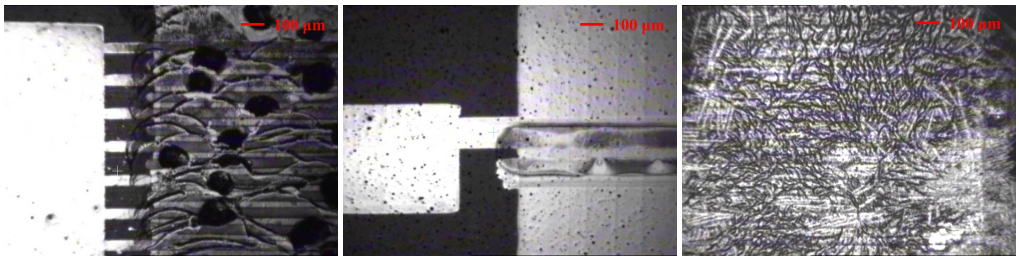

(a) (b) (c)

Figure 2.49: Inkjet printed TIPS3 layers with different approaches: (a) large-area with multiple bands, (b) small area with a single band, and (c) large-area with a single band.

sults are shown in figure 2.49, where the three different approaches employed are described as follows. In 2.49a a large area is covered with multiple runs of the carriage and 3 jetting nozzles: the line boundaries are clearly visible, which decrease the electrical performance of the device. In 2.49b a small area, *i. e.* a linear-channel OFET, is covered with TIPS3: a single carriage run print a single line with 3 jetting nozzles. Finally, in figure 2.49c, a large area, as in the first case, is covered just with a single carriage run but employing all the 16 nozzles.

2.5.2 P3HT:PCBM

P3HT-PCBM is a blend of two semiconductors, one p-type (P3HT) and one n-type (PCBM), described in section 2.5. The ink employed for the experimental activity related to this thesis was purchased from Sigma Aldrich® [107]: it is developed specifically for inkjet printing application. Its nominal viscosity is 8 cP. The main application of this semiconductor was the fabrication of organic photodiodes, with a vertical sandwich structure: a bottom electrode, an inkjet printed layer of P3HT-PCBM and a top electrode. Generally the top and bottom electrodes were thermally evaporated, but some configurations have been chosen with inkjet printed PEDOT:PSS electrodes. The complete structure is presented in section 4.1, together with the electrical performance of the devices realized. The realization of these photodiodes was part of the HYMEC project, described in the same section. One of the required specifics was the dimensions of the printed active layer: since it was the middle layer

between two crossed, 300 μm wide electrodes, the resulting pattern had to be a 300 μm · 300 μm square as most regular, flat and thin as possible. Therefore, only 1 pL cartridges have been used in order to match the requirements. Table 2.12 shows the drop diameter values

Substrate	P3HT-PCBM 1 pL
PET	55 ± 4 μm
PEN	53 ± 3 μm
Kapton	50 ± 4 μm
Gold	62 ± 5 μm
Silver	60 ± 3 μm
Aluminum	61 ± 5 μm

Table 2.12: Drop diameters of inkjet printed P3HT-PCBM on different substrates.

of inkjet printed P3HT-PCBM 1 pL droplets on different substrates. Both plastic and metallic substrates give rise to similar droplets whose diameter values are in the same range, even if it is slightly larger when droplets are deposited on metals. Printing the P3HT-PCBM with multiple carriage bands resulted in partially rough layer, as shown in figure 2.50a: when one line was printed in a carriage run, before the subsequent line could be printed a partial ink drying had already occurred, with an irregular boundary between the two lines. In order to achieve an uniform layer, the approach previously presented for TIPS3 was employed here: the total width of the square layer was covered by a single carriage run employing 13 nozzles together. The result is presented in figure 2.50b. Table 2.13 lists the reference parameters for

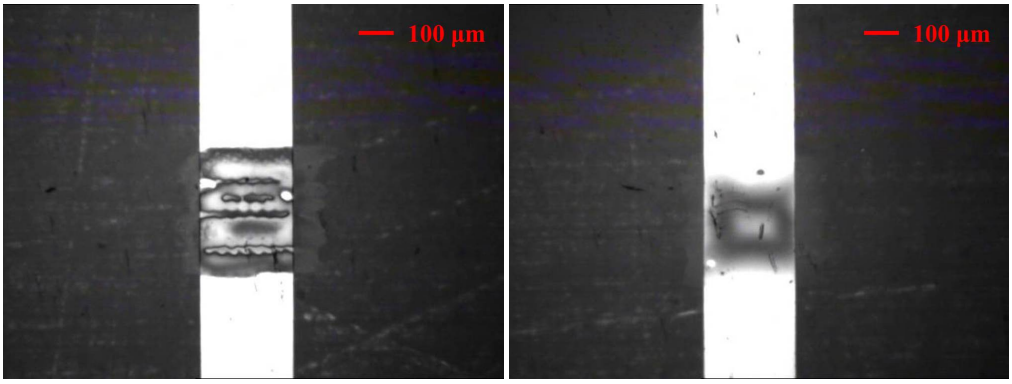

(a) (b)

Figure 2.50: Inkjet printed P3HT-PCBM layers with different approaches: (a) multiple bands and (b) single band.

the purpose described above. The best *drop spacing* is 40 μm, since for higher values some discontinuities are noticed. The other parameters, such as *firing voltage, jetting frequency*

Parameter	P3HT-PCBM 1 pL
Drop spacing	40 μm
Firing voltage	30 V
Maximum jetting frequency	1 kHz
Printing nozzles	13
Platen temperature	RT
Cartridge print height	700 μm
Number of layers	1
Cleaning before	S-P-S
Cleaning during	None

Table 2.13: Printing parameters for P3HT-PCBM ink.

and *nomber of layers*, are set in order to have an accurate printing of a high-resolution pattern, with clearly visible angles. The actual length of the square sides ranges between 400 and 500 μm, higher than the nominal 300 μm: this larger shape was set in order to help the facilitate the alignment of the shadow mask for the thermal evaporation of the upper layer.

Finally, figure 2.51 shows the cross-section of a inkjet printed P3HT-PCBM layer, obtained with a profilometry measurement. The average height is 50 nm for small layers printed with the parameters listed in table 2.13, and a fairly smooth surface is obtained.

2.6 Inkjet printing of insulators

The insulator most employed in this context was parylene-C, deposited by means of chemical vapor deposition. However, some preliminary experiments of inkjet printing of insulating layers were carried on.

2.6.1 PVDF

The first material employed was *PVDF* dissolved in RER500 with different concentrations. The standard deposition method for this ink is spin coating of a 10 wt.% solution. However, this ink could not be printed since the droplets could not be ejected from the nozzles, probably due to the high viscosity. Also solutions with lower concentrations, such as 5 wt.% and 1 wt.%, were prepared, but they gave rise to the same problem. Finally, a printable formulation was obtained by reducing the concentration to 0.5 wt.%, are reported in table 2.14. The drop ejection showed a disordered trend, with non-vertical direction and random nozzle clogging. The drop deposition parameters are listed in table 2.52. The chaotic droplet ejection resulted

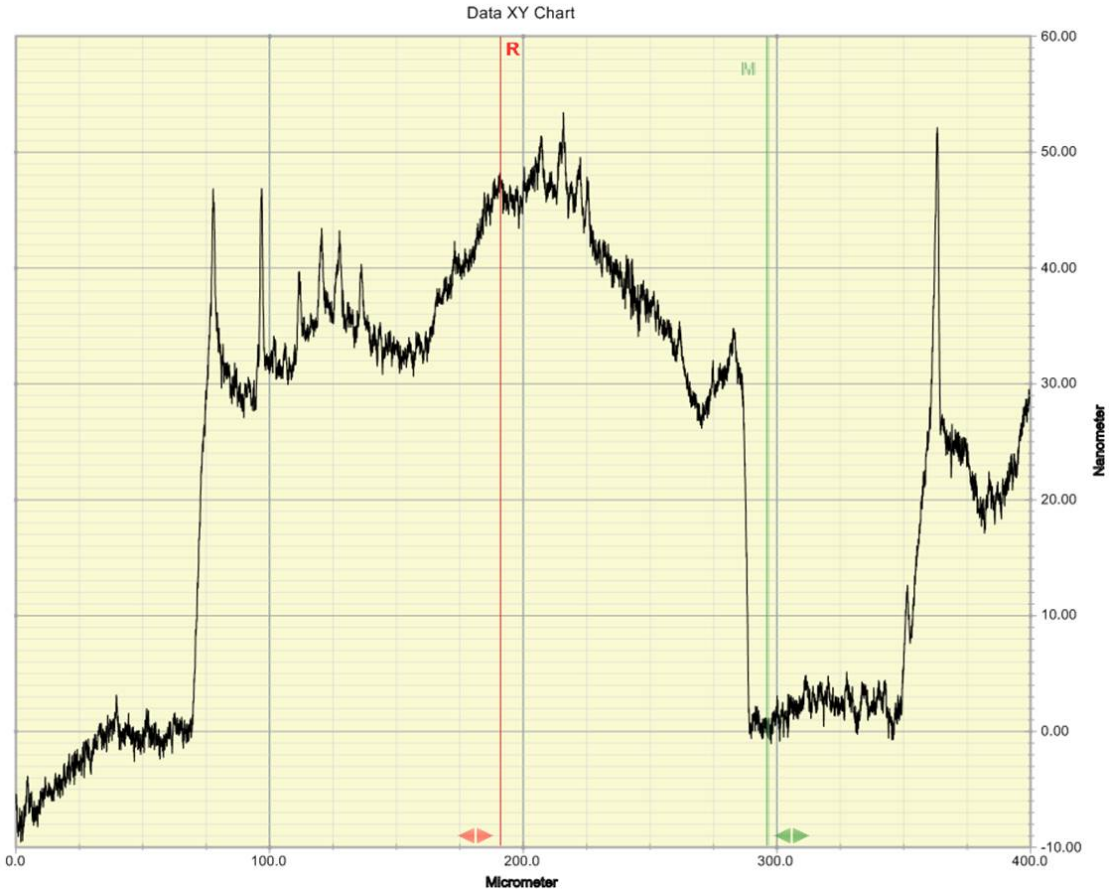

Figure 2.51: Cross-section of an inkjet printed P3HT-PCBM layer, obtained with a profilometry measurement.

RER500	PVDF	Printable
90 wt.%	10 wt.%	no
95 wt.%	5 wt.%	no
99 wt.%	1 wt.%	no
99.5 wt.%	0.5 wt.%	yes

Table 2.14: Formulation of the *PVDF* based inks.

also in a non-uniform printed layer, as shown in figure 2.52. In particular, in figure 2.52a the layer was deposited on a plastic substrate and could cover the entire pattern region, only with occasional discontinuities. On the contrary, as shown in figure 2.52b, when this ink is printed on metals, the interfacial energy was very low and continuous layers could hardly be printed. This irregular deposition resulted in bottom electrodes short-circuited with top electrodes.

Parameter	PVDF 10 pL
Drop spacing	25 μm
Firing voltage	40 V
Maximum jetting frequency	5-10 kHz
Printing nozzles	3
Platen temperature	RT
Cartridge print height	700 μm
Number of layers	1-5
Cleaning before	S-P-S
Cleaning during	S-P-S (10 bands)

Table 2.15: Printing parameters for PVDF-based ink.

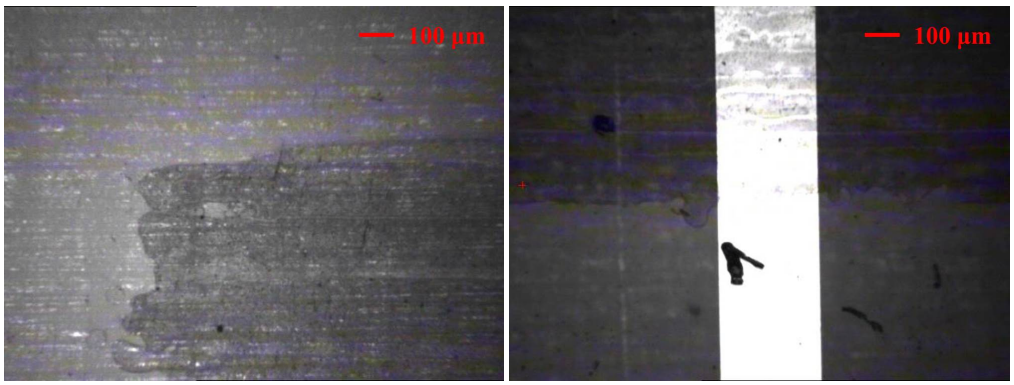

(a) (b)

Figure 2.52: Inkjet printed pvdf layers on a plastic substrate (a) and on a metal contact (b)

2.6.2 Polystyrene-based ink

Other experiments were carried on employing a *polystyrene* based ink with gold nanoparticles (Au), whose formulation is detailed in table 2.16. The drop ejection for all the inks is fair regular, with double droplets ejected from each nozzle. The printed layers, consisting of a square with 500 μm sides, were quite defined. The only exception regards ink7, which show a very poor pattern definition due to the low polystyrene concentration.

The PS-based inks were printed between two evaporated metal electrodes, in order to measure the capacitance. The results are reported in table 2.17. The results show good capacitance values for all the formulated inks, with an average value between 30 an 40 nf/cm^2. Morover, the measured resistance was negligible, ranging around 10-100 MΩ.

Ink	Solvent	Polystyrene	Au NP
PS1	Toluene	10 wt.%	200 ppm
PS2	Toluene + MB (4:1)	10 wt.%	200 ppm
PS3	Toluene	10 wt.%	1000 ppm
PS4	Toluene + MB (4:1)	10 wt.%	1000 ppm
PS5	Toluene	5 wt.%	1000 ppm
PS6	Toluene + MB (4:1)	5 wt.%	1000 ppm
PS7	Toluene	2 wt.%	2000 ppm
PS8	Toluene	5 wt.%	2000 ppm

Table 2.16: Formulation of the polystyrene-based insulating ink, employing toluene and methyl benzoate (MB) as solvents.

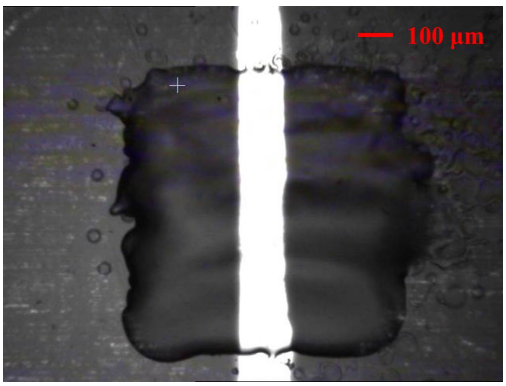

Figure 2.53: Inkjet printed of polystyrene-based ink.

Ink	Layers	Capacitance (nF/cm^2)	Thickness (nm)
PS1	1	32.9	73
PS1	2	32.0	75
PS2	1	36.5	65
PS2	2	30.9	77
PS3	1	54.6	44
PS3	2	44.4	54
PS4	1	57.1	42
PS4	2	36.8	65
PS5	1	33.1	72
PS5	2	32.5	74
PS6	1	34.8	69
PS6	2	32.2	74
PS7	1	34.9	68
PS7	2	33.0	72
PS8	1	32.5	74
PS8	2	38.0	63

Table 2.17: Capacitance values for all the formulated inks and estimated thickness.

3 Inkjet printing of Organic Field-Effect Transistors for tactile sensing

In this chapter the main application of the inkjet printing technique, developed during this work, is presented. In the first section (3.1) an overview on the tactile sensing for robotic application is given: starting from the key points desired when dealing with artificial skin, the main technologies adopted are listed and described. Then the section focuses on the employment of Organic Field-Effect Transistors (OFETs) as mechanical sensors, both for direct sensing and when they are coupled with another sensing element. Section 3.2 describes the OFETs fabrication by inkjet printing, included the printing steps and the electrical performances obtained with different semiconductors. In particular, the second part of this section focuses on inkjet printing of TIPS-pentacene. Finally, the third section (3.3) is totally devoted to the ROBOSKIN project which took more than half of the work related to this thesis: fabrication of OFET-based sensors systems, experimental setup for the electromechanical characterization, calibration of the electrical response and fabrication of PVDF-based sensors.

3.1 Tactile sensors for robotic application

The field of robotics is continuously expanding, since robots are employed in many human environments, such as homes, offices and hospitals. In order to achieve a better integration and a better functionality, as well as a better interaction with humans, robots are required to get even more human-like movements and manipulation tasks. Moreover, one of the most challenging feature is that these movements must be learned and reproduced in real time, exactly as a child learning to move when in contact with the surrounding world. One of the most important point-of-contact between inner robotic circuits and outer environment is the sense of touch: an artificial *robotic sckin* with distributed tactile sensors is a mandatory interface for robots to adequately move, recognize objects and learn how to manipulate them.

In particular, the specifications required for robotic in-hand tactile sensing are:

- Detect the contact and release of an object.
- Detect lift and replacement of an object.
- Detect shape and force distribution of a contact region for object recognition.
- Detect contact force magnitude and direction for maintaining a stable grasp during manipulation.
- Detect both dynamic and static contact forces.
- Track variation of contact points during manipulation.
- Detect difference between predicted and actual grip forces necessary for manipulation.
- Detect force and magnitude of contact forces due to the motion of the hand during manipulation.
- Detect tangential forces due to the weight and shape of the object to prevent slip.
- Detect tangential forces arising from variations in object parameters (*e. g.* surface friction, elasticity, etc.) to prevent slip.

The following short review of the tactile sensing technologies for robotic application is taken from the excellent review by Yousef *et al.*, that should be read for a more detailed overview [128].

Resistive tactile sensors

Resistive sensors are the largest family of tactile devices and include several type of sensors, such as strain gauges, piezoresistors, conductive polymers and conductive elastomer composites. They are briefly described in the followings.

Strain gauges consist of a structure that elastically deforms when subjected to a force which in turn leads to a change in its resistance. To optimize the change in resistance due to applied mechanical stress, strain gauges are typically long winding snake-like structures. In this way, when deformed, the cross-section of the strain gauge decreases while its conduction length increases. Here, typically, the change in resistance of the strain gauge material itself is secondary to the change due to its mechanical deformation. An example is shown in

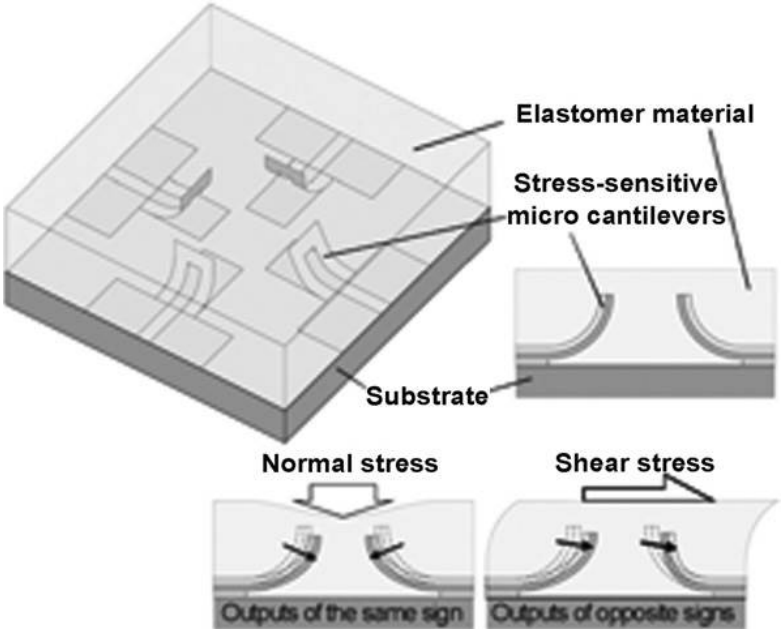

Figure 3.1: Structure and operation of embedded tilted cantilevers [8].

figure 3.1. The main advantages of strain gauges are its high sensitivity, up to 2.1%/N and 200 mV/N, its small size (1-2 mm spatial resolution), the well established design and fabrication techniques, the possibility to detect 3D forces and the easy integration with other electronic components. On the other hand, they are quite fragile and fabricated with costly materials and techniques, they usually cannot be stretched and, even if the sensor itself is small, the total package size can be large.

In *piezoresistors*, mechanical stress is detected by a change in resistance of the piezoresistive material itself. Piezoresistors in general have smaller lateral dimensions and can achieve a higher output per area than strain gauges. Silicon and other semiconductor materials have high piezoresistive responses, but are however brittle and fragile. As with strain gauges, embedding them in an elastomer allows for mechanical flexibility, but decreases sensitivity and can introduce ambiguity. Figure 3.2 shown an example of 3D force sensor array based on the piezoresistive effect. The performance of piezoresistive sensors is the same of that of strain gauge. High sensitivity up to 0.1%/N and 400 mV/N and good spatial resolution (1-3 mm) are the main advantages, together with an established, but costly, fabrication technique, the possibility of detecting 3D forces, an increased grasping quality and easy integration with MEMS. The major drawbacks are the loss of sensor sensitivity with use, the fragility, the costly materials and fabrication techniques and the ambiguity of the response when the device is

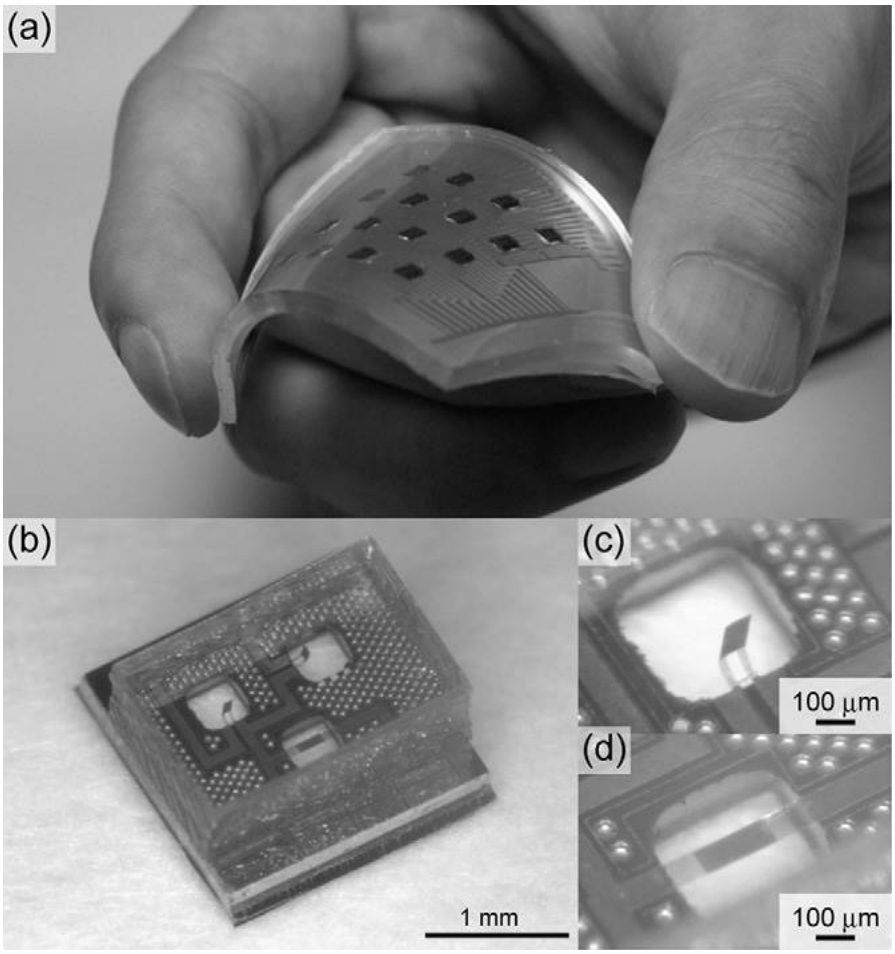

Figure 3.2: Array of 3D force piezoresistive sensors [9].

embedded in an elastomer.

Conductive polymers are mechanically flexible, robust, and can be chemically resistant. Furthermore, polymer-based sensors can be fabricated using large-area low-cost fabrication techniques, like most of the printing techniques. Simple and low-weight structures can be obtained, such as that shown in figure 3.3. The major disadvantage is the low sensitivity, not higher than 15 mV/N and 0.1%/kPa.

A common choice of pressure sensitive material is *conductive elastomer composites* that are enriched with conductive filler particles. When an external force is applied to the sensor deforming the elastomer composite layer, its resistivity changes depending on the type of conductive particles, their volume percentage in the elastomer and the resulting material stiffness. As elastomers are highly stretchable they make excellent candidates for application on curved surfaces and moving parts. Moreover, the use of a soft material mimics human skin

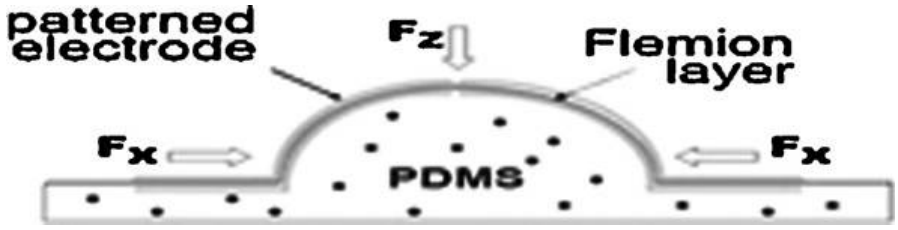

Figure 3.3: Schematic of an ion-polymer metal composite used as the sensing layer in a 3D tactile sensor [10].

and increases grasp quality. However, applications are mainly restricted to pressure sensing as the materials conduct isotropically. Further disadvantages are that the sensors suffer from hysteresis and low dynamic ranges. An application of conductive elastomers is shown in figure 3.4.

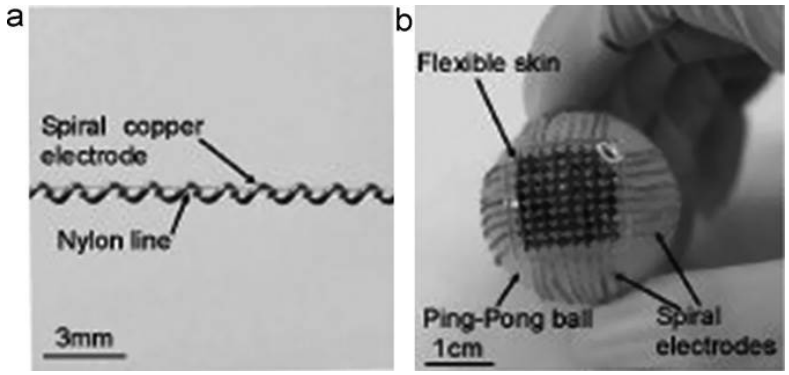

Figure 3.4: Example of tactile sensor composed of conductive elastomer, spiral copper electrodes and nylon lines [11].

Capacitive tactile sensors

Capacitive tactile sensing is one of the most sensitive techniques for detecting small deflections of structures without direct temperature dependence. Each of the capacitors consists of two parallel plates that can detect either only forces only normal to the surface or, by opportune design modification, shear forces as well. Figure 3.5 shows a possible design for the detection of normal and shear forces by means of capacitive sensors. Its greatest advantages are the very high sensitivity, 3%/N, the independence of temperature, the small size with high spatial resolution, the possibility to easily cover large areas and the possibility to detect 3D forces. On the other hand, the major drawbacks are the general sensitivity to electromagnetic field: parasitic capacitance, electromagnetic interference and cross-talking between sensing

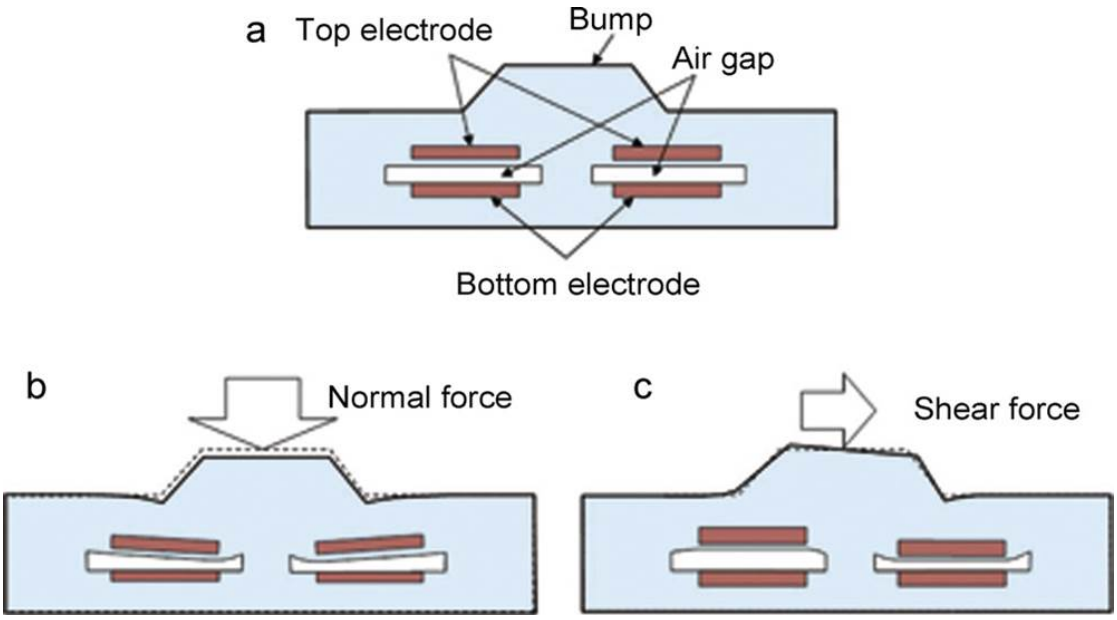

Figure 3.5: Schematic design of conductive sensors for the detection of both normal and shear forces [12].

elements.

Piezoelectric tactile sensors

Piezoelectric sensors convert an applied stress or force into an electric voltage. Piezoelectric sensors are highly sensitive with high voltage outputs even to small deformation. The sensing elements do not require a supply of electrical power, and hence the sensors are considered to be highly reliable and can be applied to a wide range of applications. The voltage output however decreases over time and piezoelectric sensors are therefore only suitable for detecting dynamic forces. PVDF films are common piezoelectric materials in tactile sensing applications due to their mechanical flexibility, high piezoelectric coefficients, dimensional stability, low weight and chemical inertness. An example of piezoelectric sensors is shown in figure 3.6. The high sensitivity (up to 500 mV/N) and the reliability are two of the most appealing properties of piezoelectric sensors. The major disadvantage is that the electrical response decreases with time, thus they are suitable only for non-static applications.

Optical tactile sensors

As the number of sensors increases in the tactile skin, wiring complexity and cross-talk become an issue when electrical signals are used. A solution is to use *fibre optic* cables to carry signals. With the introduction of plastic optical fibres (POFs), previous limitations of rigidity

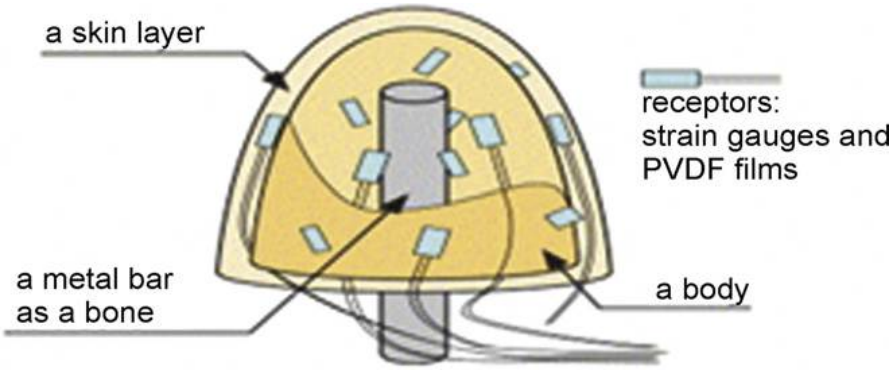

Figure 3.6: Cross section of a metal fingertip embedded with strain gauges and PVDF film receptors [13].

and fragility are overcome. Usually a *charge-coupled device* (CCD) detects the light variation, originated by LEDs and convoyed to them by opportune deflectors, when an external mechanical stimulus occurs. Figure 3.7 shows the schematic of a possible tactile sensing system involving optical sensors. A very high force resolution can be achieved by this class of sensors,

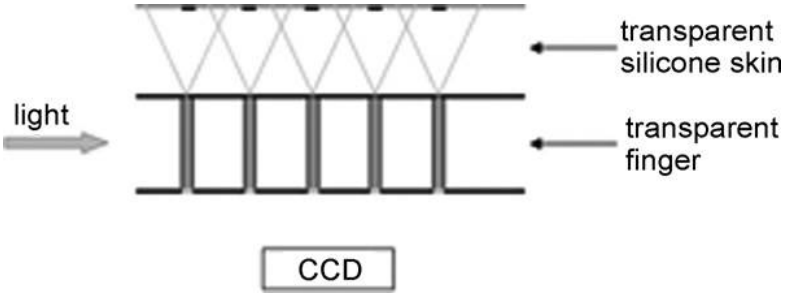

Figure 3.7: Schematic example of a robotic skin based on optical sensors [14].

with values up to 0.05 N. Moreover, they are not affected by electromagnetic interference and cross-talking. The only drawback is the possibility of signal alternation and attenuation due to bending or misalignment.

OFET-based tactile sensors

Tactile sensing can be performed also by means of Organic Field-Effect Transistors (OFETs): this is the technology employed for carrying on part of the overall work of this thesis. They take advantage of the typical features of organic electronic devices, such as flexibility, conformability, transparency, low-cost fabrication over large-area. Moreover, they usually consist of simple sensing elements which do not require large packaging and can be easily integrated with the organic circuitry Since this chapter is totally devoted to *OFET-based tac-*

tile sensors, a more detailed description of the working principles and actual applications is given. Basically, they can divided into two major groups. The first one includes all the applications where OFETs are coupled with a sensing element to amplify the electrical response. The second category includes applications where the OFET itself is the sensing element and is able to detect the strain applied on it, working at the same time as a sensor and as an amplifier. These two groups are described in sections 3.1.1 and 3.1.2 respectively.

3.1.1 Indirect mechanical sensing with Organic Field-Effect Transistors

The first approach to achieve mechanical sensing by employing Organic Field-Effect Transistors (OFETs) consists of coupling them with with an external sensing element. In this case, OFETs act only as part of the read-out electronics directly connected with the actual sensor, which modulates the OFETs electrical response when an external stimulus is applied to the sensitive area. Therefore the mechanical stimulus, which can be force, pressure or strain, is sensed not directly by the OFETs semiconductor, but by the indirect modulation of the OFETs electrical performance. Despite the processing steps required to integrate the sensing element with the OFET, which sometimes involve expensive techniques and thus reduce the typical appeal of organic electronics, high sensitivities can be achieved with indirect sensing especially in the low-pressure range; moreover, indirect sensing is a versatile approach, since a great variety of sensing elements and techniques can be employed, which give rise to different sensitivities on different ranges of mechanical stimuli applied. The scientific literature proposes two different ways to couple the sensing element with an OFET: connection to the gate electrode, in order to modulate the gate capacitance, and series connection to the drain electrode, in order to modulate the drain current flow. Both ways are analyzed in the followings.

Connection of the sensing element to the gate was used by Mannsfeld *et al.* [15] and later by Schwartz *et al.* [16]. they developed a microstructurated dielectric layer of PDMS patterned with parallel rows of identically high pyramids. Gate molds with different sizes were employed: the base and the height of the pyramids varied from 6 μm to 3 μm and the inter-pyramid space varied from 1.33 μm to 13.61 μm. Then, an *indium tin oxide* (ITO)-coated conductive PET foil was laminated on the top of the microstructured PDMS film. Figure 3.8 shows the schematic of the proposed structure. The pressure is applied in the normal direction with respect to the molded gate. The OFET response is modulated by the variation of the gate capacitance, and two main factors occur: i) the overall capacitor is composed of PDMS

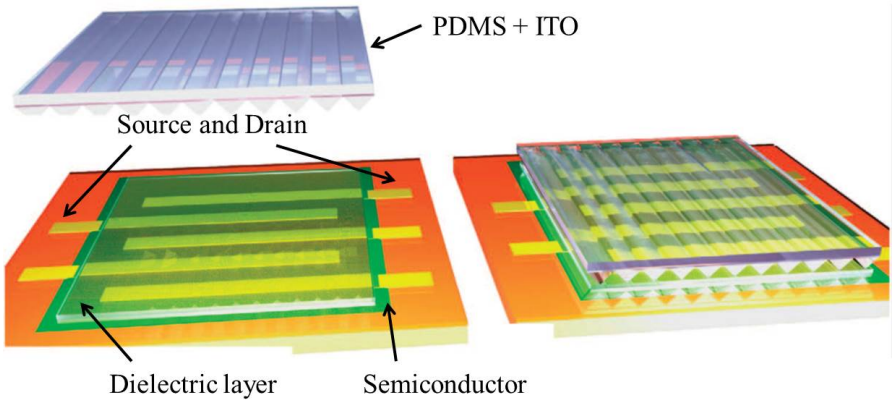

Figure 3.8: Schematic representation of the sensing structure reported in [15] and [16].

and air gaps, which far decrease the film elastic resistance, and ii) during compression, the displaced volume is air, whose dielectric constant (ε_r = 1.0) is lower than that of PDMS (ε_r ≈ 3.0). The pressure sensitivity, defined as the relative capacitance variation per unit pressure (ΔC%/P), had two different values according to the ranges considered: for low pressure range (< 1.5 kPa) the sensitivity was 0.55 kPa^{-1}, while for higher pressure range (> 2 kPa) the sensitivity decreased to 0.15 kPa^{-1}, probably due to the increasing elastic resistance with increasing compression. The calibration curve is shown in figure 3.9a. The sensitivity can be

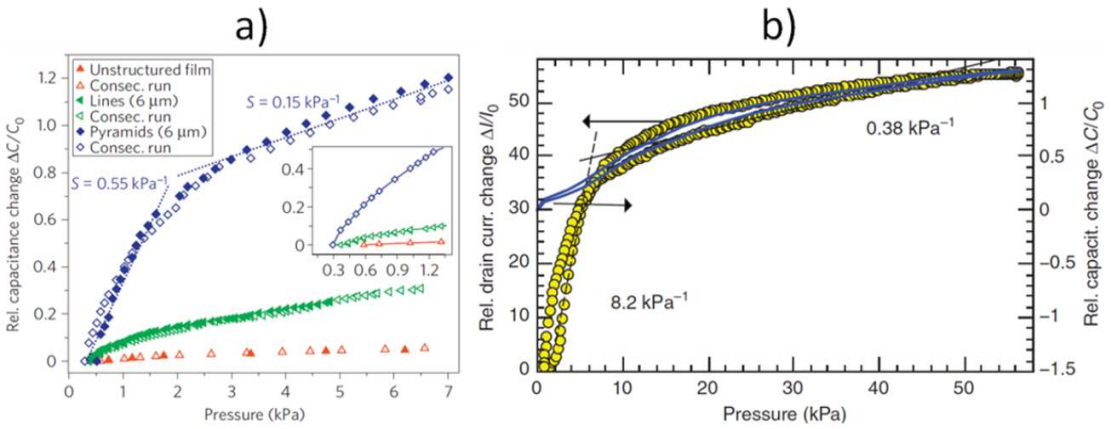

Figure 3.9: Sensitivity of the structure proposed in [15] and [16]: (a) as the relative variation of the gate capacitance and (b) as the relative variation of the drain current.

evaluated also from the relative variation of the drain current (ΔI_D%/P): in this case, as shown in figure 3.9b, the sensitivity in the low pressure range (< 5 kPa) was even higher with respect to the capacitance sensitivity, reaching the value 8.2 kPa^{-1}, while for the medium and high pressure range similar values were obtained (0.38 kPa^{-1}).

Employing a similar structure, Kim *et al.* realized a OFET having the gate capacitance modulated by an external pressure according to the dielectric shape [17]. Using *polyurethane* (PU), they created a mold formed of honeycomb structure with a very sharp nano-needle array, whose end had a radius of curvature around 10 nm and a height around 3 μm. In this case, as

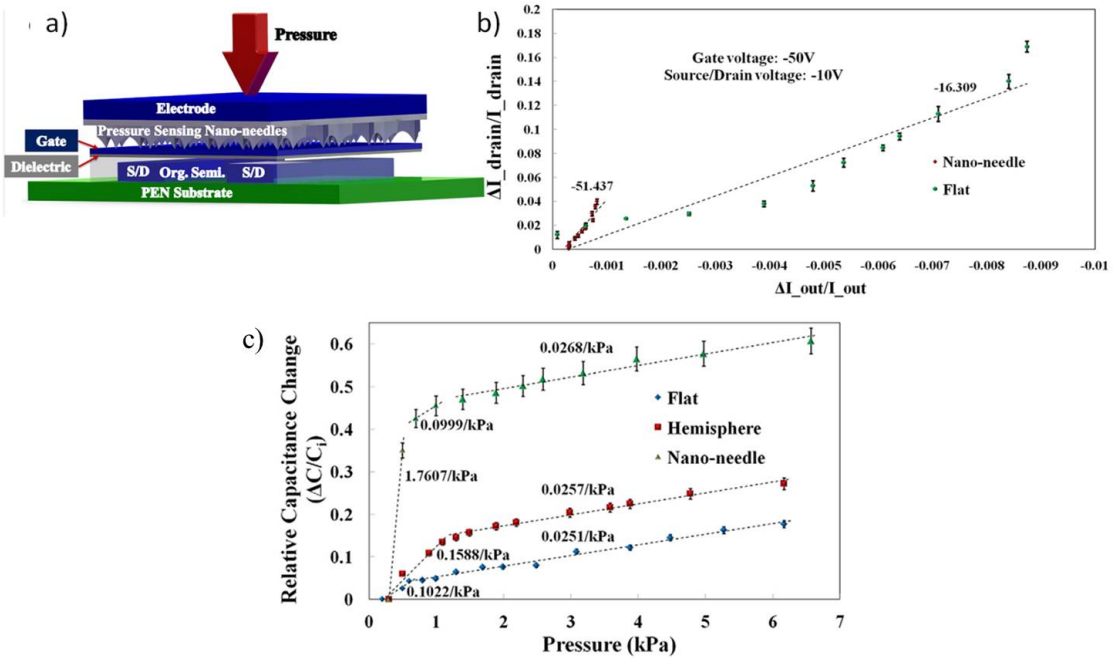

Figure 3.10: (a) Schematic and (b) current sensitivity of the structure proposed in [17]; in (c) the capacitance sensitivity is shown.

shown in figure 3.10a, the patterned PU was placed between a contact electrode and the gate electrode, thus adding a series capacitance to the gate. The OFET was realized in bottom-contact top-gate configuration, with Ag inkjet printed source and drain electrodes and PQT, a polythiophene-based p-type semiconductor, as active layer. The relative variation 3.10b of the drain current was measured versus the pressure applied, comparing the response to the honeycomb mold with that of a flat dielectric. Moreover, in 3.10c the sensitivity of the realized capacitor is shown. For pressure values above 1 kPa, a sensitivity of 0.026 kPa^{-1} was achieved, while in the low pressure range (< 1kPa) a sensitivity rose up to 1.76 kPa^{-1}.
Hsu *et al.* [18] used the gate capacitance as sensing variable but adopted a different strategy: they took advantage of the piezoelectric properties of PVDF-TrFE and used it in combination with parylene-C to form the gate dielectric. The schematic and the structure are shown in figure 3.11a and 3.11b respectively. The electromechanical characterization was carried on by means of a robotic actuator that induced regular and precise bending on the whole structure.

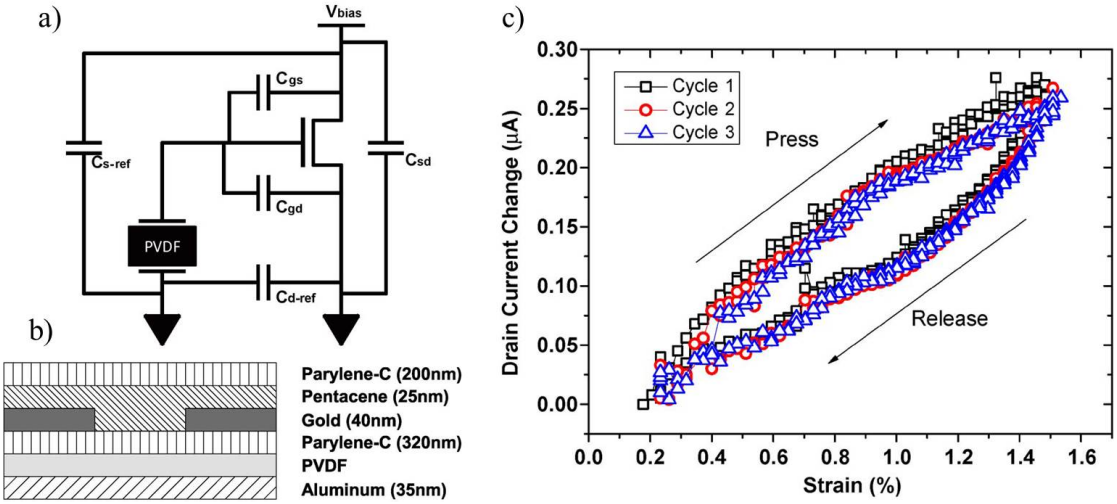

Figure 3.11: Schematic (a), structure (b) and response (c) of the device proposed in [18].

Therefore the sensitivity was defined as the drain current variation (ΔI_D) per unit strain (ε). The calibration of the device is shown in figure 3.11c, where three consecutive bending cycles were applied: despite the hysteresis, caused by charge relaxation, a good reproducibility and a sensitivity value of 0.182 μA/strain was achieved.

A major problem of all the previously reported structures is that the mechanical stimulus, *i. e.* the pressure, is directly applied to the OTFT: therefore the electromechanical performances can be degraded if the sensor is over-stimulated. To overcome this problem, Lai *et al.* [19] employed a new device structure, namely *Pressure-Modulated Organic Field-Effect Transistor* (PMOFET) in which the pressure-sensitive area is physically separated from the active area of the device. Basically, it consists of a floating-gate transistor biased through a control capacitor C_{CF} and through a variable capacitor C_V, made of PDMS, which acts as the sensing element. The structure is represented in figure 3.12a: the separation between the sensing area and the active are, thanks to the floating gate, allows the implementation of large-area sensing sheets without actually damage the readout active device. Figure 3.12b shows the sensitivity curves, defined as the $\Delta C\%/N$ and $\Delta I_D\%/N$: both have the same sub-linear trend, but the sensitivity of the current is higher due to the transistor effect.

The second type of approach, which consists in modulating the effective V_{DS} applied to an OFET, requires the employment of a conductive pressure sensor to be put in series with the source or drain electrode. The ideal candidates for this purpose are the conductive rubbers, which decrease their electrical resistance of several orders of magnitude when they are subjected to a pressure. Conductive rubbers are basically PDMS elastomers containing nanos-

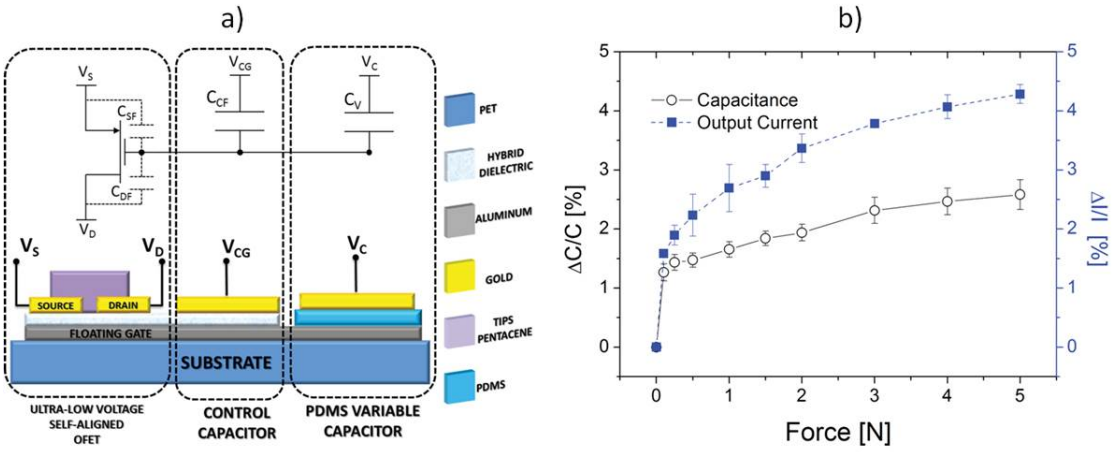

Figure 3.12: Schematic (a) and response (b) of the PMOFET [19].

tructures, such as metal or graphite nanoparticles, that maintain the high flexibility of the organic devices and therefore are suitable for pressure sensing over large area.

Someya *et al.* [20, 21] adopted this solution to create a matrix of 32x32 sensors over 8x8 cm^2. Figures 3.13a and 3.13b show the structure and some pictures of the proposed device. The OFET is realized on one side of a plastic substrate, while the rubber was laminated in the back side, where the mechanical stimulus is applied. A through hole creates the connection between the source electrode and the pressure-sensitive rubber. The device responses to pressure and to bending applied are shown in figures 3.13c and 3.13d, respectively. Starting from an unstressed condition, increasing pressures (from 10 to 30 kPa) and decreasing bending radii (from 15 to 2 mm) were applied, which resulted in a remarked current variation. The variation of the rubber resistance, from 1 MΩ to 1 kΩ, affected the drain current and showed a clear trend. The bottom limit for the bending radius was estimated to be 1 mm, since for lower values the gold electrodes crack.

Taking advantage of the same architecture, Takei *et al.* [22] fabricated an OFET with Ge/Si nanowires as semiconductor and a rubber with carbon nanoparticles. Figure 3.14a shows the transfer characteristics under different pressures applied: a clear response to mechanical stimuli is noticed, since the actual V_{DS} applied to the OFET increases as the series variable resistance decreases. The sensitivity, defined in this case as the conductance variation per unit pressure, is represented in figure 3.14b: the low pressure regime shows an exponential dependence of the current on the applied stimulus, while for higher pressures the dependence is linear, with a sensitivity around 11.5 μS kPa^{-1}. This reduced sensitivity for in the medium pressure range is due to the reduced elastic modulus of the rubber.

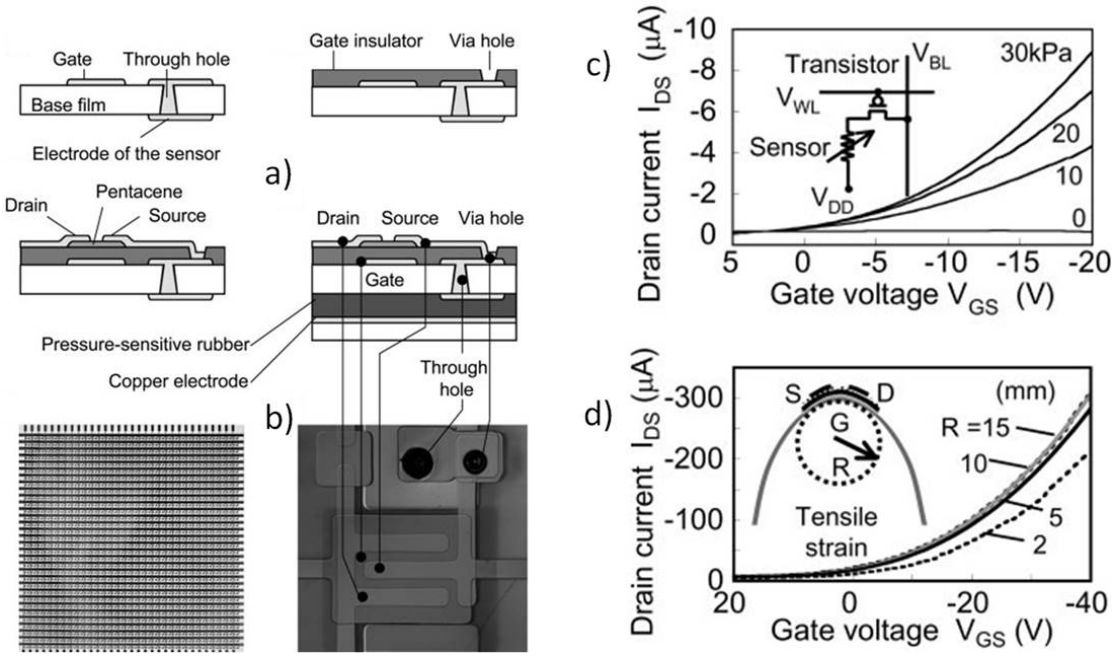

Figure 3.13: Device structure (a), pictures (b) and calibration (c)-(d) of the sensor proposed in [20, 21].

3.1.2 Direct mechanical sensing with Organic Field-Effect Transistors

Beyond their employment as amplifiers for the sensing element, OFETs can be used also as strain sensors themselves. In fact, the electrical stability of organic semiconductors during mechanical deformation constitutes a big issue for the realization of highly flexible electronic circuitry, since a pronounced variation of charge transport properties in OFETs occurs during mechanical stress.

One of the first studies on this issue was realized by Sekitani *et al.* [129]. In their investigations they demonstrated that by applying a tensile (compressive) stress in Pentacene-based OFETs a pronounced decrease (increase) of the device output current was observed. They stated that this phenomenon can be attributed to a variation of the morphological and/or structural properties of the polycrystalline semiconductor film induced by the applied mechanical stress. In fact, at the micro-scale, a tensile strain could lead to an increase of the distance between grains in the channel of the devices, whereas, at the nano-scale, it could also be possible to induce an increase of the lateral spacing between the molecules, thus affecting the π-stacking in the film. In both cases, the immediate consequence should be a reduction of the hopping probability for charge carriers, thus leading to a lowering, as experimentally observed, of the channel mobility. On the contrary, an increase of the channel

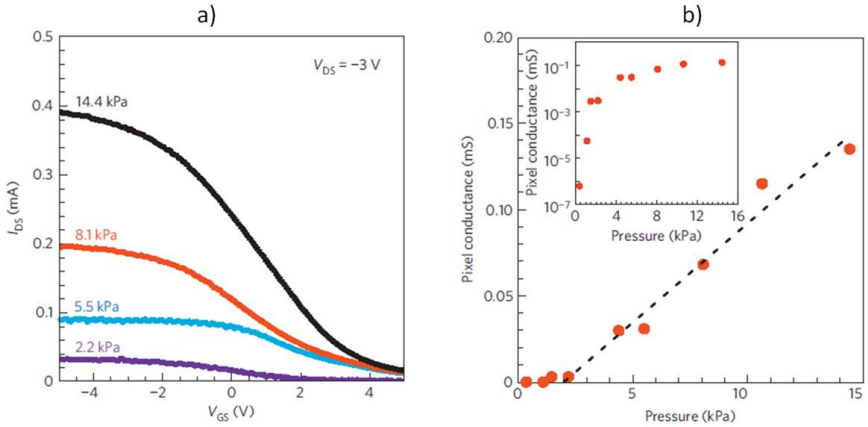

Figure 3.14: Transfer characteristics (a) and sensitivity (b) of the device proposed in [22] under different pressures applied.

mobility is obtained when a compressive strain applied induces a decrease of the distance between grains. The situation is schematized in figure 3.15.

The correlation between strain induced, ε, and bending radius, r, is explained in [130] and employed in [24] as follows. The rigorous strain is described by the following formula:

$$\varepsilon = \left(\frac{d_l + d_s}{2r}\right) \cdot \frac{\left(1 + 2\eta + \chi\eta^2\right)}{\left(1+\eta\right)\left(1+\chi\eta\right)} \tag{3.1}$$

where d_l is the thickness of the active layer, d_s is the thickness of the substrate, $\eta = d_l/d_s$, and $\chi = Y_l/Y_s$ is the ration between the Young's moduli of the active layer and the substrate, respectively. Considering that the substrate is about two orders of magnitude thicker than the active layer, the surface strain induced on the active layer can be approximated by:

$$\varepsilon = \left(\frac{d_s}{2r}\right) \tag{3.2}$$

Analogous results are found in other studies, for examples by Yang *et al.* [131] and by Scenev *et al.* [23]. In particular, the latter found that tensile stress induces a stretching of the pentacene film morphology, thus increasing the distance between adjacent domains within the active channel, as shown in figure 3.16. This, again, could very well explain the reduction of the carriers mobility observed in the electromechanical characterization of the fabricated OFETs.

A deeper investigation on the correlation between morphological structure and strain sensitivity was carried on by Cosseddu *et al.* [24]. They initially deposited a pentacene layer by

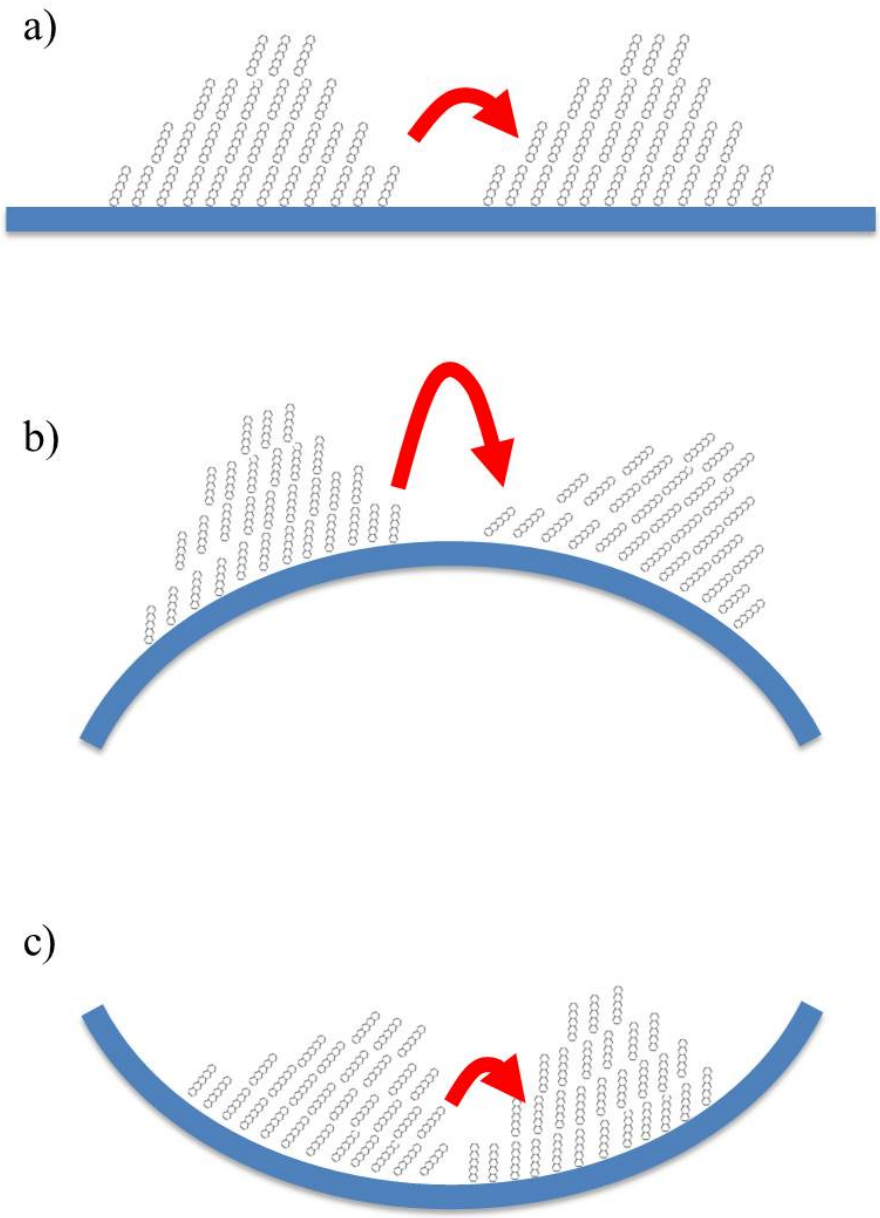

Figure 3.15: Variation of the morphological structure of a pentacene layer: (a) with flat substrate, (b) tensile-strained substrate, and (c) compressive-strained substrate.

thermal evaporation as active layer of OFETs, and by AFM they investigated the correlation between between deposition rate and grain size, shown in figure 3.17. Then, they performed an electromechanical characterization of two selected devices, thus demonstrating a clear correlation between deposition rate, grain size and mechanical sensitivity (figure 3.18).

Other studies have been carried on by several groups [132–134]: a careful reading is recommended for a better comprehension of this phenomenon. However, since several publication

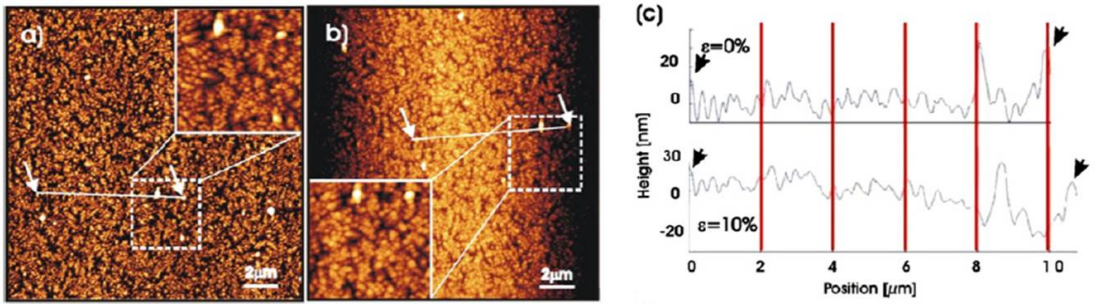

Figure 3.16: AFM micrographs of a pentacene thin film before (a) and during (b) bending, and the relative cross section showing the morphological changes induced by mechanical deformation [23].

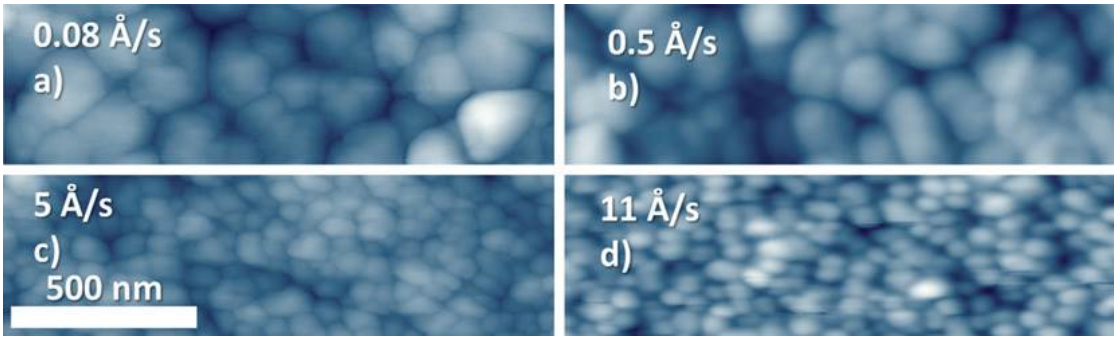

Figure 3.17: AFM micrographs of different pentacene films deposited at different deposition rates [24].

have demonstrated that this behavior is very reproducible and recoverable within a certain range of mechanical deformation, several structures, and in particular OFETs, have been developed as strain sensors.

One of the first examples was reported by Rang *et al.* [135]. The authors have investigated the hydrostatic-pressure dependence of I-V curves in organic transistors and found a large and reversible dependence of drain current and hole mobility on hydrostatic pressure, suggesting that this kind of device could be suitable for sensor applications. A different approach was used by Darlinsky *et al.* [25]. They employed OFETs as force sensors by applying a controlled force on the device area using a micro-needle controlled by a step motor. Two different configuration were designed for the sensors, depending on the channel length. In this way they managed to apply the force directly on the channel area (for large channel devices, as shown in figures 3.19a and 3.19c) or simultaneously on the channel and on the source and drain electrodes, as represented in figures 3.19b and 3.19d. These two setup resulted in different electrical responses. In particular, no significant change in the electrical characteristics

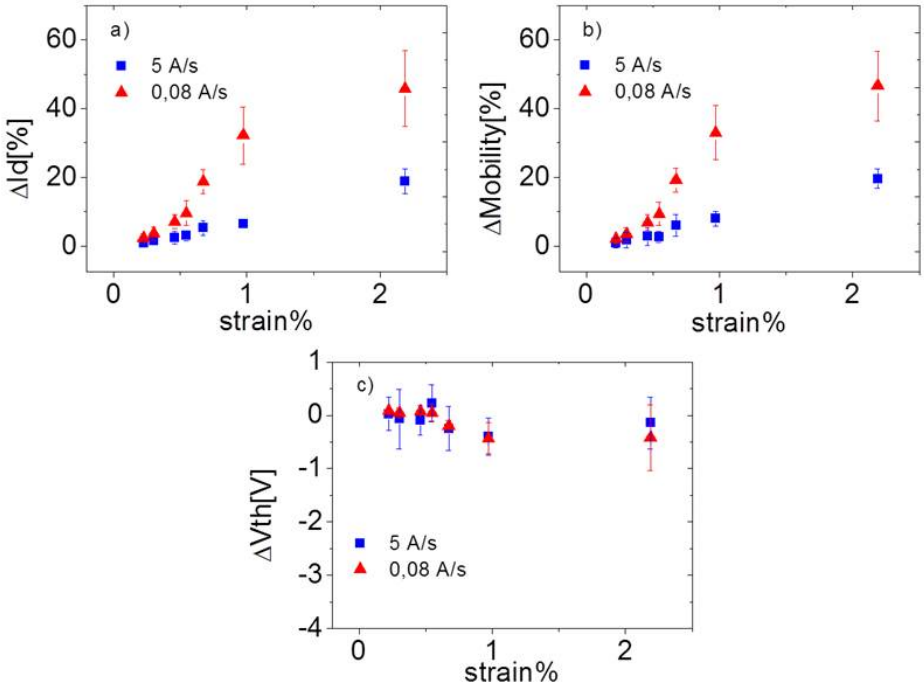

Figure 3.18: Average current (a), mobility (b) and threshold voltage (c) variation measured in two sets of transistors fabricated using different pentacene deposition rates.

was observed for the first case, when the force was exerted only in the channel area; on the contrary, a marked difference was observed for the short-channel device. This behavior was attributed to a possible activation of trap states at the dielectric/semiconductor interface induced by the applied mechanical stimulus.

The active organic semiconductor layer was also used as resistive element of a strain gauge in a Wheatstone bridge structure, as reported by Jung *et al.* [136]. Another device configuration was developed by Manunza ET AL. [137, 138]. They fabricated highly flexible OFETs on a 1.5 μm thick PET foil, namely Mylar®, which acted at the same time as gate dielectric, but also as extremely flexible substrate for the entire device structure, and using pentacene as the organic semiconductor. They found a marked and reproducible response of the device to the applied pressure. Moreover, this response was found to be linear in the range 0-10 kPa of applied pressure, thus suggesting a possible employment of this kind of devices for practical applications: monitoring bio-mechanical parameters, such as breath rhythm or joints motion, wearable electronics, and tactile transduction for the realization of artificial robot skin, which has been developed for this thesis [139].

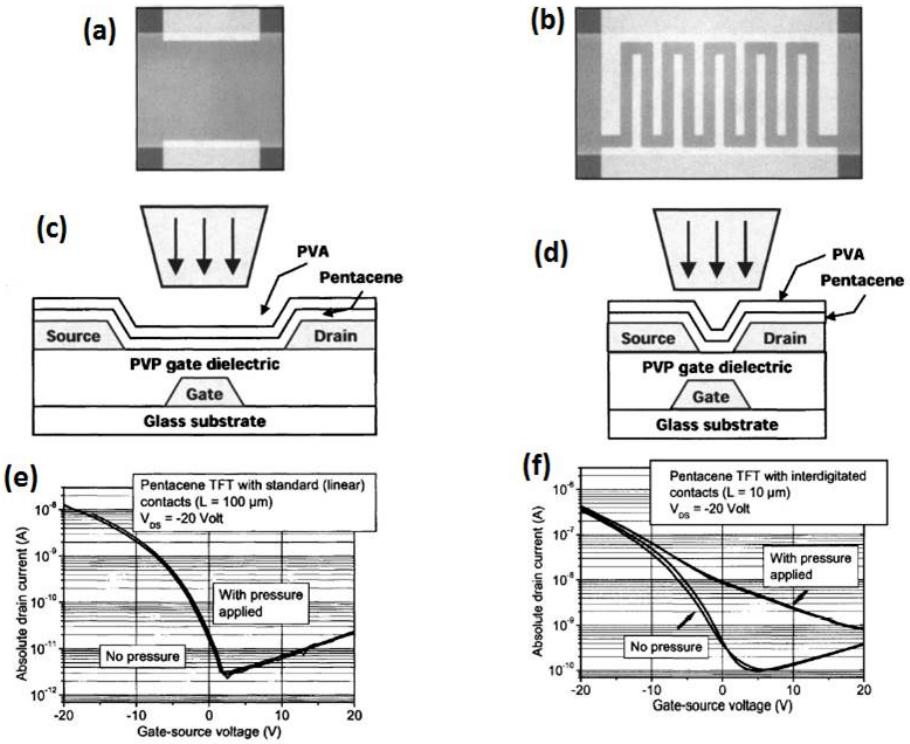

Figure 3.19: Optical images (a, b), cross sections (c, d), and response to the applied force (e, f) of the different devices fabricated in [25].

3.2 Fabrication and characterization of Organic Field-Effect Transistors

In this section an overview on the fabrication and the electrical characterization of Organic Fiel-Effect Transistors (OFETs) is given. In the first part, a step-by-step description of the OFET structure is presented. Since various semiconductors have been employed, and deposited in different ways, the electrical characterization is given individually for each semiconductor employed. The last part of this section focuses on the inkjet printing of TIPS-pentacene and describes the experiments carried on this issue.

3.2.1 Inkjet printing of OFET structures

All the OFETs of this work have been realized in bottom-gate bottom-contact configuration (read section A.2 for further details) and almost all the electrodes have been realized by inkjet printing of CCI-300 silver ink, presented in sections 2.3 and 2.4. On the other hand, the active layer has been deposited in several ways and with several semiconductors: pentacene, ActivInk™ N1400, and especially TIPS-pentacene, in all the formulations described in the

previous chapter.

Figure 3.20 represents the steps adopted to realize the OFET structures, while figure 3.21

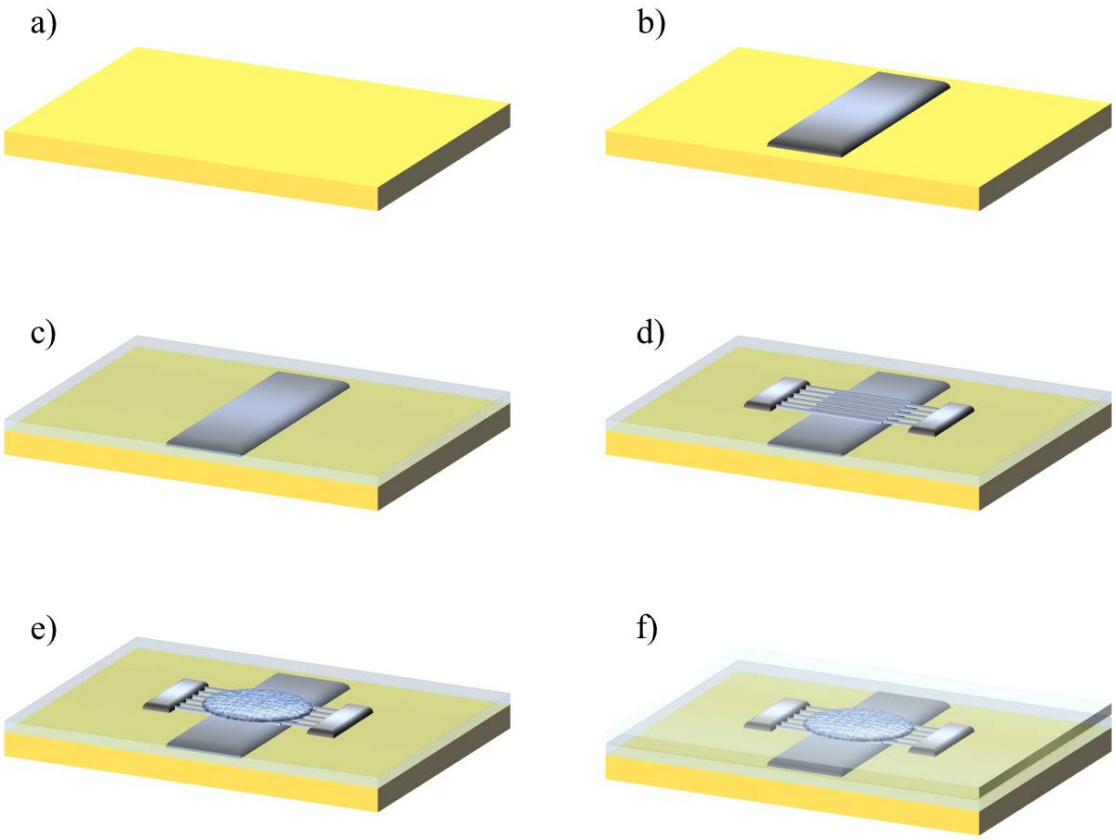

Figure 3.20: Steps for the fabrication of an OFET: (a) substrate, (b) gate deposition, (c) dielectric deposition, (d) source and drain deposition, (e) semiconductor deposition, and (f) encapsulation.

shows a picture of the final structure. Each step is described in the followings:

a) As first step, the substrate is cut out and cleaned with subsequent cycles of acetone, isopropyl alcohol and distilled water, and then dried by means of a nitrogen flow. For very thin substrates, such as 13 μm Kapton, only the nitrogen flow was performed in order to remove powder from the surface. The the substrate is blocked upon the DMP2831 platen with adhesive tape as flat as possible, in order to avoid movements caused by the carriage run.

b) The gate is printed, usually with CCI-300 silver ink. This is a low-resolution pattern, since the typical pattern is composed of 2·3 mm^2 rectangles, and the conductive traces are no less wide than 500 μm. In one case, the gate was made of evaporated Aluminum in

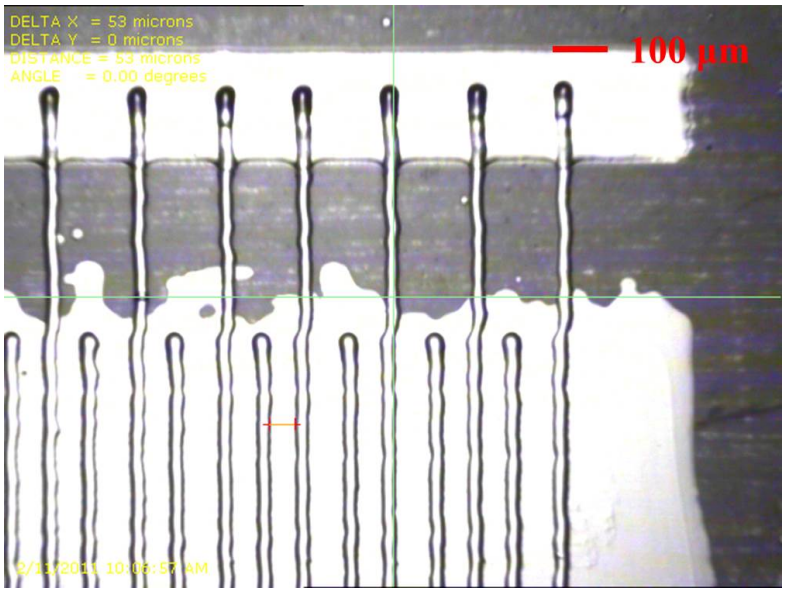

Figure 3.21: Picture, taken by the DMP2831 fiducial camera, of a printed OFET electrodes.

order to realize a thin gate dielectric to obtain low-voltage devices.

c) The gate dielectric, parylene-C, is deposited by chemical vapor deposition. Before depositing parylene, a layer of Silane A174 was deposited on gate in order to promote adhesion of the insulating layer on the metallic electrode. The thickness of the parylene-C layer was set to 1.4 μm in order to prevent high leakage currents caused by fractures and/or pinholes, with a resulting gate capacitance of 2.1 nF/cm^2.

d) After cleaning the substrate with a nitrogen flow, the source and drain electrodes are deposited by means of inkjet printing, using CCI-300. In the work related to this thesis most of the source and drain electrodes have been realized in interdigitated configuration, with an average channel length L of 50 μm and a total width W of 50 mm; thus the shape factor W/L was 1000. This is the most awkward and tricky step of all due to the high probability of short circuits or discontinuities if the printing parameters, described in section 2.4.1, are not fulfilled.

e) After another substrate cleaning with nitrogen flow, the semiconductor is deposited in the channel region by means of thermal evaporation, drop casting, spin coating or inkjet printing.

f) In necessary, another layer of Parylene-C is deposited to pretect the active layer from chemical and mechanical damaging. The thickness, in this case, is usually set to 2.5

μm.

The overall fabrication time strongly depends on the substrate employed, since it automatically set the annealing temperature: with Kapton the temperature can be set at 100 °C and the total fabrication takes 2-3 days, while if PET is used the maximum annealing temperature is 60 °C and the process takes 5-6 days at least.
The electrical characterization for each semiconductor employed is shown in the followings.

Drop-casted TIPS-pentacene

The standard procedure to deposit the active layer of an OFET is drop casting a TIPS-pentacene solution, typically the TIPS1 formulation described in section 2.5.1. A small quantity, around 1 μL, is sufficient to cover the channel area of each transistor. During the drop casting, the substrate is put on a hot plate at 90 °C in order to promote fast solvent evaporation and good molecular assembly. Then, a post-deposition annealing is carried on by means of an hot plate or a oven, at 90 °C for 15 min. The output and the transfer characteristics are shown in figures 3.22a and 3.22b respectively.

The TIPS-pentacene has been the most employed semiconductor in this work: the continuous improvement of the inkjet printing technique resulted in even better electrical performances of the final transistor. From the output characteristic, some general considerations can be done:

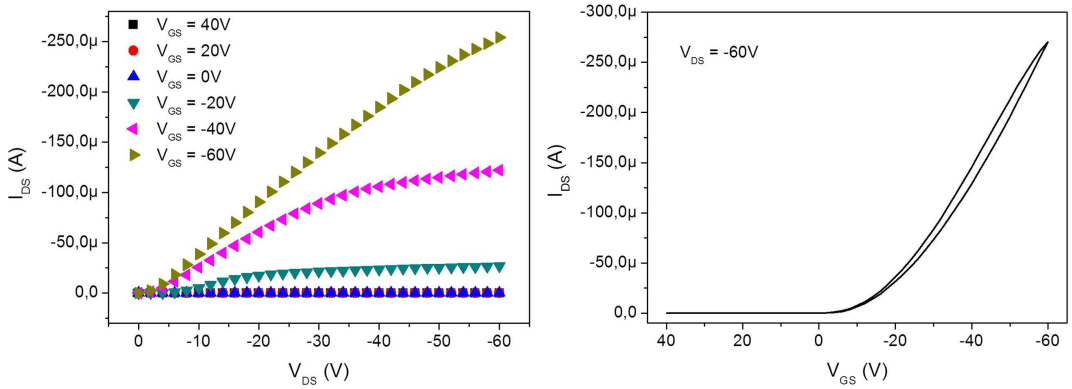

(a) (b)

Figure 3.22: Output (a) and transfer (b) characteristics of an OFET realized with drop-casted TIPS-pentacene.

- A good field effect is obtained for gate voltage V_{GS} lower then 0 V, while for upper values the resulting drain current I_{DS} is negligible.

- The saturation regime is reached for low and medium gate voltages (V_{GS} = -20 V and V_{GS} = -40 V), while for high voltages (V_{GS} = -60 V) only a beginning of the saturation regime is noticed.
- A high contact resistance is evident from the beginning of the output characteristic (V_{DS} > -10V), for every V_{GS} value: this is due to the energy barrier between the work function of the CCI-300 silver ink and the HOMO of the TIPS-pentacene.

Moreover, from the transfer characteristic, a reduced hysteresis can be noted. The achieved mobility μ was $(7\pm3)\cdot10^{-2}$ $cm^2V^{-1}s^{-1}$, with top values of $1-2\cdot10^{-1}$ $cm^2V^{-1}s^{-1}$, the threshold voltage V_T was -1.7 ± 1.6 V and the I_{ON}/I_{OFF} ratio was $8\cdot10^4$, and in several cases over 10^5.

Pentacene

Pentacene was thermally evaporated on the OFET structure, with a shadow mask which allow the deposition only in the channel region. The output and the transfer characteristics are shown in figures 3.23a and 3.23b respectively. In this case, a reduced contact resistance

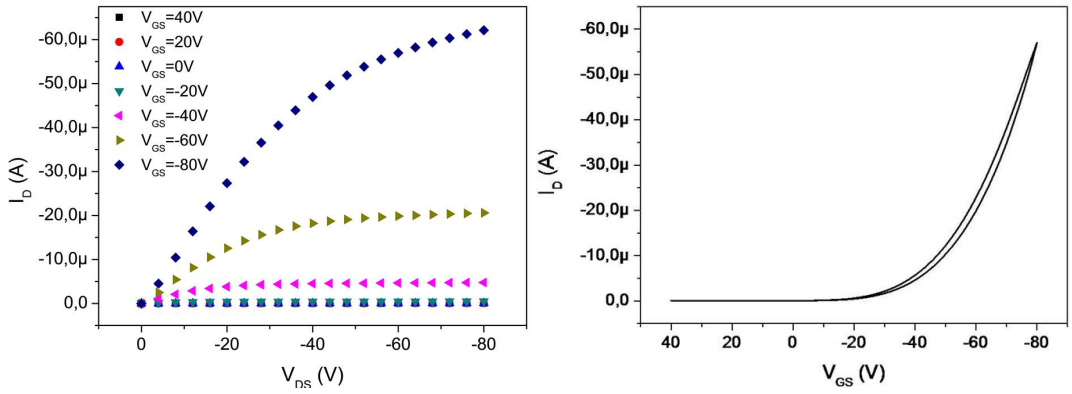

(a) (b)

Figure 3.23: Output (a) and transfer (b) characteristics of an OFET realized with evaporated pentacene.

is noted, while the average current is lower. The achieved mobility μ was $(8.3\pm1.8)\cdot10^{-3}$ $cm^2V^{-1}s^{-1}$, the threshold voltage V_T was -25.1 ± 0.8 V and the I_{ON}/I_{OFF} ratio was $(7.8\pm1.9)\cdot10^3$.

ActivInk™ N1400

This solution was prepared at 1 wt.% in dichlorobenzene and stirred at 90 °C for 15 min. Then it was deposited by spin coating (1500 rpm for 60 s). The output and the transfer characteristics are shown in figures 3.24a and 3.24b respectively. The achieved mobility μ was

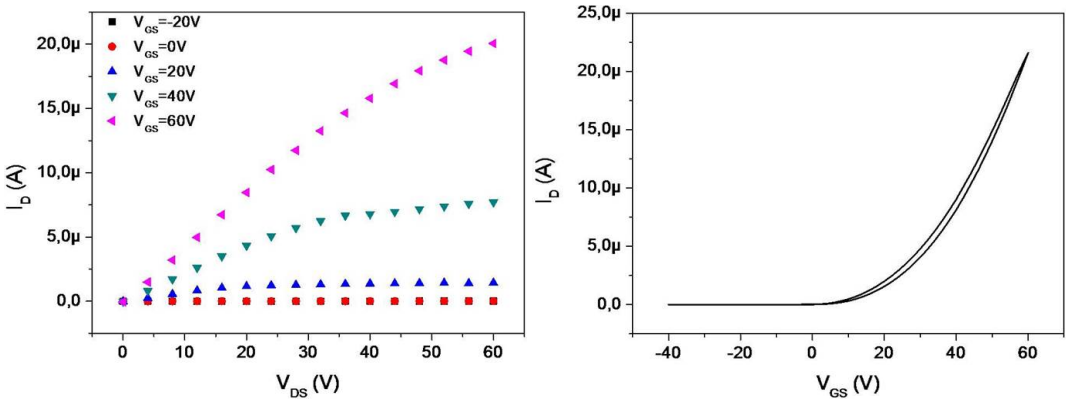

(a) (b)

Figure 3.24: Output (a) and transfer (b) characteristics of an OFET realized with spin coated N1400.

$(3.7 \pm 0.8) \cdot 10^{-3}$ $cm^2V^{-1}s^{-1}$, the threshold voltage V_T was 5.7 ± 0.2 V and the I_{ON}/I_{OFF} ratio was $1.59 \cdot 10^3$.

3.2.2 Inkjet printing of TIPS-pentacene

The experiments carried on the inkjet printing of TIPS-pentacene, described in the followings, are the continuation of the study performed by Laura Basiricò [140]. When a semiconductor is deposited by inkjet printing, two different approaches can be used:

1. *Multiple drops.* Several drops are printed on the substrate, and the drop spacing is set in order to have a good overlapping between them: the result is a continuous layer which cover the whole channel region.

2. *Single droplet.* Only one droplet is deposited on the substrate. If more drops are deposited, the drop spacing must be set much higher then the drop diameter, in order to obtain separated individual drops.

In the followings, the investigation carried on for each on of these approaches is presented.

Multiple drops approach

The *multiple drops* approach, as stated before, consists of printing multiple overlapping drops which form a continuous layer [141, 142].

In the first experiments, TIPS-pentacene, with *TIPS2* formulation (see section 2.5.1), was inkjet printed on evaporated gold drain and source electrodes with two different drop spacing: 30 μm and 50 μm. This formulation, with high TIPS-pentacene concentration, has been

chosen since with the standard formulation (*TIPS1*) too small amount of material was deposited.

Figure 3.26 shows an imagine, taken by means of the DMP2831 fiducial camera, of the

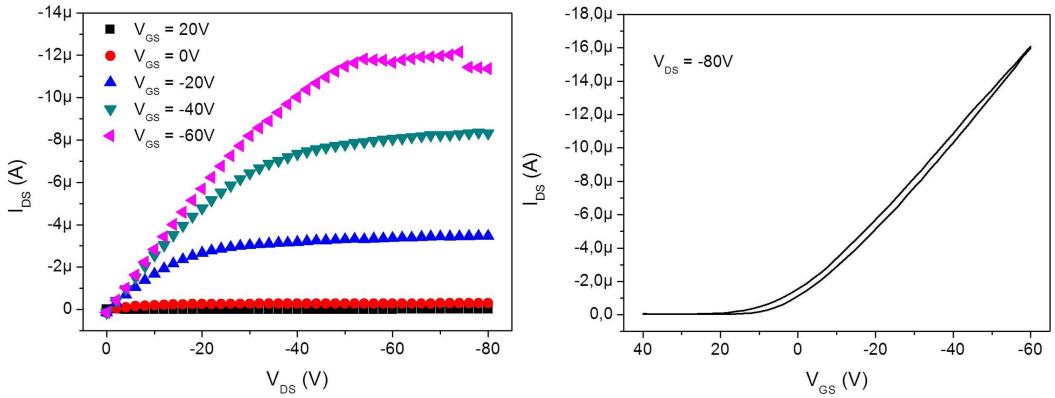

Figure 3.25: Output (a) and transfer (b) characteristics of an inkjet printed TIPS2 ink with 30 μm drop spacing.

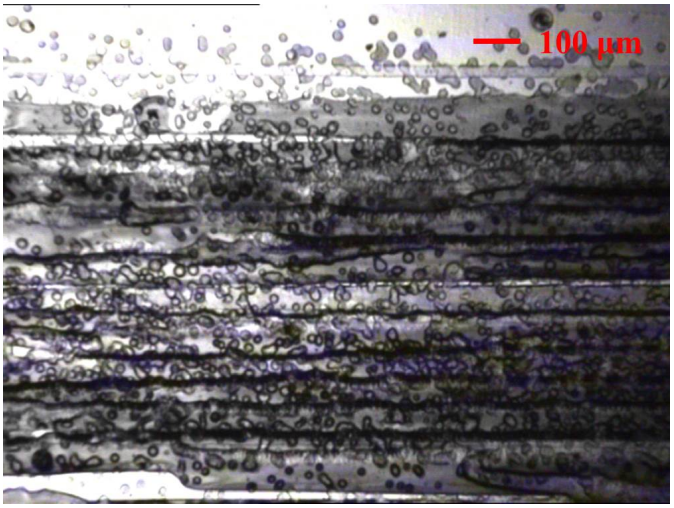

Figure 3.26: Picture of the TIPS2 inkjet printed on gold electrodes with 30 μm drop spacing.

printed layer with 30 μm drop spacing, while in figures 3.25a and 3.25b the output and the transfer characteristics of the resulting transistor are presented. The electrical behavior of these transistors was quite good but not reproducible, since the printing performances rapidly degrades due to nozzle clogging. The achieved mobility μ was $0.95 \cdot 10^{-2}$ $cm^2V^{-1}s^{-1}$, the threshold voltage V_T was 24 V and the I_{ON}/I_{OFF} ratio was $1.9 \cdot 10^3$.

Figure 3.28 shows an imagine, taken by means of the DMP2831 fiducial camera, of the

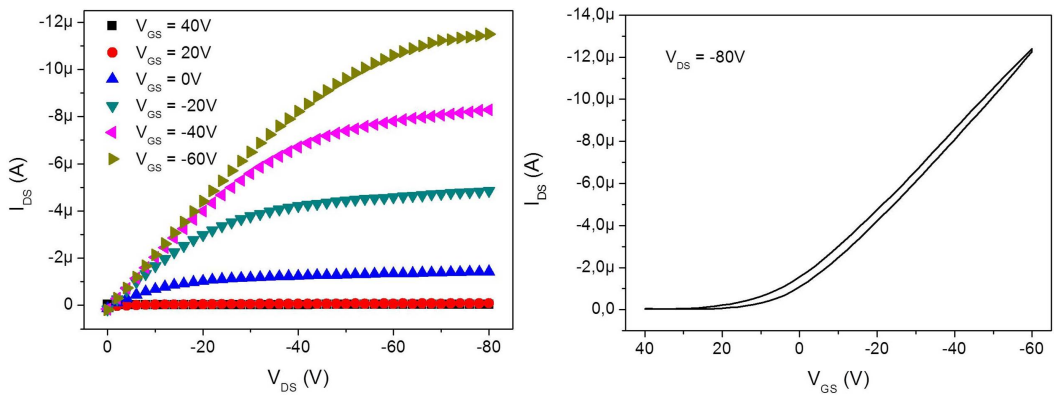

(a) (b)

Figure 3.27: Output (a) and transfer (b) characteristics of an inkjet printed TIPS2 ink with 50 μm drop spacing.

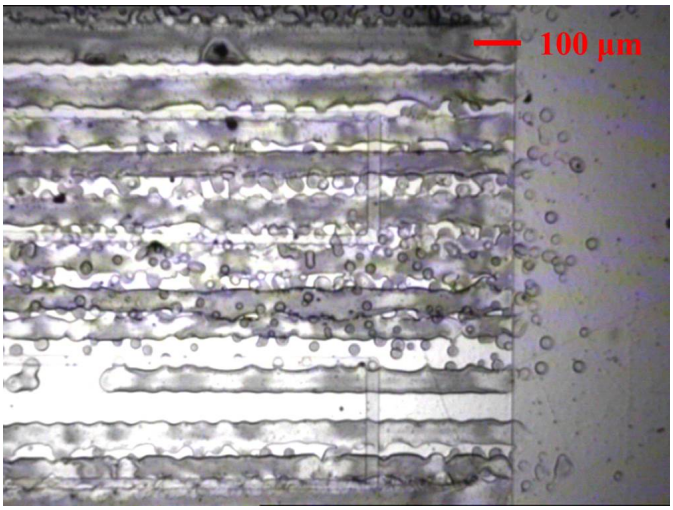

Figure 3.28: Picture of the TIPS2 inkjet printed on gold electrodes with 50 μm drop spacing.

printed layer with 50 μm drop spacing, while in figures 3.27a and 3.27b the output and the transfer characteristics of the resulting transistor are presented. As expected, the electrical performances are slightly decreased since a lower amount of material per unit area is deposited in this case. The achieved mobility μ was $3.2 \cdot 10^{-3}$ $cm^2V^{-1}s^{-1}$, the threshold voltage V_T was 22 V and the I_{ON}/I_{OFF} ratio was $4.9 \cdot 10^2$.

In a second set of experiments, the ink formulation included also polystyrene (PS) to form blends, as described in the previous chapter. At first, the TIPS-pentacene concentration was set at 0.5 wt.% and the PS was varied in order to obtain TIPS:PS blends in the following ratios: 1:0, 1:1, 1:2, 1:3. Table 3.1 reports the measured viscosity for these formulations. Unfortunately, the low amount of material and the effect of PS resulted in a very poor electri-

Anisole	TIPS-pentacene	Polystyrene	Viscosity
99.5 wt.%	0.5 wt.%	0.0 wt.%	1.27 cP
99.0 wt.%	0.5 wt.%	0.5 wt.%	1.70 cP
98.5 wt.%	0.5 wt.%	1.0 wt.%	2.35 cP
98.0 wt.%	0.5 wt.%	1.5 wt.%	3.21 cP

Table 3.1: Viscosity measurements for inks composed of blends of TIPS-pentacene and polystyrene.

cal behavior, with no field-effect noticed.

Therefore, the TIPS-pentacene concentration was set to 2.5 wt.% and the TIPS:PS ratio to 1:1: this formulation, previously named *TIPS3*, had a measured viscosity of 4.89 cP, quite good for printing purpose. Unfortunately, the electrical performance was not good, maybe due to the bad crystallization of the semiconductor. Figure 3.29 shows the transfer characteristic of

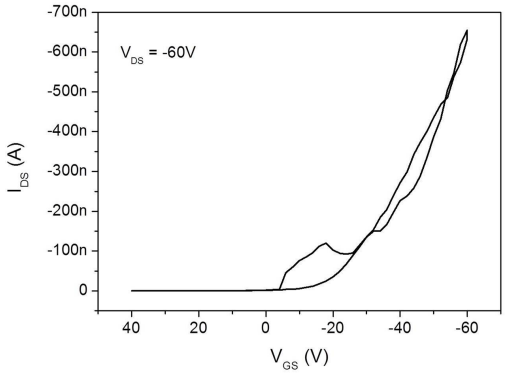

Figure 3.29: Transfer characteristic of the inkjet printed TIPS3 ink with 20 μm drop spacing.

an OFET realized with inkjet printed TIPS3 ink with 20 μm drop spacing. Very low current values and a sharp characteristic can be noted. The achieved mobility μ was $(3.6 \pm 1.5) \cdot 10^{-4}$ $cm^2V^{-1}s^{-1}$, the threshold voltage V_T was -18 ± 7 V and the I_{ON}/I_{OFF} ratio was $4.1 \cdot 10^2$.

Moreover, the same ink was inkjet printed on a different substrate, with aluminum gate, thin dielectric and inkjet printed silver source and drain electrodes. The resulting OFET operates at low voltages, due to the increase gate capacitance. Figures 3.30a and 3.30b show the output and the transfer characteristic of a low-voltage OFET realized with inkjet printed TIPS3 ink with 20 μm drop spacing. The response, even if still poor, is better than the previous case. An increase of the off current can be noted, which leads to a poor on/off ratio. The achieved mobility μ was $(5.5 \pm 1.5) \cdot 10^{-3}$ $cm^2V^{-1}s^{-1}$, the threshold voltage V_T was 22 ± 8 V and the I_{ON}/I_{OFF} ratio was $4.4 \cdot 10^1$.

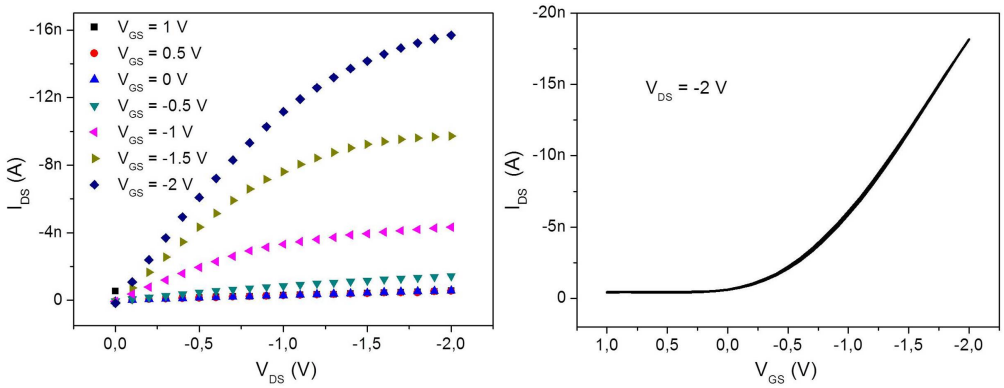

(a) (b)

Figure 3.30: Output (a) and transfer (b) characteristics of a low-voltage OFET realized with inkjet printed TIPS3 ink with 20 μm drop spacing.

Single droplet approach

The *single droplet* approach, already adopted in [140], can be defined as a controlled drop casting which employs picoliter-scale volumes. The recrystallization problems, which limit the mobility in the multiple drops approach, here are avoided, since a single droplet dries off without contacting other drops. However, other effects related to this approach could limit the electrical performance of the final transistor, especially the coffee-stain effect described in section 2.2.5. The drop diameter of TIPS-based inks was approximately 50 μm, a value

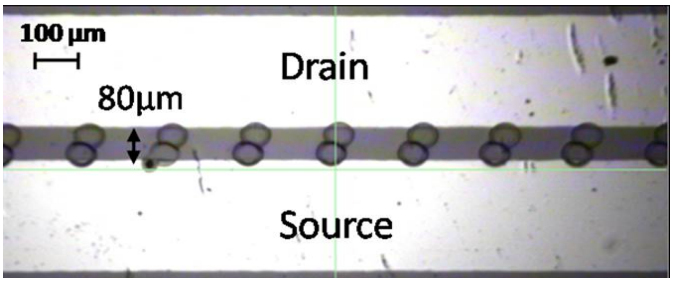

Figure 3.31: Single droplet approach employing two adjacent droplets to cover the channel length.

comparable or lower than the average channel length. As a consequence, the drop rarely can cover the whole channel length and, even when it can, the drop boundaries have only a reduced overlapping with the source and drain electrodes of the OFET. The resulting coffee stain effect is supposed responsible for the low charge-carrier mobility compared to the standard drop casting. A possible solution to partially reach the total coverage of the channel

region was adopted in [140] and is presented in figure 3.31. However, this solution does not account for the boundary effects.

Table 3.2 shows a comparison between the electrical performances obtained, by various re-

Ref.	Volume (pL)	PS Blend	μ ($cm^2V^{-1}s^{-1}$)	V_T (V)	I_{ON}/I_{OFF}
[6]	40	no	10^{-2}	-10	10^6
[141]	30	no	0.24	-2	10^7
[143]	50	no	0.48	0	10^7
[142]	80	1:1	0.046	-20	10^4
[144]	10	no	0.02	-1.2	10^4
[145]	50	4:1	1	0	10^7
[146]	40	no	0.44	0.64	10^7
[127]	40	1:1	0.19	-0.1	10^6
[147]	40	1:4	0.53	-0.7	10^6

Table 3.2: Comparison between the electrical performances obtained in literature with the single droplet approach.

search groups, adopting the single drop approach. Beyond the employment of a blend with polystyrene (PS), one of the major characteristics is that the drop volume, in almost all the cases, is much bigger than that obtained with the DMP2831 (10 pL). As a consequence, the resulting drop spreads well over the channel region with a good overlapping on the source and drain electrodes.

To achieve this aim, a collaboration with *Ente per le nuove tecnologie, l'energia e l'ambiente* (ENEA), a research center based in Portici, Naples, was activated. By means of a micro-drop inkjet printer (MDP), provided by Aurel Automation s.p.a. [148], 40-50 pL drops can be printed from a single nozzle. Moreover, this printer allows the possibility to print multiple drops in the same position at frequencies as high as 100 Hz. When a TIPS-pentacene droplet is printed on a kapton substrate, the resulting diameter is higher than 200 μm (figure 3.32), thus a good coverage of the channel region can be obtained.

In a preliminary set of experiments, single droplets were deposited adopting the formulation TIPS1. The realized transistors had a linear channel fabricated by inkjet printing silver electrodes and employing parylene-C as dielectric. The resulting droplet is shown in figure 3.34, while the output and the transfer characteristics are presented in figures 3.33a and 3.33b respectively. The curves show a standard trend of the TIPS-pentacene active layer, with a contact resistance and a good field effect. The achieved mobility μ was $2.9 \cdot 10^{-3}$ $cm^2V^{-1}s^{-1}$, the threshold voltage V_T was -4.22 V and the I_{ON}/I_{OFF} ratio was $5.93 \cdot 10^4$. The mobility

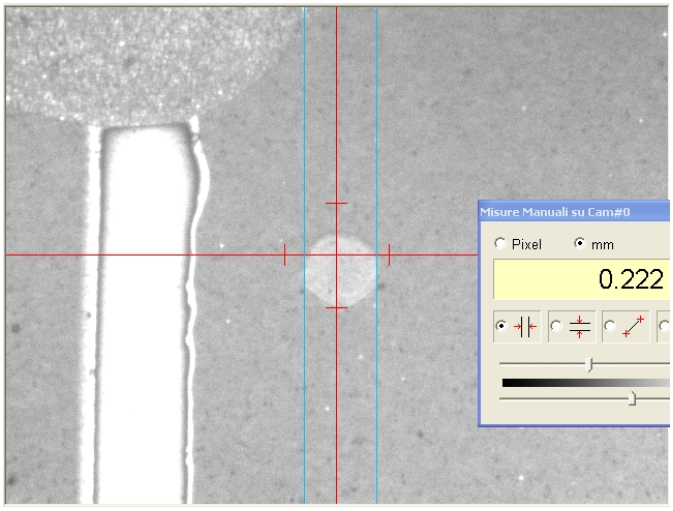

Figure 3.32: Single droplet printed with the MDP: a volume of 40 pL results in a diameter of 222 μm.

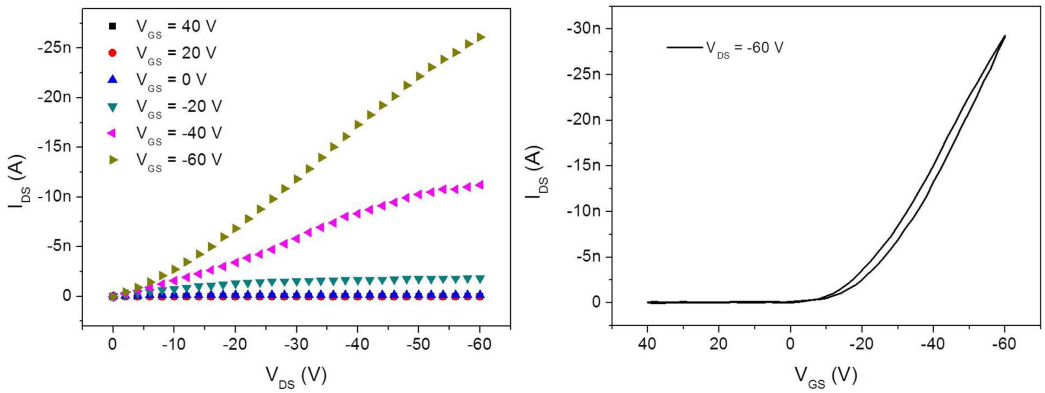

(a) (b)

Figure 3.33: Output (a) and transfer (b) characteristics of an OFET realized with inkjet printed TIPS1 with single droplet approach, employing one layer.

value is in the same order of magnitude as the mobility achieved with the DMP2831, thus indicating that the electrical performance does not depend on the coffee stain. A further profilometry investigation, reported in figure 3.35, confirmed that the drop entirely covers the channel length. The average drop height ranges between 400 and 600 nm. From figure 3.34 the printed droplet appears to spread preferably on the channel region, *i. e.* on the parylene substrate, more than on the metallic electrodes.

Starting from the latter consiederation, a second set of experiments involved the self-assembled monolayers FTP and 5FTP presented in section 2.3.6. The resulting surface energies are presented in table 3.3. From the values reported, treatment with FTP could lead to a similar

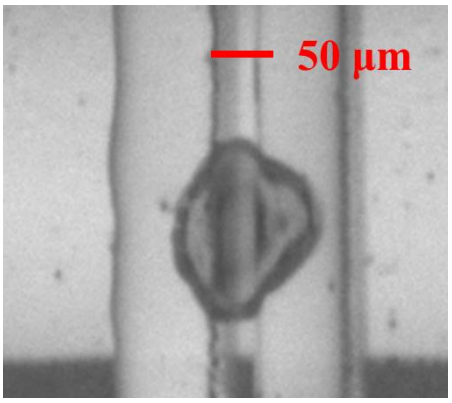

Figure 3.34: Single droplet printed on the channel of an OFET.

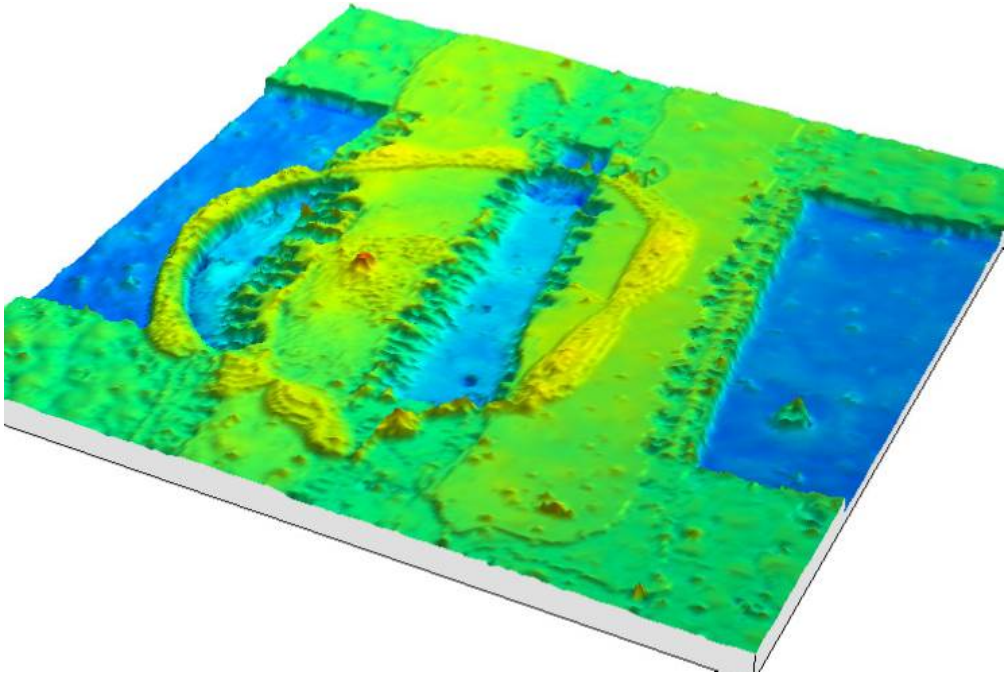

Figure 3.35: Profilometry image of a single droplet printed on the channel of an OFET.

surface energy both for Ag (40.93 mN/m) and parylene-C (42.82 mN/m), thus resulting in a uniform drop spreading on the substrate. Therefore, inkjet printed linear OFET were treated with FTP, according to the receipt described in [124]. Unexpectedly, the resulting performances were dramatically worsened, as can be clearly seen from figures 3.36a and 3.36b. The achieved mobility μ was $(2.48\pm2.06)\cdot10^{-4}$ $cm^2V^{-1}s^{-1}$, the threshold voltage V_T was -25.5 ± 3.1 V and the I_{ON}/I_{OFF} ratio was no higher than $2\cdot10^1$.

In a third experiment, more drops, one upon the other, were printed at a frequency of 50 Hz: in this way, in the same area, a bigger amount material can be deposited. Several transis-

Sample	Surface Energy	Dispersion	Polar
Ag	69.92 (mN/m)	44.32 (mN/m)	25.60 (mN/m)
Ag + FTP	40.93 (mN/m)	34.67 (mN/m)	6.26 (mN/m)
Ag + 5FTP	28.33 (mN/m)	24.18 (mN/m)	4.15 (mN/m)
Parylene	39.42 (mN/m)	39.41 (mN/m)	0.05 (mN/m)
Parylene + FTP	42.82 (mN/m)	42.27 (mN/m)	0.55 (mN/m)
Parylene + 5FTP	43.39 (mN/m)	43.11 (mN/m)	0.29 (mN/m)

Table 3.3: Comparison between the surface energy of silver (Ag) and parylene-C with and without treatment with FTP and 5FTP.

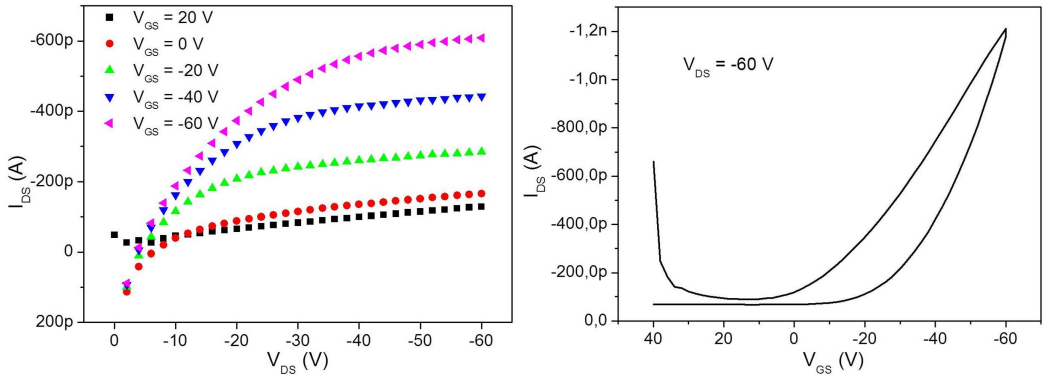

(a) (b)

Figure 3.36: Output (a) and transfer (b) characteristics of an OFET realized with inkjet printed TIPS1 with single droplet approach, pre-processing the substrate with FTP.

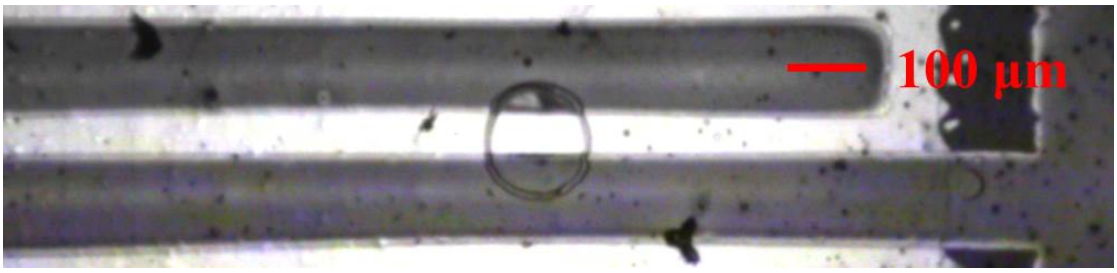

Figure 3.37: Single droplet printed on the channel of an OFET treated with FTP.

tors were realized, employing 1, 3, 5 or 10 layers and two ink formulations, TIPS1 and TIPS2. Moreover, droplets were printed in order to form single-drop transistors, *i. e.* OFET whose active layer is confined within the area of a single droplet, and linear transistors, *i. e.* OFET whose active layer extends all over the channel region and form a line. Figure 3.38 shows an example of the latter device.

Figures 3.39, 3.40 and 3.41 show the output and the transfer characteristics of single-drop

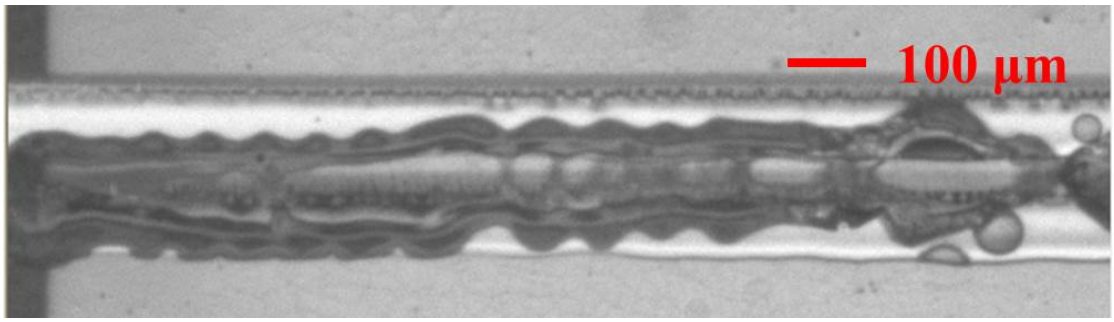

Figure 3.38: Linear OFET with the active layer printed all over the channel zone.

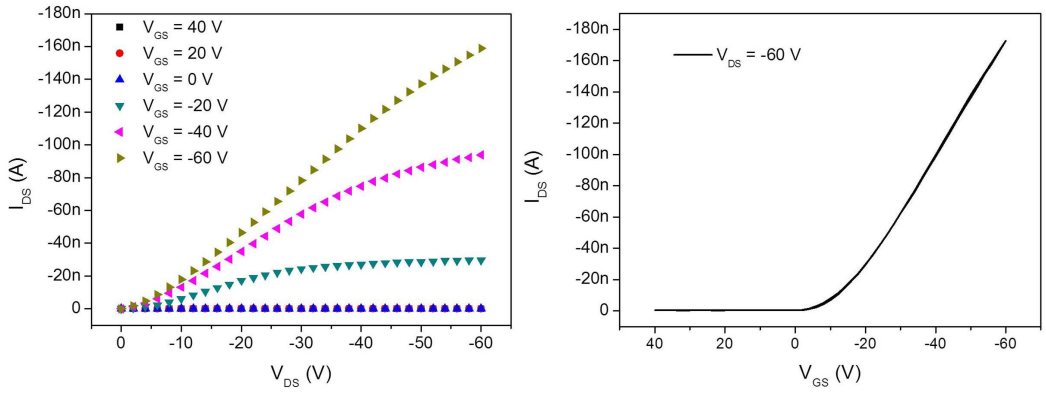

(a) (b)

Figure 3.39: Output (a) and transfer (b) characteristics of an OFET realized with 3 layers of inkjet printed TIPS-pentacene.

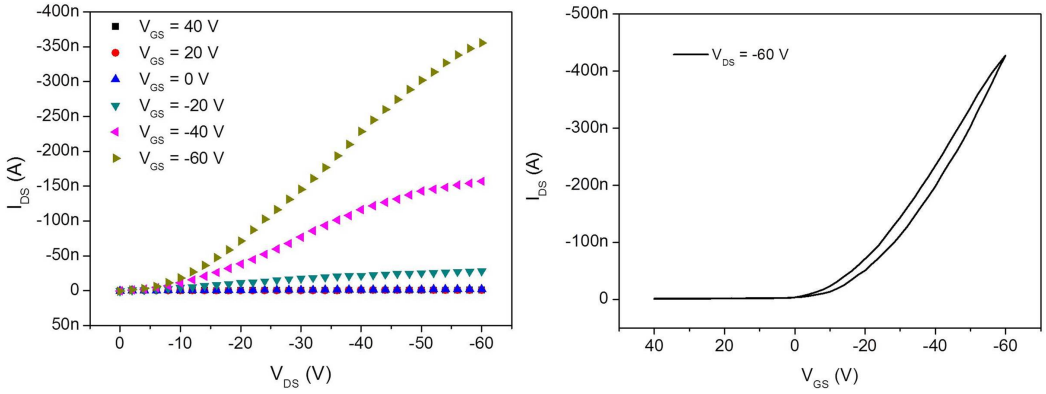

(a) (b)

Figure 3.40: Output (a) and transfer (b) characteristics of an OFET realized with 5 layers of inkjet printed TIPS-pentacene.

OFETs realized with 3, 5 and 10 layers respectively. An interesting increase of the average current can be noticed: the amount of material per unit area in the channel is directly propor-

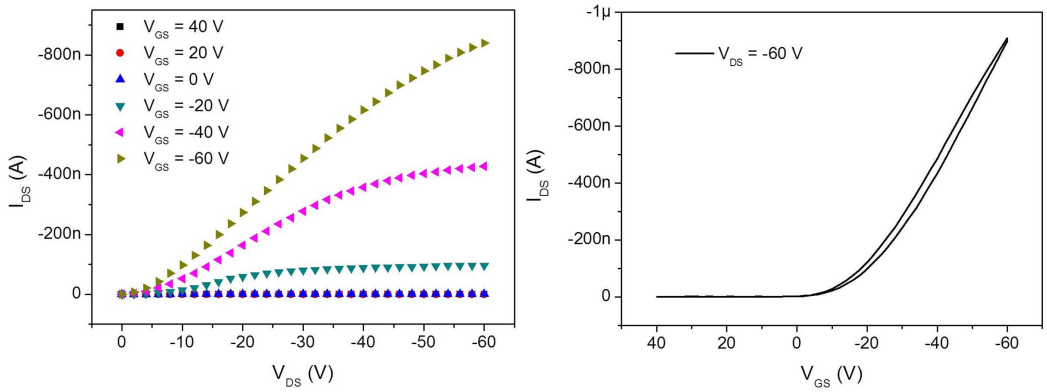

(a) (b)

Figure 3.41: Output (a) and transfer (b) characteristics of an OFET realized with 10 layers of inkjet printed TIPS-pentacene.

tional to the output source-drain current. The overall mobilities are represented and com-

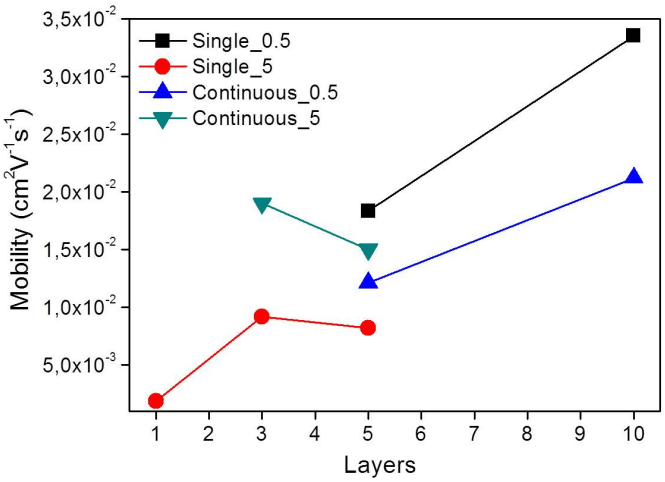

Figure 3.42: Comparison of mobilities obtained with multiple layers: the values are divided into TIPS1 (0.5 wt.%) and TIPS2 (5 wt.%), and into single-droplet OFETs and linear OFETs.

pared in figure 3.42. The OFETs have been divided into four groups, according to the ink printed (TIPS1 with a concentration of 0.5 wt.% or TIPS2 with a concentration of 5 wt.%) and to the type of transistor realized (single-droplet or linear/continuous). A clear trend can be noticed: adding more layers at high frequency, one after the other, a bigger amount of material is deposited and a higher field-effect mobility is obtained. With 10 layers, the highest value obtained was $5.8 \cdot 10^{-2}$, comparable with the mobility achieved for OFETs with drop-casted TIPS (average $7 \cdot 10^{-2}$ with top value $1.05 \cdot 10^{-1}$). In conclusion, some consideration

can be done:

- The mobility does not depends directly on the drop diameter: provided that the droplet covers the channel region from source to drain, the same mobility is achieved independently of the drop size.
- The mobility dependence on the coffee stain effect is much lower than expected: mobilities obtained with DMP2831 and with the MDP have values of the same order of magnitude when printed with the same parameters, even if in the former case the boundaries simply touch, with a poor overlapping, the source and drain electrodes.
- It can be noted a remarkable dependence of the mobility on the number of layers deposited one immediatly after the previous, up to 100 Hz: with such high frequencies, the droplet does not have time to dry and an ordered crystallization of the whole material deposited occurs.

Thus, the intrinsic limit of the DMP2831 does not rely on the printable drop size but on the drop volume and on the impossibility to print multiple droplets in rapid sequence.

3.3 The ROBOSKIN project

ROBOSKIN has been a Collaborative Project funded by European Commission through its Cognitive Systems and Robotics Unit (E5) under the Information Society Technologies component of the Seventh Framework Programme (FP7) [149]. Figure 3.43 shows a picture of iCub, one of the humanoid robots employed during the ROBOSKIN project. In particular, the project was divided into three research areas:

1. To develop new sensor technologies that could provide tactile feedback from large areas of the robot body. This development process has been incremental and took advantage of the feedback arising from the application of these technologies towards the other project objectives.
2. To develop and integrate fundamental cognitive structures for efficient and safe utilization of tactile data in terms of a robot body image, safe reflexive reactions to tactile events and flexible representations of spatially and temporally distributed patterns of physical contact.
3. To develop cognitive mechanisms that use tactile feedback to improve human-robot

Figure 3.43: iCub.

interaction capabilities particularly in the application domains of programming through demonstration and robot assisted play.

In the first research area, which provided the realization of the large-area robotic skin, three different technologies were employed: capacitive pressure sensors, piezoelectric mechanical sensors, and organic strain sensors. The role of UNICA was developing a system of sensors, based on organic transistors, which could cover large areas. In particular, taking advantage of the flexibility typical of plastic electronics, these prototypes of sensorized skin were suitable for soft surfaces where conventional tactile sensors could not be employed.
The activity carried on regarding the ROBOSKIN project, published in a *IEEE Sensors Journal* [150] is summarized in the followings. First, a description of the systems of OFETs used as strain sensors is given in section 3.3.1. The second part (3.3.2) describes the electromechanical characterization of the realized sensors, with details about sensitivity and reliability of the devices. Finally, the activity carried on in collaboration with UNIGE-DIBE on the realization and characterization of piezoelectric sensors is presented in the last section (3.3.3).

3.3.1 Systems of integrated mechanical sensors

The mechanical sensors employed were basically Organic Field-Effect Transistors (OFETs) realized as described in the previous section, with parylene-C as gate dielectric, inkjet printed gate, source and drain electrodes (employing CCI-300), and drop-cast TIPS-pentacene, using the standard formulation TIPS1: the latter has been chosen since it gives origin to the

highest mobility values obtained. Moreover, OFETs have been employed as bending sensors taking advantage of the principles described in section 3.1.2. If ε is the bending applied to the structure, the resulting sensitivity is obtained by the following equation:

$$\varepsilon \approx \frac{\Delta I_{DS}}{I_{DS}} \tag{3.3}$$

Thus the output signal, *i. e.* the electronic response to the applied bending, is given at first approximation by the relative variation of the drain current.

The systems of sensors were arranged in two configurations. The first, depicted in figure

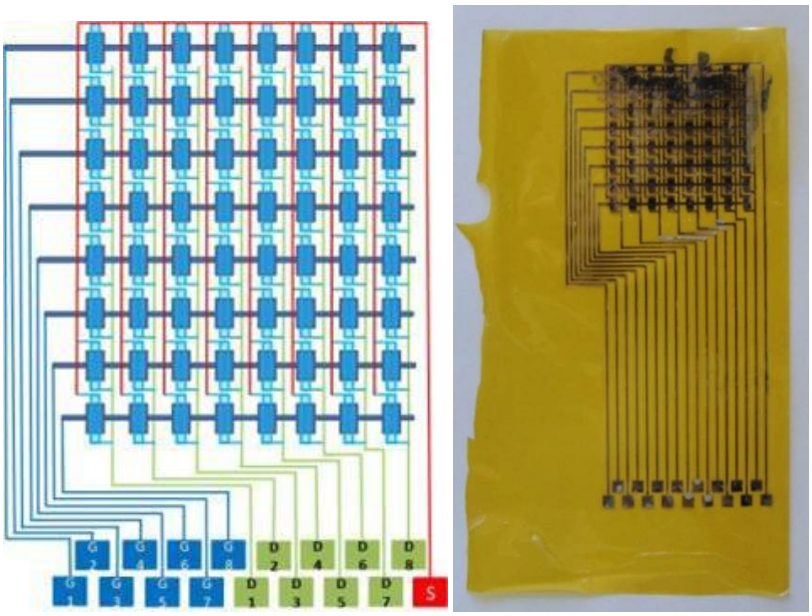

(a) (b)

Figure 3.44: (a) Schematic of the matrix of OFETs employed as mechanical sensors and (b) picture of the realized matrix on a kapton substrate.

3.44a, was called *matrix*: the sensors were organized in stacked eight rows, each one having eight elements. The 64 elements of each matrix had a common source contact (red line in the schematic), eight independent drain contacts, one per column (green lines), and eight independent gate contacts, one per row (blue lines): therefore, each device could be independently biased and its current read out. The pitch, both in X and Y directions, is 5 mm. A picture of the resulting structure is presented in figure 3.44b. Moreover, figures 3.45a and 3.45b allow to appreciate the flexibility of the realized structure: in particular, in the second picture, the extremely flexible substrate (13 μm thick kapton), is rolled around a pen.

The second configuration employed, called *array* or *double array*, consists of a single row of

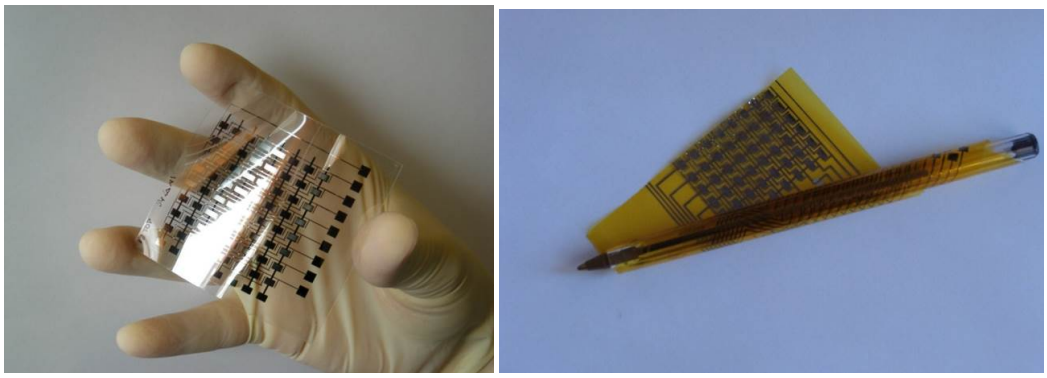

(a) (b)

Figure 3.45: Pictures of different flexible matrices realized (a) on PET and (b) on kapton.

eight sensors, with a common source contact, a common gate contact and eight independent drain contacts. The structure is represented in figure 3.46.

The inkjet printing of these structures required a major attention in designing the layout,

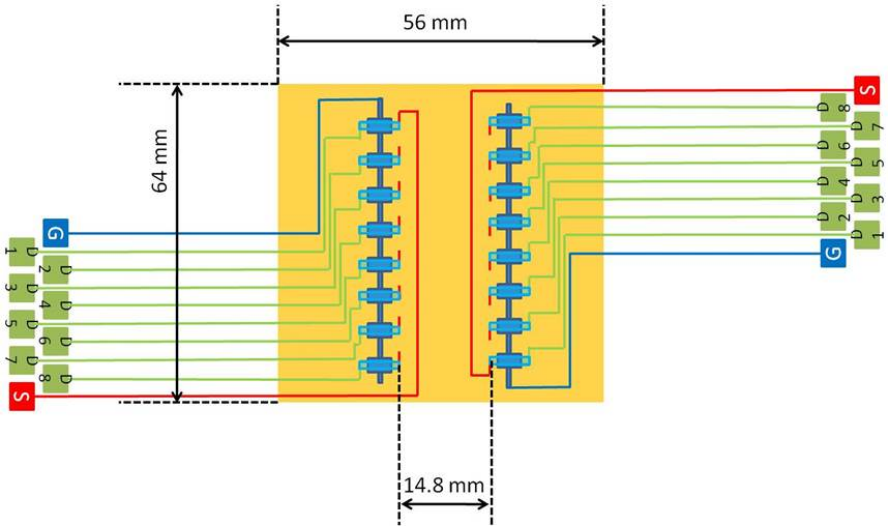

Figure 3.46: Schematic of the array configuration.

since a wrong sizing or aligning could lead to fatal short-circuits. Moreover, the interdigitated source and drain electrodes of a row were printed in the same carriage run, thus exploiting the automation potentiality of the inkjet printing technique. The most frequent causes of error have been the short circuit between the interdigitated electrodes, due to non calibrated printing parameters. However, these non-working elements of the matrix were always disconnected by manually removing the continuity of the printed layer. The overall yield, *i. e.* the number of working elements, was initially 50%, while with an accurate tuning and im-

provement of the printing technique it rose to 75% and finally to 90%. The parameters of the fabricated devices, already described in section 3.2, are briefly reported here:

- W = 50 mm.
- L = 50 μm.
- W/L = 1000.
- $C_{ins} \approx 2$ nF/cm^2.
- μ = 10^{-2} - 10^{-1} cm^{2}V^{-1}s^{-1}.
- V_T = (4 ± 5) V.

3.3.2 Electromechanical characterization

The employment of OFETs as strain sensors required an accurate electromechanical characterization. It can be conceptually split in two steps: in the first, the general experimental setup is presented, with a description of the device biasing, signal acquisition and processing; the second focuses on the sensitivity measurements and the reliability of the organic sensors.

Experimental setup

When employing an OFET as a strain sensor, the most immediate strategy would be to bias it with a DC voltage in order to read the current variation due to the mechanical stimulus applied. However, it is well known [151] that applying a DC voltage for long time causes the degradation of the electrical performances of the semiconductor, *i. e.* a reduction of the output current. For this reason, a square-wave gate voltage, alternatively positive and negative, was applied in order to reduce the bias stress effects. The best tradeoff between signal saturation and low bias stress was obtained at 100 Hz frequency and 50% duty cycle. The resulting square-wave, that was the V_{GS} applied, was comprised between +5 V (transistor switched off) and −15 V (transistor switched on), while the V_{DS} was kept constant at −5 V. The gate biasing is schematized in figure 3.47. Figures 3.48, 3.49 and 3.50 report the dynamic electrical characterization for OFETs realized with pentacene, N1400 and TIPS-pentacene respectively. The bias conditions described above were continuously applied for long time lapses, up to more than 6 hours, and the resulting on- and off-current were monitored regularly. The best response is given by the pentacene, since even applying a square-wave voltage for 107 min no degradation could be observed. On the contrary, N1400 overcame a dramatic degradation:

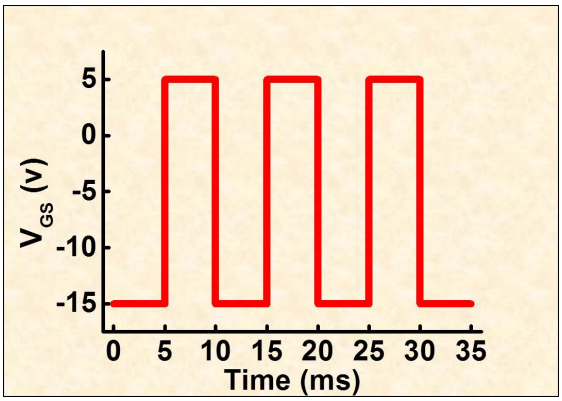

Figure 3.47: Square-wave voltage applied to the gate electrode.

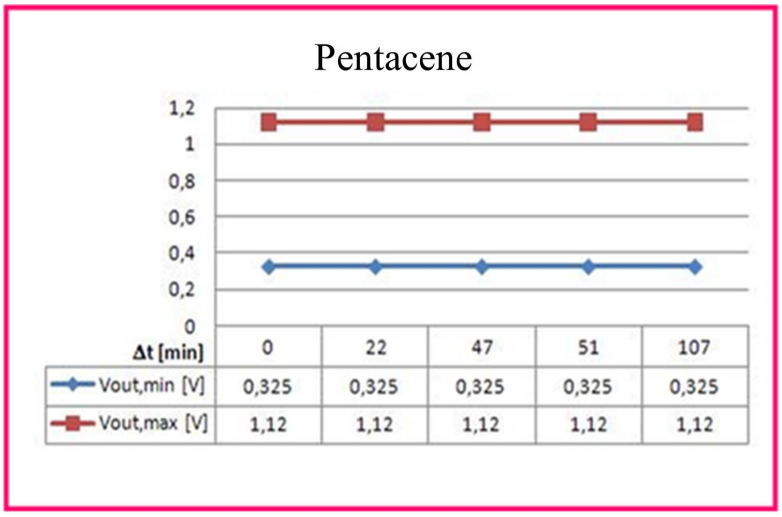

Figure 3.48: Electrical stress induced degradation of the pentacene performances over 380 minutes.

after 340 min of electrical stress, no difference between the on- and the off-states could be noted, therefore this semiconductor is not suitable for long-time biasing. An intermediate behavior was given by TIPS-pentacene: the effects of the bias stress were not very relevant, since after an initial decrease, the level of the maximum drain current did not change significantly over more than 6 hours of biasing. Other than its solubility, this is another reason why this semiconductor was largely employed during the research activity related to this thesis.
After this preliminary dynamic test, a read out circuitry was developed *ad hoc* in the laboratory, consisting of 8 input channels, an analog block (I/V converter and amplifier) and a digital block (microcontroller and analog to digital converter, with 500 Hz sampling frequency). The OFETs of an entire array, or those of a single row of a matrix, could be read with

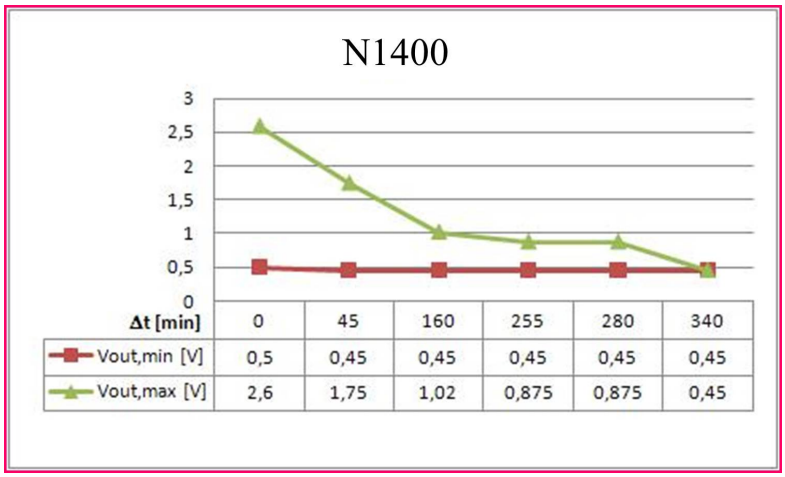

Δt [min]	0	45	160	255	280	340
Vout,min [V]	0,5	0,45	0,45	0,45	0,45	0,45
Vout,max [V]	2,6	1,75	1,02	0,875	0,875	0,45

Figure 3.49: Electrical stress induced degradation of the N1400 performances over 380 minutes.

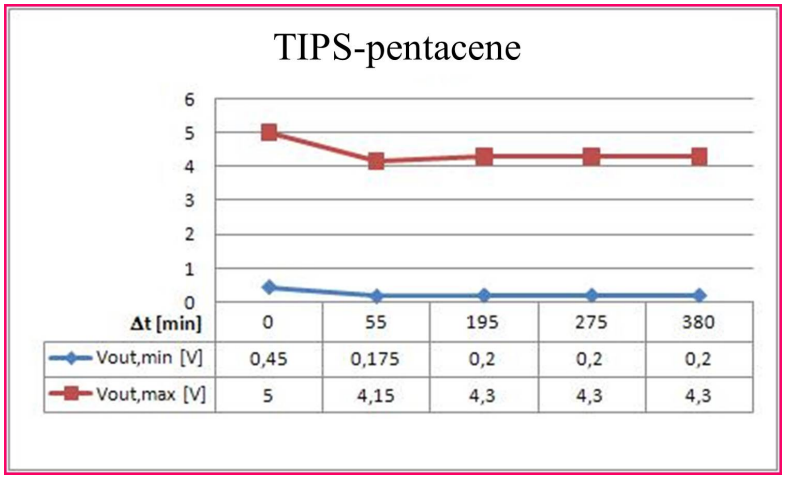

Δt [min]	0	55	195	275	380
Vout,min [V]	0,45	0,175	0,2	0,2	0,2
Vout,max [V]	5	4,15	4,3	4,3	4,3

Figure 3.50: Electrical stress induced degradation of the TIPS-pentacene performances over 380 minutes.

this circuitry, schematized in figure 3.51. Basically, when an OFET is not subjected to any mechanical stimuli, its response follows the gate bias, as shown in figure 3.52a. During a pressure event, which induces a bending on the plastic substrate, the absolute value of the output on-current decreases, as represented in figure 3.52b. The electrical response, $\Delta I_{DS}/I_{DS}$, was therefore defined as the difference between the on-state current in the "unpressed" condition and the on-state current in the "pressed" condition, divided by the on-state current in the "unpressed" condition. For post-processing applications, a moving average algorithm was developed to magnify the pressure event. On the other hand, for real-time applications, a Graphic User Interface(GUI) was developed to evaluate the average value of 5 acquisitions

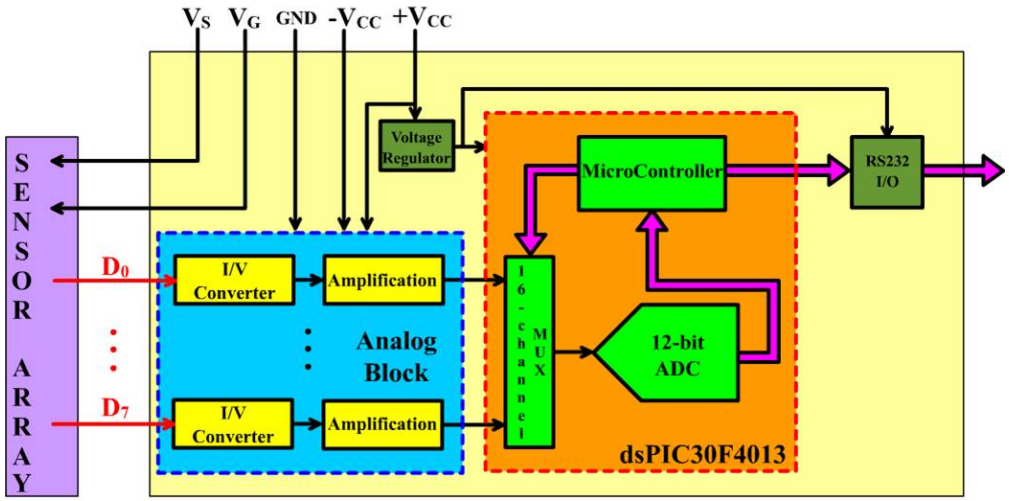

Figure 3.51: Schematics of the readout circuitry employed with the sensors systems.

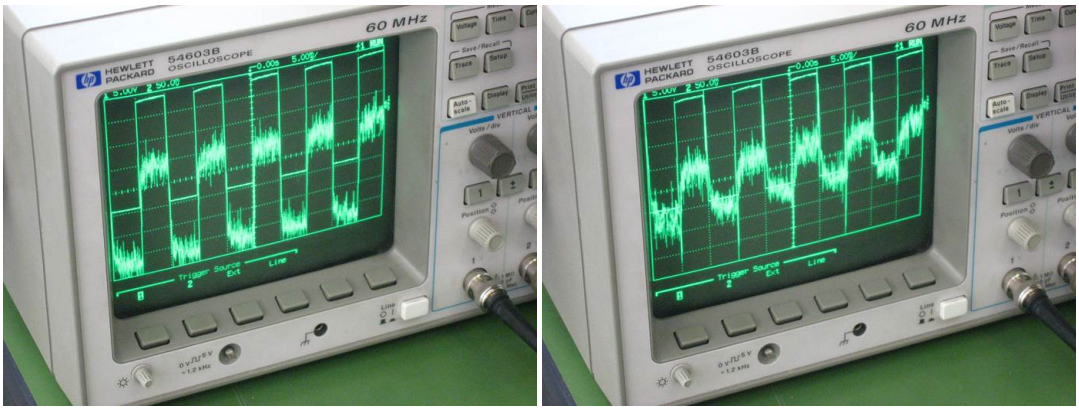

(a) (b)

Figure 3.52: Device response, read by means of an oscilloscope, (a) in the normal state and (b) in the "pressed" state.

for each device and to show the relative current variation ΔI_{DS} of the “pressed” state with respect to the initial state.

In a first experiment, an arbitrary pressure has been exerted with a finger independently on a single element of the array. In figure 3.53, the electrical response of six sensors of a single row is presented: for each sensor, the pressure was exerted two times. A clear response is visible for most of the touched devices. A similar experiment is represented in figure 3.55: in this case, the finger was moved forward and backward across a single row. Again, a marked response is clearly visible in the graph. Finally, in another experiment, the pressure events were applied on the OFET of an array and the response was visualized real-time on the mon-

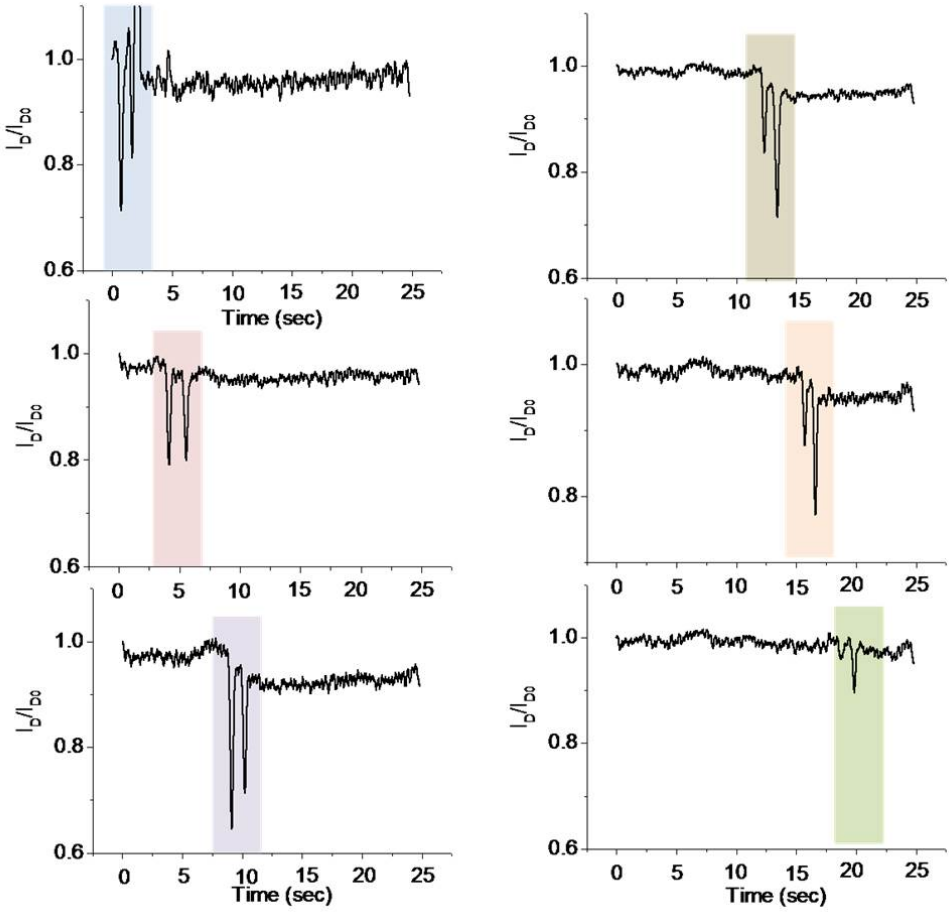

Figure 3.53: Electrical response of the organic sensors in a single row; the pressure is exerted independently, two times on each sensor.

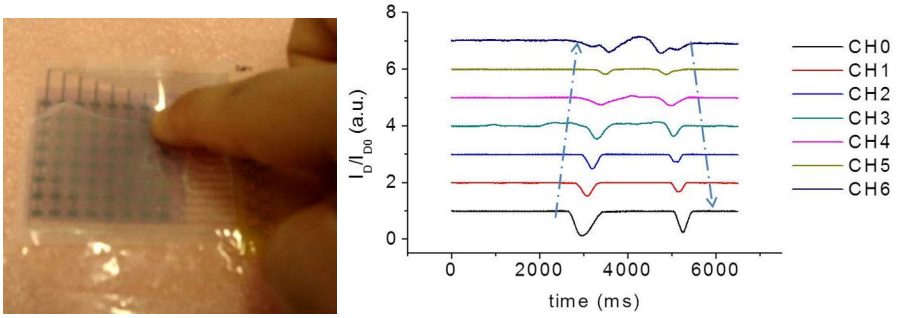

(a) (b)

Figure 3.54: Electrical reponse when the finger is moved forward and backward across a single row.

itor (figure 3.55). As a general consideration, two different points could be highlighted:

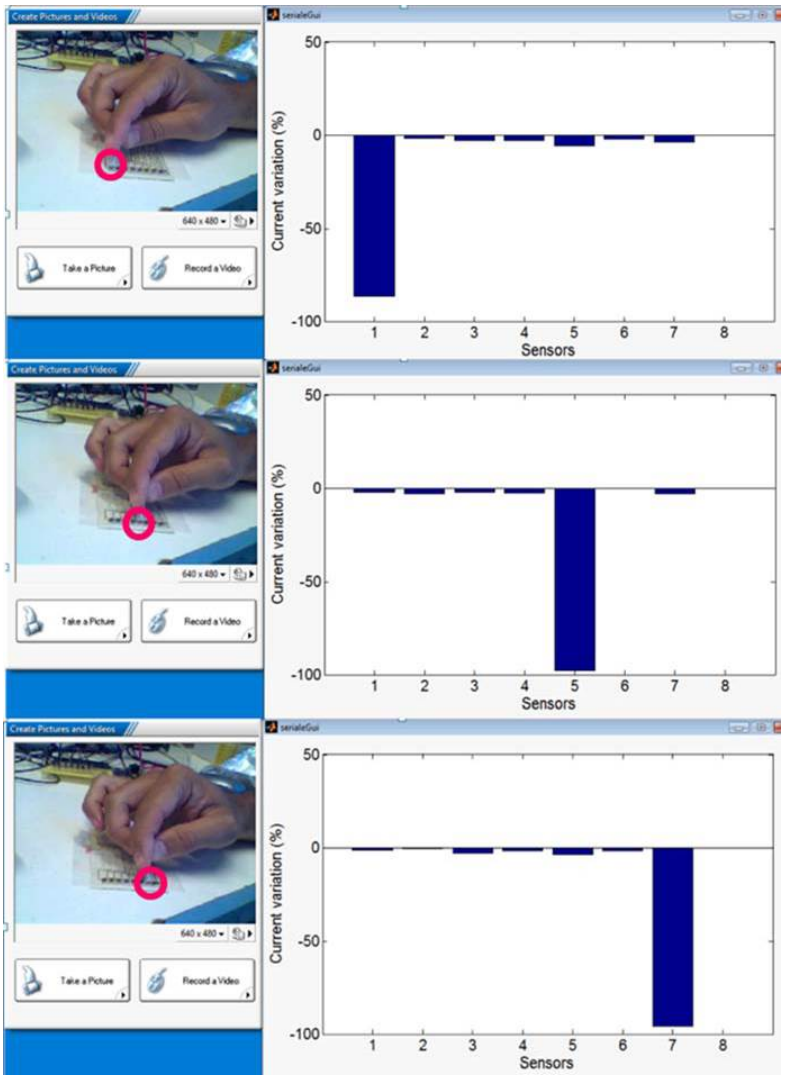

Figure 3.55: Electrical real-time response of the organic sensors in a single row.

- each device responds to the applied mechanical deformation and their electrical response is shifted in time according to the propagation of the mechanical stimulus (finger moving across the surface).

- a small, but visible, cross talking between adjacent elements can be observed. This behavior is induced by the fact that the contact area between the indenter (the finger in this case) and the active matrix is comparable to the lateral distance between two close OFETs (5mm). As a result, the mechanical deformation induced by the finger on one element is also partially applied to the adjacent elements.

Sensor calibration

In order to gain more detailed information about the sensitivity and the reliability of the robot skin, calibration and stress tests have been performed in collaboration with UNIGE-DIST. These tests have been performed by means of a mechanical indenter, shown in figure 3.56.

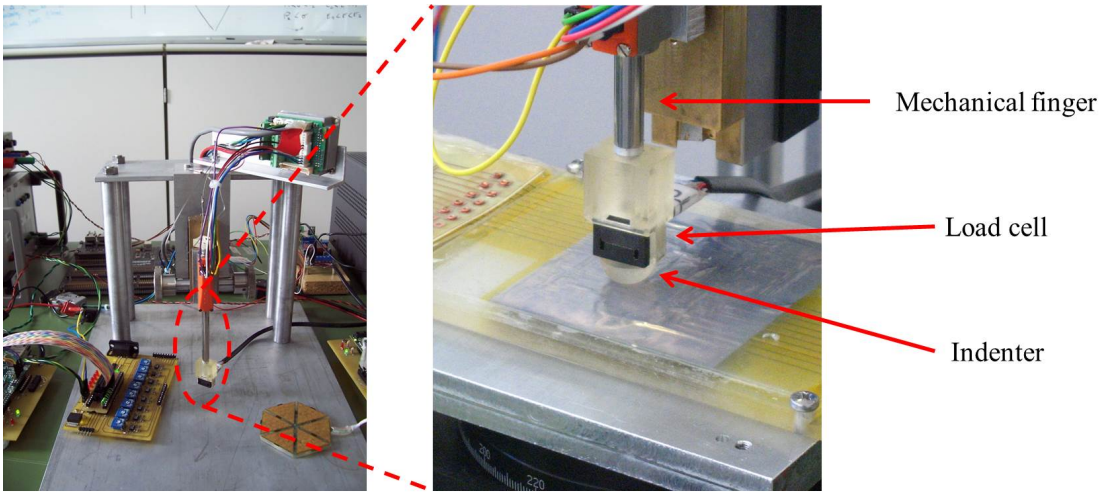

Figure 3.56: Mechanical indenter employed for the sensitivity and reliability tests.

This home-made indenter consists of a metal scaffold and a mechanical finger, controlled in vertical position, which can move up and down with high spatial resolution. A linear DC-servomotor (LM-1247-040-02, purchased from Faulhaber© [152]) was employed to calibrate the applied force. On the bottom of the mechanical finger, a load cell (Microswitch Force Sensor FS Series, purchased from Farnell© [153]) measures the force exerted on the device. The cell can detect forces up to 4.2 N. The finger ends with a hemispherical indenter of 8 mm diameter, that is a plausible value of the diameter of a human finger. The hemispherical indenter was realized by rapid prototyping a general-purpose resin (FullCure 720, purchased from Artcorp© [154]) using a Objet Eden 260. In summary, the input parameters of the system were the vertical position of the finger with respect to the *zero point* (Δz) and the force applied (F), measured by the load cell. The output was, as explained before, the relative drain current variation of the transistors ($\Delta I_{DS}/I_{DS}$) proportional to the strain induced to the substrate.

In these calibration experiments, the plastic substrates have been covered with Ecoflex® PDMS, and in one case also with Sylgard® PDMS, in order to recreate the consistency of the human skin and to protect the sensors from fatal damages. Both PDMS were provided as two-part liquid component kit comprised of an elastomer (A) and a curing agent (B). For the

Ecoflex® PDMS, components A and B were mixed together by hand in the ratio 1:1 by volume and, subsequently, in order to avoid a detriment of mechanical properties, air bubbles were extracted from the obtained compound by means of a vacuum pump. The compound was deposited over the Kapton substrate with the printed organic array in an *ad hoc* mold and was polymerized at room temperature for 4 hours. For the Sylgard® PDMS, components A and B were mixed by ratio 10:1 by weight, and the compound was degassed in a vacuum pump. In this case, the PDMS was polymerized at 100 °C for 1 hour. Four different configurations for the PDMS-sensors complex, hereafter labelled from A to D, have been tested in order to investigate which could be the best layout that maximizes the response of the devices. For each configuration, stimuli of increasing pressures were applied to the PDMS-sensors system, covering the range 0–4 N. Each cycle of increasing pressure was therefore replied in order to analyze the reproducibility of the sensor.

In configuration A (figure 3.57), Kapton was simply placed on a 5 mm thick Ecoflex layer

Figure 3.57: Schematic layout of the configuration A.

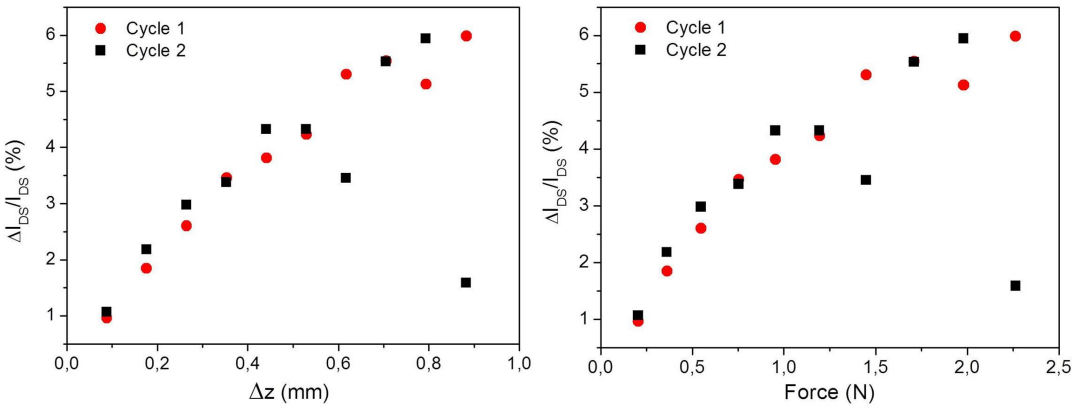

(a) (b)

Figure 3.58: Electrical reponse of the sensors with configuration A with respect to Δz (a) and with respect to F (b).

and the deformation was directly applied to the back side of the Kapton film. Two cycles and 10 steps per cycle were applied. This led to a high mortality of the devices for high pres-

sures. Sensitivity was very good, but repeatability was poor for forces above 1.25 N. Results are shown in figure 3.58.

In configuration B (figure 3.59), the Kapton substrate was placed above a Sylgard PDMS layer

Figure 3.59: Schematic layout of the configuration B.

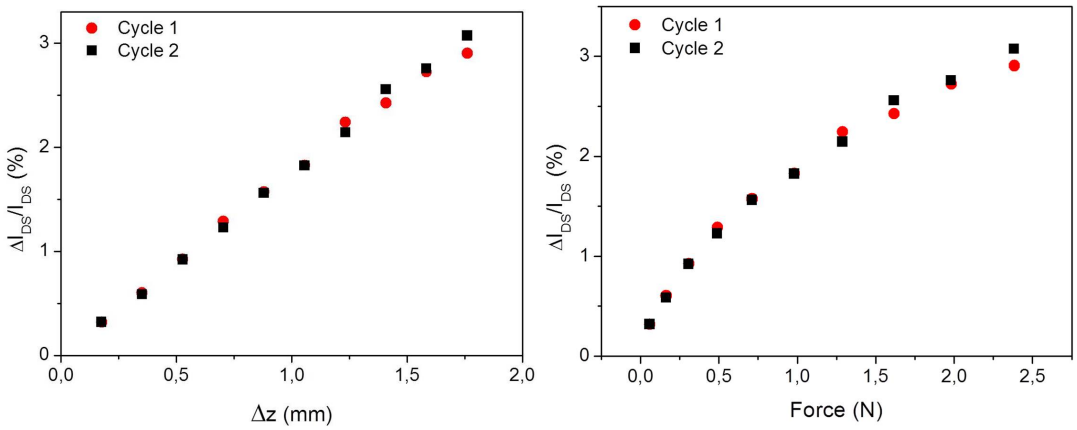

(a) (b)

Figure 3.60: Electrical reponse of the sensors with configuration B with respect to Δz (a) and with respect to F (b).

realized ad hoc as follows. Sylgard was patterned on top of a rigid substrate where a square relief was realized: in this way, after peeling off the Sylgard stamp and realizing the conformal contact with the Kapton layer, each device channel corresponds to the empty space between two PDMS micro-pillars and is therefore free to deform during pressure application. After this, the whole structure was covered with another 5 mm thick Ecoflex layer. Two cycles and 10 steps per cycle were applied. In this case, a lower sensitivity could be noticed with respect to the previous configuration, but the protective upper Ecoflex substrate covered the devices and avoided mortality. The reproducibility was very good over the two cycles. Results are shown in figure 3.62.

In configuration C (figure 3.61), Kapton was totally embedded on Ecoflex: the bottom layer

Figure 3.61: Schematic layout of the configuration C.

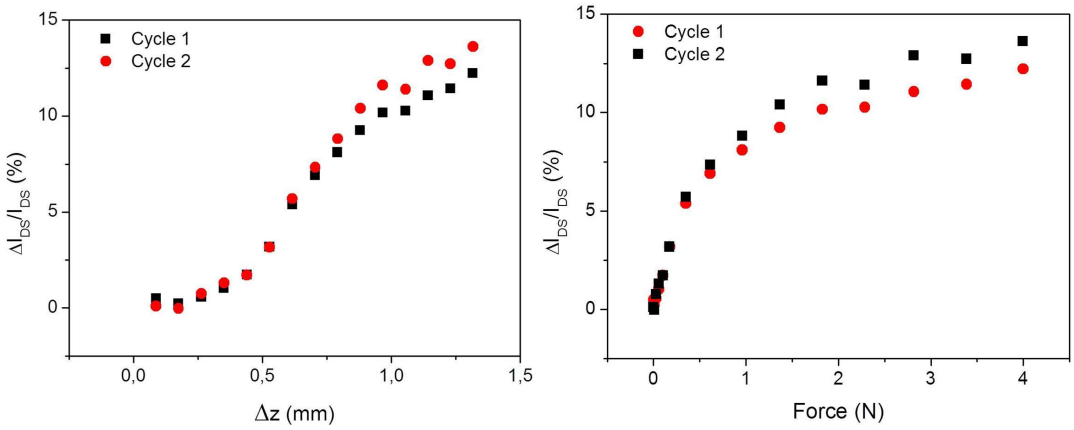

Figure 3.62: Electrical reponse of the sensors with configuration C with respect to Δz (a) and with respect to F (b).

was 2 mm thick and the top layer was 0.5 mm thick. Two cycles of increasing force and 15 steps per cycle were applied. In figure 3.62 the results are shown. In this case a very high sensitivity was obtained, up to 15%, but reproducibility was not good for pressures above 1 N. This was probably due to the small thickness of the upper layer of Ecoflex.

Finally, in configuration D (figure 3.63), Kapton was totally embedded in Ecoflex, as in con-

Figure 3.63: Schematic layout of the configuration D.

figuration C, but with a thicker upper layer (2 mm). This turned out to be the best configuration. Four cycles with 10 steps per cycle were applied. Repeatability was very good over the four cycles, as shown in figure 3.64.

Moreover, another effect could be detected with all these configurations: when the mechanical stimulus was applied on a specific sensor, also the adjacent sensors showed a lower elec-

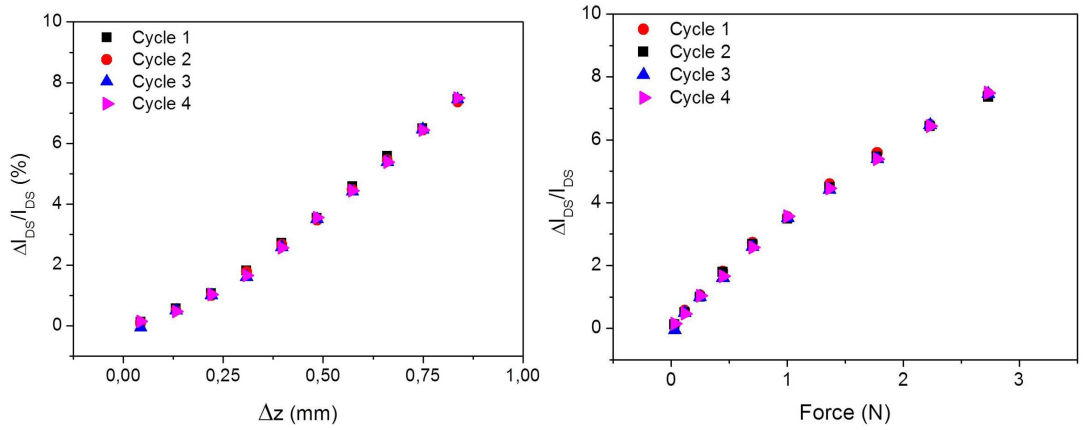

(a) (b)

Figure 3.64: Electrical reponse of the sensors with configuration D with respect to Δz (a) and with respect to F (b).

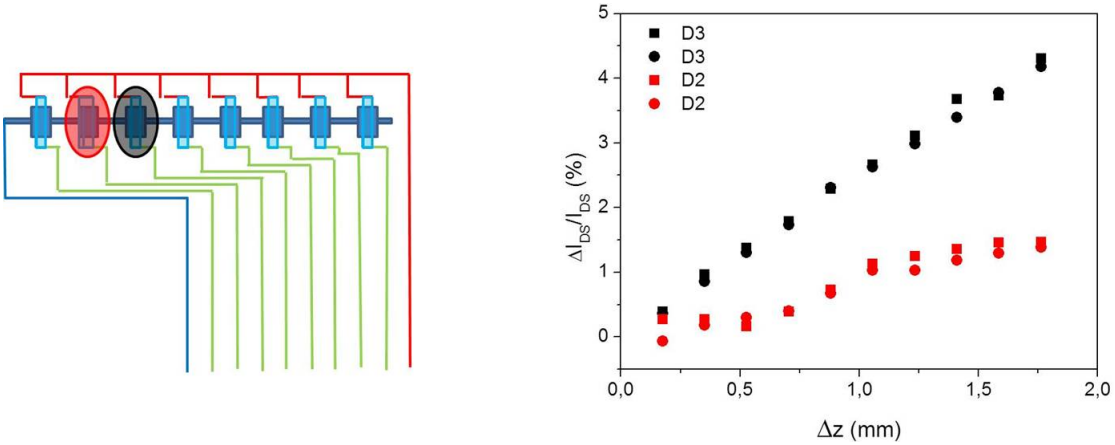

Figure 3.65: Compared response of a sensor (red circle) when the mechanical stimulus is applied on the adjacent sensor (black circle).

trical response, due to the PDMS mechanical properties which propagate the deformation induced. As shown in figure 3.65, specific for configuration B, when the stimulus was applied on device D3, black-circled, also device D2, red-circled, showed a clear response. Both responses are reported on the graph for comparison. This mechanical crosstalking could be an interesting property for matrices of sensors which detect the spatial variation of the mechanical stimulus applied.

Since configuration D was the best one, leading to very high sensitivity and good resolution, *i. e.* a minimum detectable force of 0.1 N, it was used for the calibration of the robot skin. Figures 3.66a and 3.66b show the statistics under 10 consecutive cycles of pressure applied on one single OFET. The narrow error bands highlight a very high reproducibility of the de-

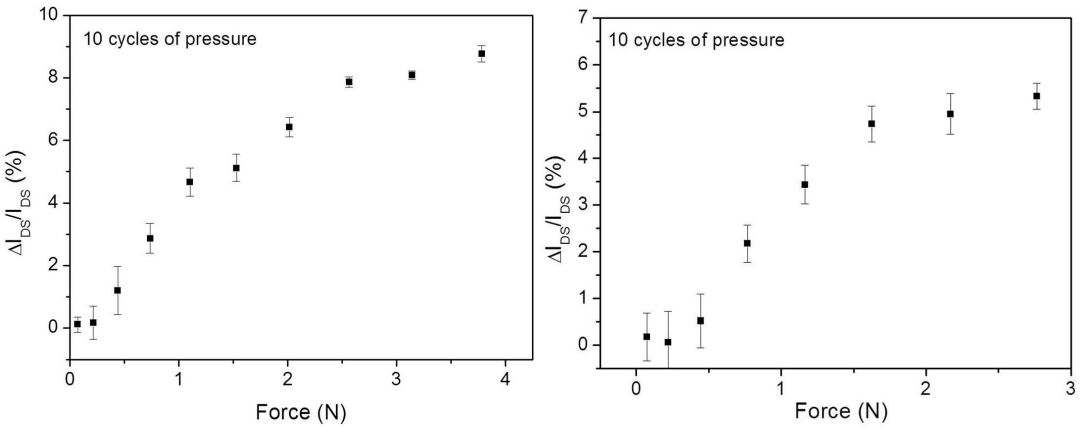

(a) (b)

Figure 3.66: Statistics of the electrical reponse of two sensors with configuration D under 10 cycles of applied pressure.

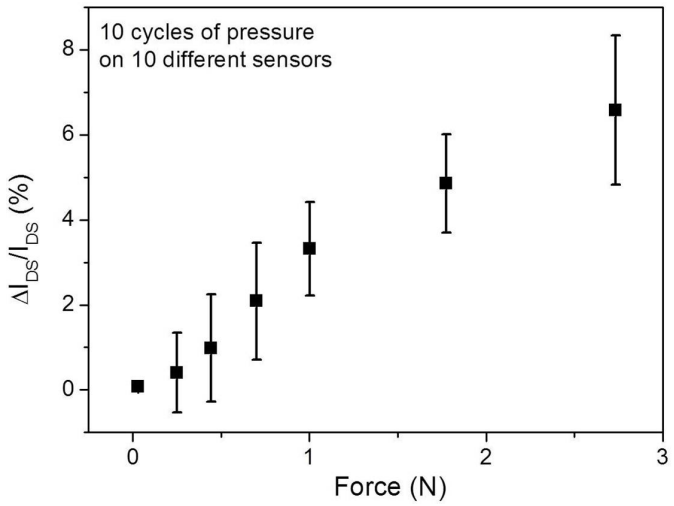

Figure 3.67: Overall statistics of the electrical reponse of ten sensors with configuration D each one under 10 cycles of applied pressure.

vice response. In figure 3.67 the overall statistics, referred to 10 cycles of pressure each one applied on 10 different devices, thus a total of 100 pressure events for each force value, is shown. Although each device has its own electrical performance, peculiar sensitivity and mechanical response, a general trend can be noticed, with a good linearity and an average maximum sensitivity up to 6% for 3 N force applied.

Finally, mechanical stress degradation tests have been performed, by means of the mechanical indenter and the human finger, in order to investigate the durability and reliability of the printed OFETs. In figure 3.68a the results of the tests performed by means of the mechanical

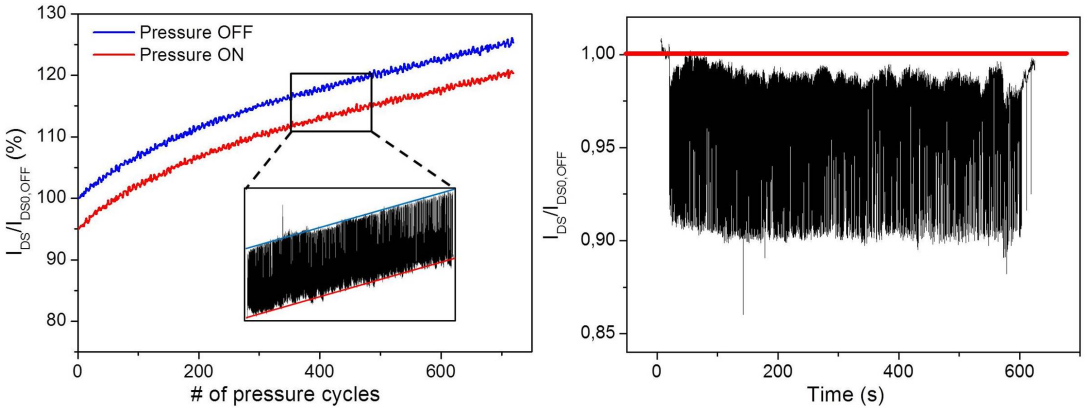

(a) (b)

Figure 3.68: Electrical response of the organic sensors under mechanical stress applied (a) by the mechanical indenter and (b) by a human finger.

indenter are shown. In this experiment consecutive mechanical stimuli over time were applied, each one having a square-wave profile: pressure released for 2.5 s and then applied for 2.5 s at a constant force of 3.7 N, as measured by the load cell of the indenter. As output signal, the percentage variation of the device response, both in the pressed (red) and released (blue) states, was evaluated with respect to the initial released state. Up to 2000 consecutive stimuli have been exerted: no degradation is noticed before 1000 stimuli, and although a slight current increase, as important result the difference between the pressed and the released state remained constant during the whole test, showing therefore a good response before irreversible degradation. In figure 3.68b the same experiment was carried out by applying the force with the finger in dark conditions, thus avoiding the current increase. The variation of the output current with respect to the initial unstressed state (highlighted by the red line) is represented. Over 1000 pressure events for 600 s were exerted and the response remained constant over the whole experiment, showing a good reliability of this system as electronic skin over the time and under mechanical stress conditions.

3.3.3 Fabrication and characterization of PVDF-based mechanical sensors

Within the ROBOSKIN project, also another technology was investigated for the creation of an artificial robotic skin. 110 μm thick PVDF substrates were employed as high-frequency pressure sensors by an opportune patterning. This activity was carried on in collaboration with UNIGE-DIBE and the results have been published in a *IEEE Sensors Journal* [155].

The role of UNICA was patterning the PVDF substrate, *i. e.* deposit the metal electrodes, by

mean of inkjet printing, using CCI-300 as the condictive ink. The pattern is represented in

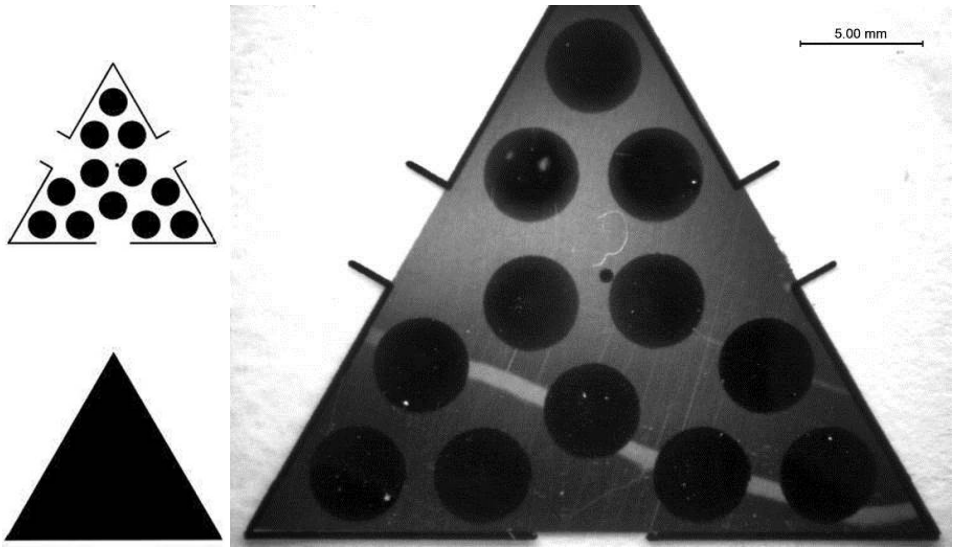

(a) (b)

Figure 3.69: Layout (a) and picture (b) of the inkjet printed patterns on a PVDF substrate.

figure 3.69a: the top contact was a full triangle with 3 cm side, printed on one side of the PVDF substrate and used as common ground, while the bottom contact was composed of 12 circle pads, called *taxels*, with a diameter of 3 mm each (same geometry of metal contacts on PCB), arranged in a triangular shape, each one being an independent sensor element. Figure 3.69b shows a picture of the patterned substrate, with the top and bottom contacts aligned on the opposite sides. The inkjet printing process itself was not too challenging, since this low-resolution pattern did not require too high printing precision. Nevertheless, the overall fabrication process took up to 10 days to be completed. In order to improve the adhesion of the printed layer to the substrate and to make it more resistant to mechanical stress, an air plasma treatment was performed for 60 s at 75 W just before the printing. This treatment led to a major spreading of the ink drops and therefore to a lower resolution which sometime resulted in undesired taxels short-circuited with the triangle boundary. The post-printing annealing was performed at 50-55 °C in order to avoid the substrate deformation.

Figure 3.70 schematizes the overall fabrication process of the sensing triangles. The Sylgard 184 PDMS layer was directly integrated on top of the PVDF film. A 2.5 mm elastomer thickness has been chosen as optimally meeting the application requirements. Patterned PVDF film triangles with elastomer on top were then glued on the PCB by the use of conductive Epoxy, patterned contacts on the PVDF bottom side corresponding to contacts on the PCB.

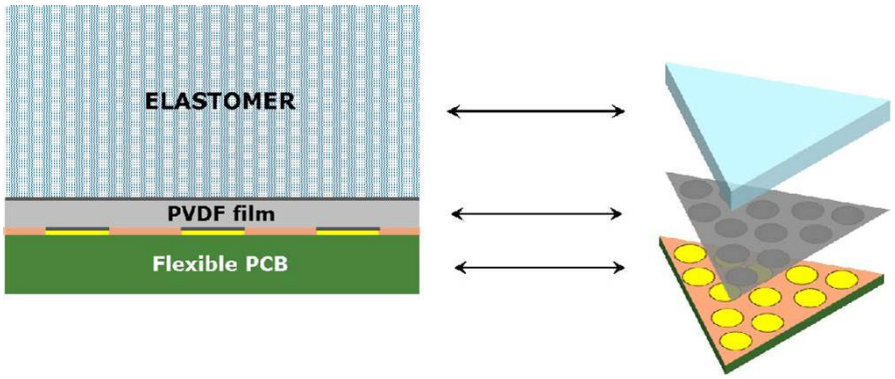

Figure 3.70: Schematic cross section of the layers which form the sensing elements.

The mechanical chain of the experimental setup was basically constituted by a mechani-

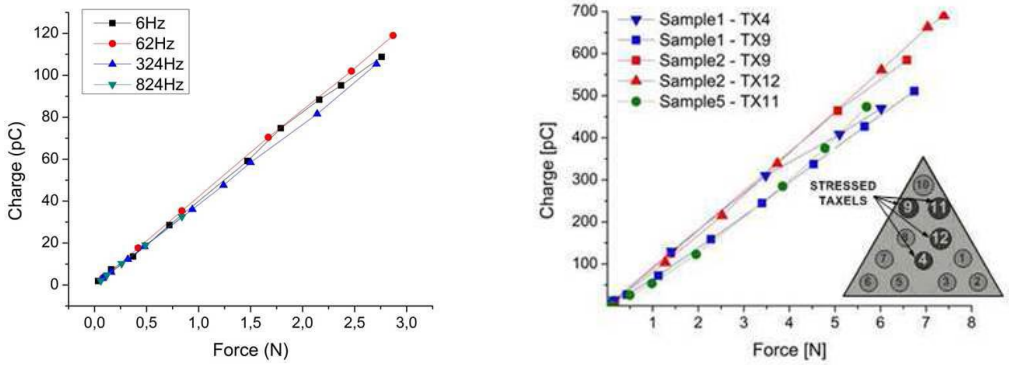

(a) (b)

Figure 3.71: Electrical response of the PVDF sensors: (a) stimuli of different frequencies applied to the same taxel and (b) stimuli of the same frequency (6 Hz) applied to different taxels.

cal shaker (TV 50018, TIRA GmbH, Schwingtechnik Vibration Test Systems), the triangular skin module (protective layer included) and a load cell (Model 208C01, PCB Piezotronics). The inductive mechanical actuator that moved the shaker was software controlled. The input parameters of the mechanical stimulus (range of frequencies, amplitude, DC offset) were set and the related signal was directly generated by the acquisition board and conveyed to the shaker via a conditioner. The charge developed by the PVDF film was measured by a charge amplifier. Figure 3.71a shows the response of a single taxel for four different stimulus frequencies belonging to the range of interest of the robotic skin application (f = 6, 62, 324, 824 Hz). As it can be seen, a linear behaviour was achieved over the whole explored range (1 Hz–1 kHz). On the other hand, by varying the amplitude of the applied stimulus at a fixed fre-

quency (6 Hz), the charge response of 5 different taxels belonging to three different triangles could be compared (figure 3.71b).

4 Inkjet printing for other applications

The final part of this thesis includes all the other application, different from the tactile sensors described in the previous chapter. The main application concerns the fabrication and the characterization of organic diodes and photodiodes, employed as photosensors. This activity has been carried on as a part of the HYMEC project, described in section 4.1. The other ongoing activities described are: realization of gustometer (section 4.3), inkjet printing of electroactuated membranes (section 4.2) and inkjet printing of a RFID tag (section 4.4).

4.1 Fabrication and characterization of organic diodes and photodiodes

One of the other applications of inkjet printing investigated during this work was the fabrication and characterization of organic diodes and photodiodes. In this section a brief review of the ongoing activity is presented, starting from the HYMEC project, in which the University of Cagliari was involved, to the characterization of the photodiodes.

4.1.1 The HYMEC project

The *HYMEC* project, namely *HYbrid organic/inorganic Memory Elements for integration of electronic and photonic Circuitry*, is a Collaborative Project funded by European Commission [156]. The role of UNICA was the fabrication and characterization of non-volatile memories based on organic semiconductors and the fabrication and characterization of organic-based photodiodes for the optical addressing of the memory elements. The latter issue has been developing within the work related to this thesis.

Basically the Schottky-type diodes, whose physical principles are described in section A.1, consist of a stacked vertical structure with a bottom electrode, an active layer of organic semi-

conductor, and a top electrode. The vertical conduction is achieved when the two electrodes are not short-circuited and when each individual electrode is continue. The first event can occur is the active layer is too thin, thus resulting in a diffusion of the upper electrode towards the bottom electrode; on the other hand, discontinuity is the result of a sharp and rough active layer where continuous upper layers can hardly be deposited. The figures-of-merit for the photodiodes are:

- *Rectifying Ratio* (RR): it is defined as the absolute value of the ratio of the current at a positive voltage $+V$ divided by the current at the corresponding negative potential $-V$. The requirement from HYMEC was RR $\geq 10^3$.
- *Photogeneration Ratio* (PR): it is the ratio of the reverse current values in dark condition and under illumination.

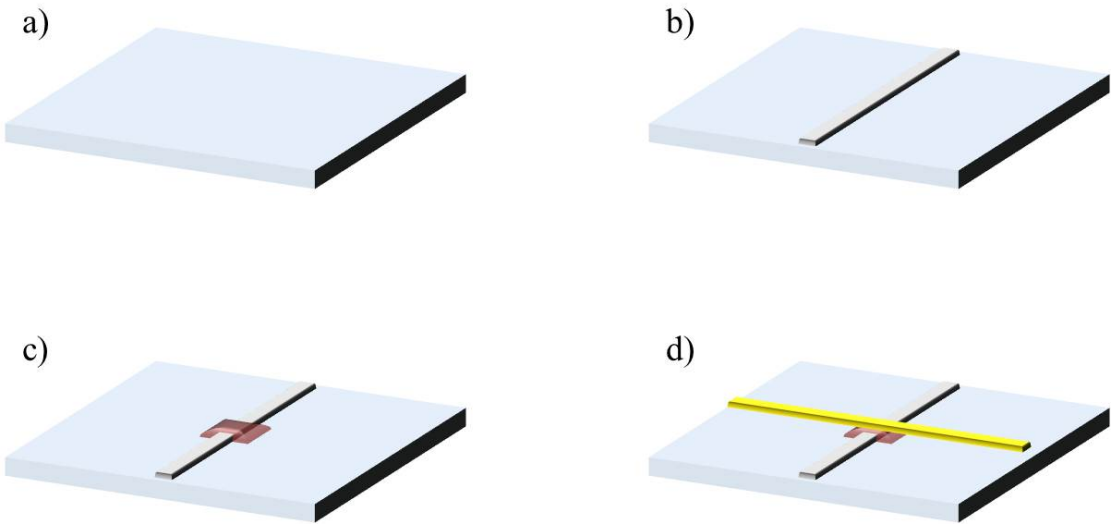

Figure 4.1: Steps for the fabrication of organic diodes and photodiodes: (a) substrate cleaning, (b) bottom electrode deposition, (c) active layer deposition, and (d) top electrode deposition.

The steps for the fabrication of organic diodes and photodiodes are represented in figure 4.1 and are described in the followings:

a) The substrate is first cut out and cleaned with subsequent cycles of acetone, isopropyl alcohol and distilled water, and then dried by means of a nitrogen flow. Two types of substrate were employed for this application: 175 μm thick PET and 125 μm thick PEN. In particular the latter was chosen as a good candidate thanks to its thermal resistance,

since the performances of P3HT-PCBM increase when it is annealed at high temperature.

b) The bottom electrode is deposited, nominally a 200 μm wide line which ends with a square pad for the electrical contact. Gold, Aluminum and Silver were employed and deposited by thermal evaporation with a shadow mask or with a common photolithography process. In some cases the bottom electrodes was made of inkjet printed PEDOT:PSS, with the same geometrical characteristics.

c) The active layer is deposited by inkjet printing. Nominally, a square with 400 μm side was chosen in order to completely cover the intersection of the two electrodes and avoid the possibility of short circuits. Two organic semiconductors were employed: TIPS-pentacene and P3HT-PCBM.

d) The top electode is evaporated only by a shadow mask, since a photolithography process could damage the active layer. The most critical step requires the careful alignment of the shadow mask with the printed small active layer, since even a small angle error could lead to short circuits between top and bottom electrodes. Also in this case, Gold, Aluminum and Silver were employed. In some cases, PEDOT:PSS was chosen and deposited via inkjet printing.

The diodes were arranged in matrices of 16 elements on each substrate, but they were characterized individually. The standard characterization consists of a sweep of the applied voltage, forward and backward, and the relative output current. Moreover, to investigate the photodiodes as light sensors, they were constantly reverse biased and light stimuli were consecutive applied, *i. e.* dark and light conditions were alternated: the output current, dependent on the illumination, was recorded over the time. Since different materials were employed for the top electrode, the bottom electrode, and the active layer, several combinations could be obtained which gave rise to different results. In the following sections, each combination investigated is described with its electrical performance. The major subdivision of the structures realized concerns the active layer employed, thus they are divided into TIPS-pentacene based diodes and P3HT:PCBM based photodiodes.

4.1.2 TIPS-pentacene based diodes

TIPS-pentacene ink was formulated using a concentration of 3 wt.% in anisole without adding polystyrene or other molecules. For each configuration, from 1 to 4 layers were printed in or-

der to investigate which could have the best characteristics. All the diodes printed with 3 and 4 layer were too rough and avoided the continuity of the upper electrode, thus hereafter only 1 and 2 layer are described. Moreover, all the devices realized with Aluminum as top electrode did not work, even when only 1 layer of TIPS-pentacene was printed. The same result was obtained for the photodiodes based on P3HT:PCBM. Therefore Aluminum was employed only as bottom electrode. All the printed layers were annealed in a hot plate at 90 °C.

PET/Al/TIPS-pentacene/Ag

Figures 4.2 shows the pictures of the printed semiconductor, respectively with 1 layer and 2 layers. The printing parameters were calibrated to obtain layers as regular and defined as

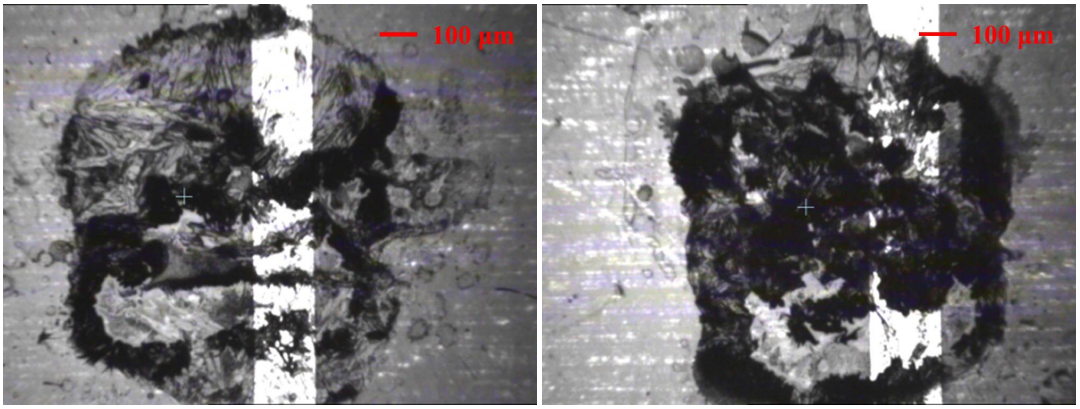

(a) (b)

Figure 4.2: Pictures of the diode active layer realized with TIPS-pentacene: (a) one layer and (b) two layers.

possible. In particular, 10 pL cartridges were employed without preliminary filtering, drop spacing 15 μm and 3 printing nozzles. The result is shown in figure 4.3. Since Silver and Aluminum have comparable work functions (around 4.3-4.4 eV), no rectification was obtained.

PET/Al/TIPS-pentacene/Au

In order to overcome the previous problem, Gold was used as top electrode, since it has a higher work function (around 5 eV). Figure 4.4 shows the pictures of the printed semiconductor, with 1 layer and 2 layers respectively. From figures 4.5 the electrical performance of the devices can be evaluated. In particular with 1 active layer of TIPS-pentacene, a poor but visible rectifying ratio at 6 V was observed (7 ± 2). The same parameter increased for the 2-layers diode, up to 31 ± 18: the high error band is mainly due to the very poor reproducibility of the printed TIPS-pentacene layer. This was the best result achieved with TIPS-pentacene

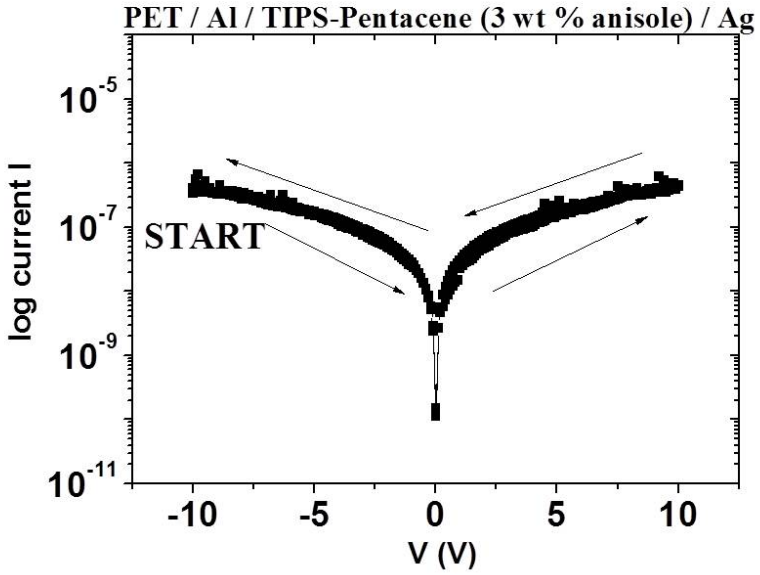

Figure 4.3: Current-voltage characteristic of the realized diode.

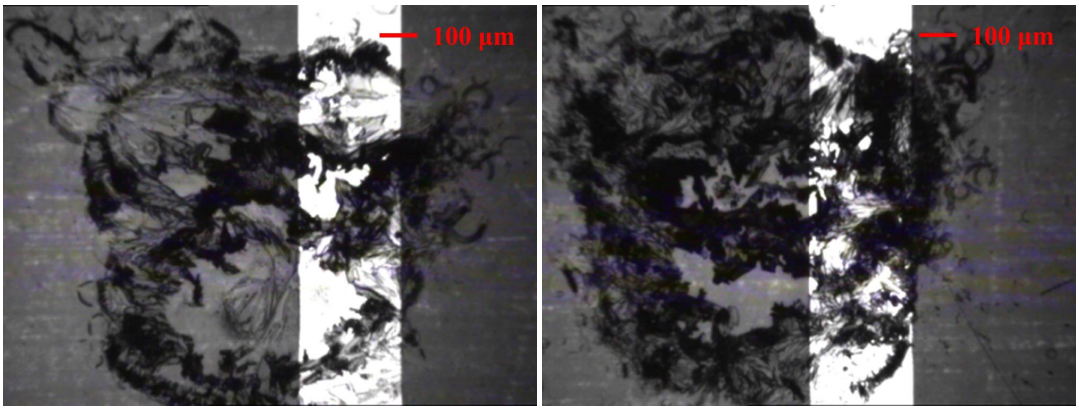

(a) (b)

Figure 4.4: Pictures of the diode active layer realized with TIPS-pentacene: (a) one layer and (b) two layers.

as active layer, far lower than the project requirements. the investigation went on employing P3HT:PCBM as semiconductor, since the printed layer was more flat and reproducible.

4.1.3 P3HT:PCBM based photodiodes

Since the results achieved with TIPS-pentacene were not satisfactory, P3HT:PCBM was employed as semiconductor, since the printed layer is more flat and reproducible. Ten different configurations were employed, as described in the followings. For the first six configurations,

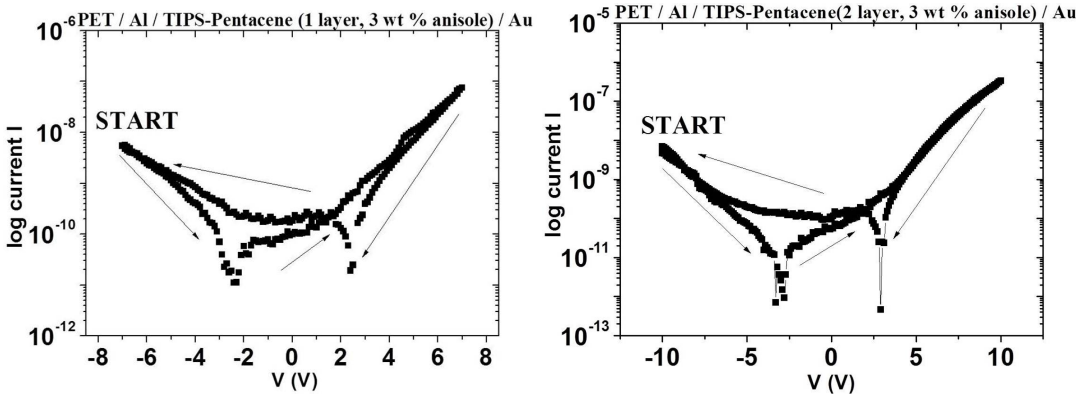

(a) (b)

Figure 4.5: Current-Voltage characteristics of the diodes realized with TIPS-pentacene: (a) one layer and (b) two layers.

PET was employed as substrate and the annealing and measurements were performed at room conditions. A marked enhancement of the electrical performances was obtained for the last four configurations, since PEN was employed as substrate, and the annealing process and the measurements were performed inside a glove box with nitrogen environment. Moreover, the annealing temperature was set up to 150 °C from the previous value of 100 °C of the first group.

PET/Ag/P3HT:PCBM (1 layer)/Au

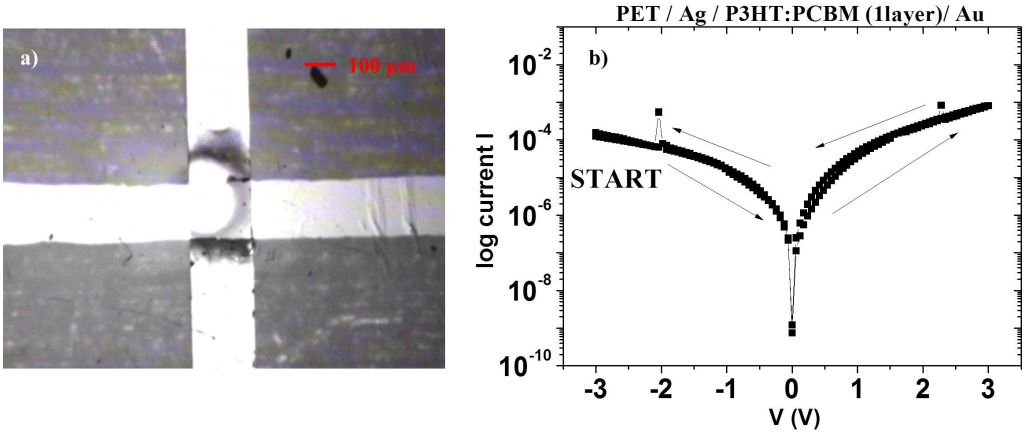

Figure 4.6: (a) Picture of the fabricated photodiode and (b) Current-Voltage characteristics.

Figure 4.6 shows the picture and the characteristics of the diodes realized in the following configuration: PET/Ag/P3HT:PCBM (1 layer)/Au. Very low rectifying values were obtained:

5.1 ± 0.6 at 3 V.

PET/Au/P3HT:PCBM (1 layer)/Ag

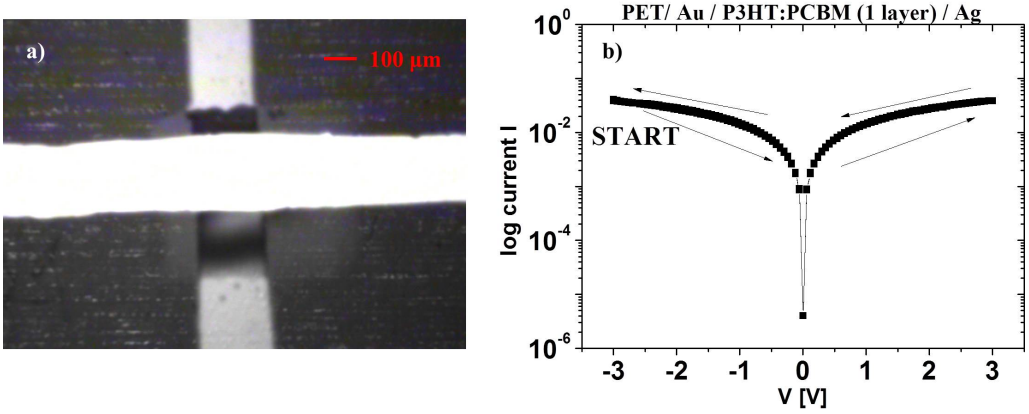

Figure 4.7: (a) Picture of the fabricated photodiode and (b) Current-Voltage characteristics.

Unfortunately, all the devices with Gold as bottom electrode were short-circuited.

PET/Ag/P3HT:PCBM (1 layer)/PEDOT:PSS

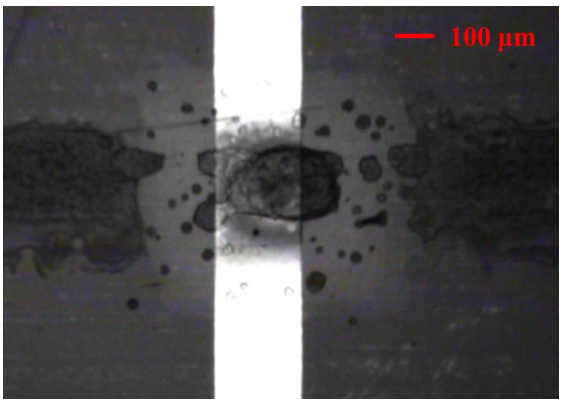

Figure 4.8: Picture of the fabricated photodiode.

PEDOT:PSS could not be printed on the P3HT:PCBM layer due to high repulsion and very low interfacial energy between these materials. This results in a discontinuity of the upper layer.

PET/PEDOT:PSS/P3HT:PCBM(1 layer)/Ag

Since PEDOT:PSS and Silver have almost the same work function, no rectification could be obtained, as shown in figure 4.9b.

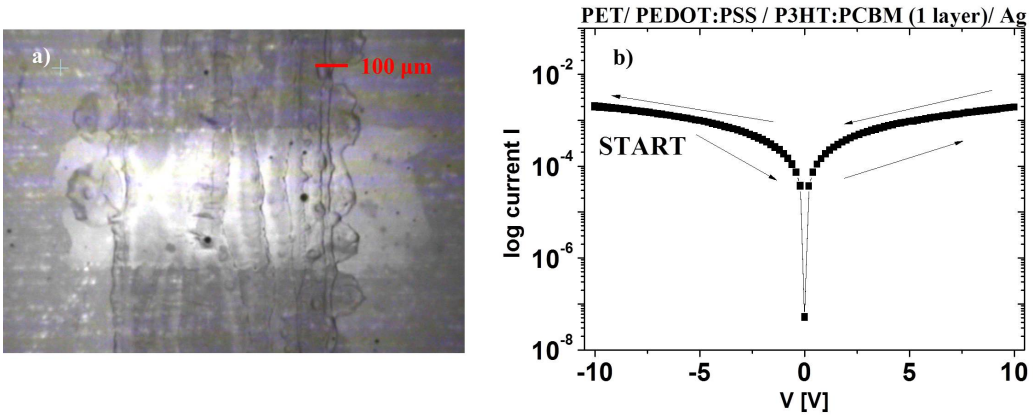

Figure 4.9: (a) Picture of the fabricated photodiode and (b) Current-Voltage characteristics.

PET/Al/P3HT:PCBM (1 layer)/Au

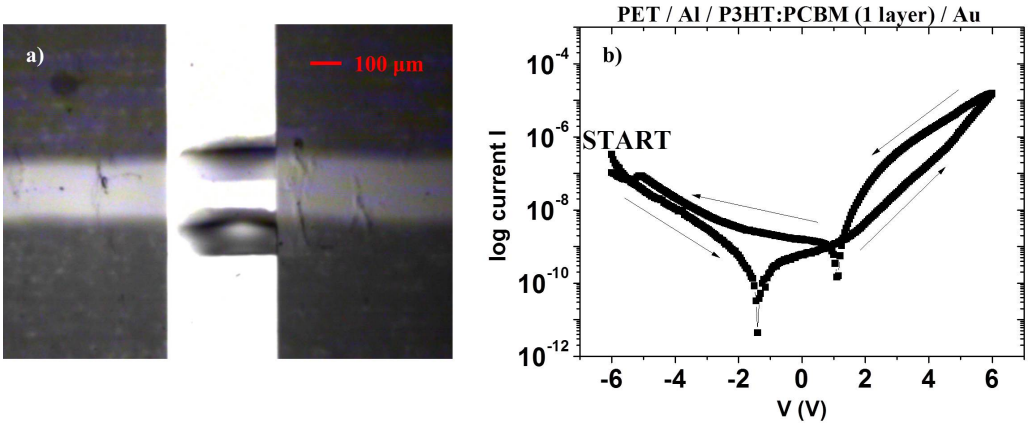

Figure 4.10: (a) Picture of the fabricated photodiode and (b) Current-Voltage characteristics.

In this case some rectifying behavior was observed, even if very poor. The rectifying ratio at 3 V was 5.1 ± 1.3, while it rose to 69 ± 23 at 6 V.

PET/Al/P3HT:PCBM (1 layer)/PEDOT:PSS

Depositing the PEDOT:PSS on P3HT showed the same problem as in the inverse situation. However, as it can be noted from figure 4.11a, some continuity could be obtained in this case, for some diodes. Only printing 3 layers of PEDOT:PSS lead to the small conductive pattern above the P3HT:PCBM layer. However, this resulted in a very poor rectifying ration: 4.9 ± 0.4.

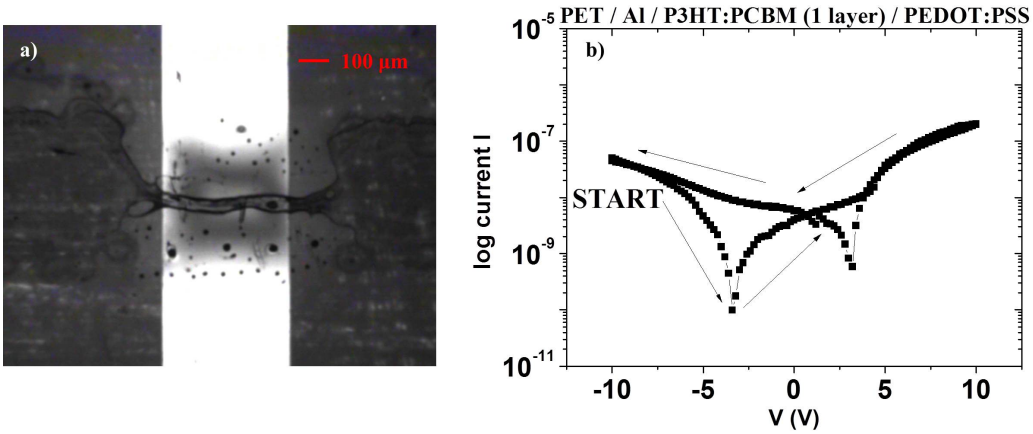

Figure 4.11: (a) Picture of the fabricated photodiode and (b) Current-Voltage characteristics.

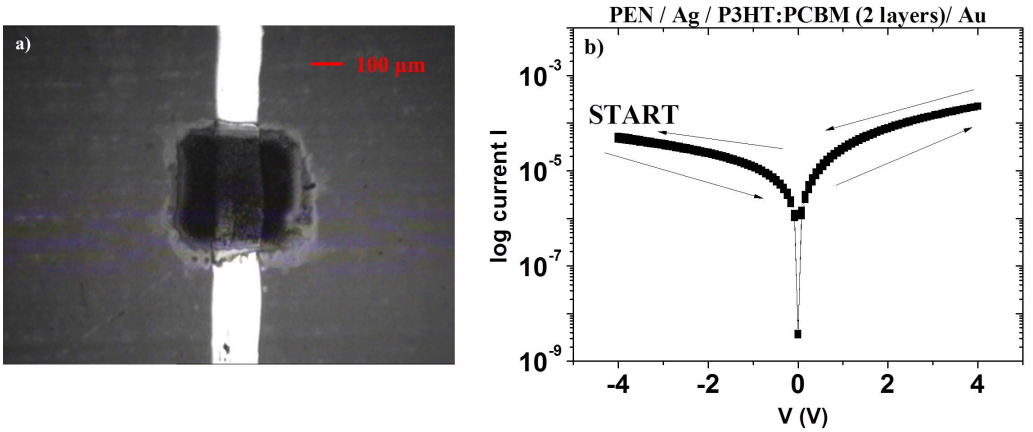

Figure 4.12: (a) Picture of the fabricated photodiode and (b) Current-Voltage characteristics.

PEN/Ag/P3HT:PCBM (2 layers)/Au

From this case on, PEN was employed as substrate and a higher annealing temperature was set for P3HT:PCBM. Also for this configuration, at 4 V, low rectifying ratio was achieved: 5.4 ± 0.2.

PEN/Al/P3HT:PCBM (1 layer)/Au

This was the configuration with the best electrical response obtained. In dark conditions, the rectifying ratio was $(9.2 \pm 0.2) \cdot 10^3$, higher than the requirements of the HYMEC project. Moreover, the photosensitivty was exploited by alternating changing dark and light on the devices. Figure 4.14 shows the electrical response of the device to light when it is reverse biased at -4 V. The current variation is higher than a order of magnitude.

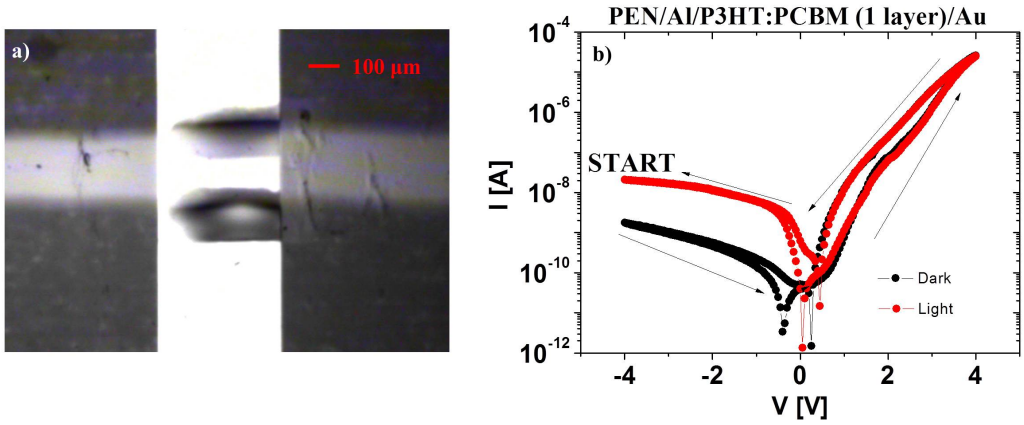

Figure 4.13: (a) Picture of the fabricated photodiode and (b) Current-Voltage characteristics.

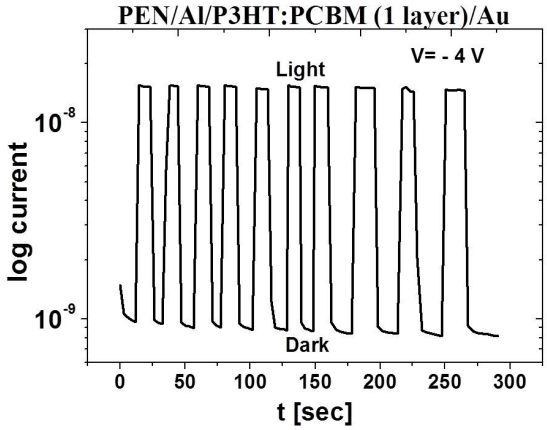

Figure 4.14: Time response of the reverse current to dark and light condition.

PEN/Al/P3HT:PCBM (1 layer)/(HTL)/PEDOT:PSS

In this case, a further layer (HTL, purchased together with the P3HT:PCBM ink) was printed upon the active layer in order to promote the charge carrier transfer to PEDOT:PSS. Wettability was improved and a fair continuity was obtained. Also, the rectifying ratio achieved was good: $(1.7 \pm 0.2) \cdot 10^3$. Also in this case the photosensitivity was investigated, and the results are shown in figure 4.16: the current value change more than one order of magnitude when passing from dark to light condition. This excursion was higher than the previous case, and this could be due to the transparency of PEDOT:PSS, which help the light penetration to the active layer.

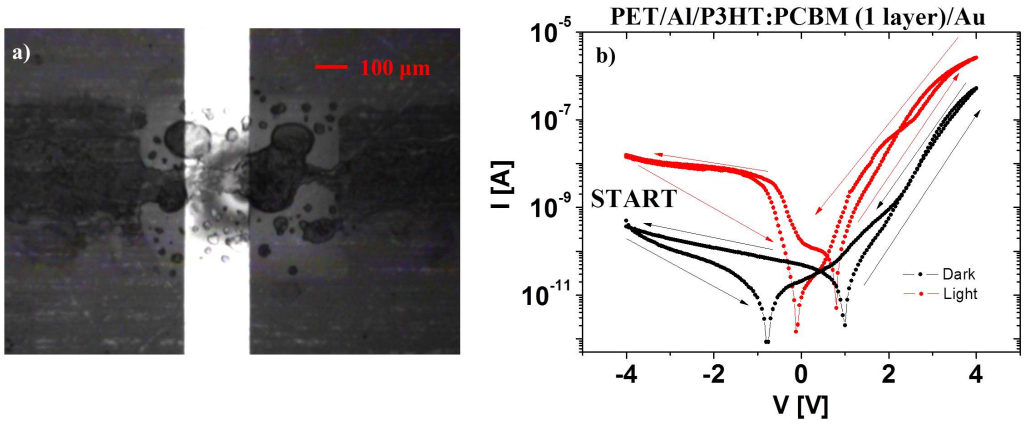

Figure 4.15: (a) Picture of the fabricated photodiode and (b) Current-Voltage characteristics.

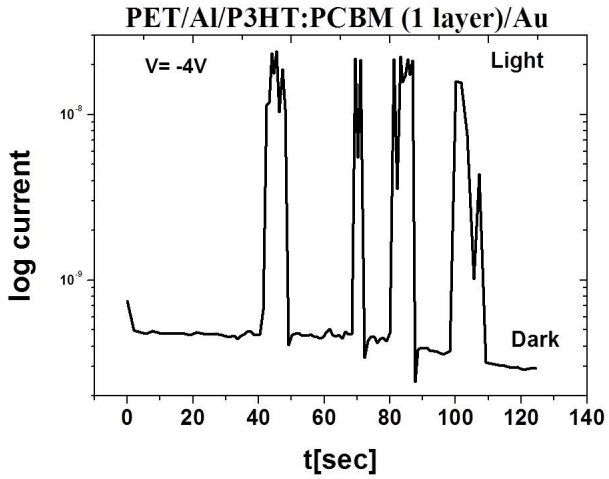

Figure 4.16: Time response of the reverse current to dark and light condition.

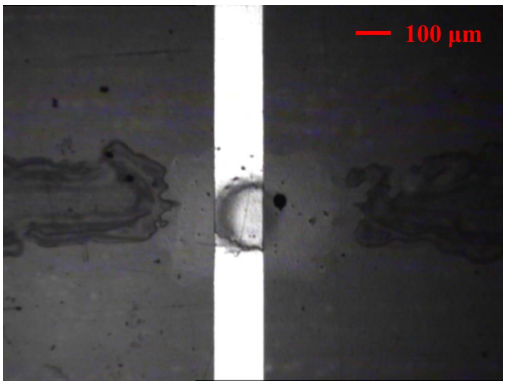

Figure 4.17: Picture of the fabricated photodiode.

PEN/Al/P3HT:PCBM (1 layer)/ PEDOT:PSS

Also, the previous structure was replied without printing the HTL ink: as supposed, the poor wettability of the P3HT:PCBM did not allow the continuity of PEDOT:PSS and thus no diode could be realized.

4.1.4 Treatment with PEIE

A preliminary investigation was performed on the PEIE treatment of the bottom electrodes of the photodiodes. The PEIE solution was prepared with 0.4 vol.% in 2-methoxyethanol, deposited on the bottom electrodes and spin coated at 5000 rpm for 60 s. After 10 min of drying in oven at 100 °C, the substrate was then rinsed for 60 s. The employment of the

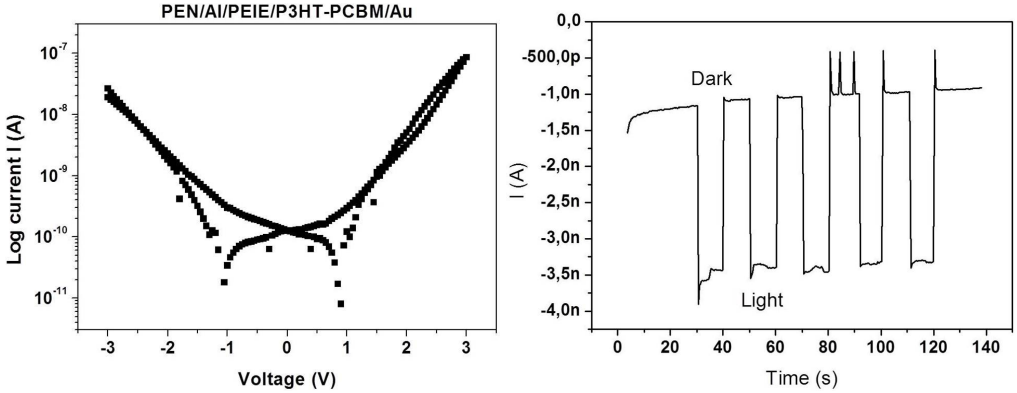

(a) (b)

Figure 4.18: (a) Current-Voltage of a photodiode treated with PEIE and (b) time response of the reverse current to dark and light condition.

PEIE, as reported by Azzellino *et al.*, is expected to increase the work function between silver and P3HT:PCBM and therefore to decrease the reverse current. However, as shown in figure 4.18a, the opposite effect was reached: a reverse current increase of one order of magnitude is noted, with a rectifying ratio not higher than 3. The photosensitivity is quite evident, with a current variation of 200% in the light with respect to dark condition.

4.2 Electroactuated membrane

The inkjet printing technique was also employed for the deposition of patterned layers on electroactuated membranes. The description reported in the followings is a part of the ongoing activity concerning this application.

The aim of this application is investigating the electrical response of cells when they are subjected on a mechanical stress, simulating the behavior of a stomach wall. In order to obtain

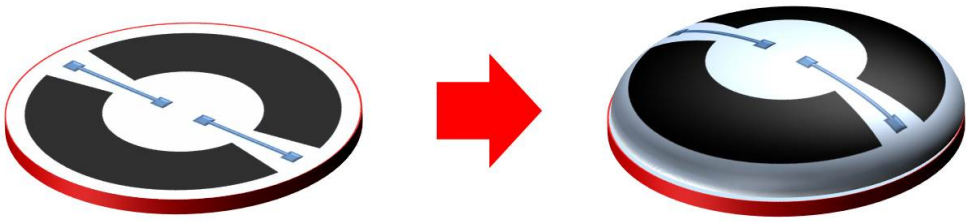

Figure 4.19: Scheme of the electroactuated membrane.

it, a membrane is adopted as shown in figure 4.19. Two different inks are used for the final patter. An annulus is printed with a Carbon-black (CB) based ink , which allows the deformation of the electroactuated membrane thanks to its electrical conductivity. On the other hand, small electrodes going from the center to the external part of the frame are printed with PEDOT:PSS based inks, since this material is biocompatible and thus suitable for cell growing. Therefore, in the final application, a cell culture is deposited in the center of the frame, the cells grow in the PEDOT:PSS pads and the membrane is deformed by applying a high voltage to the CB layer. The printing activity was split in two parallel phases: inkjet printing of PEDOT:PSS (Clevios™ CPP 105D) and inkjet printing of CB.

Inkjet printing of PEDOT:PSS

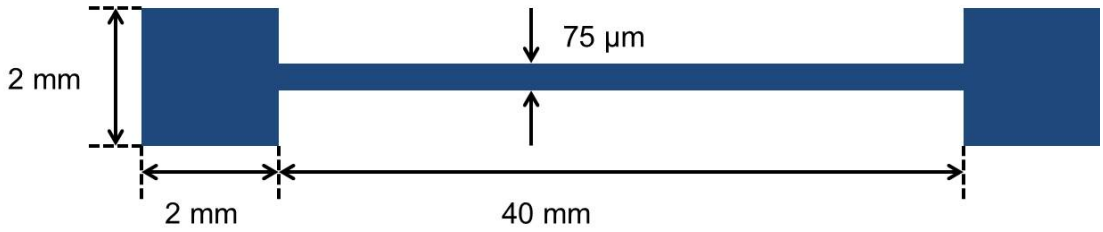

Figure 4.20: Layout of the printed PEDOT:PSS electrode.

The layout of the printed PEDOT:PSS electrodes is shown in figure 4.20: it consists of two square pads, with 2 mm side, connected with a 75 μm wide line. Due to the small width of the line, this can be classified as a high-resolution pattern. Therefore it was printed with a single nozzle, with a 40 μm drop spacing. Figure 4.21 shows the resulting printed layer. The measured resistance was $3 \cdot 10^6 \Omega$, quite too high to detect the electrical signals of the cell activity. A future steps require the formulation of an ink comprised of PEDOT:PSS and ethylene glycol,

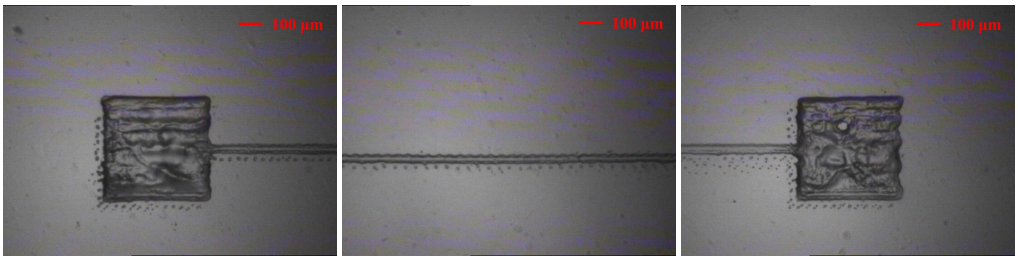

(a) (b) (c)

Figure 4.21: Inkjet printed PEDOT:PSS patterns on the electroactuated membrane.

which could enhance the conductivity of the printed layer and therefore allow the detection of the cell signals.

Inkjet printing of Carbon black

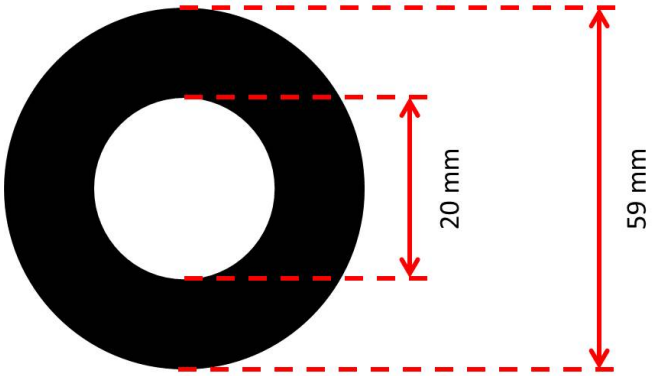

Figure 4.22: Layout of the printed carbon-black electrode.

Figure 4.22 schematizes the layout of the first prototype of the CB-based electrode. It basically consists of an annulus with external diameter of 59 mm and inner diameter of 20 mm. Since the CB is usually deposited by brushing, an opportune formulation of a CB-based ink for inkjet printing is mandatory even for this low-resolution pattern.
Two different formulations were investigated. The first one employs a varnish and a alcohol solvent as a basis for the solution. Moreover, DBSA was used as surfactant to increase the viscosity and decrease the surface tension of the ink. Table 4.1 shows the specific formulations for the first type of CB-based ink. As it can be noticed, adding CB powder to the solution does not affect the viscosity value more than some fraction of centipoise. On the contrary, adding DBSA, even if in minimal quantity, considerably affects the viscosity of the formulated ink. Using the last formulation, with DBSA added, a 10 pL cartridge was filled. The drop ejection

CB	Varnish	Solvent	DBSA	Viscosity
0.00 g	1 g	5 g	0 μL	1.78 cP
0.05 g	1 g	5 g	0 μL	1.82 cP
0.10 g	1 g	5 g	0 μL	1.88 cP
0.10 g	1 g	5 g	20 μL	4.52 cP

Table 4.1: Ink formulation and measured viscosity for the first type of CB-based ink.

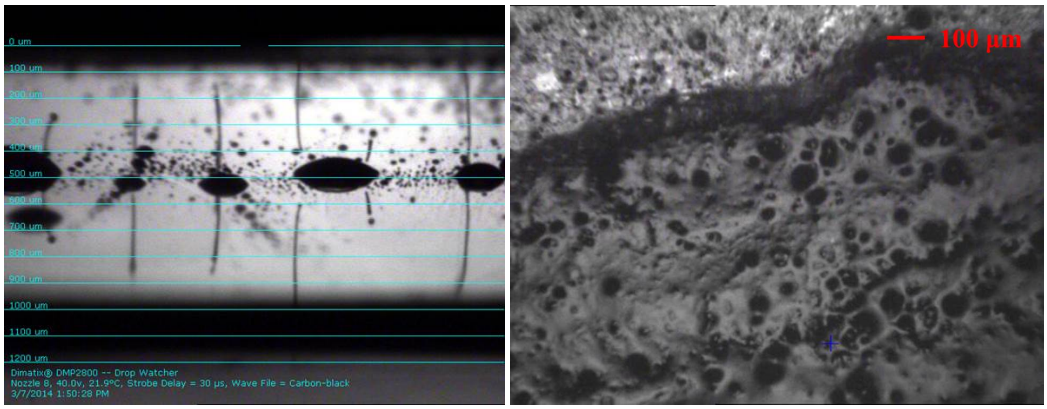

(a) (b)

Figure 4.23: (a) Drop ejection and (b) printed layer of the first type of CB ink formulation.

of this ink was not very good, as shown in figure 4.23a, since the droplets were chaotic. Anyways, no nozzle clogging occurred. The printed layer is shown in figure 4.23b: it was optically continuous, but the whole pattern could not be printed since the cartridge overcame ink depletion. The layer was then annealed at 60 °C for 3 days, but no electrical conductivity could be measured.

The second type of ink formulation employs water and isopropylic alcohol as solvents. Also in this case DBSA was added to increase the viscosity and decrease the surface tension. The

CB	Water	Isopropyl alcohol	DBSA	Viscosity
0.00 g	20 mL	10 mL	0 μL	1.32 cP
0.05 g	20 mL	10 mL	0 μL	1.40 cP
0.05 g	20 mL	10 mL	10 μL	3.56 cP

Table 4.2: Ink formulation and measured viscosity for the second type of CB-based ink.

formulation is presented in table 4.2. As state before, the major contribution to viscosity was given by the addition of DBSA. The results are shown in figure 4.24. In particular, from figure 4.24a a good drop ejection can be noticed. Anyways, as seen from figure 4.24b, the printed

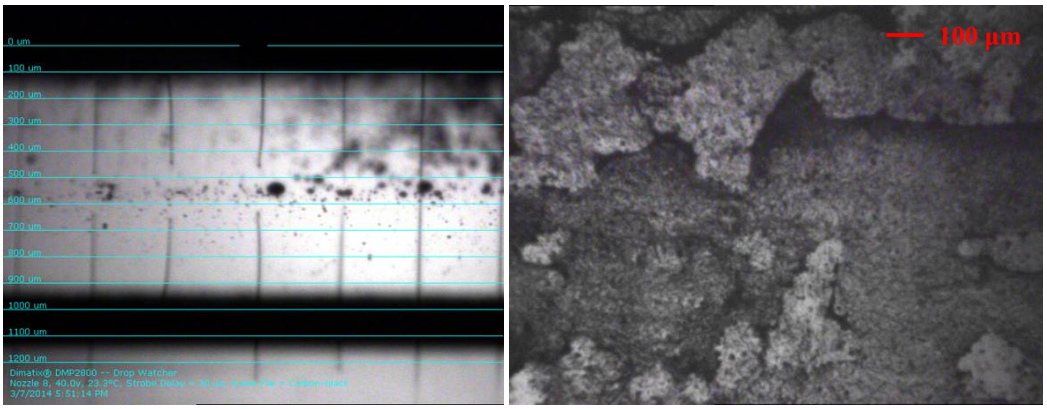

(a) (b)

Figure 4.24: (a) Drop ejection and (b) printed layer of the second type of CB ink formulation.

layer was discontinuous, since the acetate substrate resulted quite hydrophobic. A solution to this issue could be a preliminary plasma treatment of the substrate and the investigation of new ink formulations.

4.3 Gustometer

An interesting application of inkjet printing, ranging out from the classical field of organic electronic devices, is the *gustometer*, *i. e.* an instrument used to measure a predetermined amount of a taste or a gustatory stimulus applied to the tongue of a person over a specified period of time [157]. Standard measurements consist of a combination of Electroencephalography (EEG) and Magnetoencephalography (MEG) signals recorded when the taste buds are stimulated [158]. However, another approach could be detecting directly the electrical signals of the taste buds by means of an electrode applied on the tongue [159]. The printed organic electronics can be employed in this field as an innovative, low-cost technology for creating thin film patterned electrodes for gustatory signal applications.

The original idea consisted of employing a thin PDMS substrate, which makes a conformal contact on every kind of surface, and depositing on it a patterned electrode through inkjet printing. The Sylgard® PDMS substrate was prepared as described in section 3.3.2, first preparing the solution, then spinning it on a flat silicon wafer and last annealed in oven. The layout of the printed electrode is shown in figure 4.25: it is basically composed of a square frame, with an internal side of 15 mm, ending with a long trace. The inner square of the electrode is the place where the test solutions are deposited on the tongue, thus the stimulated taste buds are surrounded by an electrode which carries the signals to the readout circuitry.

Figure 4.25: Layout of the printed electrode.

The long trace provides a separation between the signal generation and the circuitry, avoiding the salivary liquid to damage the electrical contact.
A first trial was made by printing CCI-300 on PDMS. As stated in section 2.4.1, printing silver ink and PEDOT:PSS ink on PDMS results in very discontinued structures, due to the low interfacial energy between these materials. Thus, a plasma treatment is required before printing (60 s, 75 W). After the plasma treatment, a silver ink layer was deposited on PDMS, as shown

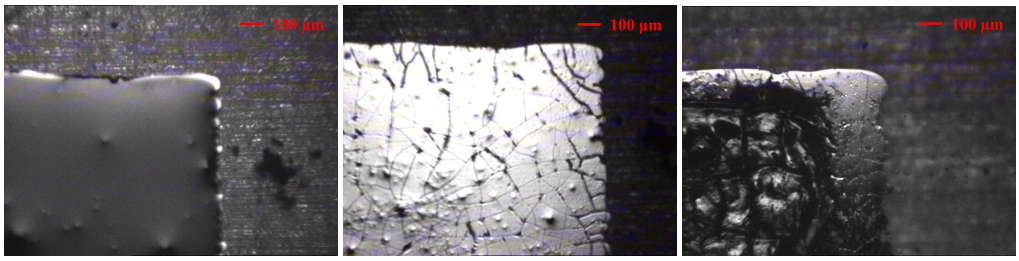

(a) (b) (c)

Figure 4.26: (a) Ag ink printed on a PDMS substrate previously subjected to plasma treatment; (b) Ag layer annealed with cracks; (c) an additional PEDOT:PSS layer printed on the structure.

on figure 4.26a. Unfortunately, due to the high surface strane which the deposited layer was subjected to, many cracks were formed after the annealing process (figure 4.26b), which created many discontinuities. In oder to overcome this problem, a further PEDOT:PSS layer was inkjet printed, allowing the electrical conductivity over the whole pattern.
After the fabrication, experimental tests were performed to study the conductivity of the electrode. An *agar agar* substrate, prepared from a solution with sodium chloride (NaCl), was used to reproduce the consistency of the human tongue and to measure the electrical conductivity of the layer. Unfortunately, minimum scratching of the layer, or sliding it onto the wet substrate, caused the immediate removal of the combined silver/PEDOT:PSS layer. This

represents therefore a major limit of the printed electronics. n fact, later silver was thermally evaporated on 13 μm kapton substrates. The same mechanical test, performed both on an agar agar substrate and on a human tongue, revealed that a good mechanical resistance could be obtained in this case. This is due to the micro-structure of the two types of layer: the evaporated silver has a compact crystalline structure, whereas the printed silver layer is composed of nanoparticles whose continuity is guaranteed by theraml sintering, but which do not form a uniform crystalline layer. This results in a more fragile structure.

4.4 Radio Frequency Identification tag

This section describes another application of the inkjet printing technique: the fabrication of *Radio Frequency IDentification tags* (RFIDs). The growing interest on this field has been already described in section 1.1.3. The activity and the results described in the followings, carried on in collaboration of the Group of Electromagnetic Fields at the University of Cagliari, have been published in a *IEEE Antennas and Wireless Propagation Letters* [160].

Passive RFIDs, whose principles have been studied since 1948, have nowadays become standard devices in fields such as retail and distribution logistics. RFID systems operating in a range greater than a meter are classified as long-haul systems and operate using electromagnetic waves at UHF frequencies (860-960 MHz). Great work for the fabrication of RFIDs is made in order to fulfill several requirements, such as reduction of costs, weight, size, complexity, and no need of special maintenance. Printed Electronics, and especially inkjt printing, can easily satisfy these requirements. Recent literature reports the realization of several inkjet printed RFID tags by employing cheap substrates as PET [161–163].

The antenna realized by inkjet printing in this work was designed to cover the whole UHF band by using a meandered dipole, which results in a compact structure with an omnidirectional far-field pattern in the plane perpendicular to the axis of the meander. The layout

L_1	L_2	L_3	L_4	L_5	L_6	L_{s1}	L_{s3}
14	29.8	12.3	10.3	8.3	13.7	2.7	3

Table 4.3: Geometry of the antenna realized in figure 4.27. All dimensions are in mm.

of the printed RFID tag is presented in figure 4.27 and the geometry is specified in table 4.3. From a printing point-of-view, this is a low-resolution pattern which did not require any particular calibration: the stantard parameters, listed in section 2.4.1, were set. 175 μm thick PET was used as substrate and CCI-300 silver ink was conductive ink. Some rare pattern dis-

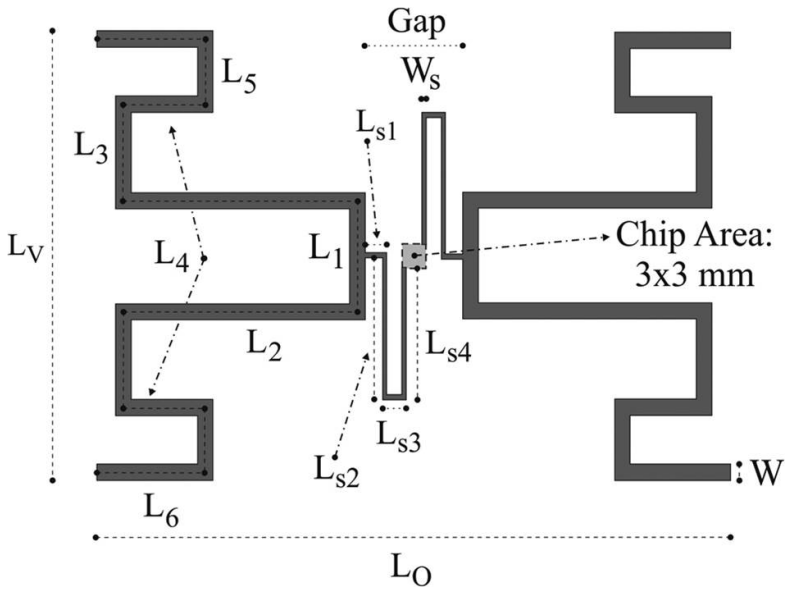

Figure 4.27: Layout of the designed RFID tag. L_O = 80.9 mm, L_V = 57.2 mm, W = 2 mm, W_s = 5 mm, Gap = 12.5 mm.

continuities were easily filled by printing an additive layer. After printing, this pattern was annealed in oven at 60 °C for 3 days. After the annealing procedure, the PET substrate was

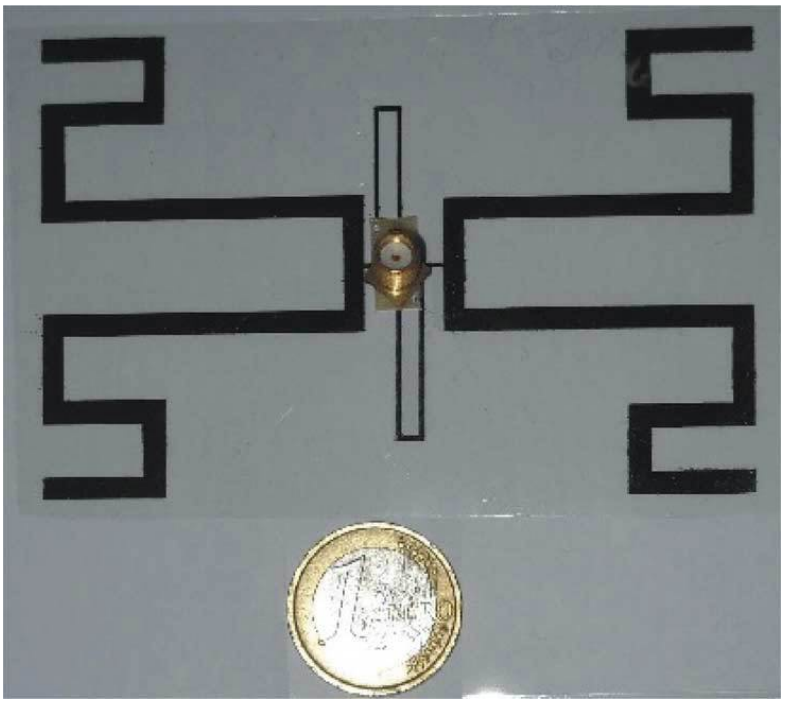

Figure 4.28: Picture of the realized antenna.

connected to a SMA connector by two rivets and the electrical contact between SMA and sil-

ver ink has been realized through a conductive silver paste. The final structure is shown in figure 4.28.

Figure 4.29a shows the E-plane and the H-plane radiation patterns, simulated and mea-

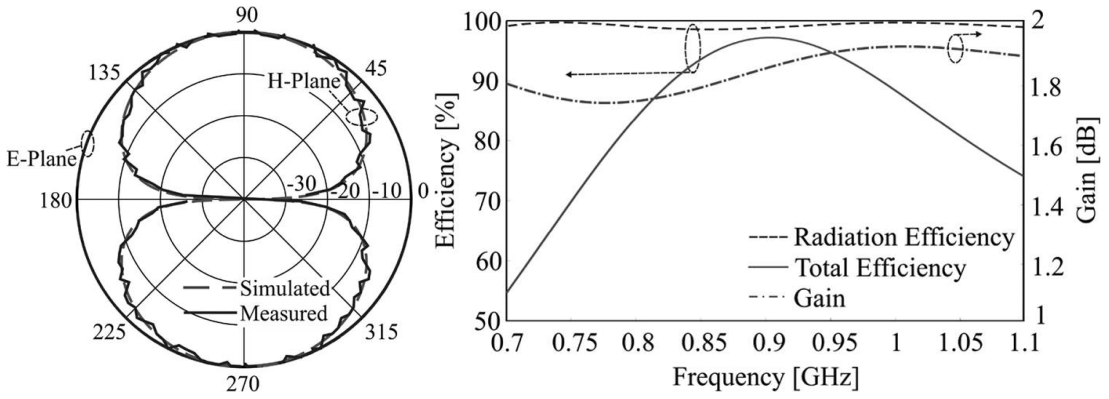

(a) (b)

Figure 4.29: (a) Normalized far-field pattern (dB) at 900 MHz and (b) gain in the broadside direction and efficiency of the designed RFID tag antenna.

sured at 900MHz. In particular, the H-plane is broadside and bidirectional, while the E-plane is omnidirectional over all the operating bandwidth, with a peak antenna gain equal to 1.9 0.15 dBi and a cross-polar component 40 dB below the copolar one. Also the gain and the efficiency were investigated, as reported in figure 4.29b. The simulated gain in the broadside direction, in a wide frequency band, namely from 700 to 1100 MHz, remains almost constant even in this large frequency range. Also the simulated radiation efficiency is very high in this frequency band, as it remains almost constant in the whole range. Moreover, the total efficiency, which takes account both of the antenna and the microchip impedance, is higher than 80% in a wide energy band, from 825 to 1025 MHz. Moreover, a parametric analysis demonstrated the robustness of the realized antenna: even changing the substrate thickness from 100 to 400 μm and its dielectric constant from 2 to 5, the electromagnetic behavior, *i. e.* the complex impedance, of the realized structure remains very stable.

Conclusions

Inkjet Printing has been investigated as a successful deposition technology to be employed in Organic Electronics. The printing technique has been analyzed and described in order to fabricate several types of organic electronic devices for various applications. The key requirement in this thesis was that all printable materials were soluble, *i. e.* could be processed in liquid form to create an ink. In particular, a drop-on-demand piezoelectric printer has been employed.

A detailed experimental procedure has been set up, starting from the ink composition, which accounted for the specific requirements of the final device. A continuous feedback of the devices' electrical performance has been used to tune the ink formulation, the printing parameters and in general all the experimental conditions which affect the final result. Several materials have been printed, both conductors, semiconductors and insulators, in order to realize different patterns, mainly divided in low-resolution patterns and high-resolution patterns. For each ink type, a complete empirical printing setup has been reported which could optimize the deposition process.

The major application of the Inkjet Printing technique in this thesis concerned the realization of Organic Field-Effect Transistors (OFETs) to be employed as strain sensors over large area. OFETs have been realized in bottom-gate/bottom-contact configuration, mainly with interdigitated source and drain electrodes. Thanks to the refinement of the printing procedure, the channel length has been scaled down from 50 μm to 23 μm; moreover the process yield, *i. e.* the number of working devices, rose from 75% to more than 90%. Several types of semiconductor were deposited both by inkjet printing, drop casting and spin coating. In particular, the best performances have been obtained with drop cast TIPS-pentacene, with mobility values up to $2 \cdot 10^{-1}$ cm^{2}V^{-1}s^{-1}. A study on inkjet printing of TIPS-pentacene has been carried out adopting both the multiple-drops approach and the single-droplet approach, the latter by means of a micro-drop printer. In the first case, mobilities up to 10^{-2} cm^{2}V^{-1}s^{-1} have been obtained, while in the second case they reached $6 \cdot 10^{-2}$ cm^{2}V^{-1}s^{-1}. Moreover, with the

single-droplet approach a stronger dependence of mobility on the drop volume, *i. e.* on the amount of material per unit area, than on the *coffee-stain* effect has been demonstrated.
The electromechanical characterization of OFETs, arranged in $8 \cdot 8$ matrix structures, showed a good time response, only with a small mechanical and electrical crosstalking. A deep study on the response calibration has been carried out when the substrates are combined with PDMS elastomer. Results showed a good reproducible sensitivity, with a resolution of 0.1 N and linear trend up to 1 N. Moreover, stress tests have been performed which highlighted the electrical response stability over a large number of cyclic mechanical stimuli.
Finally, the versatility of Inkjet Printing has been exploited to realize other types of organic devices. Organic Diodes and Photodiodes have been realized as vertical structures, employing a wide range of materials combinations for the bottom and top electrodes. The resulting devices showed good rectifying characteristics and good sensitivity to light. In particular, a rectifying ratio up to 10^4 have been reached, and a currenct increase higher than one order of magnitude from dark to light condition has been obtained. As a collateral application, organic electrodes have been printed to be employed for the monitoring of electrical activity of cells and taste buds. Finally, Inkjet Printing was employed to successfully realize a low-cost RFID tag on a plastic substrate.

A Devices

This appendix briefly describes the structure and the working principles of the main organic devices fabricated: Organic Diodes (section A.1) and Organic Field-Effect Transistors (OFETs, section A.2).

A.1 Diodes

Diode structures of inorganic electronics can be basically of two types: diodes based on p-n junctions and diodes based on metal-semiconductor junctions, referred as Schottky diodes. In organic electronics, because of the morphology of the organic semiconductors, the most employed type is the Schottky diode, schematized in figure A.1. It basically consists of a

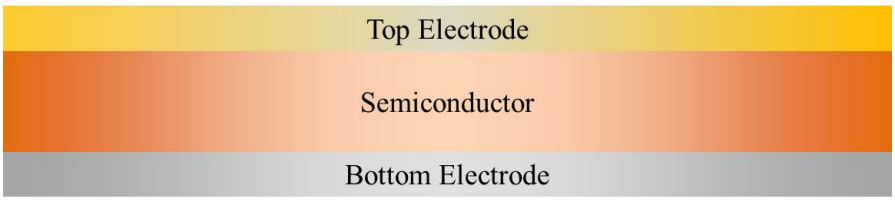

Figure A.1: Schematics of a organic Schottky-type diode.

semiconductor layer comprised between two conductive layers, therefore formic two metal-semiconductor contacts. The charge carriers injection from the conductor to the semiconductor, and *vice versa*, is strongly influenced by the difference between the Fermi level of the conductor and the HOMO and LUMO levels of the semiconductor, as shown in figure A.2a. A more accurate model, provided by Kahn *et al.* [164], takes account of the adsorption of atoms and molecules on the metal surface, which results in a misalignment of the vacuum levels and a shift of the energy levels (figure A.2b). In both figures, $q\phi_{Be}$ and $q\phi_{Bh}$ are the electron and hole barrier respectively. When a positive voltage is applied to the conductor with re-

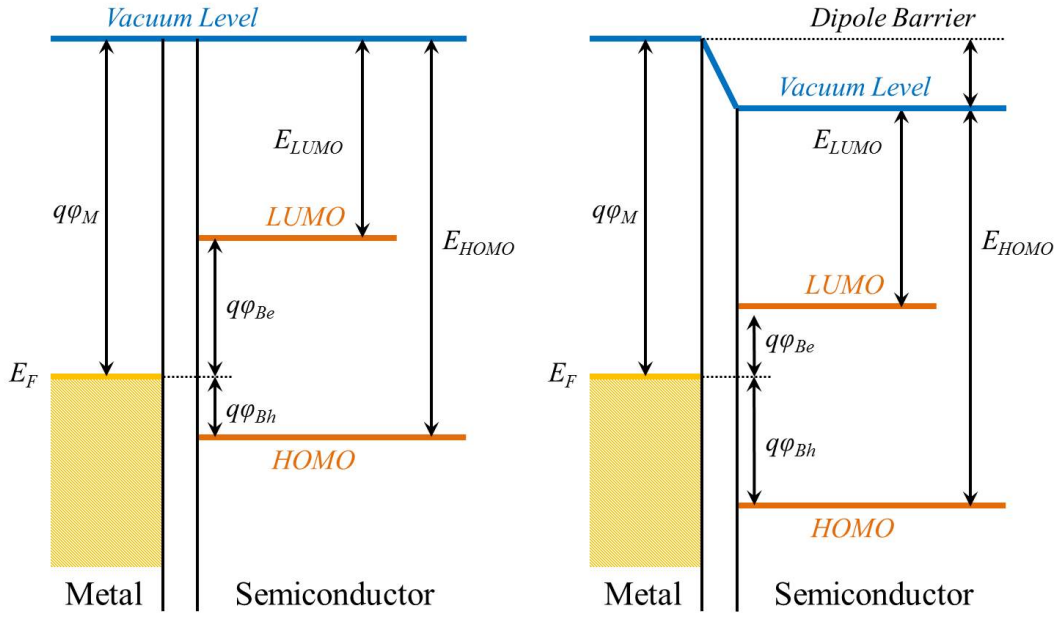

Figure A.2: Energy diagram of a metal-organic semiconductor interface without (a) and with a dipole barrier.

spect to the semiconductor, the hole injection to the semiconductor is eased if $q\phi_{Bh}$ is low; similarly, when a negative is applied to the conductor with respect to the semiconductor, the electron injection to the semiconductor is eased if $q\phi_{Be}$ is low. In both cases, a ohmic contact is formed. Therefore, unlike the inorganic counterpart, organic semiconductors are not intrinsically n-type or p-type. Moreover, if $q\phi_{Be}$ and $q\phi_{Bh}$ are sufficiently high, the charge injection is limited and a rectifying contact is formed.

The Schottky diode is obtained by the combination of an ohmic contact and a rectifying contact. Several models have been formulated for the current flowing in a organic diode [165, 166] which account for the thermal traps and low-voltage effects. However, a first approximation equation for the current is:

$$J = J_s\left(e^{\frac{qV}{kT}-1}\right) \tag{A.1}$$

A.2 Organic Field-Effect Transistors

In silicon-based transistors(MOSFETs), each component of the devices, such as the metal electrodes and the gate oxide, are deposited on the silicon wafer, which therefore acts as the bulk substrate. On the contrary, Organic Field-Effect Transistors (OFETs) are based on

organic semiconductors which cannot be free-standing. The whole structure is fabricated on a substrate, usually plastic, by means of a layer-by-layer deposition. According to the order

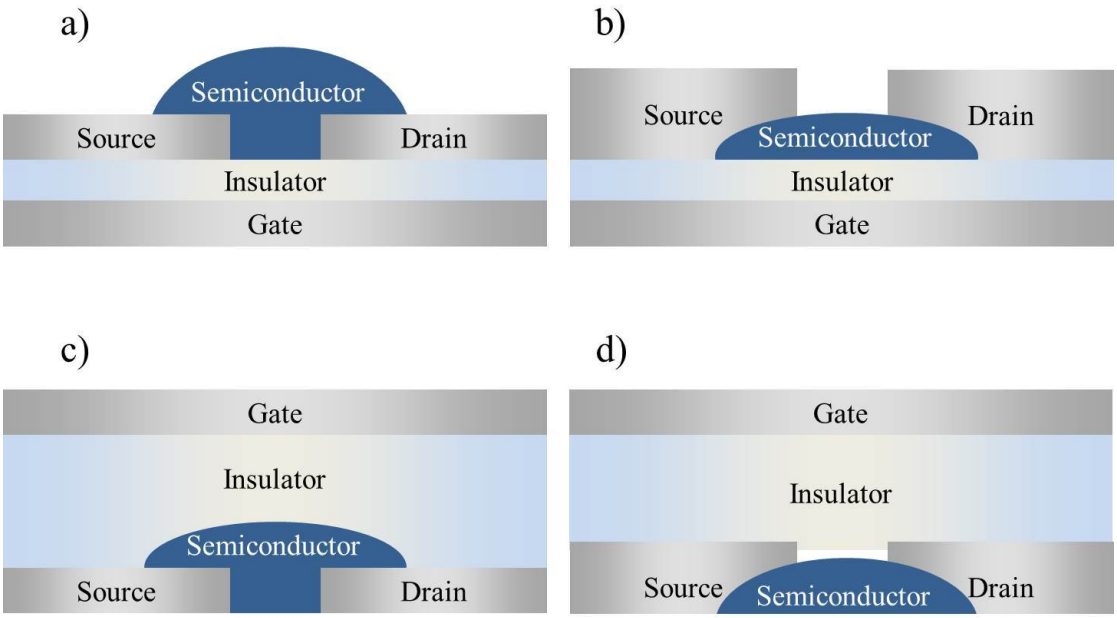

Figure A.3: Possible structures for an OFET: (a) bottom-gate/bottom-contact, (b) bottom-gate/top-contact, (c) top-gate/bottom-contact, (d) top-gate/top-contact.

od the layer deposition, four different OFET configurations can be employ, as schematized in figure A.3:

a) *bottom-gate/bottom-contact*: the gate, source and drain electrodes are deposited before the semiconductor, which is the final layer.

b) *bottom-gate/top-contact*: the gate is deposited as first layer, but the source and drain electrodes are deposited on the semiconductor.

c) *top-gate/bottom-contact*: the source and drain electrode are deposited as first layer, then the semiconductor, and the gate electrode is the final layer.

d) *top-gate/top-contact*: the semiconductor is deposited as first layer, and then the source, drain and gate electrode are deposited above it.

Horowitz *et al.* [167] gave a very detailed description of the OFETs working principle. OFETs operate in the *accumulation* regime, where the gate voltage is polarized positively (negatively) versus the n-type (p-type) substrate. Accordingly, the source and drain consist of simple ohmic contacts on a thin semiconductor film. In such a geometry, there is no depletion

layer to isolate the conducting channel from the substrate, as in MOSFETs, and a very low conductivity is therefore required. Another consequence of the absence of a depletion layer is that in principle, the threshold voltage should be nil. However, in most real OFETs, a threshold voltage is indeed found, which is ascribed to a *gate-bias-dependent* mobility, a feature that is tentatively attributed to the charge transport mechanism in organic materials.
As a consequence, a non-zero value for the threshold voltage V_T is measured, and two operative regimes, namely *linear regime* and *saturation regime*, are described by the following equations:

$$I_{DS,lin} = \frac{W}{L}\mu C_{ins}\left[(V_{GS} - V_T)\,V_{DS} - \frac{V_{DS}^2}{2}\right] \tag{A.2}$$

$$I_{DS,sat} = \frac{W}{2L}\mu C_{ins}\,(V_{GS} - V_T)^2 \tag{A.3}$$

where W and L are the channel width and length respectively, μ the field-effect mobility of the semiconductor (already described in section 1.2.1) and C_{ins} the gate capacitance. It is worth remarking that the considerations made in the previous paragraph about the metal/semiconductor interface can be applied also to the metal/insulator/interface. As a consequence, OFETs work in *accumulation* regime rather than *inversion* regime as MOSFETs.

B Characterization techniques

In this appendix a brief description of the characterization techniques is given. More specifically, in section B.1 the electrical characterization of organic devices is presented, while in section B.2 the working principle of a viscometer is described.

B.1 Electrical characterization

The electrical characterization of the organic devices was performed by means of a Keithley Sourcemeter 2612. The characteristics were taken by applying a voltage to the electrodes and measuring the current. For the diode characterization, two electrodes are employed. The main figure-of-merit, *i. e.* the rectifying ration at V_0, is calculated by dividing the current value at V_0 by the current value at $-V_0$.

On the contrary, the electrical characterization of the OFETs is performed by biasing three electrodes and the calculation of the main figures-of-merits, *i. e.* the field-effect mobility μ and the threshold voltage V_T, require a mathematical rearrangement of the characteristics. In particular the square-root can be calculated from equation A.3:

$$\sqrt{I_{DS,sat}} = \sqrt{\frac{W}{2L}\mu C_{ins}} \cdot (V_{GS} - V_T) \tag{B.1}$$

This is a linear equation of the form $y = mx + q$, where

$$y = \sqrt{I_{DS,sat}} \quad x = V_{GS} \quad m = \sqrt{\frac{W}{2L}\mu C_{ins}} \quad q = -\sqrt{\frac{W}{2L}\mu C_{ins}} \cdot V_T$$

The parameters m and q can be extracted by a linear fitting of equation B.1. Finally, μ and V_T can be extracted as follows:

$$V_T = -\frac{q}{m} \quad \mu = \frac{m^2}{\frac{W}{2L}C_{ins}} \tag{B.2}$$

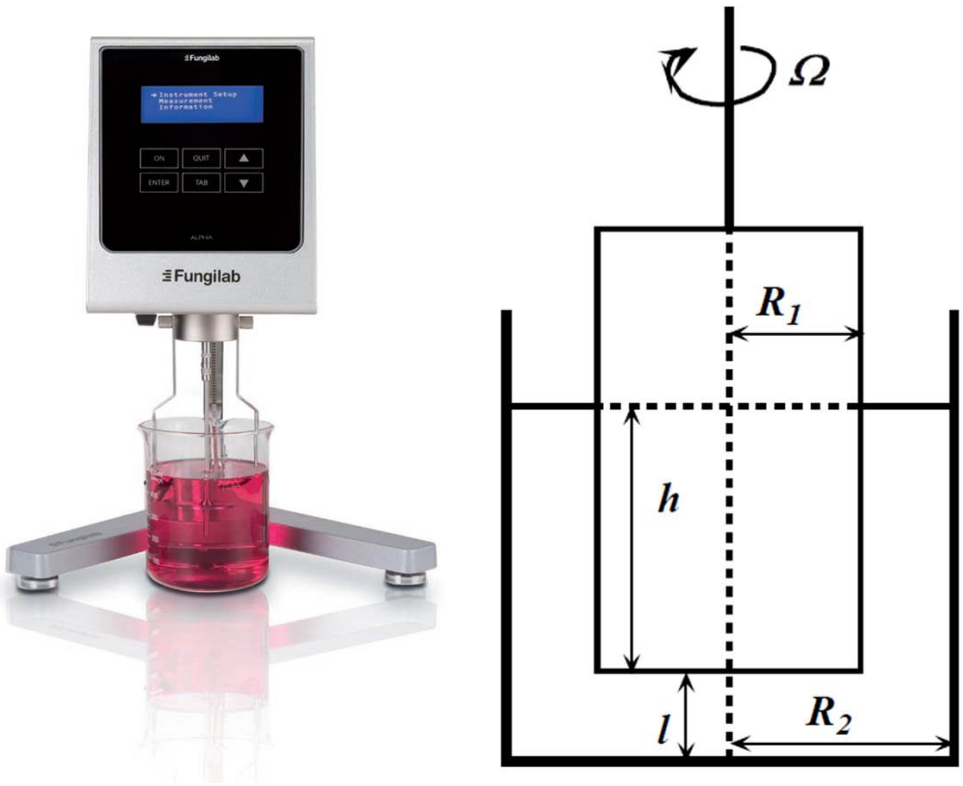

(a) (b)

Figure B.1: (a) Fungilab® viscometer *Alpha L* employed for this thesis. (b) Schematic of the working principle of a rotational coaxial-cylinder viscometer.

B.2 Viscosity measurement

The ink viscosity, described in paragraph 2.2.2, is measure by means of an instrument called *viscometer*. In particular, the viscometer employed during the work of this thesis was purchased by Fungilab® and is shown in figure B.1a. The standard version can measure viscosity in the range 20-2000000 cP, but by the addition of an adaptor viscosities as low as 1 cP can be measured. According to the viscosity range, 18 rotational speeds can be set.

The working principle of this rotational viscometer, of coaxial-cylinder type, is schematized in figure B.1b. Further details can be found in [2]. The viscometer consists of an inner cylinder of radius R_1 and height h, and an outer cylinder of radius R_2. The latter, which contains the ink sample, is stationary, while the former, suspended by a fine wire, is rotated at a constant speed Ω (rad/s). The resultant torque T (dyne $\cdot$ cm) is measured by the angular deflection of the inner cylinder. If a newtonian fluid is considered, the dynamic viscosity is

obtained from the following expression:

$$T = \frac{4\pi R_1^2 R_2^2 h\eta\Omega}{R_2^2 - R_1^2} = C \cdot \eta \cdot \Omega \tag{B.3}$$

where C contains all the constant specific of the instrument. Basically, given C, set Ω as input and measured T as output, the dynamic viscosity η can be evaluated as a proportional factor between T and Ω.

Bibliography

[1] C. D. Dimitrakopoulos and D. J. Mascaro, "Organic thin-film transistors: a review of recent advances," *IBM J. Research Devel.*, vol. 45, no. 1, pp. 11–27, 2001.

[2] D. S. Viswanath, T. K. Ghosh, D. H. L. Prasad, N. V. K. Dutt, and K. Y. Rani, *Viscosity of Liquids. Theory, Estimation, Experiment, and Data.* Springer, 2007.

[3] B.-J. de Gans, P. C. Duineveld, and U. S. Schubert, "Inkjet Printing of Polymers: State of the Art and Future Developments," *Adv. Mater.*, vol. 16, no. 3, pp. 203–213, 2004.

[4] A. L. Yarin, "DROP IMPACT DYNAMICS: Splashing, Spreading, Receding, Bouncing," *Ann. Rev. Fluid Mech.*, vol. 38, pp. 159–192, 2006.

[5] G. Whyman, E. Bormashenko, and T. Stein, "The rigorous derivation of Young, Cassie–Baxter and Wenzel equations and the analysis of the contact angle hysteresis phenomenon," *Chem. Phys. Lett.*, vol. 450, no. 4-6, pp. 355–359, 2008.

[6] J. A. Lim, W. H. Lee, H. S. Lee, J. H. Lee, Y. D. Park, and K. Cho, "Self-Organization of Ink-jet-Printed Triisopropylsilylethynyl Pentacene via Evaporation-Induced Flows in a Drying Droplet," *Adv. Funct. Mater.*, vol. 18, no. 2, pp. 229–234, 2008.

[7] H. Hu and R. G. Larson, "Marangoni Effect Reverses Coffee-Ring Depositions," *J. Phys. Chem. B*, vol. 110, no. 14, p. 7090–7094, 2006.

[8] E.-S. Hwang, J.-H. Seo, and Y.-J. Kim, "A Polymer-Based Flexible Tactile Sensor for Both Normal and Shear Load Detections and Its Application for Robotics," *J. Microelectromech. Syst.*, vol. 16, no. 3, pp. 556–563, 2007.

[9] K. Noda, Y. Hashimoto, Y. Tanaka, and I. Shimoyama, "MEMS on robot applications," in *Proc. of the Solid-State Sensors, Actuators and Microsystems Conference*, pp. 2176–2181, 2009.

[10] L. C. Tsao, D. R. Chang, W. P. Shih, and K. C. Fan, "Fabrication and Characterization of Electro-Active Polymer for Flexible Tactile Sensing Array ," *Key Eng. Mater.*, vol. 381-382, pp. 391–394, 2008.

[11] M.-Y. Cheng, C.-M. Tsao, Y. Lai, and Y.-J. Yang, "A novel highly-twistable tactile sensing array using extendable spiral electrodes," in *Proc. of the IEEE 22nd Int. Conf. on Micro Electro Mechanical Systems (MEMS)*, pp. 92–95, 2009.

[12] H. Lee, J. Chung, S. Chang, and E. Yoon, "Normal and Shear Force Measurement Using a Flexible Polymer Tactile Sensor With Embedded Multiple Capacitors," *J. Microelectromech. Syst.*, vol. 17, no. 4, pp. 934–042, 2008.

[13] K. Hosoda, Y. Tada, and M. Asada, "Anthropomorphic robotic soft fingertip with randomly distributed receptors," *Proc. of the 8th Conf. on Intelligent Autonomous Systems*, vol. 54, no. 2, pp. 104–109, 2006.

[14] Y. Yamada, M. Morizono, U. Umetani, and T. Takahashi, "Highly Soft Viscoelastic Robot Skin With a Contact Object-Location-Sensing Capability," *IEEE Trans. Ind. Electron*, vol. 52, no. 4, pp. 960–968, 2005.

[15] S. C. B. Mannsfeld, B. C.-K. Tee, R. M. Stoltenberg, C. V. H.-H. Chen, S. Barman, B. V. O. Muir, A. N. Sokolov, C. Reese, and Z. Bao, "Highly sensitive flexible pressure sensors with microstructured rubber dielectric layers," *Nat. Mater.*, vol. 9, no. 10, pp. 859–864, 2010.

[16] G. Schwartz, B. C.-K. Tee, J. Mei, A. L. Appleton, D. H. Kim, H. Wang, and Z. Bao, "Flexible polymer transistors with high pressure sensitivity for application in electronic skin and health monitoring," *Nat. Commun.*, vol. 4, no. 5, p. 1859, 2013.

[17] J. Kim, T. N. Ng, and W. S. Kim, "Highly sensitive tactile sensors integrated with organic transistors," *App. Phys. Lett.*, vol. 101, no. 10, p. 103308, 2012.

[18] Y.-J. Hsu, Z. Jia, and I. Kymissis, "A Locally Amplified Strain Sensor Based on a Piezoelectric Polymer and Organic Field-Effect Transistors," *IEEE Trans. Elec. Dev.*, vol. 58, no. 3, pp. 910–917, 2011.

[19] S. Lai, P. Cosseddu, A. Bonfiglio, and M. Barbaro, "Ultralow Voltage Pressure Sensors Based on Organic FETs and Compressible Capacitors," *IEEE Elec. Dev. Lett.*, vol. 34, no. 6, pp. 801–803, 2013.

[20] T. Someya, T. Sekitani, S. Iba, Y. Kato, H. Kawaguchi, and T. Sakurai, "A large-area, flexible pressure sensor matrix with organic field-effect transistors for artificial skin applications," *PNAS*, vol. 101, no. 27, p. 9966–9970, 2004.

[21] T. Someya, Y. Kato, T. Sekitani, S. Iba, Y. Noguchi, Y. Murase, H. Kawaguchi, and T. Sakurai, "Conformable, flexible, large-area networks of pressure and thermal sensors with organic transistors active matrixes," *PNAS*, vol. 102, no. 35, p. 12321–12325, 2005.

[22] K. Takei, T. Takahashi, J. C. Ho, H. Ko, A. G. Gillies, P. W. Leu, R. S. Fearing, and A. Javey, "Nanowire active-matrix circuitry for low-voltage macroscale artificial skin," *Nat. Mater.*, vol. 9, no. 10, pp. 821–826, 2010.

[23] V. Scenev, P. Cosseddu, A. Bonfiglio, I. Salzmann, N. Severin, M. Oehzelt, N. Koch, and J. Rabe, "Origin of mechanical strain sensitivity of Pentacene thin-film transistors," *Org. Elect.*, vol. 14, no. 5, pp. 1323–1329, 2013.

[24] P. Cosseddu, G. Tiddia, S. Milita, and A. Bonfiglio, "Continuous tuning of the mechanical sensitivity of Pentacene OTFTs on flexible substrates: From strain sensors to deformable transistors," *Org. Elect.*, vol. 14, no. 1, pp. 206–211, 2013.

[25] G. Darlinski, U. Böttger, R. Waser, H. Klauk, M. Halik, U. Zschieschang, G. Schmid, and C. Dehm, "Mechanical force sensors using organic thin-film transistors," *J. Appl. Phys.*, vol. 97, no. 9, p. 093708, 2005.

[26] J. C. Maxwell, "A Dynamical Theory of the Electromagnetic Field," *Phil. Trans. R. Soc. Lond.*, vol. 155, pp. 459–512, 1865.

[27] M. Faraday, *Experimental Researches in Electricity*. Richard and John Edward Taylor., 1839.

[28] P. R. Morris, *A History of the World Semiconductor Industry*. Peter Peregrinus Ltd., 1990.

[29] A. Wilson, "The theory of electronic semi-conductors I," *Proc. R. Soc. Lond. A*, vol. 133, p. 458, 1931.

[30] A. Wilson, "The theory of electronic semi-conductors II," *Proc. R. Soc. Lond. A*, vol. 38, no. 8, pp. 114–117, 1965.

[31] G. Moore, "Cramming more Components onto Integrated Circuits," *Electronics*, vol. 134, p. 277, 1931.

[32] B. Nordén, "The Nobel Prize in Chemistry, 2000: Conductive Polymers," *www.nobelprize.org*, 2000.

[33] F. G. Brunetti, R. Kumar, and F. Wudl, "Organic electronics from perylene to organic photovoltaics: painting a brief history with a broad brush," *J. Mater. Chem.*, vol. 20, pp. 2934–2948, 2010.

[34] A. Moliton and R. C. Hiorns, "The origin and development of (plastic) organic electronics," *Polym. Int.*, vol. 61, pp. 337–341, 2012.

[35] J. Berzelius, *Jahres-Bericht über die Fortschritte der physischen Wissenschaften.* Eilfter Jahrgang, 1832.

[36] H. Letheby, "On the production of a blue substance by the electrolysis of sulphate of aniline," *J. Chem. Soc.*, vol. 15, pp. 161–163, 1862.

[37] A. Pochettino and A. Sella, "Photoelectric behavior of anthracene," *Atti Acad. Lincei*, vol. 15, pp. 355–363, 1906.

[38] H. Akamatu, H. Inokuchi, and Y. Matsunaga, "Electrical Conductivity of the Perylene-Bromine Complex," *Nature*, vol. 173, no. 4395, pp. 168–169, 1954.

[39] J. A. Pople and S. H. Walmsley, "Bond alternation defects in long polyene molecules," *Molecular Phys.*, vol. 5, no. 1, pp. 15–20, 1962.

[40] G. Natta, P. Pino, G. Mazzanti, U. Giannini, E. Mantica, and M. Peraldo, "The nature of some soluble catalysts for low pressure ethylene polymerization," *J. Pol. Sci. Pol. Chem.*, vol. 26, no. 112, pp. 120–123, 1957.

[41] A. Fredga, "The Nobel Prize in Chemistry, 1963: Ziegler-Natta polymerization," *www.nobelprize.org*, 1963.

[42] W. A. Little, "Superconductivity of organic polymers," *J. of Polym. Sci. C*, vol. 17, no. 1, pp. 1–12, 1967.

[43] V. V. Walatka, M. M. Labes, and J. H. Perlstein, "Polysulfur Nitride — a One-Dimensional Chain with a Metallic Ground State," *J. of Polym. Sci. C*, vol. 17, no. 1, pp. 1–12, 1967.

[44] T. Ito, H. Shirakawa, and S. Ikeda, "Thermal *cis-trans* isomerization and decomposition of polyacetylene," *J. Pol. Sci. Pol. Chem*, vol. 13, no. 8, pp. 1943–1950, 1975.

[45] H. Shirakawa, E. J. Louis, A. G. MacDiarmid, C. K. Chiang, and A. J. Heeger, "Synthesis of Electrically Conducting Organic Polymers: Halogen Derivatives of Polyacetylene, $(CH)_x$," *J. Chem. Soc. Chem. Comm*, pp. 578–580, 1977.

[46] C. K. Chiang, C. R. Fincher, Y. W. Park, A. J. Heeger, H. Shirakawa, E. J. Louis, S. C. Gau, and A. G. MacDiarmid, "Electrical Conductivity in Doped Polyacetylene," *Phys. Rev. Lett.*, vol. 39, no. 17, pp. 1698–1701, 1977.

[47] W. P. Su, J. R. Schrieffer, and A. J. Heeger, "Solitons in Polyacetylene," *Phys. Rev. Lett.*, vol. 42, no. 25, pp. 1098–1101, 1979.

[48] J. L. Brédas, R. R. Chance, and R. Silbey, "Comparative theoretical study of the doping of conjugated polymers: Polarons in polyacetylene and polyparaphenylene," *Phys. Rev. B*, vol. 26, no. 10, pp. 5843–5854, 1982.

[49] A. J. Heeger, S. Kivelson, J. R. Schrieffer, and W. P. Su, "Solitons in conducting polymers," *Rev. Modern Phys.*, vol. 60, no. 3, pp. 781–851, 1988.

[50] C. W. Tang and S. A. VanSlyke, "Organic electroluminescent diodes," *Appl. Phys. Lett.*, vol. 51, no. 12, pp. 913–915, 1987.

[51] J. H. Burroughes, D. D. C. Bradly, A. R. Brown, R. N. Marks, K. Mackay, R. H. Friend, P. L. Burns, and A. B. Holmes, "Light-emitting diodes based on conjugated polymers," *Nature*, vol. 347, pp. 539–541, 1990.

[52] N. Geacintov and M. Pope, "Generation of Charge Carriers in Anthracene with Polarized Light," *J. Chem. Phys.*, vol. 47, pp. 1194–1195, 1967.

[53] H. Antoniadis, B. Hsieha, M. Abkowitza, S. Jenekhea, and M. Stolka, "Photovoltaic and photoconductive properties of aluminum/poly(*p*-phenylene vinylene) interfaces," *Synt. Metals*, vol. 62, no. 3, pp. 265–271, 1994.

[54] N. S. Sariciftci, L. Smilowitz, A. J. Heeger, and F. Wudl, "Photoinduced Electron Transfer from a Conducting Polymer to Buckminsterfullerene," *Science*, vol. 258, no. 5087, pp. 1474–1476, 1992.

[55] J. J. M. Halls, C. A. Walsh, N. C. Greenham, E. A. Marseglia, R. H. Friend, S. C. Moratti, and A. B. Holmes, "Efficient photodiodes from interpenetrating polymer networks," *Nature*, vol. 376, pp. 498–500, 1995.

[56] J. H. Burroughes, C. A. Jones, and R. H. Friend, "New semiconductor device physics in polymer diodes and transistors," *Nature*, vol. 335, pp. 137–141, 1988.

[57] F. Garnier, G. Horowitz, X. Peng, and D. Fichou, "An all-organic "soft" thin film transistor with very high carrier mobility," *Adv. Mater.*, vol. 2, no. 12, pp. 592–594, 1990.

[58] L. Kergoat and B. Piro and M. Berggren and G. Horowitz and M.-C. Pham, "Advances in organic transistor-based biosensors: from organic electrochemical transistors to electrolyte-gated organic field-effect transistors," *Anal. Bioanal. Chem.*, vol. 402, pp. 1813–1826, 2012.

[59] C. D. Dimitrakopoulos and P. R. L. Malenfant, "Organic Thin Film Transistors for Large Area Electronics," *Adv. Mater.*, vol. 14, no. 2, pp. 99–117, 2002.

[60] H. Sirringhaus, "Device Physics of Solution-Processed Organic Field-Effect Transistors," *Adv. Mater.*, vol. 17, no. 20, pp. 2411–2425, 2005.

[61] H. Sirringhaus, "25th Anniversary Article: Organic Field-Effect Transistors: The Path Beyond Amorphous Silicon," *Adv. Mater.*, 2014.

[62] T. A. Finland, "The Millennium Technology Prize 2010," *www.technologyacademy.fi*, 2010.

[63] "IC Insights Expects Big Changes to 2013 Top 20 Semi Supplier Ranking." *www.icinsights.com*, 2013.

[64] "The Promise Of Organic Electronics." *www.pddnet.com*, 2009.

[65] K. Myny and S. Steudel and P. Vicca and M. J. Beenhakkers and N. A. J. M. van Aerle and G. H. Gelinck and J. Genoe and W. Dehaene and P. Heremans, "Organic RFID Tags," in *Radio Frequency Identification Fundamentals and Applications. Design Methods and Solutions*, ch. 18, pp. 311–324, InTech, 2010.

[66] J. Heikenfeld and P. Drzaic and J.-S. Yeo and T. Koch, "A critical review of the present and future prospects for electronic paper," *J. Soc. Inf. Display*, vol. 19, no. 2, pp. 129–156, 2011.

[67] D. Tobjörk and R. Österbacka, "Paper Electronics," *Adv. Mater.*, vol. 23, pp. 1935–1961, 2011.

[68] M. Gross and D. C. Müller and H.-G. Nothofer and U. Scherf and D. Neher and C. Bräuchle and K. Meerholz, "Improving the performance of doped π-conjugated polymers for use in organic light- emitting diodes," *Nature*, vol. 405, pp. 661–665, 2000.

[69] F. A. Carey, *Organic Chemistry*. McGrow-Hill, 2001.

[70] W. Demtröder, *Atoms, Molecules and Photons. An Introduction to Atomic-, Molecular- and Quantum-Physics*. Springer, 2006.

[71] M. C. Petty, *Molecular Electronics. From Principles to Practice*. Wiley, 2007.

[72] M. C. J. M. Vissenberg and M. Matters, "Theory of the field-effect mobility in amorphous organic transistors," *Phys. Rev. B*, vol. 57, no. 20, pp. 12964–12967, 1998.

[73] G. Horowitz and M. H. Hajlaoui, "Mobility in Polycrystalline Oligothiophene Field-Effect Transistors Dependent on Grain Size," *Adv. Mater.*, vol. 12, no. 14, pp. 1046–1050, 2000.

[74] A. Facchetti, "Semiconductors for organic transistors," *Mater. Today*, vol. 10, no. 3, pp. 28–37, 2007.

[75] W. J. Feast, J. Tsibouklis, K. L. Pouwer, L. Groenendaal, and E. W. Meijer, "Synthesis, processing and material properties of conjugated polymers," *Polymers*, vol. 37, no. 22, pp. 5017–5047, 1996.

[76] P. F. Moonen, I. Yakimets, and J. Huskens, "Fabrication of Transistors on Flexible Substrates: from Mass-Printing to High-Resolution Alternative Lithography Strategies," *Adv. Mater.*, vol. 24, no. 41, pp. 5526–5541, 2012.

[77] B. Kang, W. H. Lee, and K. Cho, "Recent Advances in Organic Transistor Printing Processes," *ACS Appl. Mater. Interf.*, vol. 5, no. 7, pp. 2302–2315, 2013.

[78] A. Teichler, J. Perelaer, and U. S. Schubert, "Inkjet printing of organic electronics – comparison of deposition techniques and state-of-the-art developments," *J. Mater. Chem. C*, vol. 1, no. 10, pp. 1910–1925, 2013.

[79] F. C. Krebs, M. Jørgensen, K. Norrman, O. Hagemann, J. Alstrup, T. D. N. andJ. Fyenbo, K. Larsen, and J. Kristensen, "A complete process for production of flexible large area polymer solar cells entirely using screen printing—First public demonstration," *Sol. En. Mat. Sol. Cells*, vol. 93, no. 4, pp. 422–441, 2009.

[80] K. K. B. Hon, L. Li, and I. M. Hutchings, "Direct writing technology—Advances and developments," *CIRP Annals - Manuf. Tech.*, vol. 57, no. 2, pp. 601–620, 2008.

[81] J. C. Ribierre, T. Fujihara, S. Watanabe, M. Matsumoto, T. Muto, A. Nakao, and T. Ayoama, "Direct Laser Writing of Complementary Logic Gates and Lateral p–n Diodes in a Solution- Processible Monolithic Organic Semiconductor," *Adv. Mater.*, vol. 22, no. 15, pp. 1722–1726, 2010.

[82] C. Duty, D. Jean, and W. J. Lackey, "Laser chemical vapour deposition: materials, modelling, and process control," *Intern. Mater. Rev.*, vol. 46, no. 6, pp. 271–287, 2001.

[83] R. J. von Gutfeld, E. E. Tynan, R. L. Melcher, and S. E. Blum, "Laser enhanced electroplating and maskless pattern generation," *Appl. Phys. Lett.*, vol. 35, p. 651, 1979.

[84] C. L. Kang, Y. Xu, K. L. Yung, and W. Chen, "Laser Induced Forward Transfer," *Adv. Mater. Res.*, vol. 591-593, pp. 1135–1138, 2012.

[85] H. P. Le, "Progress and Trends in Ink-jet Printing Technology," *J. Imag. Sci. Tech.*, vol. 42, no. 1, pp. 49–62, 1998.

[86] T. Kawase, T. Shimoda, C. Newsome, H. Sirringhaus, and R. H. Friend, "Inkjet printing of polymer thin film transistors," *Thin Solid Films*, vol. 438-439, pp. 279–287, 2003.

[87] M. Singh, H. M. Haverinen, P. Dhagat, and G. E. Jabbour, "Inkjet Printing - Process and Its Applications," *Adv. Mater.*, vol. 22, no. 6, pp. 673–685, 2010.

[88] "Dimatix Materials Printer DMP-2831." *www.fujifilmusa.com/products/industrial_inkjet_printheads/deposition-products/dmp-2800/*.

[89] "Dimatix Materials Printer DMP-2800 Series User Manual." Fujifilm Dimatix, 2008.

[90] J. E. Fromm, "Numerical Calculation of the Fluid Dynamics of Drop-on-Demand Jets," *IBM J. Res. Dev.*, vol. 28, no. 3, pp. 322–333, 1984.

[91] N. Reis, C. Ainsley, and B. Derby, "Ink-jet delivery of particle suspensions by piezoelectric droplet ejectors," *J. Appl. Phys.*, vol. 97, no. 094903, 2005.

[92] R. Rioboo, M. Marengo, and C. Tropea, "Time evolution of liquid drop impact onto solid, dry surfaces," *Exp. Fluids*, vol. 33, no. 1, pp. 112–124, 2002.

[93] J. N. Israelachvili, "Adhesion and Wetting Phenomena," in *Intermolecular and Surface Forces, 3rd Edition*, ch. 17, pp. 415–468, Academic Press, 2011.

[94] C. Kim, M. Nogi, and K. Suganuma, "Electrical conductivity enhancement in inkjet-printed narrow lines through gradual heating," *J. Micromech. Microeng.*, vol. 22, no. 3, p. 035016, 2012.

[95] R. D. Deegan, O. Bakajin, T. F. Dupont, G. Huber, S. R. Nagel, and T. A. Witten, "Capillary flow as the cause of ring stains from dried liquid drops," *Nature*, vol. 389, pp. 827–829, 1997.

[96] *www.goodfellow.com*.

[97] *www.dupont.com*.

[98] *www.piezotech.fr*.

[99] *www.smooth-on.com*.

[100] *www.dowcorning.com*.

[101] *www.3m.com*.

[102] P. Cosseddu, S. Lai, M. Barbaro, and A. Bonfiglio, "Ultra-low voltage, organic thin film transistors fabricated on plastic substrates by a highly reproducible process," *Appl. Phys. Lett.*, vol. 100, p. 093305, 2012.

[103] *www.cabot-corp.com*.

[104] H.-H. Lee, K.-S. Chou, and K.-C. Huang, "Inkjet printing of nanosized silver colloids," *Nanotech.*, vol. 16, no. 10, pp. 2436–2441, 2005.

[105] L. Groenendaal, F. Jonas, D. Freitag, H. Pielartzik, and J. R. Reynolds, "Poly(3,4-ethylenedioxythiophene) and Its Derivatives: Past, Present, and Future," *Adv. Mater.*, vol. 12, no. 7, pp. 481–494, 2000.

[106] *www.heraeus-clevios.com*.

[107] *www.sigmaaldrich.com*.

[108] P. G. Schroeder, C. B. France, J. B. Park, and B. A. Parkinson, "Energy level alignment and two-dimensional structure of pentacene on Au(111) surfaces," *J. Appl. Phys.*, vol. 91, p. 3010, 2002.

[109] Y.-Y. Lin, D. J. Gundlach, S. F. Nelson, and T. N. Jackson, "Stacked pentacene layer organic thin-film transistors with improved characteristics," *IEEE Elec. Dev. Lett.*, vol. 18, no. 12, pp. 606–608, 1997.

[110] F.-J. Meyer zu Heringdorf, M. C. Reuter, and R. M. Tromp, "Growth dynamics of pentacene thin films," *Nature*, vol. 412, pp. 517–520, 2001.

[111] B. Stadlober, M. Zirkl, M. Beutl, G. Leising, S. Bauer-Gogonea, and S. Bauer, "High-mobility pentacene organic field-effect transistors with a high-dielectric-constant fluorinated polymer film gate dielectric," *Appl. Phys. Lett.*, vol. 86, p. 242902, 2005.

[112] O. L. Griffith, J. E. Anthony, A. G. Jones, and D. L. Lichtenberger, "Electronic Properties of Pentacene versus Triisopropylsilylethynyl-Substituted Pentacene: Environment-Dependent Effects of the Silyl Substituent," *J. Am. Chem. Soc.*, vol. 132, no. 2, pp. 580–586, 2010.

[113] S. K. Park, T. N. Jackson, J. E. Anthony, and D. A. Mourey, "High mobility solution processed 6,13-bis(triisopropyl-silylethynyl) pentacene organic thin film transistors," *Appl.Phys. Lett.*, vol. 91, no. 6, p. 063514, 2007.

[114] C. W. Sele, B. K. C. Kjellander, B. N. andM. J. Thornton, J. B. P. H. van der Putten, K. Myny, H. J. Wondergem, A. Moser, R. Resel, A. J. J. M. van Breemen, N. van Aerle, P. Heremans, J. E. Anthony, and G. H. Gelinck, "Controlled Deposition of Highly Ordered Soluble Acene Thin Films: Effect of Morphology and Crystal Orientation on Transistor Performance," *Adv. Mater.*, vol. 21, no. 48, pp. 4926–4931, 2009.

[115] M. T. Dang, L. Hirsch, and G. Wantz, "P3HT:PCBM, Best Seller in Polymer Photovoltaic Research," *Adv. Mater.*, vol. 23, no. 31, pp. 3597–3602, 2011.

[116] J. Piris, T. E. Dykstra, A. A. Bakulin, P. H. M. van Loosdrecht, W. Knulst, M. T. Trinh, J. M. Schins, and L. D. A. Siebbeles, "Photogeneration and Ultrafast Dynamics of Excitons and Charges in P3HT/PCBM Blends," *J. Phys. Chem. C*, vol. 113, no. 32, pp. 14500–14506, 2009.

[117] M. Ramuz, L. Bürgi, C. Winnewisser, and P. Seitz, "High sensitivity organic photodiodes with low dark currents and increased lifetimes," *Org. Elect.*, vol. 9, no. 3, pp. 369–376, 2008.

[118] *www.polyera.com*.

[119] *www.scscoatings.com*.

[120] *www.archchemicals.com*.

[121] J. C. Love, L. A. Estroff, J. K. Kriebel, R. G. Nuzzo, and G. M. Whitesides, "Self-Assembled Monolayers of Thiolates on Metals as a Form of Nanotechnology," *Chem. Rev.*, vol. 105, no. 4, p. 1103–1170, 2005.

[122] X. Crispin, S. Marciniak, W. Osikowicz, G. Zotti, A. V. Denier van der Gon, F. Louwet, M. Fahlman, L. Groenendaal, F. De Schryver, and W. R. Salaneck, "Conductivity, morphology, interfacial chemistry, and stability of poly(3,4-ethylene dioxythiophene)–poly(styrene sulfonate): A photoelectron spectroscopy study," *J. Polym. Sci. B Polym. Phys.*, vol. 41, no. 21, p. 2561–2583, 2003.

[123] J. Ouyang, Q. Xu, C.-W. Chu, Y. Yang, G. Li, and J. Shinar, "On the mechanism of conductivity enhancement in poly(3,4-ethylenedioxythiophene):poly(styrene sulfonate) film through solvent treatment," *Polymer*, vol. 45, no. 25, p. 8443–8450, 2004.

[124] J.-P. Hong, A.-Y. Park, S. Lee, and J. Kang, "Tuning of Ag work functions by self-assembled monolayers of aromatic thiols for an efficient hole injection for solution processed triisopropylsilylethynyl pentacene organic thin film transistors," *Appl. Phys. Lett.*, vol. 92, no. 14, p. 143311, 2008.

[125] Y. Zhou, C. Fuentes-Hernandez, J. Shim, J. Meyer, A. J. Giordano, H. Li, P. Winget, T. Papadopoulos, H. Cheun, J. Kim, M. Fenoll, A. Dindar, W. Haske, E. Najafabadi, T. M. Khan, H. Sojoudi, S. Barlow, S. Graham, J.-L. Brédas, S. R. Marder, A. Kahn, and B. Kippelen, "A Universal Method to Produce Low–Work Function Electrodes for Organic Electronics," *Science*, vol. 336, no. 6079, pp. 327–332, 2012.

[126] M.-B. Madec, P. J. Smith, A. Malandraki, W. Nan, J. G. Korvink, and S. G. Yeates, "Enhanced reproducibility of inkjet printed organic thin film transistors based on solution processable polymer-small molecule blends," *J. Mat. Chem.*, vol. 20, no. 41, pp. 9155–9160, 2010.

[127] S. Y. Cho, J. M. Ko, J.-Y. Jung, J. Y. Lee, D. H. Choi, and C. Lee, "High-performance organic thin film transistors based on inkjet-printed polymer/TIPS pentacene blends," *Org. Elec.*, vol. 13, no. 8, p. 1329–1339, 2012.

[128] H. Yousef, M. Boukallel, and K. Althoefer, "Tactile sensing for dexterous in-hand manipulation in robotics — A review," *Sens. Act. A Phys.*, vol. 167, no. 2, p. 171–187, 2011.

[129] T. Sekitani, Y. Kato, S. Iba, H. Shinaoka, T. Someya, T. Sakurai, and S. Takagi, "Bending experiment on Pentacene field-effect transistors on plastic films," *Appl. Phys. Lett.*, vol. 86, no. 7, p. 073511, 2005.

[130] Z. Suo, E. Y. Ma, H. Gleskova, and S. Wagner, "Mechanics of rollable and foldable film-on-foil electronics," *Appl. Phys. Lett.*, vol. 74, no. 8, pp. 1177–1179, 1999.

[131] C. Yang, J. Yoon, S. H. Kim, K. Hong, D. S. Chung, K. Heo, C. E. Park, and M. Ree, "Bending-stress-driven phase transitions in Pentacene thin films for flexible organic field-effect transistors," *Appl. Phys. Lett.*, vol. 92, no. 24, p. 243305, 2008.

[132] P. Cosseddu, S. Milita, and A. Bonfiglio, "Strain Sensitivity and Transport Properties in Organic Field Effect Transistors," *IEEE Elect. Dev. Lett.*, vol. 33, no. 1, pp. 113–115, 2012.

[133] A. Jedaa and M. Halik, "Towards strain resistant flexible organic thin film transistors," *Appl. Phys. Lett.*, vol. 95, no. 10, p. 103309, 2009.

[134] A. N. Sokolov, Y. Cao, O. B. Johnson, and Z. Bao, "Mechanistic Considerations of Bending-Strain Effects within Organic Semiconductors on Polymer Dielectrics," *Adv. Func. Mater.*, vol. 22, no. 1, pp. 175–183, 2012.

[135] Z. Rang, M. I. Nathan, P. P. Ruden, V. Podzorov, M. E. Gershenson, C. R. Newman, and C. D. Frisbie, "Hydrostatic pressure dependence of charge carrier transport in single-crystal rubrene devices," *Appl. Phys. Lett.*, vol. 86, no. 12, p. 123501, 2005.

[136] S. Jung, T. Ji, and V. K. Varadan, "Pentacene-based low-voltage strain sensors with PVP/Ta2O5 hybrid gate dielectrics," *IEEE Trans. Elect. Dev.*, vol. 57, no. 2, pp. 391–396, 2010.

[137] I. Manunza, A. Sulis, and A. Bonfiglio, "Pressure sensing by flexible, organic, field effect transistors," *Appl. Phys. Lett.*, vol. 89, no. 14, p. 143502, 2006.

[138] I. Manunza and A. Bonfiglio, "Pressure sensing using a completely flexible organic transistor," *Biosens. Bioelect.*, vol. 22, no. 12, p. 2775–2779, 2007.

[139] A. Loi, L. Basiricò, P. Cosseddu, S. Lai, P. Maiolino, E. Baglini, S. Denei, F. Mastrogiovanni, G. Cannata, C. Palomba, M. Barbaro, and A. Bonfiglio, "Matrices of inkjet printed OFETs for the realization of artificial robotic skin," in *MRS Proceedings*, vol. 1401, Cambridge University Press, 2012.

[140] L. Basiricò, *Inkjet Printing of Organic Transistor Devices*. PhD thesis, PhD School in Information Engineering, 2012.

[141] S. H. Lee, M. H. Choi, S. H. Han, D. J. Choo, J. Jang, and S. K. Kwon, "High-performance thin-film transistor with 6,13-bis(triisopropylsilylethynyl) pentacene by inkjet printing," *Org. Elect.*, vol. 9, no. 5, p. 721–726, 2008.

[142] M.-B. Madec, P. J. Smith, A. Malandraki, N. Wang, J. G. Korvink, and S. G. Yeates, "Enhanced reproducibility of inkjet printed organic thin film transistors based on solution processable polymer-small molecule blends," *J. Mater. Chem.*, vol. 20, no. 41, pp. 9155–9160, 2010.

[143] B. K. C. Kjellander, W. T. T. Smaal, J. E. Anthony, and G. H. Gelinck, "Inkjet Printing of TIPS-PEN on Soluble Polymer Insulating Films: A Route to High-Performance Thin-Film Transistors," *Adv. Mater.*, vol. 22, no. 41, p. 4612–4616, 2010.

[144] S. Chung, S. O. Kim, S.-K. Kwon, C. Lee, and Y. Hong, "All-Inkjet-Printed Organic Thin-Film Transistor Inverter on Flexible Plastic Substrate," *IEEE Elect. Dev. Lett.*, vol. 32, no. 8, pp. 1134–1136, 2011.

[145] X. Li, W. T. T. Smaal, C. Kjellander, B. van der Putten, K. Gualandris, E. C. P. Smits, J. Anthony, D. J. Broer, P. W. M. Blom, J. Genoe, and G. Gelinck, "Charge transport in high-performance ink-jet printed single-droplet organic transistors based on a silylethynyl substituted pentacene/insulating polymer blend," *Org. Elect.*, vol. 12, no. 8, p. 1319–1327, 2011.

[146] M. W. Lee, G. S. Ryu, Y. U. Lee, C. Pearson, M. C. Petty, and C. K. Song, "Control of droplet morphology for inkjet-printed TIPS-pentacene transistors," *Microelect. Eng.*, vol. 95, pp. 1–4, 2012.

[147] S. Y. Cho, J. M. Ko, J. Lim, J. Y. Lee, and C. Lee, "Inkjet-printed organic thin film transistors based on TIPS pentacene with insulating polymers," *J. Mater. Chem. C*, vol. 1, no. 5, pp. 914–923, 2013.

[148] *www.aurelautomation.com*.

[149] *www.roboskin.eu*.

[150] A. Loi, L. Basiricò, P. Cosseddu, S. Lai, M. Barbaro, A. Bonfiglio, P. Maiolino, E. Baglini, S. Denei, F. Mastrogiovanni, and G. Cannata, "Organic Bendable and Stretchable Field Effect Devices for Sensing Applications," *IEEE Sensors J.*, vol. 13, no. 12, pp. 4764–4772, 2013.

[151] S. J. Zilker, C. Detcheverry, E. Cantatore, and D. M. de Leeuw, "Bias stress in organic thin-film transistors and logic gates," *Appl. Phys. Lett.*, vol. 79, no. 8, pp. 1124–1126, 2001.

[152] *www.faulhaber.com*.

[153] *it.farnell.com*.

[154] *www.artcorp.com*.

[155] L. Seminara, L. Pinna, M. Valle, L. Basiricò, A. Loi, P. Cosseddu, A. Bonfiglio, A. Ascia, M. Biso, A. Ansaldo, D. Ricci, and G. Metta, "Piezoelectric Polymer Transducer Arrays for Flexible Tactile Sensors," *IEEE Sensors J.*, vol. 13, no. 10, pp. 4022–4029, 2013.

[156] *hymec2.physik.hu-berlin.de*.

[157] K. Ohla, N. A. Busch, and J. N. Lundström, "Time for Taste—A Review of the Early Cerebral Processing of Gustatory Perception," *Chemosens. Percep.*, vol. 5, no. 1, pp. 87–99, 2012.

[158] N. Chaudhari and S. D. Roper, "The cell biology of taste," *J. Cell Biol.*, vol. 190, no. 3, pp. 285–296, 2010.

[159] G. M. Feldman, A. Mogyorósi, G. L. Heck, J. A. DeSimone, C. R. Santos, R. A. Clary, and V. Lyall, "Salt-Evoked Lingual Surface Potential in Humans," *J. Neurophysiol.*, vol. 90, p. 2060–2064, 2003.

[160] G. A. Casula, G. Montisci, and G. Mazzarella, "A Wideband PET Inkjet-Printed Antenna for UHF RFID," *IEEE Antennas Wireless Propag. Lett.*, vol. 12, pp. 1400–1403, 2013.

[161] J. Virtanen, T. Björninen, L. Ukkonen, and L. Sydänheimo, "Passive UHF Inkjet-Printed Narrow-Line RFID Tags," *IEEE Antennas Wireless Propag. Lett.*, vol. 9, pp. 440–443, 2010.

[162] T. W. Koo, D. Kim, J. I. Ryu, H. M. Seo, J. G. Yook, and J. C. Kim, "Design of a label-typed UHF RFID tag antenna for metallic objects," *IEEE Antennas Wireless Propag. Lett.*, vol. 10, pp. 1010–1014, 2011.

[163] M. A. Ziai and J. C. Batchelor, "Temporary On-Skin Passive UHF RFID Transfer Tag," *IEEE Trans. Antennas Propag.*, vol. 59, no. 10, pp. 3565–3571, 2011.

[164] A. Kahn, N. Koch, and W. Gao, "Electronic structure and electrical properties of interfaces between metals and π-conjugated molecular films," *J. Polym. Sci. B Polym. Phys.*, vol. 41, no. 21, p. 2529–2548, 2003.

[165] A. Haldi, A. Sharma, W. J. Potscavage, and B. Kippelen, "Equivalent circuit model for organic single-layer diodes," *J. Appl. Phys.*, vol. 104, no. 6, p. 064503, 2008.

[166] C. Hyun Kim, O. Yaghmazadeh, Y. Bonnassieux, and G. Horowitz, "Modeling the low-voltage regime of organic diodes: Origin of the ideality factor," *J. Appl. Phys.*, vol. 110, no. 9, p. 093722, 2011.

[167] G. Horowitz, R. Hajlaoui, H. Bouchriha, R. Bourguiga, and M. Hajlaoui, "The Concept of "Threshold Voltage" in Organic Field-Effect Transistors," *Adv. Mater.*, vol. 10, no. 12, pp. 923–927, 1998.